# Comparative Study of Nonlinear Acoustic and Guided Wave Methods for Structural Damage Detection

by

Kai Yang

Submitted for the degree of Doctor of Philosophy

November 2014


The University Of Sheffield.

Department of Mechanical Engineering

Supervisors: Prof. Keith Worden and

Dr. Jem Rongong

# Abstract

The overall purpose of this research work is to use nonlinear acoustic techniques and Lamb wave methods for Structural Health Monitoring (SHM). The work constitutes fatigue crack detection studies on glass and aluminium plates as well as low-velocity impact damage and compression damages on carbon fibre reinforced polymer. In addition, the SHM techniques were evaluated by detecting damage on a hammer impacted wind turbine blade.

For nonlinear acoustic tests, *Finite Element* (FE) modeling was used to calculate the crack edge divergence for three different crack modes. After that, FE modeling extracted the modal parameters (e.g. natural frequencies and mode shapes) of vibration modes for the corresponding crack modes. These selected vibration modes were used for low frequency excitation in nonlinear acoustic experiments. Experimental work was performed to analyse the effect of nonlinear acoustics by signal wave excitation, *Frequency Response Function*s (FRFs) with varying excitation levels and Vibro-acoustic excitation. Various physical mechanisms to account for these effects have been investigated. The experimental results present three main nonlinear effects. These effects are non-classical *Luxemburg-Gorky* (L-G) type dissipation, the dissipation mechanism related to crack-wave interaction and nonlinear elasticity.

The application of outlier analysis on Lamb wave tests is a novelty detection method. This method has indicated successful classification for undamaged and damaged data in fatigue tests, compression tests and impact tests. In addition, outlier analysis is able to give an indication of damage severity in the glass plate test. Moreover, outlier analysis gives the information to localise damage in the wind turbine blade test.

# Acknowledgements

I express my sincere gratitude to my supervisor Prof. Keith Worden for his endless support, invaluable guidance and patience throughout this study. His supervision has taught me how to do research and I have gained a lot from his knowledge. Meanwhile, I would like to thank Dr. Jem Rongong for providing brilliant suggestions and helpful feedback. I continue my appreciation to Prof. Wieslaw Staszewski for supervision of my early research work and providing the idea for the glass plate test.

I wish to thank Professor Russell Hand for his advice on how to introduce and grow a crack on the glass plate. Without his help, the glass plate test would not have been possible to complete. I also extend my thanks to Dr. Evangelos Papatheou for helping me with the LMS system. I would like to thank Austin Lafferty for assisting me in manufacturing composite laminates.

I would like to acknowledge Les Morton for his eagerness in preparing test rig and assisting in the impact test. I also thank Mike Rennison for helping me in the fatigue test. Special thanks to Chris Grigson for adjusting test equipment.

Thanks must also go to all my colleagues and officemates in the *Dynamics Research Group* (DRG), for their warm advices and support.

Lastly, I would like to extend my sincere thanks to my parents for their support and encouragement throughout the entire time of my study.

# Table of Contents

# List of Figures

# List of Tables

# List of Abbreviations

| | |
|---|---|
| SHM | Structural Health Monitoring |
| FE | Finite Element |
| FRF | Frequency Response Function |
| L-G | Luxemburg-Gorky |
| DRG | Dynamics Research Group |
| SDD | Structural damage detection |
| CFRP | *Carbon Fiber Reinforced Polymer* |
| BVID | Barely Visible Impact Damage |
| NDT/E | Non-Destructive Test/Evaluation |
| NDT | Non-Destructive Test |
| VI | Visual Inspection |
| UI | Ultrasonics Inspection |
| EC | Eddy Current |
| AE | Acoustic Emission |
| AC | Alternating Current |
| DIC | Digital image correlation |
| PR | Pattern Recognition |
| CED | Crack Edge Divergence |
| NRUS | Nonlinear resonant ultrasound spectroscopy |
| US | *United States* |
| HF | High Frequency |
| LF | Low Frequency |

| | |
|---|---|
| PZT | Piezoelectric Transducers |
| FFT | Fast Fourier Transform |
| EMD | Empirical Mode Decomposition |
| MSD | Mahalanobis Squared Distance |
| ACG | Advanced Composite Group |
| AMRC | Advanced Manufacturing Research Centre |
| PCB | PicoCoulomB |
| LMS | Least Median of Squares |
| LTS | Least Trimmed Squares |
| MVE | Minimum Volume Ellipsoid |
| MCD | Minimum Covariance Determinant Estimateion |

# List of Symbols

| | |
|---|---|
| mm | millimetre |
| J | Joule |
| $\sigma$ | stress |
| ε | strain |
| $K$ | a function of strain $\varepsilon$ and the time derivative of strain $\dot{\varepsilon}$ |
| $K_0$ | linear modulus |
| $\beta$ | 1st order perturbation coefficient |
| $\delta$ | 2nd order perturbation coefficient |
| $\omega$ | angular frequency |
| $A$ | magnitude of frequency component |
| $x$ | wave propagation distance |
| $c$ | wave velocity |
| α | a measure of the material hysteresis |
| Δε | local strain amplitude ( $10^{-6} - 10^{-7}$ ) over the previous load cycling period |
| $f_0$ | linear resonance frequency |
| $f$ | resonance frequency |
| $R$ | modulation intensity |
| $B_0$, $B_1$, $B_2$ | magnitude of the high frequency ultrasonic component and the first pair of modulation sidebands |

| | |
|---|---|
| $k$ | wave number |
| $\lambda_{wave}$ | wavelength of the wave |
| $h_{half}$ | half thickness of the plate |
| $C_L$ | velocities of longitudinal mode |
| $C_T$ | velocities of transverse/shear mode |
| $E$ | Young's modulus |
| $\upsilon$ | Poisson ratio |
| $\rho$ | density |
| $S_0$, $S_1$, $S_{2...}$ | symmetric modes |
| $A_0$, $A_1$, $A_{2...}$ | antisymmetric modes |
| $C_p$ | the phase velocity |
| $C_g$ | the group velocity |
| $\bar{k}$ | average wave number |
| $\bar{\omega}$ | average frequency |
| $h(n)$ | hanning function |
| $N$ | sample point |
| $x_\zeta$ | potential outlier |
| $\bar{x}$ | sample mean |
| $S$ | standard deviation of training data |
| $\boldsymbol{D}_\zeta$ | Mahalanobis Squared Distance |

| | |
|---|---|
| $T$ | transpose |
| $p$ | dimension |
| $m$ and $n$ | sample sizes |
| $h_0$ | null hypothesis |
| $h_a$ | alternative hypothesis |
| $\alpha_{error}$ | probability of a *Type* I *error* |
| $\beta_{error}$ | probability of a *Type* II *error* |
| $\mu$ | unknown population means |
| $\alpha_s$ | statistical significance level |
| $f_{t,k}$ | tensile strength |
| $g/cm^3$ | gram per cubic centimetre |
| $f_{c,k}$ | compressive strength |
| Mpa | Mega pascal |
| G | shear modulus |
| Gpa | Giga pascal |
| $f_n$ | resonance frequency of n-th mode |
| $k_s$ | stiffness of the structure |
| $m$ | mass of the structure |
| Hz | hertz |
| a | length of plate |

| | |
|---|---|
| b | width of plate |
| $\lambda_{i,j}$ | a dimensionless frequency parameter for rectangular plates |
| γ | mass of per unit area of plate |
| Vpp | peak-to-peak voltage |
| GS/s | Giga samples per second |
| kg | kilogram |
| V | voltage |
| df | degree of freedom |
| $t_{a_s,n}$ | test statistic value |
| dB | decibel |
| μs | microsecond |
| $\Delta k$ | the range of stress intensity factor |
| $a_c$ | crack length |
| z and d | material constants |
| $\Delta k_{th}$ | threshold value of stress intensity factor |
| $\Delta k_{max}$ | maximum value of stress intensity factor |
| $k_c$ | fracture toughness |
| $\sigma_{c,max}$ | maximum stress |
| $\sigma_0$ | nominal stress |
| $K_c$ | stress intensity factor |

| | |
|---|---|
| $K_t$ | stress concentration factor |
| $\beta_c$ | a dimensionless factor depending on the geometric aspects of the specimen |
| $\sigma_{max}$ | maximum applied stress |
| $\sigma_{min}$ | minimum applied stress |
| $p_{max}$ | maximum applied load |
| $p_{min}$ | minimum applied load |
| $h$ | thickness of the specimen |
| $R_s$ | stress ratio |
| kN | kilonewton |
| g/m$^2$ | gram per square metre |
| °C | degree Celsius |
| °C/min | degree Celsius per minute |
| m/s | metre per second |
| $E_k$ | kinetic energy |
| $E_p$ | potential energy |
| $v$ | velocity of impact |
| g | gravitational acceleration |
| $h_g$ | drop height |

# Chapter 1

# 1 Introduction

## 1.1 Structural damage detection

*Structural damage detection* (SDD) is an element of maintenance activity for ensuring that structures operate safely within their service life. *Structural Health Monitoring* (SHM) is the process of nondestructively identifying damage problems. Monitoring for structural damage is important in many areas of engineering to guarantee safety and operational availability of structures, to extend structural life, to minimise costs associated with maintenance and to predict any future performance. This is particularly relevant to transportation, civil or mechanical infrastructure, energy production and process industries.

General speaking, damage can be defined as changes of material and/or geometric properties introduced into a system that could adversely influence the performance of that system [1]. In a homogeneous material like glass or metal, Jean Lemaitre *et al* [2] described damage as a generation and propagation of microvoids or microcracks, which results in discontinuities in the media. It is worthy to note that the major damages formed in metallic structures are fatigue cracks and corrosion, while in composite structures, the major damages are impact damages and delamination [3].

Fatigue failures in service of metallic structures are well-known phenomena. In a specimen subjected to a cyclic load, a fatigue crack nucleus can be initiated, followed by crack propagation and final fracture of a structure during a cumulative process, even though the highest stress occurring in the structure may be lower than the material yield stress. Usually, the crack initiation stage includes crack nucleation and short crack grown, which may not affect the performance of the structure as its initial

design life. However, the performance level of the structure gradually reduces and after this stage, damage can progress very quickly to catastrophic failure. It is therefore clear that addressing damage in its early stage is essential to prolong the life of the ageing structures.

When a crack is present in the structure, there are three typical crack modes resulting from crack motion, as shown in Figure 1.1. Any deformation of the crack can be considered as a superposition of these three modes, which can be described as follows:

1) Mode-I (opening mode): the crack faces move directly apart from each other in a y-direction in this case (see in Figure 1.1). The tensile stress is perpendicular to the crack plane and tries to open the crack.

2) Mode-II (sliding mode): under the cyclic shear stress, the crack faces slide relative to each other in a direction perpendicular to the crack front.

3) Mode-III (tearing mode): under the cyclic shear stress, the crack faces slide relative to each other in a direction parallel to the crack front.

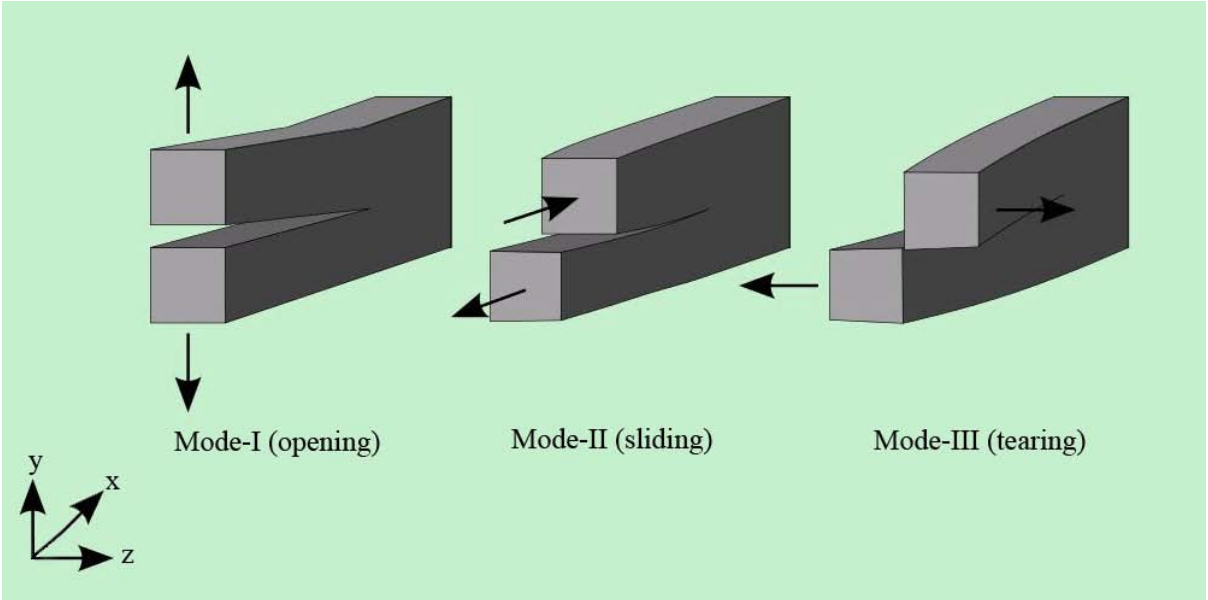


Figure 1.1: Different modes of loading of a crack tip.

Various studies investigated how crack-related elastic nonlinearities contribute to crack wave interactions, as summarised by Jenal [4]. Nazarov *et al* [5] described that acoustic waves can interact with the cracks or micro-cracks in damaged materials much more intensively than in materials with no damage. Johnson *et al* [6], Guyer *et al* [7] and Solodov *et al* [8] stated that acoustic waves exhibit elastic nonlinear effects when they interact with cracks. In addition, other mechanisms of crack-type defects, like crack breathing [9], friction [10] and locally-enhanced thermoelastic coupling at the inner crack contacts [11] were presented in a great number of studies.

When composites were introduced into the aerospace industries, damage from sudden application of an impulse force, i.e., impact, could be expected to occur during manufacturing, service and maintenance operations. A large number of examples are presented to show the impact events that result from hail, wildlife strikes in service and dropped tools during maintenance work. An example of a US flight after suffering a bird strike on its radome during flight operation is shown in Figure 1.2. The air flight was luckily able to return to Orlando airport, but there is no doubt that the performance of the flight was reduced to a lower level after being struck. Due to the limited capability of absorbing energy through plastic deformation and to the brittle nature of the matrix system used to bind the reinforcing fibres together, *Carbon Fiber Reinforced Polymer* (CFRP) is vulnerable to low-velocity impact damage. For low-velocity impacts in CFRP, it is possible to create internal damage that often cannot be detected by eye. Such hidden damage can cause a significant reduction in the strength of a component and can lead to catastrophic failure of the structure in extreme scenarios. This phenomenon is usually named *Barely Visible Impact Damage* (BVID). Compared with visible damage like that shown in Figure 1.2, BVID demands effective ways of detecting such damage. Thus, understanding of the behaviour of impact loading is essential in finding more reliable and effective damage detection methods.

Figure 1.2: Bird strike on Boeing 757 with Radome Damage [12].

Damage detection gives a qualitative indication that damage might be present in the structure and the damage assessment gives an estimate of the severity of damage. *Non-Destructive Test/Evaluation* (NDT/E) as a diagnostic maintenance tool has been extensively used for damage detection. Widely used *Non-Destructive Test* (NDT) techniques are *Visual Inspection* (VI), *Ultrasonics Inspection* (UI), vibration-based techniques, *Eddy Current* (EC), *Acoustic Emission* (AE) and X-ray, as summarized by Staszewski *et al* [3].

VI is the oldest and most widely used NDT technique for evaluating the structural integrity of material components. It based on the physical principle that visible light is reflected from a surface to human eyes. It is an immediate and economical way of detecting large size fatigue cracks in metallic structures or delamination in composite elements. However, it is restricted to surface damages and restricted by accessibility of the inspection area; this means that some internal damage in composite structures cannot be detected by this technique.

UI is a well established and understood method for damage detection in both metallic and composite structures. Ultrasonic transducers inject low-intensity stress waves into the material and the transmitted signals are recorded by other transducers. A change in the received signal of velocity or amplitude may refer to damage due to the interaction between elastic waves and flaws. This technique is very sensitive to small damages in most cases and relatively inexpensive. However, it often does not detect closed cracks as mentioned by Staszewski *et al* [3], and it is restricted by certain examples.

AE shows great promise as a passive technique for detecting damage. It is a burst elastic stress wave emitted by fatigue fracture in metallic materials or matrix cracking, fibre fracture and delamination in composites, and then captured by an appropriate sensor. This approach can be applied for damage initiation and growth but it requires the specimen to be loaded and the data obtained from the sensors are complicated to interpret.

EC is a surface and near surface inspection technology which monitors the change in the electromagnetic impedance due to strain in the material. ECs are created by using a coil to introduce an *Alternating Current* (AC) into a conductive material. All potential damages in a conductor surface or subsurface (up to 6mm) behave as an obstacle to these ECs, influence the magnetic field and so, can be captured by a probe. This technique has proved to be a valuable monitoring technology used in aerospace maintenance. However, it is sometimes limited by high power requirements and poor penetration.

*Digital Image Correlation* (DIC) is a standard *Pattern Recognition* (PR) technique to measure the full field strain/displacement in experimental mechanics. The physical principle behind this is to track the gray value pattern that covers the object surface before and after loading. This method is accurate with high resolution video equipment. However, it demands a high speed computer to continuously make comparison during testing and the cost of equipment (e.g. digital camera, light system,

post-processing) is relatively expensive.

Ultrasonic waves and their propagation have shown good sensitivity to impact damage and fatigue crack detection. There are two typical methods based on sound and ultrasound for nondestructive testing. The first technique uses Lamb waves which also known as plate-waves. Lamb waves are ultrasonic plane strain waves that propagate in thin plate-like structures and are guided by two free boundaries – the upper and lower surfaces. Lamb waves are particularly attractive ultrasonic inspection methods used for damage detection due to their long-range inspection capacity and high sensitivity. However, the complex wave propagation mechanisms (dispersion and multiple modes) of Lamb waves are not readily understood or easily interpreted. Vibro-acoustics is a method that relies on combined modal and ultrasonic excitation leading to nonlinear modulations [13-15]. In other words, a standing longitudinal ultrasonic wave is introduced to the structure and at the same time modal excitation is applied. Usually the modal excitation frequency coincides with the frequency of one of the structural resonances in order to amplify nonlinear acoustic effects, which are wave distortion effects caused by interaction of the acoustic wave with changes in material or geometric properties.

In recent years, there has been a considerable interest in nonlinear phenomena in ultrasonic wave propagation. In general, nonlinear methods are divided into two groups concerned with: classical and non-classical nonlinearity. Classical nonlinear acoustics and methods developed for material defects can be traced back to the 1970s and they were used to identify nondestructive characterisation of materials by higher harmonic generations or frequency mixing. Classical nonlinear elasticity is a well established theory based on a nonlinear form of Hooke's law which describes the relationship between stress and strain [16]. On the other hand, non-classical nonlinear methods have been developed over the last 15 years and researchers have presented a number of theoretical tools. Different nonlinear phenomena such as various contact type nonlinearities related to crack wave interactions, vibro-acoustic modulations and

energy dissipation via hysteresis or L-G effect, are involved in the non-classic nonlinear method [17].

It appears that there is still limited understanding of all these nonlinear phenomena despite many research efforts. Classical nonlinear phenomena such as the generation of harmonics can be explained using the theory of elasticity when various nonlinear forms of Hooke's law are used [18]. Wave modulations can be explained by local asymmetric stiffness characteristics of crack faces [19] or nonlinear coupling between strain and auxiliary fields [20]. Frequency shifting can be explained by stiffness reduction when large cracks under large strain fields are analysed in metals [21] or by hysteretic behaviour when small cracks under small strain fields are analysed in mesoscopic materials [20]. A summary of some recent developments in this area is given by Klepka *et al* [22]. Nevertheless, there is a general consensus that these nonlinear phenomena are relatively weak in undamaged and remarkably strong in damaged components. This is the major attraction of nonlinear acoustics when used for crack detection. Various practical approaches have been developed for crack detection. Most of these methods can be classified into three major categories with respect to excitation. These are:

(1) single wave excitation techniques (e.g. methods based on frequency shifting [23] or higher harmonic generation [24] ).

(2) vibro-acoustic excitation techniques (methods based on combined modal and ultrasonic excitation leading to nonlinear modulations [13, 15, 25] ).

(3) cross-modulation techniques (methods that utilise modulated low-frequency excitation of the low-frequency wave [26-27]).

Various methods can be used for excitation including impact hammer [19], electromagnetic shakers [15, 23], ultrasonic transducers [28], air-coupled ultrasonic transducers [29], low-profile piezoceramic transducers [13, 30] and lasers [31].

Utilising statistical methods for analysing the data from experiments or other industry

applications seems to become common practice in all engineering discipline. Statistics is concerned with events which occur by chance [32] and provides ways of gaining insights into the behaviour of these events. Statistical concepts and methods are not only guiding engineers to make intelligent decisions in the presence of uncertainty, but also assisting engineers and scientists in understanding the world better. A generalised framework of the specific requirements with respect to a statistical approach results in the five essential steps [33]:

1) State the problem or question
2) Collect and analyse data
3) Interpret the data and make decisions
4) Implement and verify the decisions
5) Plan next action

A test of small sample hypotheses is a statistical approach for using small number of sample data to determine whether the null hypothesis, which refers to any hypothesis that reflects the current state of nature and is assumed to be true, should be rejected [34]. In general, a statistical hypothesis is any claim made about a set of parameters of a population distribution. The following procedure is to determinate the consistency of a random sample from the population with the hypothesis. The aim of a hypothesis test is to find out whether a result is statistically significant or if it occurs by coincidence.

Outlier analysis describes a statistical approach for discriminating a potential outlier from a data set, which is considered to be generated by an alternate mechanism in comparison to the rest of the data [35]. The outlier analysis method has been successfully implemented in a variety of damage detection problems. Application examples in this area include damage in composite plates [36] and metallic structures [37-38].

## 1.2 Aims and Objectives of this research

The current research aims to compare various approaches based on nonlinear acoustics and Lamb waves for structural damage detection.

The main objectives of this research are listed below:

- Select different methods for nonlinear acoustic experimental test, such as analysis of harmonics, frequency shifting, analysis modulation intensity and damping estimation.
- Perform nonlinear acoustic and Lamb wave tests to three different materials-glass (transparent, the crack could be easily seen, being the only defect in the material), metal and composite material.
- Create fatigue cracks on glass plate by using a Vickers indenter to get various crack lengths from 2 mm to 35 mm. Perform a fatigue test on an aluminium plate to get different damage severities from 2 mm to 18 mm.
- Conduct impact test on CFRP plates to simulate increased impact energy level from 5J to 40J. Perform a compression test on a CFRP panel until it fractures.
- Conduct impact test on a wind turbine blade
- Perform nonlinear acoustics and Lamb waves to three different materials after damage formed.
- Establish advanced signal processing tools to analyse all experimental data.
- Perform statistical PR for damage assessment
- Compare methods with respect to damage detection sensitivity

## 1.3 Thesis layout

A brief summary of this thesis is listed as following:

Chapter 2 reviews the theoretical background of nonlinear acoustics and Lamb wave

techniques. The statistical approaches used for damage detection are presented in this chapter.

Chapter 3 evaluates the fatigue damage on the alumnium and glass plates. The modal characteristics and *Crack Edge Divergence* (CED) are obtained by a FE method. Different nonlinear acoustic methods are applied for damage detection and assessment. Outlier analysis is applied on Lamb wave signals to detect and assess the fatigue crack.

Chapter 4 demonstrates damage detection on impacted composite laminates by nonlinear acoustic and Lamb wave methods. In addition, compression damages on composite laminates are analysed by Lamb wave methods.

Chapter 5 focuses on an impacted wind turbine blade. Damage detection and localisation are investigated in this case.

Chapter 6 gives the conclusions from the above mentioned studies and the proposal for future works.

# Chapter 2

# 2 Literature review

## 2.1 Nonlinear acoustics

Usually, the presence and severity of damage are detected by linear acoustics. This technique is sensitive to gross defects or open cracks, where the effects of reflection, scattering, transmission and absorption of probe acoustic energy occur. However, it is less sensitive in identifying contacting defects, such as a closed crack, disbonding and delamination. More recently, there have been extensive studies in using nonlinear vibration and acoustic phenomena for damage detection. Various nonlinear effects that are highly dependent on the nonlinear acoustic wave propagations have been studied. These include generation of harmonics, amplitude dissipation, resonant frequency shifting, generation of sidebands and the Luxemburg-Gorky (L-G) effect which is based on nonlinear coupling between the strain and temperature fields. These alternative techniques overcome the limitations of linear acoustics and correlate well with micro-inhomogeneities present in the materials or structures.

By the early 1960s, nonlinear acoustics were found to be strongly sensitive to the intrinsic or global material nonlinearity and have been applied for detecting material imperfections [16, 39-41]. Starting from the 1970s, numerous investigations were carried out regarding the nonlinear effects of elastic wave propagation in various materials. Morris *et al* and Buck *et al* [24, 42] demonstrated that second acoustic harmonic generation can be used for investigating micro-crack development on the surface of aluminium during fatigue tests. Shkolnik [43] used nonlinear acoustics to measure the material characteristics of concrete. Korotkov *et al* [44] reported that high-frequency acoustic wave modulation successfully detects the cracks in a steel

sample. Nagy [45] presented that nonlinear acoustic parameters are highly sensitive to fatigue damages in various materials including plastics, metals, composites and adhesives. Van Den Abeele *et al* [46] proved that nonlinear interactions of vibro-acoustic methods are effective in discerning small cracks in Plexiglas and sandstone. Zaitsev [47] proposed a novel nonlinear modulation method for crack detection in glass samples.

In addition, nonlinear acoustics have been applied to detect various types of defects. Donskoy *et al* [48] suggested that nonlinear acoustics is capable of detecting cracks and corrosion in reinforced concrete. Aymerich *et al* [27] reported a cross-modulation method to detect a delamination in composite laminates introduced by low-velocity impact. Donskoy *et al* [49] carried out nonlinear acoustics for detection of bonding quality in titanium and thermoplastic plates.

The mechanisms related to nonlinear acoustics for damage detection are most likely to be diverse and are still not completely understood. Solodov [50] experimentally illustrated that the acoustic wave introduced a contact nonlinearity due to a local open and closure of a contact interface. Duffour *et al* [15] stated that vibro-acoustic modulation effects were caused by the shifts of transfer function from the most openning crack stage to the most closed crack stage; the same idea is also mentioned by Kim *et al* [51]. Broda *et al* [52] explained the cracked-induced nonlinearity as a bilinear spring with varying elastic moduli for the breathing crack. Friswell *et al* [53] demonstrated a bilinear stiffness model for a crack opening and closing. Muller *et al* [54] explored the nonlinear resonance frequency shifting by local stiffness reduction (fatigue damage accumulates in bone). Nazarow [5] claimed that natural elastic nonlinearity is caused by various discrete inhomogeneities in the medium. . Nazarov *et al* [55] observed a decrease of resonance frequency with an increase of excitation amplitude and amplitude-dependences of nonlinear loss in a sandstone bar, and explained the mechanism as both hysteretic nonlinearity and dissipative acoustic nonlinearity. Zaitsev *et al* [56-57] presented a novel non-classical effect, The L-G

effect, which is a kind of locally enhanced nonfriction and nonhysteretic dissipation coupling with thermoelastics. Van Den Abeele *et al* [46] demonstrated the nonclassical nonlinear elasticity of hysteresis at defects (micro cracks or micro-inhomogeneous) due to the breaking of interatomic bonds. Ostrovsky *et al* [58] explained classical amplitude-dependent dissipation, which is attributed to hysteresis at dislocations. Pecorari [59] reported adhesion hysteresis for an interface between two rough surfaces. Guyer *et al* [60] proposed slow elastic dynamics, which is related to the slow relaxation of the resonance frequency of a system with defects after a static or dynamic load is applied to the system

Although there have been many research efforts attributed to theoretical studies of nonlinear acoustic mechanisms, there are still two major barriers for these nonlinear mechanisms involved in real engineering applications. As summerised by Klepka *et al* [22], the first problem is the overlapping effects of the various proposed nonlinear mechanisms. That means similar nonlinear effects may be relevant to different mechanisms and vice versa. For instance, energy dissipation can result from adhesive, hysteretic or thermoelastic mechanisms. According to this, it is difficult to isolate all the mechanisms involved. The second problem is the nonlinear effects caused by other factors rather than only from damage. Typical factors introducing nonlinearity are friction between elements at structures joints or boundaries, coupling between sensors and material surfaces or electrical interference from the instrumentation measurement chain.

### 2.1.1 Theoretical Background

For one-dimensional quasi-static problems the well known constitutive stress-strain equation can be expressed as:

$$\sigma = \int \mathrm{K}\left(\varepsilon, \dot{\varepsilon}\right) d\varepsilon \tag{2-1}$$

where $\sigma$ is stress, K is a function of strain $\varepsilon$ and the time derivative of strain $\dot{\varepsilon}$. If the analysed material is linear, K becomes constant and the equation results in the well known Young's modulus relation. When a linear material is excited with a cyclic, pure harmonic load, strain is also harmonic in the time domain and exhibits only one component in the spectrum. For nonlinear materials or various nonlinear local inclusions in linear material (e.g. cracks), K is nonlinear and can be expressed as [18]:

$$\mathrm{K}\left(\varepsilon,\dot{\varepsilon}\right)=\mathrm{K}_0\left\{1-\beta\varepsilon-\delta\varepsilon^2+\cdots\right\}, \tag{2-2}$$

So $$\sigma=K_0\varepsilon-\frac{1}{2}K_0\beta\varepsilon^2-\frac{1}{3}K_0\delta\varepsilon^3+... \tag{2-3}$$

where $K_0$ is the linear modulus, $\beta$ and $\delta$ are classical nonlinear perturbation coefficients. The above equation can describe two types of classical elastic nonlinearities, i.e. the 2nd ($\beta\neq0$ and $\delta=0$) and 3rd ($\beta=0$ and $\delta\neq0$) order perturbations . Both types of nonlinearities will produce distorted harmonic strains in the time domain under cyclic, pure harmonic excitation. As a result, higher harmonics will be generated in the strain spectra. However, only odd harmonics will be present for the 3rd order perturbation. Harmonic generation is a classical nonlinear phenomenon observed in vibration, acoustical or ultrasonic responses in inhomogeneous materials or homogenous materials containing voids and/or cracks/micro-cracks. There are two major physical mechanisms that contribute to harmonic generation. These are material nonlinearity and contact-type nonlinearity. The latter is produced by the asymmetric stiffness for the tension and compression of a breathing crack. Both mechanisms are related to nonlinear elasticity and can be described using Equation (2.2). Various methods based on harmonic generation have been developed for crack detection [23-24, 61]. For most solids, the first nonlinear perturbation coefficient, i.e., the $\beta$ parameter, can be experimentally obtained from the amplitude $\mathrm{A}_2$ of the second harmonic generated at a distance $x$ from a single frequency $(\omega)$ source signal [62].

$$\beta = \frac{8c_0^2}{\omega^2 x}\left(\frac{\mathrm{A}_2(\omega)}{\mathrm{A}_1^2(\omega)}\right) \tag{2-4}$$

where $x$ is the wave propagation distance, $c_0$ is the wave velocity, $\mathrm{A}_1$ is the magnitude of the fundamental frequency component and $\mathrm{A}_2$ is the magnitude of the 2$^{nd}$ harmonic.

Now, the nonlinear effects caused by damage will be discussed.

### 2.1.2 Contact acoustic nonlinearity

Higher harmonic waves are generated by the incident acoustic wave interacting with the damage interfaces. This effect is the so called Contact Acoustic Nonlinearity (CAN) [18]. Two mechanisms of nonlinear vibrations contribute to this effect, as concluded by Klepka *et al* [63]. The first is the clapping mechanism that is caused by the repetition of collisions between the two surfaces with incident acoustic waves. When acoustic waves reach the non-uniform stiffness of material or inhomogenerous material properties such as micro-cracks or other imperfect contact interfaces, the compression part of the wave can penetrate it. On the other hand, the tensile part of wave is obstructed. Therefore, after passing through the discontinuities, only half waves remain, which is clearly a form of nonlinearity. The second nonlinear mechanism is relevant to the interaction between shear acoustic waves and damages. When the amplitude of shear waves is low, the contact damage interfaces are under the micro slip action. This effect changes the stiffness twice and results in the generation of odd harmonics in the spectra of the system response. When the amplitude of shear waves is high enough, the surface of the contact damage interfaces start to slide against each other, under the stick and slide modes [64].

### 2.1.3 Nonlinear resonance frequency shifting

Payan *et al* [65] demonstrated that the resonance frequency decreases as a function of wave amplitude due to a softening or hardening of the material with increasing

driving amplitude. In other words, fatigue cracks lead to local stiffness reduction due to nonlinear stress-strain behaviour. As a result, the fundamental harmonic in the strain power spectrum is shifted towards lower frequencies. Figure 2.1 shows the peak resonance frequency shifting for the undamaged and damaged samples.

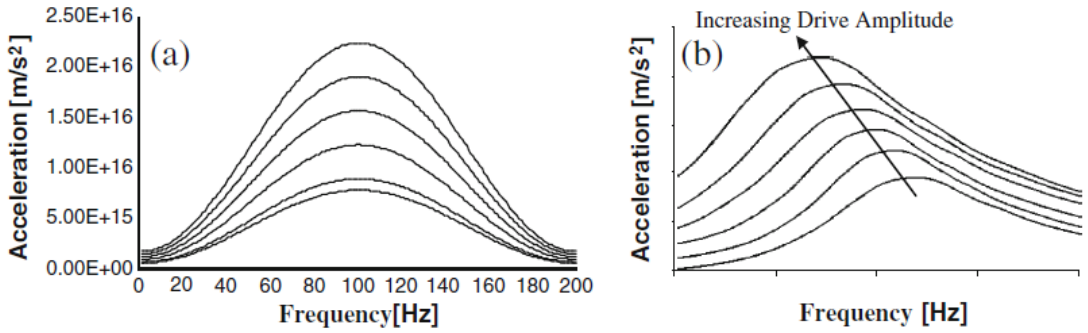


Figure 2.1: Examples of resonance frequency against drive amplitude (a) undamaged sample (b) damaged sample [66].

Frequency shifting is used as a symptom of nonlinearity to detect fatigue cracks in vibration analysis. In ultrasonic testing, Nonlinear Resonant Ultrasound Spectroscopy (NRUS) uses a sweep excitation centered at resonance frequency to reveal resonance frequency shifting as introduced by Van Den Abeele *et al* [23]. Equation (2.2) describes the nonlinear elastic phenomena, but does not provide any description related to energy dissipation. This can be obtained when a hysteretic mechanism is added to Equation (2.2), leading to the following stress-strain formula:

$$K\left(\varepsilon,\dot{\varepsilon}\right)=K_0\left\{1-\alpha\left[\Delta\varepsilon+\varepsilon\left(t\right)sign\left(\dot{\varepsilon}\right)+\cdots\right]\right\} \tag{2-5}$$

where $\alpha$ is a measure of the material hysteresis, $\Delta\varepsilon$ is the local strain amplitude ($10^{-6}-10^{-7}$) over the previous load cycling period. According to empirical evidence [46], a nonlinear hysteretic system with large strain amplitude behaviour proportional to $\alpha$ dominates, and a first order approximation gives:

$$\frac{f_0-f}{f_0}\approx\alpha\Delta\varepsilon \tag{2-6}$$

where $f_0$ is the linear resonance frequency and $f$ is the resonance frequency for an increasing driving amplitude.

Some research works on the application of this modal have been reported. Van Den Abeele *et al* [46] revealed that the hysteretic nonlinearity in the quasi-brittle material dominates the classical atomic nonlinearity. Cheong *et al* [67] used *Nonlinear Resonant Ultrasound Spectroscopy* (NRUS) to detect microcracks in low carbon steel. Muller *et al* [54, 68] successfully applied NRUS to assess the fatigue damage accumulation in bone. In addition, Meo *et al* [66] highlighted the nonlinear features in a carbon fibre laminate by using NRUS.

### 2.1.4 Frequency mixing

The phenomena of frequency mixing was first presented in a *United States* (US) patent in 1975 [69] and in the last decade, this phenomena applied to nondestructive evaluation has been widely studied [4, 9, 13, 15, 17, 22, 27, 44, 48, 70-77]. One of the efficient techniques of frequency mixing is called vibro-acoustic modulation，which relies on simultaneous excitation of a monitored structure with two waves, i.e. a high-frequency acoustic/ultrasonic wave and a low-frequency vibration mode. In other words, a standing longitudinal ultrasonic wave is introduced to the structure and at the same time modal excitation is applied. Usually the low-frequency excitation frequency coincides with the frequency of one of the structural resonances. The ultrasonic response signal is then acquired by a different transducer. If the specimen is undamaged, the response signal exhibits the fundamental harmonic of the standing ultrasonic wave and the low-frequency wave in the power spectrum. However, if the specimen is cracked, modulation sidebands around the high-frequency fundamental harmonic can be observed [13]. The frequency spacing of these sidebands corresponds to the modal excitation frequency. The method is illustrated graphically in Figure 2.2

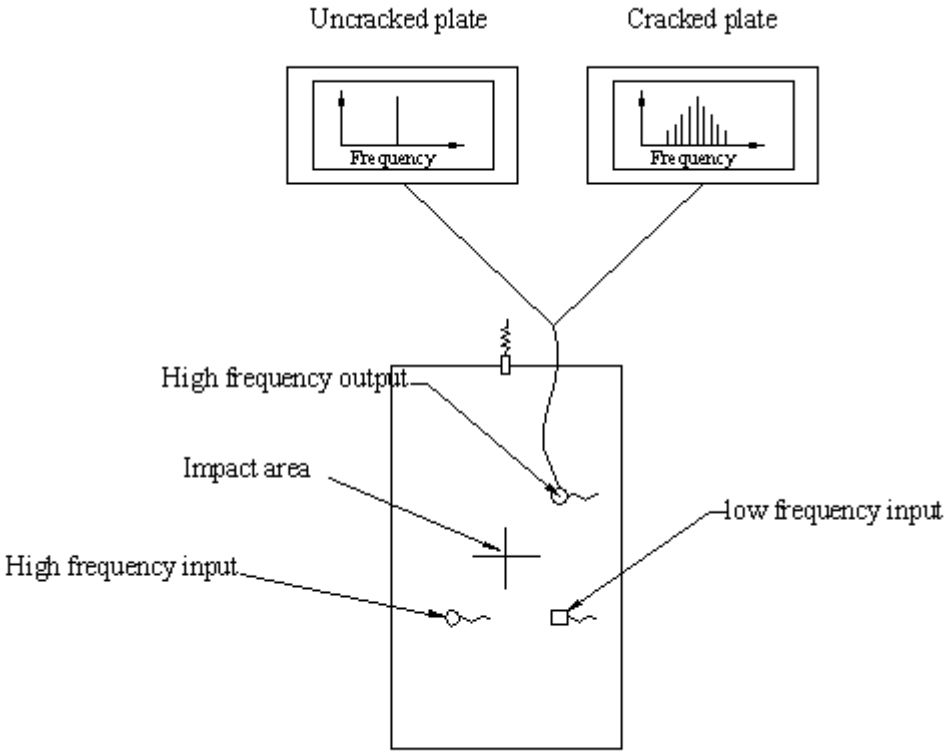


Figure 2.2: Graphical illustration of frequency modulation in the vibro-acoustic method.

Various theories have been proposed to explain the vibro-acoustic wave modulations resulting from crack-wave interactions, as explained by Duffour *et al* [15, 19, 23, 49, 70, 76, 78]. These include the classical nonlinear effects of opening-closing cracks that relates to crack-induced elastic nonlinearities [9], the dissipative mechanism of elastic hysteresis [7, 79] and the so-called L-G effect [56-57, 76]. The latter is a non-classical, non-frictional and non-hysteretic energy dissipation mechanism and can be explained by a locally enhanced thermo-elastic coupling, i.e. nonlinear coupling of the strain with the auxiliary thermal field produced by the crack. Theoretical studies [56, 80] demonstrate that near the crack vicinity, wave induced temperature gradient depends on defect size L and the temperature wavelength $\delta$. For estimating temperature gradients and the respective losses in the crack vicinity, Zaitsev *et al* [56] derived the asymptotic expression for the losses per cycle in three groups: the low

frequency limit (when $L \ll \delta$), the high frequency limit (when $L \gg \delta$) and the relaxation maximum (when $L \sim \delta$). The expressions are shown blow:

$$W_{LF} = 2\pi\omega T(\alpha^2 K^2 / k)L^5\varepsilon^2 \tag{2-7}$$

$$W_{HF} = 2\pi T(\alpha K / \rho C)^2[1/(k\rho C\omega)]^{1/2}L^2\varepsilon^2 \tag{2-8}$$

$$W_{\max} = 2\pi T(\alpha^2 K^2 / \rho C)L^3\varepsilon^2 \tag{2-9}$$

where ω is the wave cyclic frequency, T is the temperature, α is the temperature expansion coefficient of the solid, K is the bulk elastic modulus, ρ is the density, C is the specific heat, ε is the average strain and k is the thermal conductivity.

The most important conclusion from these investigations is that the total loss at the whole crack and the small inner contact are of the same order. Thus relatively small strain levels can lead to large energy dissipation due to nonlinear thermo-elastic coupling. Guyer *et al* [20] proposed two theoretical explanations for this nonlinear coupling mechanism: (1) an elastic wave raises the temperature from which there is a further elastic-wave scattering; and (2) the temperature carries the elastic wave and transfers to a scattered wave. Zaitsev *et al* [76] illustrated that the high frequency energy losses may be caused by the thermal dissipation when the crack edges are contacting. Those losses are dramatically increased because of the high-temperature gradients around the edges. Landau *et al* [81] showed that a thermal mechanism results in a significant sound dissipation in polycrystalline structure. Recent experimental evidence by Klepka *et al* [22] confirmed the importance of these findings and shows that the major mechanism behind vibro-acoustic wave modulations caused by crack-induced nonlinearities in metals is related rather to nonlinear dissipation (either by hysteresis or the L-G effect) than elastic behaviour.

The analysis of vibro-acoustic wave modulation can be used for crack detection, as demonstrated in numerous publications by Duffour *et al* [9, 13, 82]. The intensity of the modulation parameter, $R$ is defined as:

$$R = \frac{B_1 + B_2}{B_0} \tag{2-10}$$

where $B_0$ is the magnitude of the *High Frequency* (HF) ultrasonic component, while $B_1$ and $B_2$ are the magnitudes of the first pair of modulation sidebands, $R$ is often used to detect a crack and assess its severity. Alternatively, instantaneous amplitudes and/or frequency can be used for crack detection, as illustrated by Hu *et al* [77].

Other methods based on vibro-acoustic wave modulations include: amplitude analysis of higher harmonics and modulation sidebands [23] and wave dissipation analysis [76]. The former analyses the relevant harmonic and sideband amplitudes against *Low Frequency* (LF) and HF excitation amplitudes and reveals elastic type nonlinearities.

## 2.2 Lamb wave

Lamb waves, also known as plate-waves, are ultrasonic plane strain waves which propagate in thin plate-like structures and are guided by two free boundaries – the upper and lower surfaces [83]. The well-known Rayleigh-Lamb equation determines the phase and group propagation velocities as a function of frequency for isotropic and homogenous plates. The equations for symmetric modes and antisymmetric modes are as follows [84],

$$\frac{\tan\left(qh_{half}\right)}{\tan(ph_{half})} = -\frac{4k^2qp}{\left(k^2-q^2\right)^2} \text{ for symmetric modes.} \tag{2-11}$$

$$\frac{\tan\left(qh_{half}\right)}{\tan(ph_{half})} = -\frac{\left(k^2-q^2\right)^2}{4k^2qp} \text{ for antisymmetric modes.} \tag{2-12}$$

where the non-dimensional parameters are

$$p^2 = \frac{\omega^2}{c_L^2} - k^2, \quad q^2 = \frac{\omega^2}{c_T^2} - k^2, \quad k = \frac{2\pi}{\lambda_{wave}} = \frac{\omega}{c_P} \tag{2-13}$$

where $k$, $\omega$ and $\lambda_{wave}$ are the wave number, angular frequency and wavelength of the wave, respectively. $h_{half}$ is the half thickness of the plate. $c_L$ and $c_T$ are the velocities

of longitudinal and transverse/shear modes, respectively and these velocities can be defined by Lamé constants:

$$\mu = \frac{E}{2(1+\upsilon)}, \quad \lambda = \frac{E\upsilon}{(1-2\upsilon)(1+\upsilon)} \tag{2-14}$$

$$c_T = \sqrt{\frac{\mu}{\rho}}, \quad c_L = \sqrt{\frac{\lambda+2\mu}{\rho}} \tag{2-15}$$

Observed from the derived Rayleigh-Lamb frequency equation, the solution of the equation cannot be analytically solved, but requires advanced numerical methods. It is clear that for a given material, if the Young's modulus, $E$, Poisson's ratio, $\upsilon$, and the density, $\rho$, are known, the only indeterminate values are the velocity, $c_p$, the angular frequency, $\omega$ and the thickness of the plate, $2h$. Worden [85] demonstrated two key notes from the derived equation. Firstly, the waves are dispersive as the phase velocity, $c_p$ is dependent to the value of the product of frequency and thickness, $\omega \cdot 2h$. This dispersion property results in difficulties for data interpretation due to their being more than one mode. A graphical representation of the dispersion curve can be seen in Figure 2.3. Before the cut-off frequency, the $S_0$ mode travels faster than $A_0$. Therefore, $A_0$ has a shorter wavelength which is an advantage for detecting small size damage. In addition, studies [86-88] show that $S_0$ features lower attenuation which is suitable for long distance detection. Su *et al* [86] illustrated that both $S_0$ and $A_0$ can be used for damage detection: $S_0$ is better suited for damage detection through the structure thickness, e.g. delamination, whereas $A_0$ exhibits higher sensitivity to surface damage, e.g. cracks or corrosion. The second point is that the derived equations are transcendental, and they may have any number of real solutions. The waveforms of Lamb waves appear with symmetric and antisymmetric properties, as shown in Figure 2.4 (a) and Figure 2.4 (b) respectively. Both the symmetric modes, denoted as $S_0$, $S_1$, $S_2$... and antisymmetric modes, labeled as $A_0$, $A_1$, $A_2$... have an infinite number of waveforms/modes. Generally speaking, the Rayleigh-Lamb equation is intended for

isotropic materials, however, Birt [89] illustrated that $A_0$ is mainly unchanged for composite laminates and can be estimated by using the bulk laminate properties.

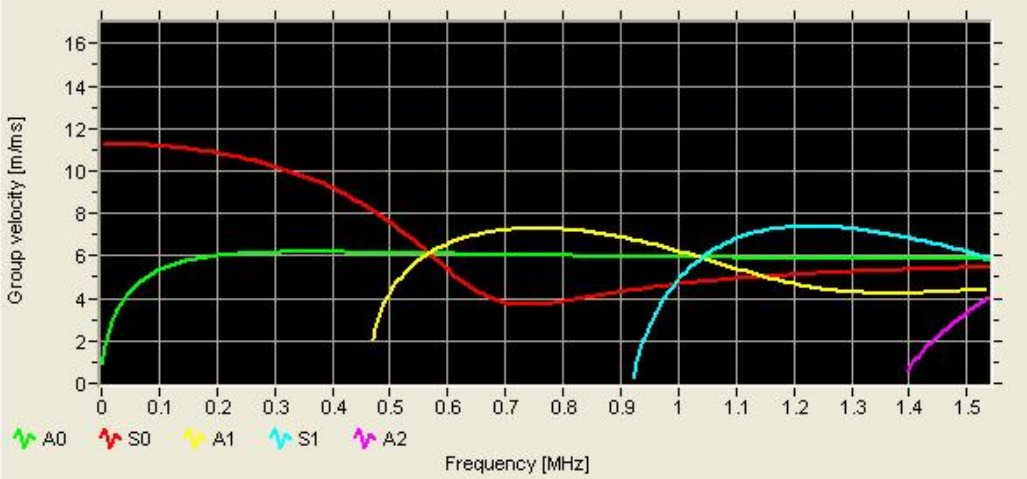


Figure 2.3: Lamb wave dispersion curves for a composite with thickness 6.5 mm.

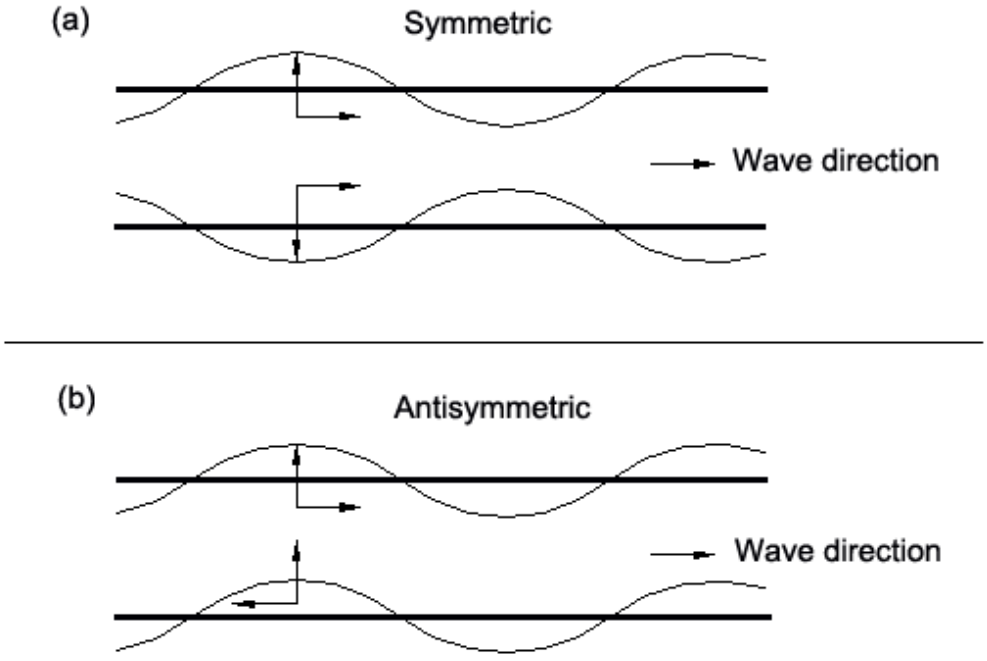


Figure 2.4: (a) Symmetric and (b) Antisymmetric Lamb wave modes.

### 2.2.1 Phase and group velocities

The propagation of the Lamb wave can be characterised by two important features of Lamb waves, $c_p$ (the Phase velocity) and $c_g$ (the Group velocity). The Phase velocity

of a wave can be defined as the propagation speed of the wave phase at a given frequency and it can be introduced as being equal to $(\omega / 2\pi) \cdot \lambda_{wave}$ [86]. The group velocity is referred to as the propagation velocity of a group of waves of similar frequency [90]. A brief analytical explanation of how the group velocity of the Lamb waves is derived will be presented, as stated by Graff [91].

Assuming that two propagating harmonic waves have the same amplitude, $A$ with different frequencies, $\omega_1$ and $\omega_2$, the displacement formula can be expressed as:

$$u = A\cos(k_1 x - \omega_1 t) + A\cos(k_2 x - \omega_2 t), \tag{2.16}$$

where $k_1 = \omega_1 / c_1$ and $k_2 = \omega_2 / c_2$. Using trigonometric identities,

$$A(\cos\alpha + \cos\beta) = 2A\left[\cos\left(\frac{\alpha-\beta}{2}\right)\cdot\cos\left(\frac{\alpha+\beta}{2}\right)\right], \tag{2.17}$$

Then,

$$u = 2A\cos\left\{\frac{1}{2}(k_2 - k_1)x - \frac{1}{2}(\omega_2 - \omega_1)t\right\}\cdot\left\{\frac{1}{2}(k_2 + k_1)x - \frac{1}{2}(\omega_2 + \omega_1)t\right\}, \tag{2.18}$$

where the following substitutions can be made:

$$\Delta\omega = \omega_2 - \omega_1 \tag{2.19}$$

$$\Delta k = k_2 - k_1 \tag{2.20}$$

and the average frequency and wave number can be defined as:

$$\bar{\omega} = \frac{1}{2}(\omega_2 + \omega_1) \tag{2.21}$$

$$\bar{k} = (k_2 + k_1) \tag{2.22}$$

thus the expression of Equation (2.17) can be obtained as,

$$u = 2A\cos\left[\frac{1}{2}\Delta k x - \frac{1}{2}\Delta\omega t\right]\cdot\cos(\bar{k}x - \bar{\omega}t) \tag{2.23}$$

The first part enclosing the difference terms $\Delta k$ and $\Delta\omega$ is the low frequency term and gives the definition of the Group velocity as:

$$c_g = \frac{\Delta\omega}{\Delta k} \tag{2.24}$$

The second part containing the average terms $\overline{k}$ and $\overline{\omega}$ is the high frequency term that travels at average velocity. The high frequency carrier is modulated by the low frequency group velocity as shown in Figure 2.5.

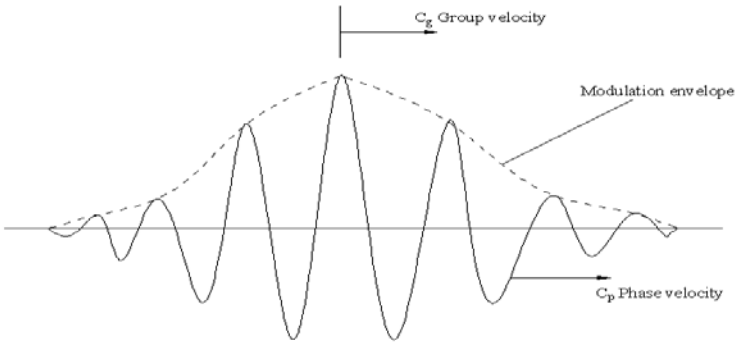


Figure 2.5: Group ($c_g$) and Phase ($c_p$) velocity of a pulse.

For a constant phase, i.e. $\Delta kx - \Delta\omega t = const$, the Group velocity at the limit transition $\Delta\omega \to 0$, $\Delta k \to 0$ is defined as:

$$c_g = \frac{d\omega}{dk} \tag{2.25}$$

Substituting $k = \omega / c_p = 2\pi f / c_p$ into Equation (2.22) yields:

$$c_g = d\omega\left[d\left(\frac{\omega}{c_p}\right)\right]^{-1} = c_p^2\left(c_p - \omega\frac{dc_p}{d\omega}\right)^{-1} = c_p^2\left(c_p - (2fh)\frac{dc_p}{d(2fh)}\right)^{-1} \tag{2.26}$$

where $2fh$ denotes frequency times thickness.

### 2.2.2 Piezoelectric transducers

Lamb waves for damage detection can be activated and sensed by *piezoelectric transducers* (PZTs). Traditional PZTs used for Lamb wave activation are the permanent and direct attachment of piezoelectric elements to an inspection structure. These are the most widely used sensors for structural health monitoring due to their low cost, low weight and convenience for majority of damage detection applications. The piezoelectric effect is an electric polarization effect that converts electric energy

into mechanical strains and vice versa [92]. In other words, when a stress is applied on the material, an electrical charge can be found on its surface. This phenomenon has a converse effect, namely when a voltage is applied on the piezoelectric material, mechanical strains are generated. Both effects are shown in Figure 2.6.

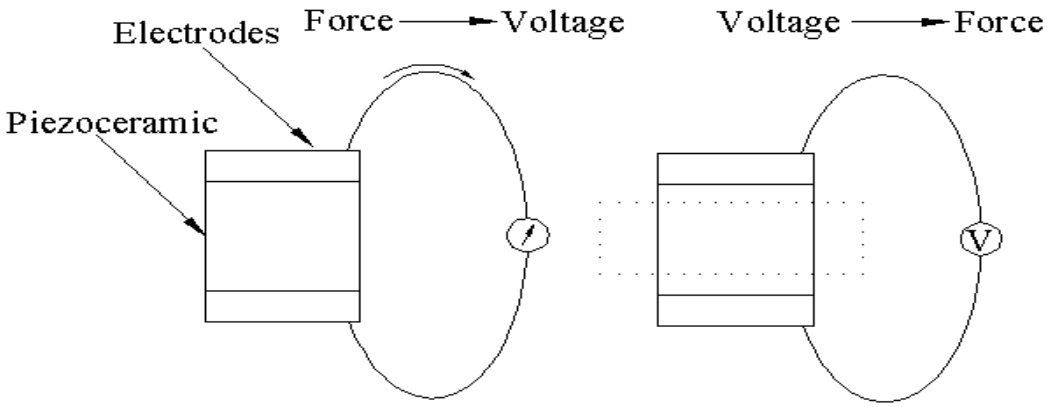


Figure 2.6: (a) Direct and (b) inverse piezoelectric effects.

In this work, thin and circular transducers from the PI Company were chosen for the activation and sensing of Lamb waves. According to the product manual [93], these circular transducers have two oscillation modes; the radial mode and the thickness mode, as illustrated in Figure 2.7. Lamb waves can be activated and received by a variety of transducers, such as angle wedge transducers, comb ultrasonic probes and Hertzian contact probes. The weight and size of these transducers are normally non-negligible. A PZT transducer was chosen for exciting and receiving signals due to its small size and light weight. The drawbacks of this type of transducers are their extremely fragility and their vulnerability to damage during the attachment procedure. In addition, compared to a wedge transducer, the PZT inevitably excites multiple wave modes.

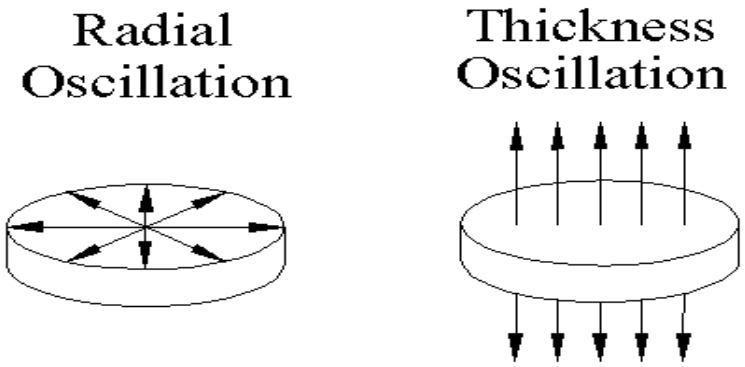


Figure 2.7: Resonance modes of circular piezoelectric transducer.

### 2.2.3 Optimisation for excitation signals and mode selection

Although Lamb wave testing has been widely applied for damage detection in the last 30 years, there is still no best-practice procedure for standard testing due to the complexity of Lamb wave propagation properties [94], i.e. their dispersive/modal nature. As mentioned in Section 2.1, many of the possible modes and their velocities are dependent on a given frequency and specimen thickness. It is noticeable that when the gradient of phase velocity with regards to product of frequency and thickness tends to infinity, i.e. at the cut-off frequency, the group velocity converges to zero [87]. In order to achieve the best results for interpreting the response signals, it is reasonable to narrow the bandwidth of the excitation, preferably to cover less dispersion and concentrate on the two fundamental modes $A_0$ and $S_0$ which are determined by the first cut-off frequency [3].

Various factors influence the sensitivity of damage detection. First of all, choosing a proper phase shape seems to be an efficient way of narrowing down the excitation bandwidth. Kessler *et al* [94] described that pure sinusoidal shapes are periodic, smooth and have a shorter time span to reach the their peak amplitude as compared with parabolic shapes. Meanwhile, The Hanning window technique is used to narrow the bandwidth of a selected Lamb mode. The Hanning function, $h(n)$, is defined as [86]:

$$h(n) = \frac{1}{2}\left[1 - \cos(2\pi \frac{n}{N-1})\right] \quad (n = 1, 2, \cdots, N), \tag{2.27}$$

where $h(n)$ is discretised into N sample points. The effect of applying a *Hanning* window to a pure sinusoidal wave can be seen in Figure 2.8. In general, this window technique helps to concentrate the incident energy into the desired actuation frequency and refine the frequency bandwidth by reducing some striking side lobes. The second important factor is the number of cycles. The *Fast Fourier Transform* (FFT) of a continuous sine wave with a single frequency would give a single peak. On the other hand, for a few finite cycles, the FFT appears as a Gaussian curve with a peak at the input frequency. Based on this fact, the more cycles of a wave excited within a drive pulse, the narrower will be the bandwidth and the less dispersion [94]. The pulse amplitude is another issue of optimisation. Obviously, increasing the driving voltage would increase the magnitude of Lamb wave strain and further increase the signal-to-noise ratio to produce a distinct driving frequency component. However, as mentioned by Kessler *et al* [95], higher amplitudes cause drifts in the signal, and result in lower resolution. So a balance of considering both sides must be met in practice. Pulse frequency is also a key factor to optimise excitation. The selected excitation frequency below the first cut-off frequency ensures that the response signal only includes fundamental Lamb wave modes $A_0$ and $S_0$. Meanwhile, the lower velocity gives more time to separate the actuated and sensed signals. In addition, the frequency will determine the wavelength for different modes ($\lambda = c / f$). The wavelength is a crucial factor for damage sensitivity since the wavelength of the ultrasonic wave must less than half the size of damage [96]. For a given velocity, $c$, higher frequency provides higher damage sensitivity but exhibits more dispersive modes. So balancing the excitation frequency becomes a challenge in different studies. As mentioned in Section 2.2.2, the selected circular piezoelectric transducers have two resonance frequencies. When the pulse frequency is close to or at these frequencies, the transducer gives the maximum output.

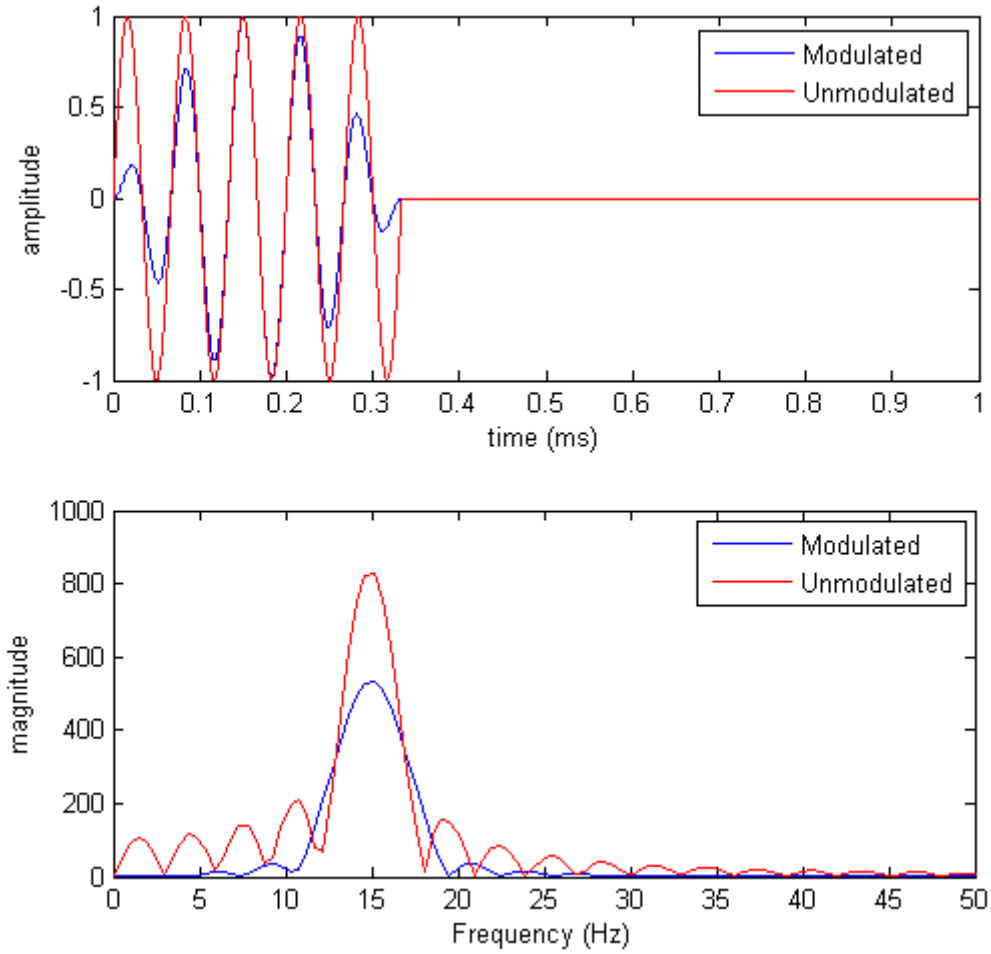


Figure 2.8: The effect of windowing on the excitation pulse of a Lamb wave in time domain and frequency domain.

### 2.2.4 Lamb waves for structural damage detection

In recent years, Lamb waves have attracted attention in damage detection. It is well understood that damage can induce changes in the local or global properties of a structure.

When the Lamb waves interact with discontinuities, some phenomena associated with damage is analogous with propagation waves. *Attenuation* refers to the gradual decay in magnitude of the travelling Lamb waves as a result of energy absorption when the waves pass over a long distance. The existent damage area or inhomogeneities may increase the energy absorption as compared to the undamaged area. *Scattering* can occur when the Lamb waves encounter discontinuities or any obstacle along with

wave propagation. As a result, the waves spread out in all directions as well as decrease in magnitude. *Mode conversion* refers to the energy redistribution among the multimodes [97]. Mode conversion to other modes within the Lamb waves may be caused by any discontinuity along with the traveling waves. *Reflection and refraction* can occur at boundaries when the Lamb waves change the direction and velocity as they cross a defect boundary or structure boundary. This phenomenon leads to the turning back of a wave. The *dispersion* nature of Lamb wave causes the various characteristic propagation velocities travelling with a characteristic frequency bandwidth. This phenomenon brings out a broadening wave packet and causes a drop in signal magnitude.

When Lamb waves travel through a region where a discontinuity exists, the above mentioned phenomena may distort or influence the incident waves and decrease their wave energies in the direction of propagation as compared with an undamaged condition. By analysing the energy of the transmitted signal, it is possible to detect the presence of damage.

## 2.3 Statistical approach

The problems confronting structural health monitoring today often involve nondeterministic analysis data. The statistical approaches are designed to help engineers and scientists extracting any useful information that hides in data sets, and then contributing to the process of aiding decision-making in the presence of variability and uncertainty. The following sub-section presents statistical approaches to damage detection: hypothesis testing for the small samples, novelty detection and outlier analysis.

### 2.3.1 Novelty detection

*Novelty detection* is based on a two-class classifier that indicates whether the obtained data are from a normal operating condition or not [98]. This term is also referred to as

*outlier detection* in many works [99-100]. Novelty detection is a challenging task and draws great attention in various engineering fields [101-104]. The basic principle of novelty detection is to create a given single class from a model, which is guaranteed to be from the normal condition of a system or structure, and then use the modal to test for any abnormality from new test data. Consequently, the nonconformity refers to damage [1]. Novelty detection has been successfully applied in many structural healthy monitoring cases. Manson *et al* [105] used the transmissibility function to analyse data coming from different test specimens including a metallic aircraft wing box. Worden *et al* [36] used a similar methodology to analyse experimental data obtained from two different types of composite plates. Propagation Lamb waves in a sample may refer to damages when the wavefield is scattering and modified. Three different novel detection methods were introduced in this study: two statistical methods (outlier analysis and kernel density estimation) and one neural network approach (auto-associative network). All the results in this study had a good agreement with regard to basic algorithms and exhibited promising results for damage detection in composite plates by using Lamb waves. Ruotolo *et al* [106] applied a hypothesis test to detect defects in beam structures. The approach procedure first took $n_1$ measurements of natural frequency from undamaged structures, and then compared the values with new data sets from the following test by using a statistical t-test. Any significant difference between two data sets can be referred to damage. This statistical technique was found to perform well. Besides the above mentioned techniques, there are various successful methods used for novelty detection such as artificial neural networks [107], wavelet analysis [108], knn based approaches [109-110], Parzen window density estimation [111], string matching [112] and clustering [113].

### 2.3.2 Outlier analysis

The statistical technique of outlier analysis is used here for novelty detection. The main idea of novelty detection is to establish a set of normal data from the undamaged

condition and then test for abnormality when new data comes [35]. Outlier analysis highlights the potential outlier, i.e. an observed significant deviation from normal data, which may be considered to be produced by a dissimilar mechanism. It is important to know that lots of factors might influence the recorded data, such as temperature, environmental noise, boundary conditions and sensor coupling issues. In this current study, all these factors were assumed to be constant in the experimental procedure. According to this assumption, the distribution of experimental results is considered to be a Gaussian distribution.

Outlier analysis has been widely applied for damage detection. Worden [35] demonstrated four case studies on damage detection by using outlier analysis: one simulation, two pseudo-experimental and one experimental. Chetwynd [38] experimentally proved that outlier analysis successfully detected damages on a curved aluminium plate. Antoniadou *et al* [114] combined outlier analysis with the *empirical mode decomposition* (EMD) method to detect simulated gear tooth faults. Pavlopoulou *et al* [115] Assessed the damage development (crack propagation and debonding) in an aluminium repaired structure by outlier analysis.

Outlier analysis can deal with either univariate or multivariate data. For univariate data, i.e. one dimensional data, the deviation statistic is an effective way to detect outliers and is given by,

$$Z_{\zeta} = \frac{\left| x_{\zeta} - \overline{x} \right|}{S}. \tag{2.28}$$

where $x_{\zeta}$ is the potential outlier; $\overline{x}$ and $S$ are the sample mean and standard deviation of the training data respectively. Outlier analysis for univariate data is relatively straightforward and will be extended to multivariate data in further studies.

In multivariate data analysis, data is composed of more than one dimension for a given set of observations and detection of outliers in this case is more complicated

than analysing univariate data. The relevant discordancy measure is the Mahalanobis Squared-Distance (MSD).

$$\boldsymbol{D}_{\zeta} = \left(\boldsymbol{x}_{\zeta} - \overline{\boldsymbol{x}}\right)^{T} \boldsymbol{S}^{-1} \left(\boldsymbol{x}_{\zeta} - \overline{\boldsymbol{x}}\right). \tag{2.29}$$

where $x_{\zeta}$ is the potential outlier, $\overline{x}$ is the mean vector of the sample observation, $T$ indicates transpose and $S$ is the sample covariance matrix.

In addition, a threshold value which is used for determining whether a new datum is an outlier or inlier can be calculated by a Monte Carlo method. The Monte Carlo method is a computational method that repeats an experiment substantially many times to calculate a result [116-117]. In other words, the observations made for many repetitions of the same experiment can simulate the closed form of theoretical probability. The detailed procedure to achieve the threshold value is summarised by Worden *et al* [35] and is shown below:

(1) Compose a $p \times n$ ( $p$ -dimensions, $n$ -observations) matrix, whose components are randomly generated and have a zero mean and unit standard deviation.

(2) Evaluate of the Mahalanobis squared-distance $D_{\zeta}$ using Equation (2.29) for all experimental data and store the largest value.

(3) Repeat Steps (1) and (2) for a great number of trials to produce an array of largest Mahalanobis squared-distances, and then order them in terms of magnitude.

(4) The threshold is addressed as a critical value obtained by Mahalanobis squared-distance corresponding with a percentage of the resulting array in Step (3). In the current work, a 99% confidence interval was set. That means the possibility of any value exceeding the threshold is less than 1%

The general procedure for multivariate outlier analysis is as follows:

(1) Acquire training data from undamaged structure

(2) Pre-process data then extract features

(3) Calculate Gaussian statistics for normal condition features

(4) Acquire test data, pre-process and extract the same features an previously

(5) Calculate MSD values

(6) Calculate the threshold value by Monte Carlo trials of algorithm

(7) Compare MSD values to threshold value. If any value is greater than the threshold value, damage is inferred.

### 2.3.3 Hypothesis testing for the small samples

Devore *et al* [34] defined a *statistical hypothesis* as a claim or assertion either about the value of a single parameter, about the values of several parameter or about the form of an entire probability distribution. Moreover, *hypothesis testing* is a method of using sample data to decide whether a null hypothesis should be rejected. $h_0$ (the null hypothesis) here refers to an assertion that is assumed to be true until test evidence suggests otherwise. Conversely, $h_a$ (the alternative hypothesis) is the claim that conflicts $h_0$. In other words, the $h_a$ is assumed to be true when the test evidence suggests $h_0$ is false. As has been presented above, the hypothesis testing eventually leads to two possible results, i.e. either reject $h_0$ or fail to reject $h_0$.

Based on the sample data, a test procedure calculates a test statistic value and then judges whether the test statistic value falls into a rejection region or not. Consequently, the null hypothesis will be either rejected or fail to reject [34]. Here, the test statistic is a function of sample data which provides a basis for the validity of the null hypothesis and the rejection region is the region that includes a set of all test statistical values that rejects $h_0$. There is no doubt that the choosing of a rejection region may deeply impact the final results. The key thing is relevant to the relationship between the rejection regions and the errors. Two possible errors need to be considered in the test procedure. That is, $h_0$ may be rejected when it is true or $h_0$ may fail to reject when it is false. The former case is called a Type I error and the latter is named as a Type II error. The

conclusions for a hypothesis test are shown in Table 2.1. In an ideal world, neither of these errors may occur. However, this is usually impossible in practice because a great number of factors may affect the experimental results and it is hard for scientists and engineers to validate them. Instead of pursuing error-free procedures, it is better to seek a procedure that makes either type of error as small as possible. The option of a specific rejection region cutoff value must compromise between confidence and accuracy. An ultimate example is a rejection region cutoff value corresponding to a 100% confidence interval. This value is 100% correct but meaningless in practice. Moreover, Devore *et al* [34] suggested that choosing a largest value of $\alpha_{error}$ ( probability of a *Type* I *error*) within tolerance may help to balance $\alpha_{error}$ and $\beta_{error}$ ( probability of a *Type* II *error*). In SHM, the null hypothesis is usually assumed to be no structural damage. $\alpha_{error}$ here refers to a false alarm when these is no damage in the structure. On the other hand, $\beta_{error}$ refers to damage occurrence when there is no alarm. It is clear that identifying damage is the priority and to guarantee the safety of structures. According to this, a small value of $\beta_{error}$ is necessary for SHM. The resulting value of $\alpha$ is referred as a significant level of test and is generally chosen as 0.1, 0.05 or 0.01 in practice. In addition, the rejection region also should be considered as *upper-tailed*, *lower-tailed* or *two-tailed* tests which correspond to only large values, only small values or both large and small value of the test statistic, respectively.

Table 2.1: The conclusions for a hypothesis test

| Conclusion | True State of Nature | |
|---|---|---|
| | $h_0$ is true | $h_a$ is true |
| $h_0$ is true | Correct decision | A Type II error |
| $h_a$ is true | A Type I error | Correct decision |

In practice, it is usual that the population variances are unknown to researchers and the sample size is small. Assuming that the population of any two samples is normally distributed, the statistical t-test is given as below [118]:

$$t = \frac{\bar{X}_1 - \bar{X}_2 - (\mu_1 - \mu_2)}{\sqrt{\frac{S_1^2}{m} + \frac{S_2^2}{n}}} \tag{2.30}$$

Where subscripts 1 = the sequence of sample data one, 2 = the sequence of sample data two, $\bar{X}_1$ and $\bar{X}_2$ are the sample means of data set 1 and 2 respectively, $m$ and $n$ are the sample sizes, $\bar{S}_1$ and $\bar{S}_2$ are sample standard deviation of data set 1 and 2 respectively, $\mu_1$ and $\mu_2$ are unknown population means. In SHM, it is natural to assume that the null hypothesis is the case in which damage is not present, i.e. $\mu_1 - \mu_2 = 0$. Furthermore, different sample tests would use the same sample size. The alternative to Equation (2.24) can be expressed as:

$$t_{\alpha_s n} = \frac{\bar{X}_1 - \bar{X}_2}{\sqrt{\frac{S_1^2 + S_2^2}{n}}} \tag{2.31}$$

An outline of the hypothesis test with small sample size is given below:

(1) State the null hypothesis

(2) State the alternative hypothesis.

(3) Select appropriate significance level, $\alpha_s$

(4) Compute the value of the test statistic

(5) Decide whether the null hypothesis $h_0$ should be rejected. If $h_0$ is not rejected, the structures or systems are still considered in normal condition. Otherwise, it may be assumed that damage is present.

To the author's knowledge, this hypothesis testing has not yet been applied in the context of vibro-acoustic SHM. Consequently, this approach will be explored in later chapters.

## 2.4 Summary

This literature review exposed a great number of research efforts investigating the sensitivity of nonlinear acoustics and Lamb waves' propagation for damage detection. The material damage includes fatigue cracks for metals, debonding and delamination for composite laminates. Both the nonlinear acoustic waves and Lamb waves are well established and widely used in diagnosing defects at an early stage for most type of material with various geometries.

The physical mechanisms related to nonlinear acoustics for damage detection are complicated to understand because similar nonlinear effects may be caused by different mechanisms and vice versa. These mechanisms include nonlinear elasticity, contact-type nonlinearity, vibro-acoustic modulation, crack-induced nonlinearity, the resonance frequency shifting, amplitude dissipation due to hysteresis, adhesive or themo-elasticity, as well as the Luxembourg-Gorki effect.

The nature of Lamb waves was presented in this chapter. The characteristic equation, phase and group velocity were derived. Furthermore, the optimisation for the excitation Lamb wave excitation signals and mode selection was discussed in some detail. In addition, the piezoelectric transducers employed in this work were described.

Statistical analysis is a powerful tool to help engineers and scientists extract useful information from raw data and make proper decisions in the presence of variability and uncertainly. Hypothesis testing for the small samples, novelty detection and outlier analysis were demonstrated in this chapter.

The main novel element of this work for SHM is to compare various nonlinear acoustic techniques with lamb wave methods through different damage severities.

# Chapter 3

# 3 Fatigue Crack Detection on Glass and Aluminium Plates

Detecting fatigue damage is an important factor for structural health monitoring. This chapter constitutes a damage detection study on glass and aluminium plates by using the nonlinear acoustic and guided wave methods. The statistical approaches, hypothesis test and outlier analysis, are applied to damage detection. The study reveals a distinction between the damaged and the undamaged plates, and also assesses the severity of damage.

## 3.1 Glass plate test

### 3.1.1 Test specimen

The specimen used in the current study was a rectangular 150x400x2mm glass plate. Soda lime glass was chosen because it is widely used in many industrial productions (e.g. windowpanes, glass containers or glass bakeware). The main material properties are shown in Table 3.1.

Wurm [119] described glass as a supercooled liquid due to its non-crystalline molecular structure. Glass is isotropic, i.e. its properties are uniform in all orientations. Meanwhile, glass is a brittle material that can deform linear-elastically under increasing load until it exceeds its load-bearing capacity, and then the fractures take place without warning. A graphic illustration of glass linear deformation can be seen in Figure 3.1. The reason for choosing glass as a test sample is that a crack on a transparent material could be easily visible, being the only defect in the material.

Table 3.1: Soda-lime glass properties [119].

| | Soda-lime glass |
|---|---|
| Density $\rho$ [g/cm$^3$] | 2.44 |
| Modulus of elasticity $E$ [GPa] | 72 |
| Tensile strength $f_{t.k}$ [MPa] | 33 |
| Compressive strength $f_{c.k}$ [MPa] | 325 |
| Poisson's ratio $\upsilon$ | 0.23 |
| Shear modulus G [GPa] | 28.5 |

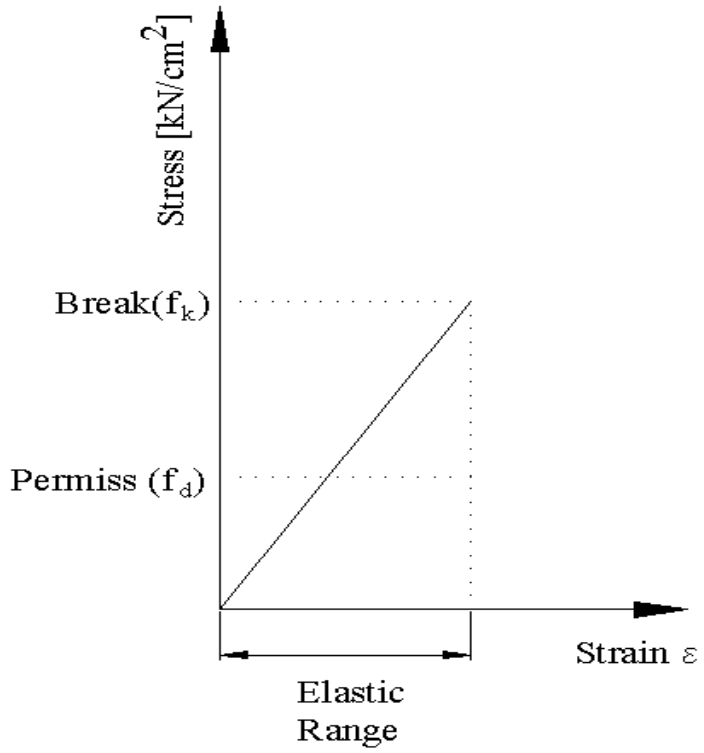


Figure 3.1: Linear elastic deformation behaviour of glass.

### 3.1.2 Modal analysis

Modal analysis is the process of determining the vibration characteristics (mode shapes, damping factors and natural frequencies) of a structure [120]. Modes, as unique features of a structure, are highly dependent on the mass, damping, stiffness and boundary conditions of the structure. When a fatigue crack exists in a plate, modal analysis provides useful information about how the crack edge moves corresponding to the low frequency excitation. In the current study, modal analysis is implemented using Finite Element (FE) modeling and Leissa modeling [121] to obtain analytical solutions. The results are then validated by experimental modal testing.

The determination of the natural frequencies of vibration is an essential element for investigating the behaviour of vibration of structures or systems. It is well known that a structure or system excited at one of its resonance frequencies will result in extensive vibration amplitude and dynamic stress as well as noise level [122]. In the current study, the test structure will be excited at various resonance frequencies. Consequently, the structure responds with a characteristic displacement pattern, named the mode shape. Each mode shape matches a natural frequency and the mode shape is determined by the boundary conditions and the shape of the body surface. The magnitude of the mode shape is time variant except at nodal points where the displacement of the mode shape is zero. There are two important things that need to be considered in this study. First of all, the vibration excitation point should avoid a nodal position for corresponding natural frequencies; otherwise, the plate will remain at rest during the test. Secondly, the modal shape determines the particle motion in the body.

The natural frequency can be defined as the square root of the ratio of stiffness and mass. The equation is shown as below [123]:

$$f = \frac{1}{2\pi}\sqrt{\frac{k}{m}} \tag{3-1}$$

where $f$ is resonance frequency (in Hz), $k$ is the modal stiffness of the structure and $m$ is the modal mass of the structure. Observed from Equation (3-1), the natural frequency depends only on the properties of the structure, i.e. the mass and stiffness. It is clear that this equation is only applicable to a single degree of freedom system. The thin plate structure in the current study is a continuous system and has an infinite number of degrees of freedom and becomes far more complicated than the former system.

#### 3.1.2.1 Modal analysis by the finite element method

The modal characteristics of the glass plate were obtained from a modal analysis, using standard commercial finite element software, for varying natural frequencies and mode shapes.

The material properties used in this study are mentioned in Table 3.1. The geometry of the plate is a rectangular solid with size 150x400x2 mm. The plate is modelled using 20 node quadratic brick element. Each node has three degrees of freedom ($x$, $y$ and $z$ direction). The plate was discretised into 360 elements with 2733 nodes and there is one element through the thickness. In addition, the block Lanczos method was used to extract the natural frequencies and mode shapes of the plate due to its wide application and high efficiency. Furthermore, the modal analysis identified the first 6 vibration modes by eliminating rigid-body modes whose frequencies are around 0Hz. Rigid body modes are detected because no constraint is applied on the model in the current investigation.

Modelling a crack is another challenging work within FE analysis. Here the crack area has been removed and replaced by two pieces of component. The component and plate were bonded together at the contact region. This arrangement introduced the

discontinuity on the border between two components to simulate a crack moving action (opening-closing, sliding, etc.) between the contact surfaces. A graphical representation of modeling a crack can be seen in Figure 3.2.

(a)

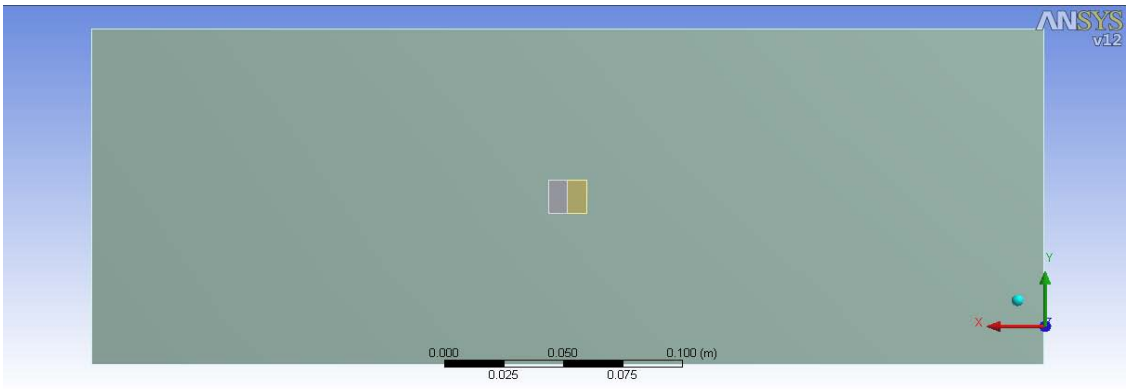


(b)

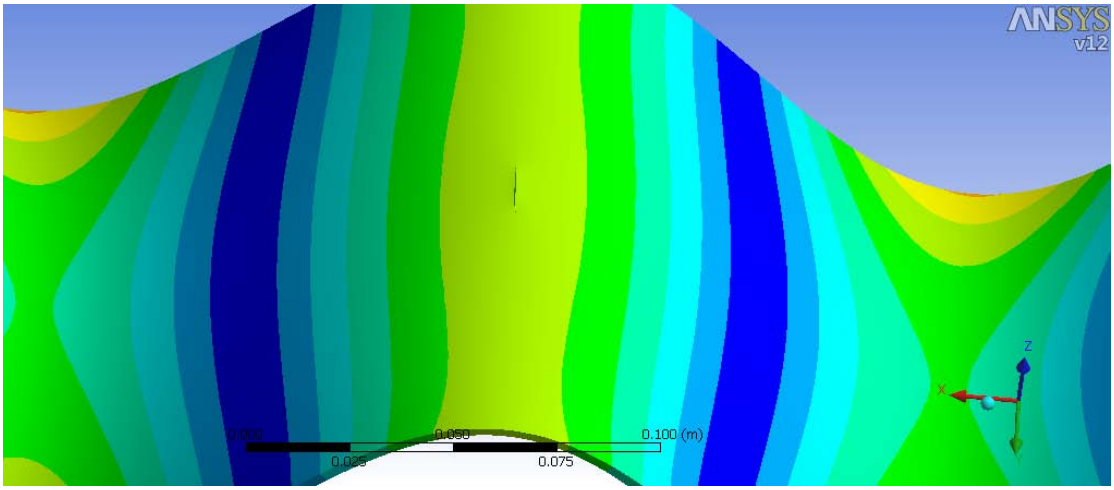


Figure 3.2: Modeling a crack in (a) two-dimensional (2-D) diagram (b) 3-D diagram.

As mentioned in Chapter 1, there are three fundamental modes of a moving crack. Crack mode I is where a tensile strain perpendicular to the crack plane moves the crack faces apart from each other leading to opening and closing of the crack (i.e. in the $x$-direction). Crack mode II is where the crack faces slide on each other due to shear stress (i.e. in $y$-direction). Crack mode III is where the crack exhibits tearing action under a strain field perpendicular to the plate (i.e. in $z$-direction).

Crack edge divergence (CED) was modeled by two nodal points (A and B) located in

the middle of both crack edges [22], as shown in Figure 3.3. It is apparent that two nodal points overlap when the crack faces are fully closed. When the plate is excited, the two points move away from the original location in three different directions ($x$, $y$ and $z$), as previously mentioned. The divergence between two crack edges, with respect to the different directions, was recorded for various excited vibration modes. It is known that the crack motion in different directions corresponds to the three crack modes and these three crack modes can be observed with different divergence levels. However, Klepka *et al* [22] illustrated that only one dominant crack mode corresponds to a given excited vibration mode. In other words, the largest divergence in one direction is far larger than the other directions. Three different crack modes introduce various crack edge behaviours with regards to the closing-opening action, friction, energy dissipation, stiffness or thermo-elasticity. As a result, these crack edge behaviours could heavily influence the interaction between the crack and ultrasonic wave.

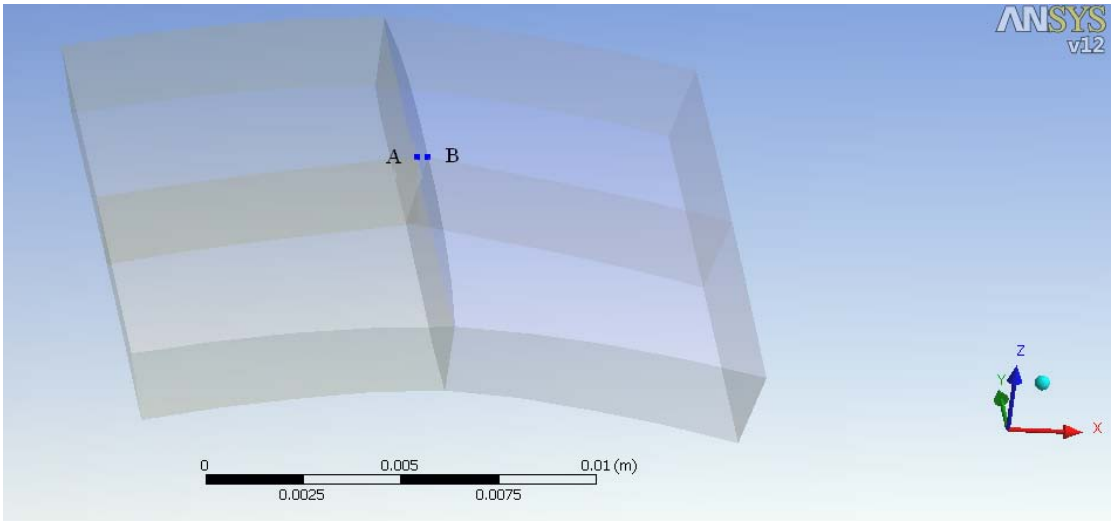


Figure 3.3: Crack edge divergence for two nodal points.

The bar chart in Figure 3.4 shows the first six vibration modes corresponding to various crack mode behaviours. It should be noted that the bars in Figure 3.4 are vertically stacked bars which display the results of all 3 dimension crack edge divergence. Due to the overwhelming value of the largest divergence in one direction, the values of the other directions are hardly observed in the chart. Observed from

Figure 3.4, the dominant crack edge divergence in the *x* direction as an opening-closing action (crack mode I ) was obtained when the glass plate was excited with the 1st and 5th vibration modes. In the same way, the dominant crack edge divergence in the *y* direction is a sliding action (crack mode II ) and was found when the glass plate was excited with the frequencies corresponding to the 2nd and 6th modes. Similarly, the largest crack edge divergence in the *z* direction, a tearing action (crack mode III ), was obtained when the glass plate was excited with the 3rd and 4th vibration modes. It is noticable that the crack edge divengence for modes 1, 3, 5 and 6 were far more prominent than modes 2 and 4. So modes 1, 3 and 6 were chosen for low frequency excitation which correspond to crack mode I (opening-closing action), crack mode III (tearing action) and crack mode II (sliding action), respectively.

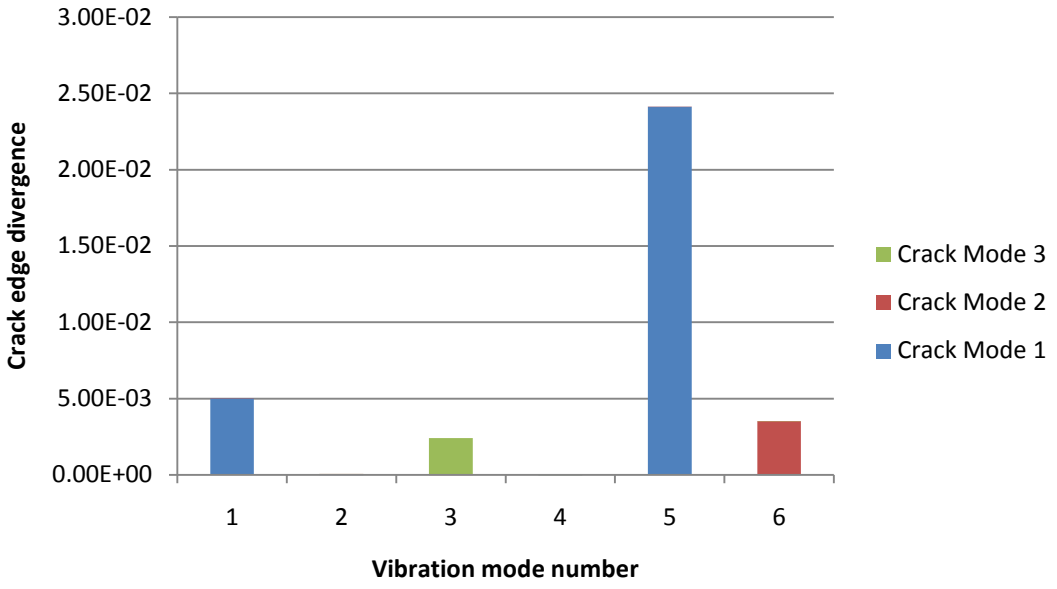


Figure 3.4: Crack edge divergence against various vibration modes with respect to crack modes.

The natural frequencies and mode shapes for modes 1, 3 and 6 of an undamaged glass plate are shown in Figure 3.5. These are the 69.0Hz first bending vibration mode (mode 1), 191.2Hz second bending mode (mode 3) and 404.3Hz third torsional mode (mode 6).

Mode 1

69.0 Hz

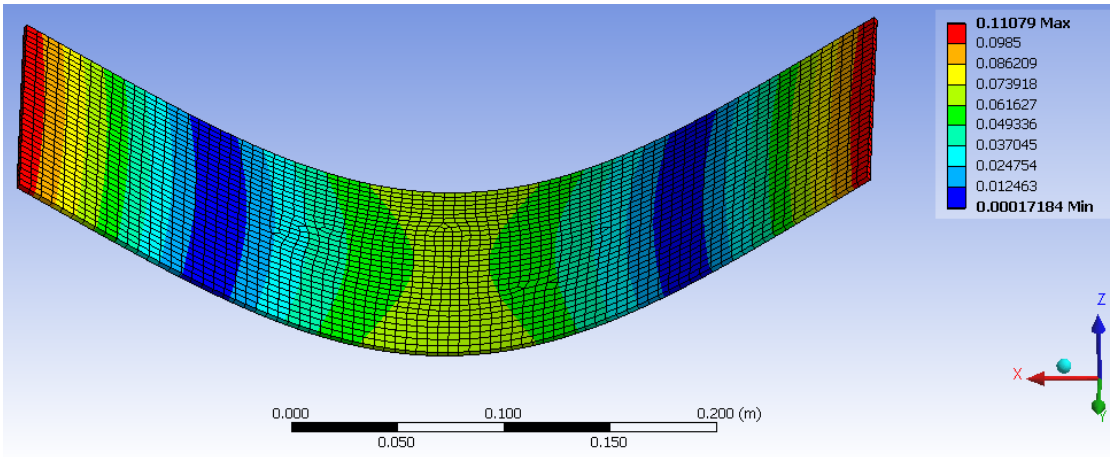


Mode 3

191.2 Hz

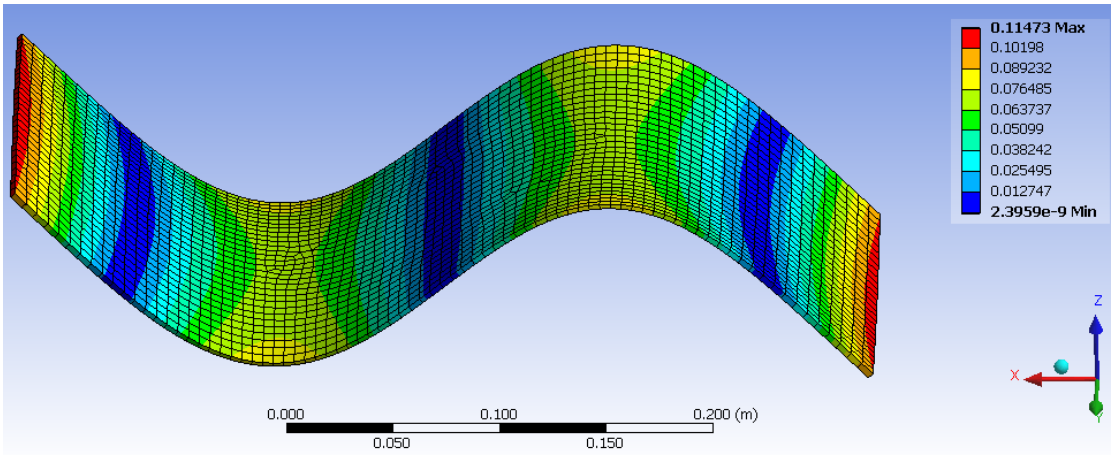


Mode 6

404.3 Hz

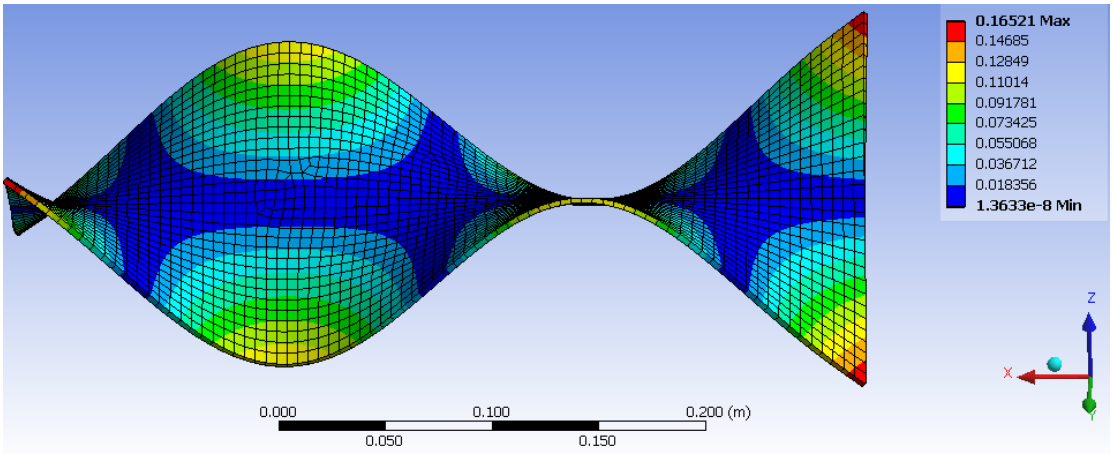


Figure 3.5: Natural frequencies and mode shapes for uncracked glass plate.

Mode shape describes characteristic displacement patterns of a structure. The most effective excitation location must always be determined based on the mode shape of the structure. If the excitation point is located on a node which has zero displacement, the structure will not respond due to its mode shape. The low frequency excitation point has a great impact on the response signals and it should be kept away from the nodal areas. Meanwhile, the target area of excitation is better located close to the received sensors in order to avoid energy attenuation when the acoustic wave is travelling long distances. In this study, the ideal excitation point was selected around the middle of the plate. It is placed 42mm from the right edge and 163mm from the bottom edge of the plate. Although exciting this point may not actuate the maximum amplitude response, it can produce responses for all three modes.

#### 3.1.2.2 Modal analysis by analytical calculation

Leissa [121] presented an analytical model for finding the modal properties of a plate. In his work, the classical Rayleigh-Ritz method was employed with beam functions to calculate the dimensionless frequency parameters of a plate. Based on this, Blevins [124] created a table for calculating the natural frequencies of the first six modes of a rectangular plate for all 21 possible boundary conditions. There are three typical boundary conditions related to four edges of rectangular plates, i.e. free, simply supported and clamped. In the current study, only the plate model with all free edges will be considered.

The formula for obtaining the natural frequency of the rectangular plate is given below [124]:

$$f_{ij} = \frac{\lambda_{ij}^2}{2\pi a^2}\left[\frac{Eh^3}{12\gamma\left(1-\upsilon^2\right)}\right]^{\frac{1}{2}};\ \text{i=1, 2, 3…; j=1, 2, 3…;} \qquad (3\text{-}2)$$

where $f_{ij}$ is natural frequency in Hz, $\lambda_{ij}$ is a dimensionless frequency parameter for rectangular plates, $a$ is the length of the plate, $b$ is the width of the plate, $h$ is the

thickness of the plate, $E$ is young's modulus of elasticity, $\gamma$ is mass of per unit area of the plate and $\upsilon$ is Poisson's ratio.

For the case of a plate with free (F-F-F-F) boundary conditions, the calculation results are presented in Table 3.2.

Table 3.2: Dimensionless frequency parameters $\lambda_{ij}^{2}$ for a rectangular plate with free boundary conditions [124].

| **a/b** | **Mode sequence** | | | | | |
|---|---|---|---|---|---|---|
| | **1** | **2** | **3** | **4** | **5** | **6** |
| **0.4** | 3.463 | 5.288 | 9.622 | 11.44 | 18.79 | 19.10 |
| **2/3** | 8.946 | 9.602 | 20.74 | 22.35 | 25.87 | 29.97 |
| **1** | 13.49 | 19.79 | 24.43 | 35.02 | 35.02 | 61.53 |
| **1.5** | 20.13 | 21.60 | 46.65 | 50.29 | 58.20 | 67.49 |
| **2.5** | 21.64 | 33.05 | 60.14 | 71.48 | 117.5 | 119.4 |

According to the soda-lime glass properties in Table 3.1, the analytical values for the 1st, 3rd and 6th modes are obtained and shown in Table 3.3

Table 3.3: The analytical natural frequency values for 1st, 3rd and 6th modes

| Mode sequence | 1 | 3 | 6 |
|---|---|---|---|
| Analytical mode value | 69.4 Hz | 192.8 Hz | 382.8 Hz |

### 3.1.2.3 Experimental modal analysis

Experimental modal analysis was performed to establish the resonance frequencies of low-frequency modal excitation for the nonlinear acoustic tests. A 100V swept sine signal, starting at 1Hz and increasing to 2000Hz in 2s was used to excite the intact (i.e. uncracked) plate. The response signal was sampled with a frequency of 5kHz.

Three low-profile, surface-bonded piezoceramic transducers were installed on the plate. A HBM-X60 2-component fast curing glue was used to attach the transducers.
A PI Ceramics PL-055.31 stack actuator ($5\times5\times2$ mm) was used for low-frequency modal excitation. Two PI Ceramics PIC155 transducers (diameter 10 mm; thickness 0.5 mm) were used for ultrasonic wave excitation (this high frequency excitation was used in future vibro-acoustic tests rather than for the modal analysis here) and for all response sensing. Figure 3.6 shows a schematic diagram of the plate with transducer locations.

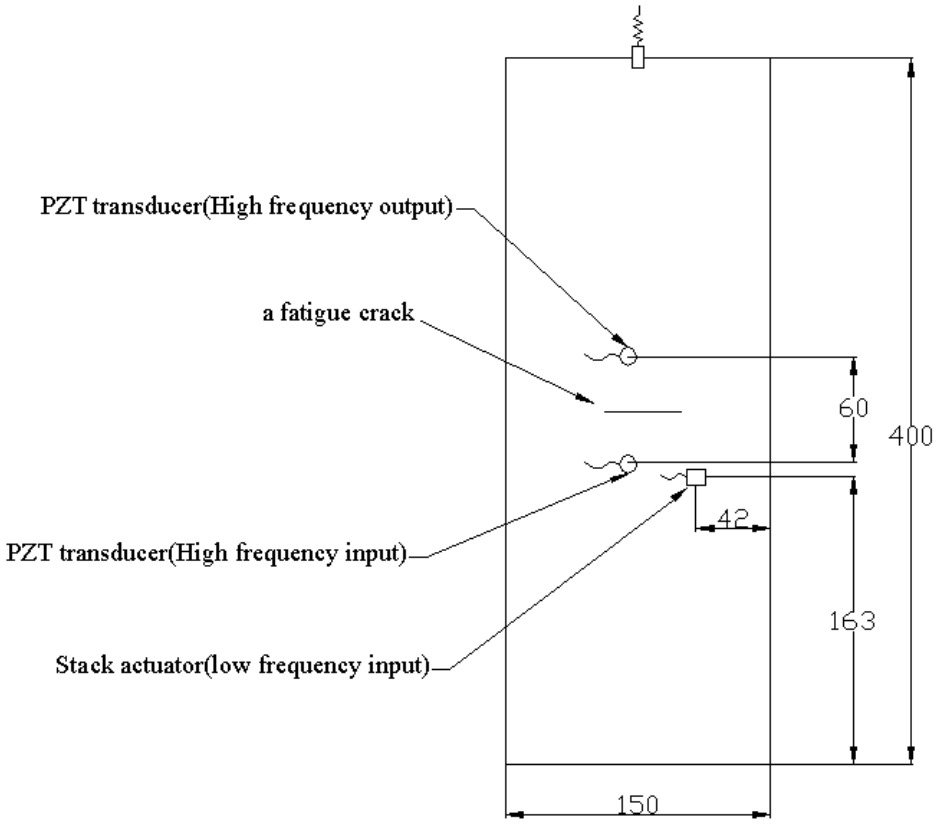


Figure 3.6: Schematic diagram of the glass plate.

The excitation and response data were used to calculate the frequency response function in order to reveal resonance frequencies. Figure 3.7 gives the amplitude of the experimental FRF. The first three excited modes were confirmed as the 1st, 3rd and 6th vibration modes for the analysed plate. The 2nd, 4th and 5th vibration modes did not

appear or appeared only slightly in this plot; this is because the plate is excited in a nodal area and/or the response measured in this area. These are the first three vibration modes leading to the largest crack divergence associated with the three crack modes shown in Figure 1.1. Based on numerical simulations of crack edge divergence (Section 3.1.2.1), excitation of the plate with the frequency corresponding to the 1st, 3rd, and 6th mode leads to crack mode I (opening), mode III (tearing) and mode II (sliding), respectively. As mentioned in Section 3.1.2.1, these crack modes lead to different nonlinear phenomena with respect to elastic and dissipative behavior. Therefore, frequencies 73.9, 204.5 and 398.6Hz - corresponding to the 1st, 3rd and 6th vibration modes, respectively - were selected for low-frequency excitation in the current nonlinear acoustic investigations.

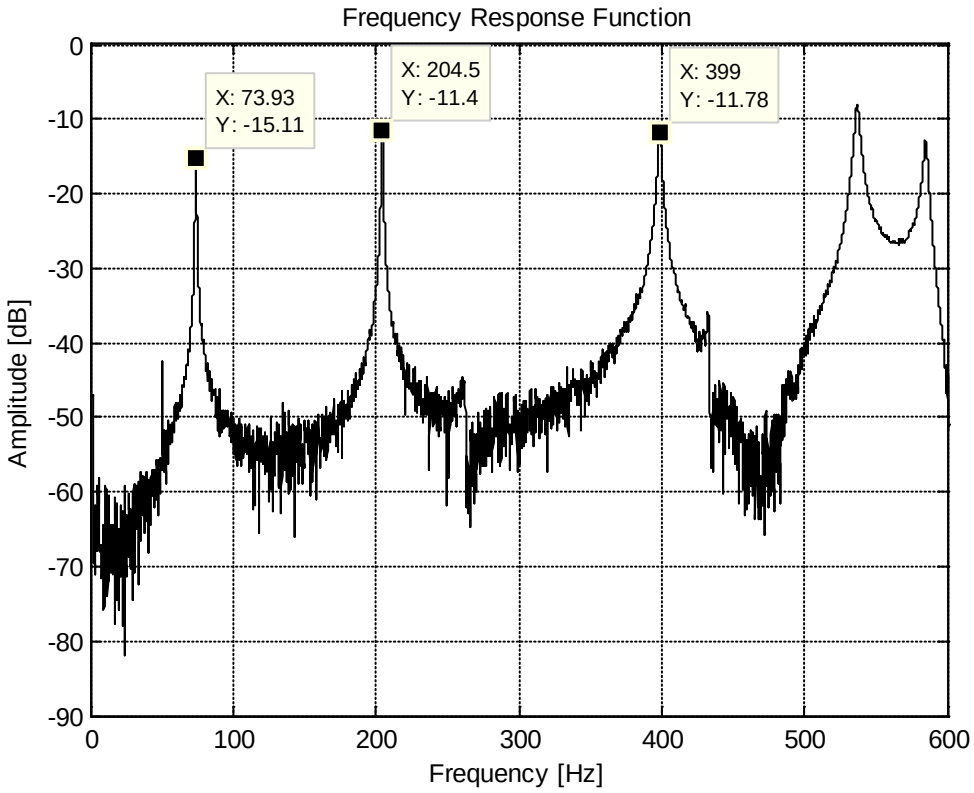


Figure 3.7: Modal analysis result: vibration FRF.

The comparison of extracted natural frequencies methods based on FE, analytical and experimental methods are summarised in Table 3.4. The deviation between the analytical and experimental results ranges from 7.1% to 1.3%. The deviations from

the analytical method are mainly because of the differences between the estimated values of *a/b* in calculation, which is 2.5 and the actual geometrical value is equal to 2.66. In addition, the deviation from the FE method is due to refined mesh size and imprecise material input properties. Furthermore, the mass and stiffness of the transducers and the mass of the wiring also affect the result.

Table 3.4: Comparison of extracted natural frequency methods base on FE, analytical and experimental methods

| | Mode 1 (Hz) | Mode 3 (Hz) | Mode 6 (Hz) |
|---|---|---|---|
| Natural frequency from experimental method | 73.9 | 204.5 | 399 |
| Natural frequency from Analytical method | 69.4 | 192.8 | 382.8 |
| Percentage deviation between experimental and analytical results % | -6.5 | -6.1 | -4.2 |
| Natural frequency from FE method | 69 | 191.2 | 404.3 |
| Percentage deviation between experimental and FE results % | -7.1 | -7.0 | 1.3 |

### 3.1.3 Experimental procedures for nonlinear acoustic tests

The experimental work was performed on a rectangular $150 \times 400 \times 2$ mm glass plate as mentioned in Section 3.1.1. It included a classical modal test (Section 3.1.2.3), a single wave vibration test, a vibro-acoustic test and FRFs with varying excitation levels.

The low- and high-frequency excitation signals were generated using a two-channel TTi-TGA 1242, 40MHz arbitrary waveform generator. The low-frequency signal driving the stack actuator was additionally amplified to the required level with a PI

E-505 LVPZT piezo-amplifier. Signal responses were acquired using a four-channel LeCroy Waverunner LT264, 350MHz, 1GS/s digital oscilloscope. The experimental setup is shown schematically in Figure 3.8.

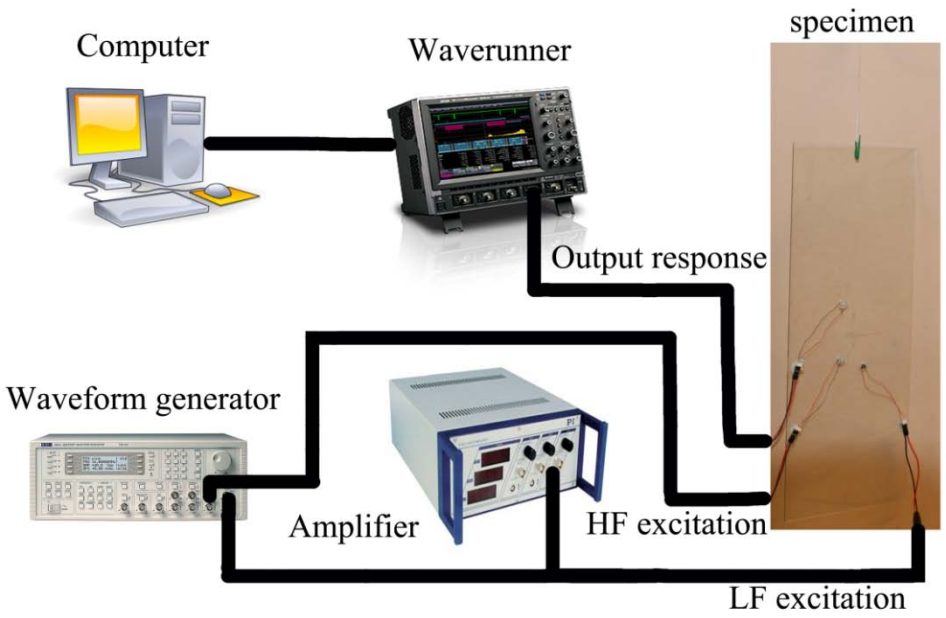


Figure 3.8: Experimental setup for the nonlinear acoustic test.

A Vickers indenter, as shown in Figure 3.9, was used to introduce and grow a crack in the centre of the glass plate. The force and dwell time of the indenter were set to 10kg and 25s, respectively. Various cracks lengths were analysed, i.e. 2, 4, 6, 8, 10, 12, 14, 16, 20, 25, 30 and 35mm. Figure 3.10 shows the glass plate with a crack close-up.

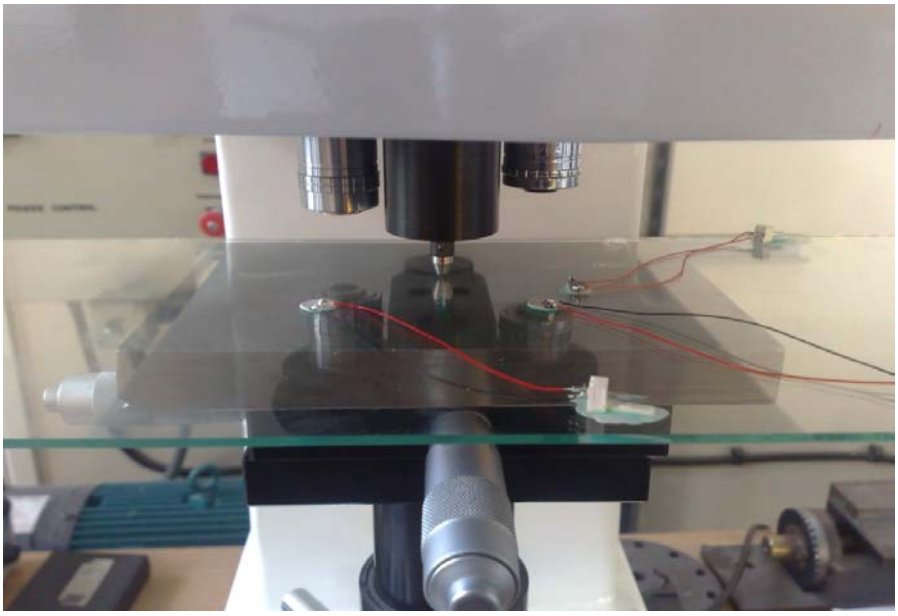

Figure 3.9: Vickers Indenter was used to produce a crack.

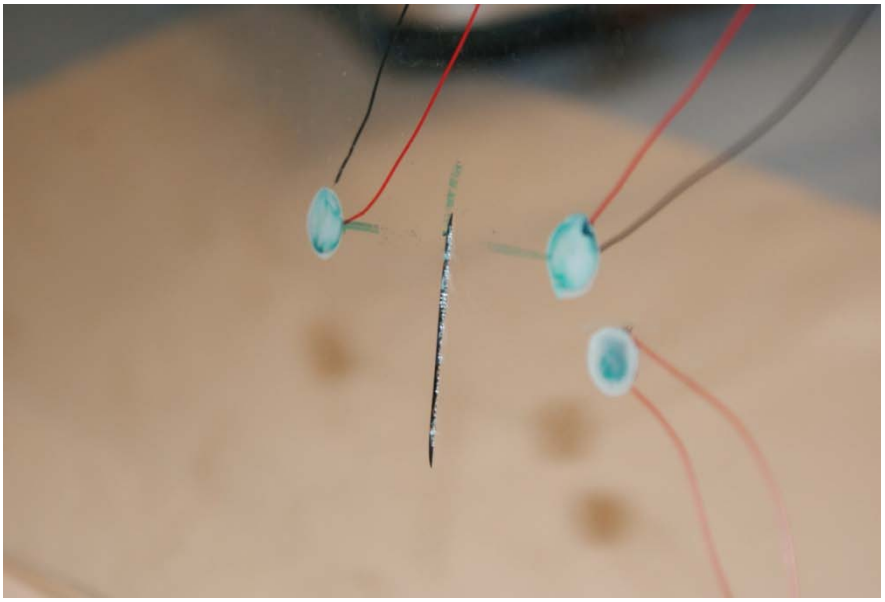

Figure 3.10: Glass plate with a crack close-up.

The plate was freely suspended in all experimental tests using rubber cords to simulate free vibration boundary conditions and to eliminate possible spurious nonlinearities in nonlinear acoustic tests.

The intact and cracked glass plate was tested using various nonlinear acoustic approaches as described in Chapter 2. The experiments involved single-wave (vibration and ultrasound), combined vibro-acoustic excitation and FRFs with varying

excitation levels. Vibration excitation always involved one of the selected vibration modes, as described in Section 3.1.2.1. Various amplitude excitation levels were used. The maximum peak-to-peak amplitudes of the low-frequency and high-frequency excitation used were equal to 100V and 20V, respectively. Two factors were considered in choosing excitation amplitude: Large amplitude improves signal-to-noise ratio. Meanwhile, the maximum amplitude must not exceed the maximum voltage limit of a transducer. It is compulsory to use a sampling frequency which is at least twice the highest waveform frequency. Otherwise, data cannot be correctly constructed due to aliasing. In addition, higher sampling frequency gives lower frequency resolution. Therefore, the sampling rate used to acquire responses from the single-wave vibration excitation test was equal to 20kHz. The sampling rate for all other response signals was 500kHz. For the FRFs with varying excitation levels test, the glass plate was actuated using a step-sweep frequency around one of the natural frequencies. This process was repeated by increasing the drive voltage from 10Vpp to 100Vpp. The sampling rate for all other response signals of the FRFs with varying excitation levels test was 5kHz.

Once signal responses were gathered from all tests performed, various analyses were used to reveal possible nonlinear features that could be attributed to crack-wave interactions and further used for crack detection. The study involved analysis of frequency shifting, damping estimation, higher harmonic generation and modulation sidebands, as described in Chapter 2.

In order to test and estimate the differences between two population means, statistic researchers draw random samples from each of the two populations. Then, a hysteresis test can be used to model whether these two population have the same mean value based on these samples [34, 125-126]. In the current study, if the sample is not consistent with the hypothesis, the nonlinearity contributed by a fatigue crack will overweight the effect of coincidence.

The following steps describe, in detail, the procedure that is adopted to derive the hypothesis test:

1. Based on Equation 2-4, 19 of the $\beta$ values for each damage level are chosen for sample data. Due to the constant values for the wave propagation distance, wave velocity and excitation frequency in this study, $\beta$ values are simplified as the ratio of the magnitude of the 2nd harmonic to the square magnitude of the fundamental frequency.
2. A t distribution is based on the assumption of normal distribution. According to this, 19 of the $\beta$ values for each damage level were examined for fitting a normal distribution. MATLAB code 'normplot' graphically assesses whether the data in X could come from a normal distribution. The assessment of normal distribution results for each damage level is shown in **Appendix B**. If the sample data are normal distribution, the plot will be linear. Otherwise, it will be the curvature plot.
3. After justifying whether the data comes from the normal distribution, a hypothesis test follows the procedure mentioned in Section 2.3.3:

   Null hypothesis: $h_0 : \mu_2 - \mu_1 = 0$

   Alternative hypothesis: $h_a : \mu_2 > \mu_1$

   Degree of freedom: $df = 18$

   Significant level: $\alpha_s = 0.05$

   Test statistic value: $t_{\alpha_s n} = \dfrac{\bar{X}_1 - \bar{X}_2}{\sqrt{\dfrac{S_1^2 + S_2^2}{n}}}$

   Rejection region: The form of $h_a$ implies the use of right tail $\alpha_s$ with rejection region: $t_{\alpha_s n} > 1.734$ (see **Appendix A**).

### 3.1.4 Experiment results

#### 3.1.4.1 Single-wave vibration excitation

Figure 3.11 shows examples of power spectra from single-wave excitation tests using the 1st, 3rd and 6th vibration modes. Two different plate conditions are analysed, i.e. the intact (or uncracked) plate and the plate with a 35mm crack (most severe). A clear pattern of higher harmonics can be observed in all analysed spectra, even for the uncracked plate. Observed from Figure 3.11(a), Figure 3.11(b) and Figure 3.11(c), the amplitudes of second harmonics for the 35mm cracked plate with excitation of 1st, 3rd and 6th vibration modes increasing 20dB, 10dB and 10dB respectively.

The amplitude of the second harmonic is shown further in Figure 3.12 for all crack lengths in order to reveal possible changes in the nonlinear perturbation coefficient β. The figure gives the test statistic value for the perturbation coefficient β against the crack length. Any test statistic value above the critical value line is considered as a nonlinearity resulting from damage. Observed from Figure 3.12(a), when the crack length reaches 16mm and beyond, the nonlinearity contributed by a fatigue crack can be detected for the first mode excitation. Similarly, statistically significant results are found for the 14mm crack and beyond with excitation of the third vibration mode. Unfornately, the results for mode 6 are not statistically significant for detecting a crack.

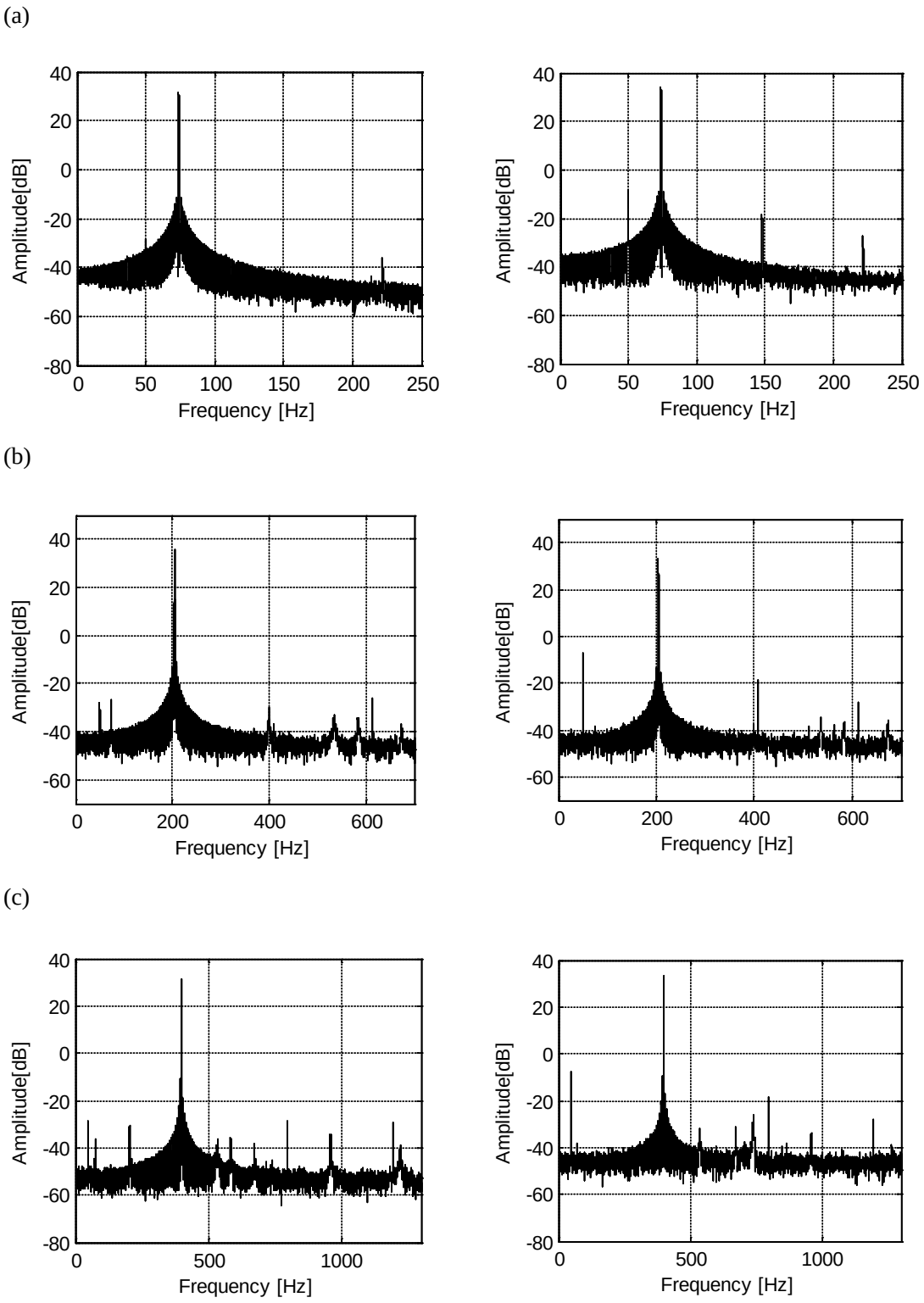


Figure 3.11: Power spectra density showing the fundamental peak and harmonics for the uncracked (left column) and 25mm cracked (right column) plate excited by (a) 1st, (b) 3rd and (c) 6th mode.

(a)

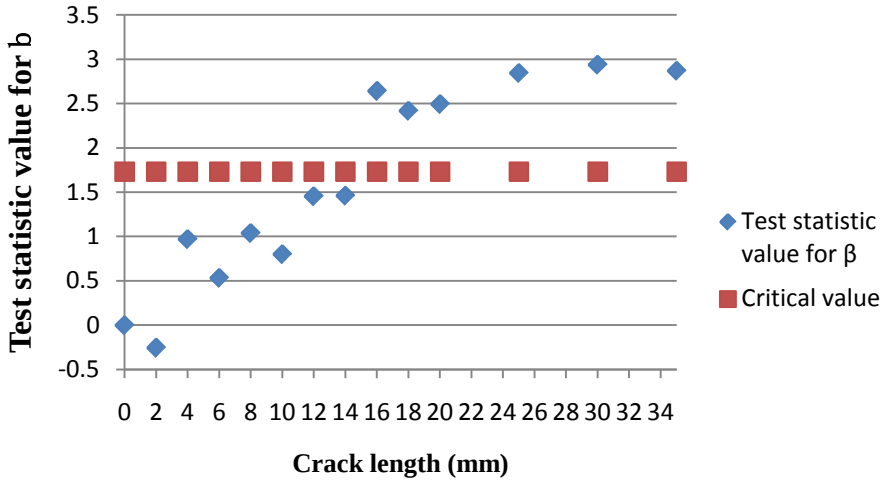


(b)

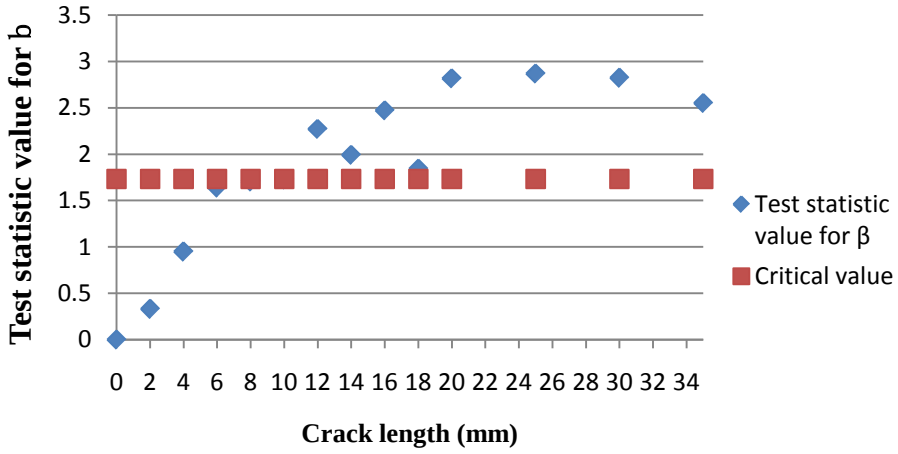


(c)

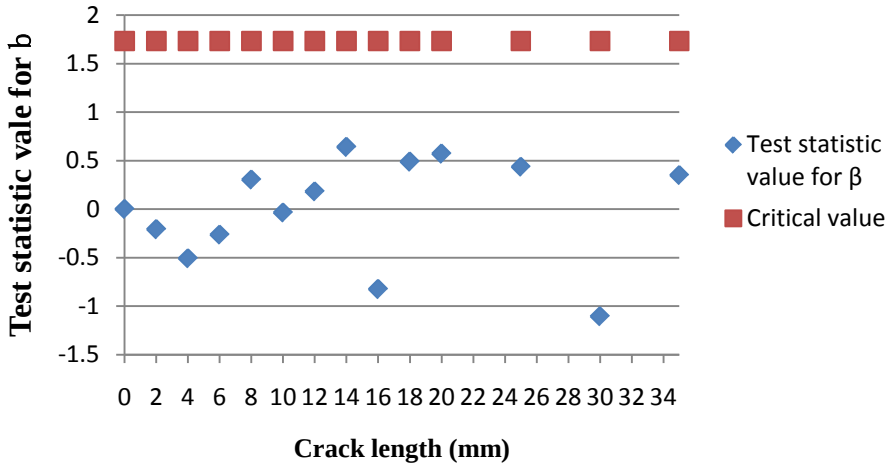


Figure 3.12: Test statistical value for $\beta$ against various crack severities for (a) 1$^{st}$, (b) 3$^{rd}$ and (c) 6$^{th}$ mode.

### 3.1.4.2 FRFs with varying excitation levels test

Figure 3.13 shows examples of zoomed frequency response functions around the 1st, 3rd and 6th mode, respectively. The spectra were obtained for various excitation amplitudes. Although, the response amplitude increases with excitation – as expected – no frequency shifts (1st and 3rd mode) or only slight shifts (6th mode) are observed.

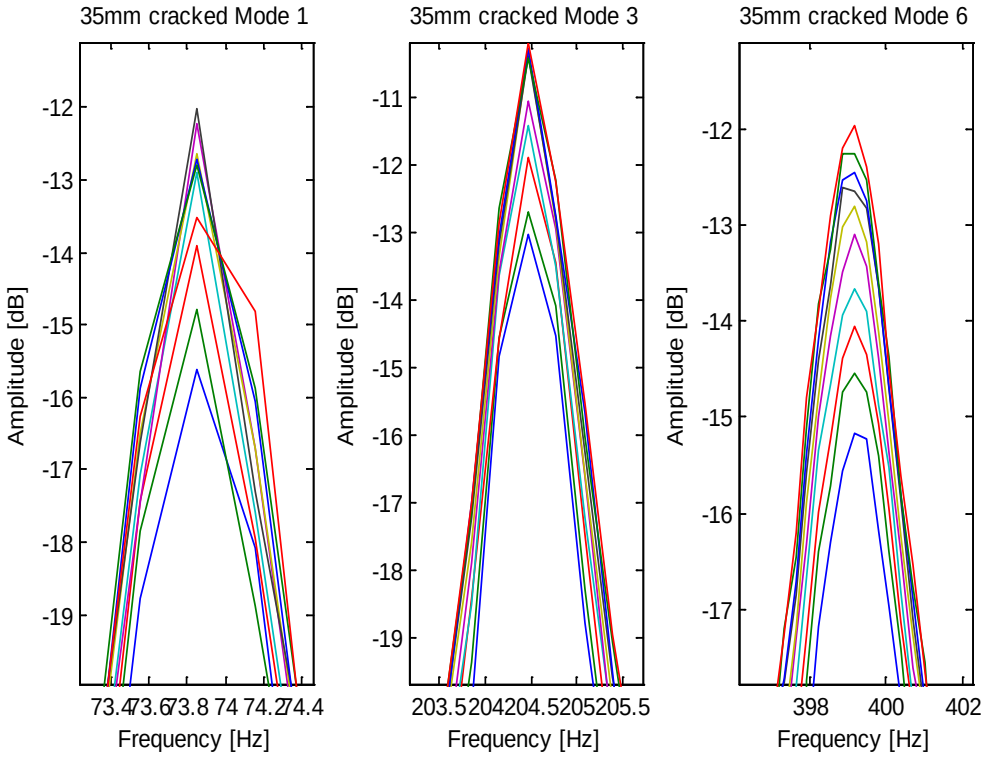


Figure 3.13: Zoomed frequency response function around (a) 1st mode, (b) 3rd mode and (c) 6th mode for 35mm cracked plate.

Similar work was achieved by using a single degree of freedom curve fitting method. The measured FRF data points were fitted to a single degree freedom Nyquist plot which displays the real and the imaginary parts of the receptance. The natural frequency is located at the maximum change rate in arc length with frequency. The natural frequencies for Mode 1, 3 and 6 with different crack lengths are shown in Figure 3.14. Observed from the results, the natural frequencies do not show shifting with increasing excitation voltage. Meanwhile, the natural frequencies of the uncracked plate and with various crack lengths are almost overlapping in a limited frequency range. The frequency shifting approach does not show too much

information. In other words, the nonlinear hysteresis effect is negligible for the damaged glass plate.

(a)

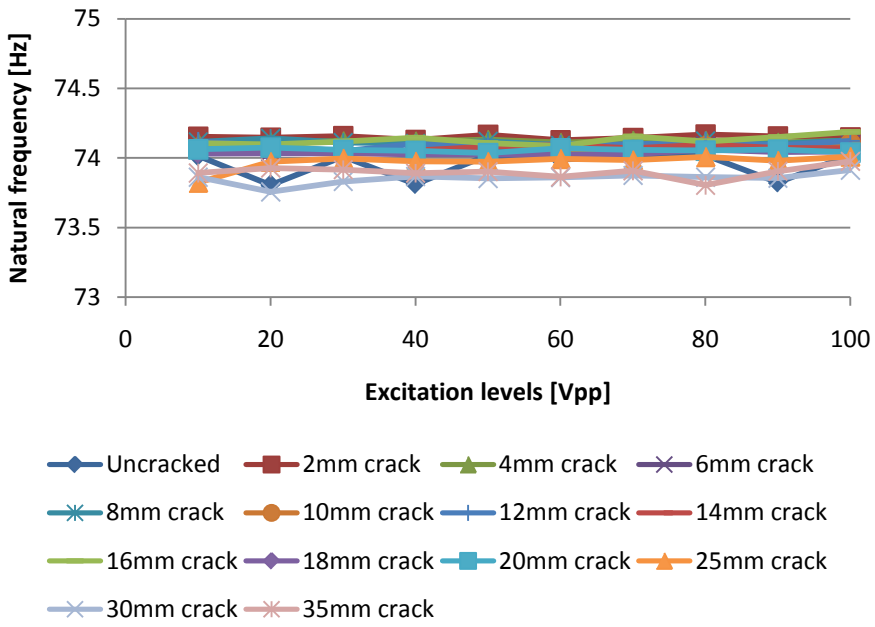


(b)

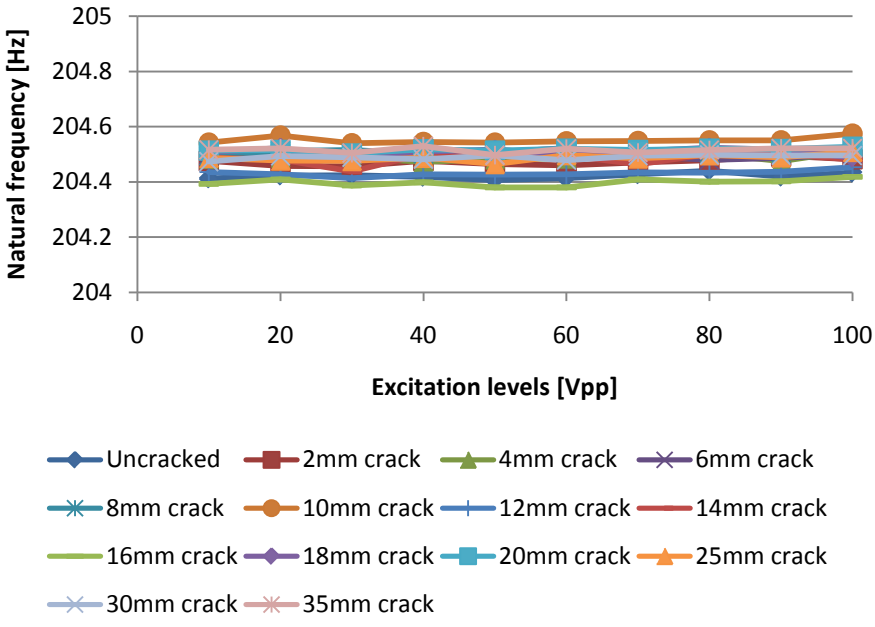

(c)

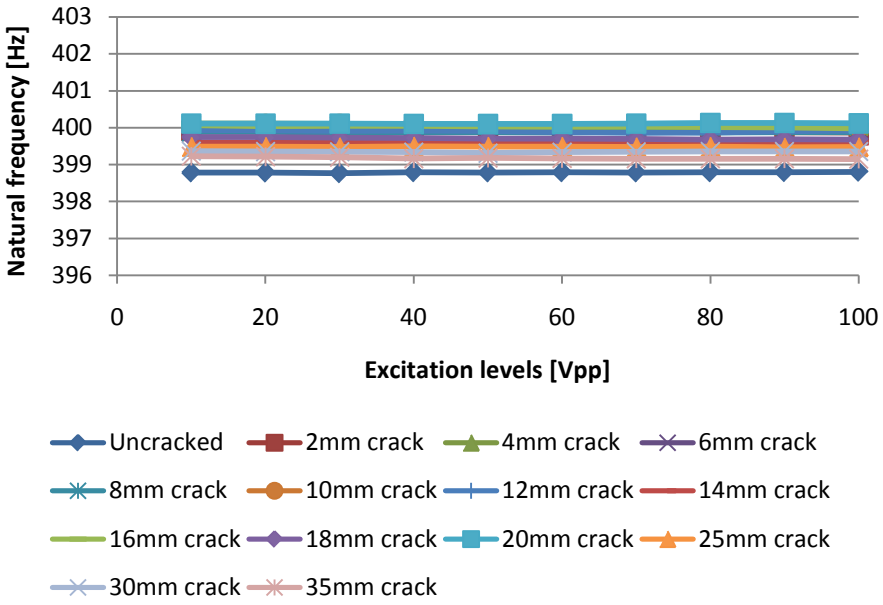


Figure 3.14: Comparisons of natural frequency with various crack severities for (a) 1st mode, (b) 3rd mode and (c) 6th mode.

Damping estimation analysis was performed in the next step for FRFs used. Due to no frequency shifting being observed in the previous study, a half-power band width method was applied for damping estimation. The damping ratio for the 1st, 3rd and 6th vibration modes with different crack lengths are shown in Figure 3.15. No significant changes are observed in the results.

(a)

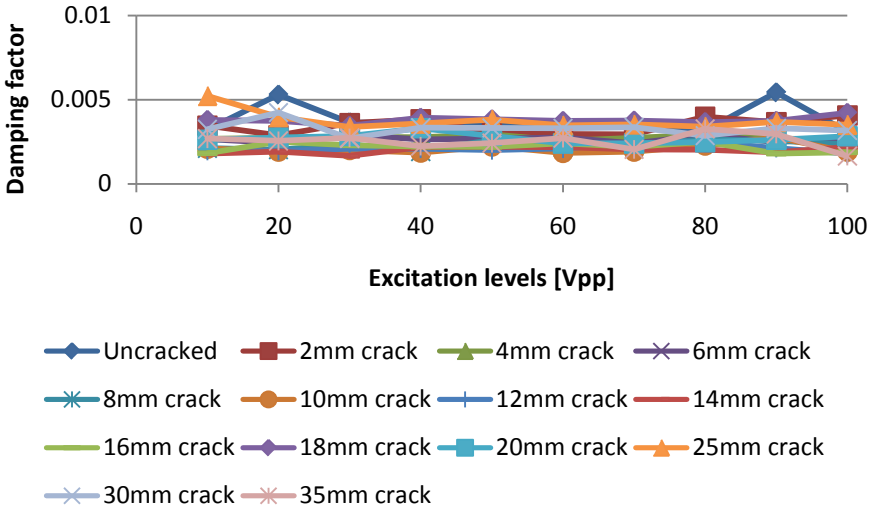

(b)

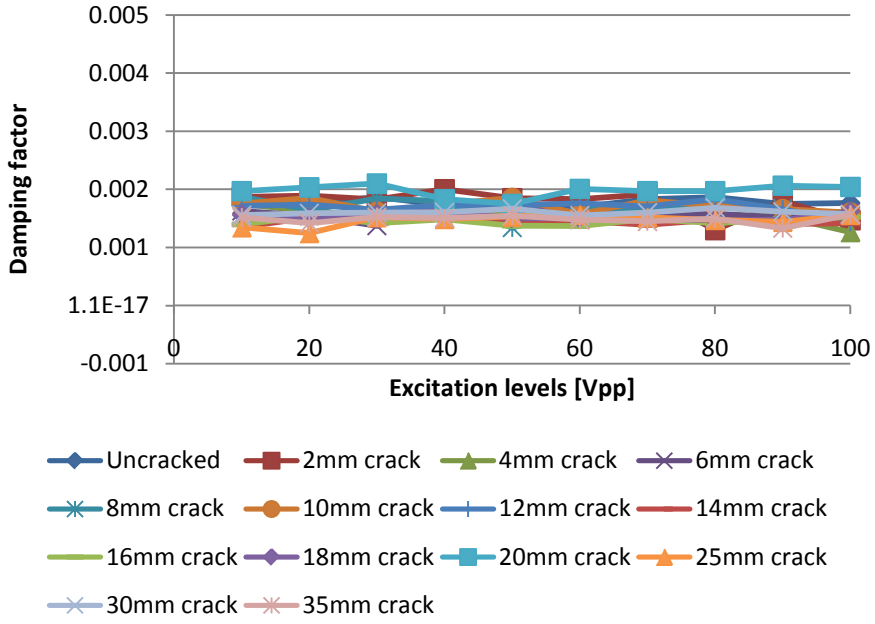


(c)

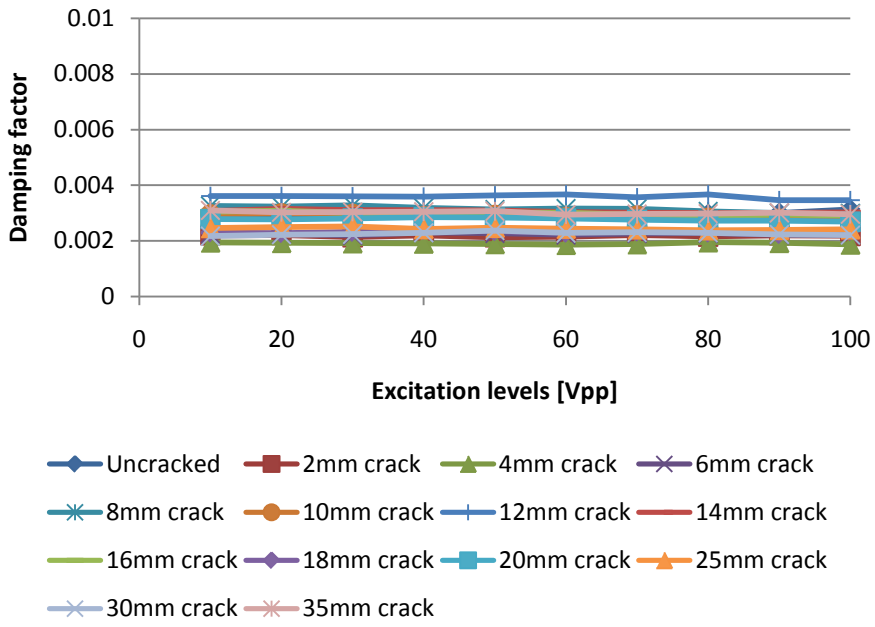


Figure 3.15: Comparisons of damping factor with various crack severities for (a) 1st mode, (b) 3rd mode and (c) 6th mode.

### 3.1.4.3 Combined vibro-acoustic excitation

The zoomed power spectra in Figure 3.16 reveal that the frequency spacing of sidebands corresponds to the low-frequency modal excitation, as expected. Although some sidebands can be observed for the uncracked plate, their numbers and

amplitudes increase significantly when the 35mm crack is present in the plate.

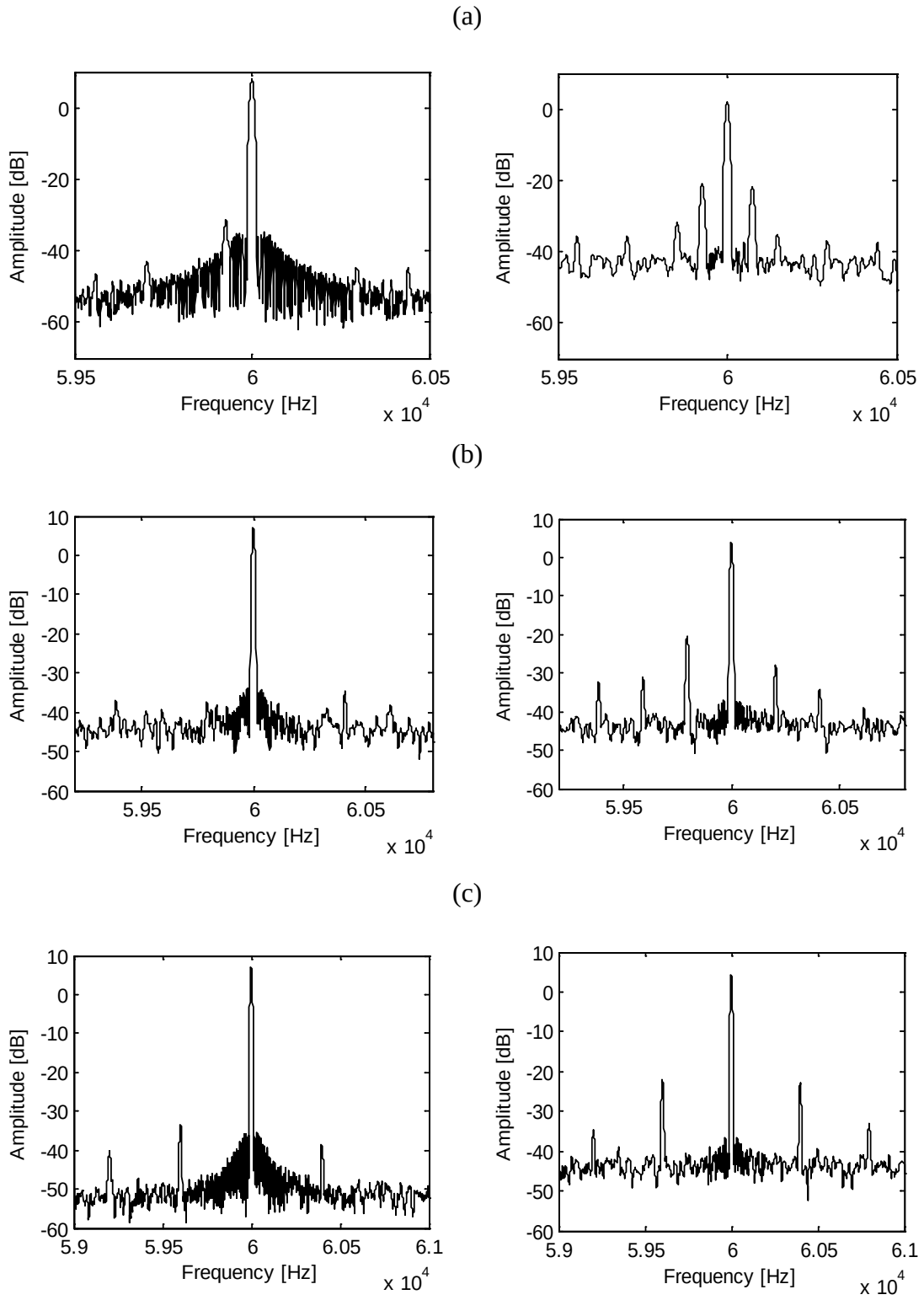


Figure 3.16: Zoomed power spectra from vibro-acoustic excitation tests using (a) 1st, (b) 3rd and (c) 6th vibration mode. Left column: uncracked plate; right column: 35mm cracked plate.

The amplitude of the carrier fundamental ultrasonic frequency and the first pairs of sidebands was used to calculate the intensity of the modulation parameter $R$ from Equation (2-7). The $R$ values for various amplitude levels of low-frequency vibration excitations are used as sample data for the hypothesis test. Figure 3.17(a) shows that the statistical test values for the 1$^{st}$ vibration mode excitation stay relatively unchanged (not statistically significant) until the crack length reaches 35mm. Observed from Figure 3.17(b) and 3.17(c), the smallest detectible crack lengths for the 3$^{rd}$ and 6$^{th}$ vibration mode excitations are 6mm and 25mm respectively. As mentioned before, the tearing motion and sliding motion were obtained when the glass plate was excited with the 3$^{rd}$ and 6$^{th}$ vibration modes respectively. Both tearing and sliding motion can produce friction forces and then cause a stiffness change by interaction of the damage interface with a micro-slip displacement. Meanwhile, the tearing and sliding motion may produce friction heat and high stress intensity in the crack interface which result in amplitude dissipation. In addition, the movement of crack surface for tearing and sliding modes are cross-directional to the propagation of the acoustic wave: this may effectively distort the acoustic wave amplitude and speed. All these factors may contribute to higher sensitivity for small crack detection.

(a)

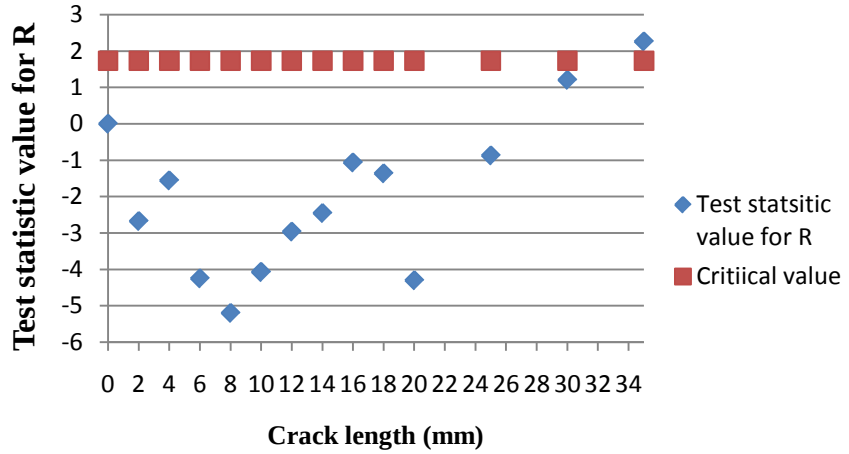


(b)

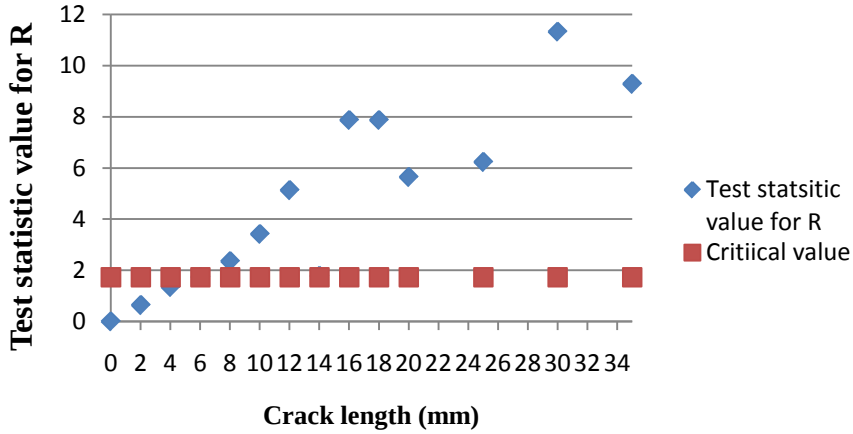


(c)

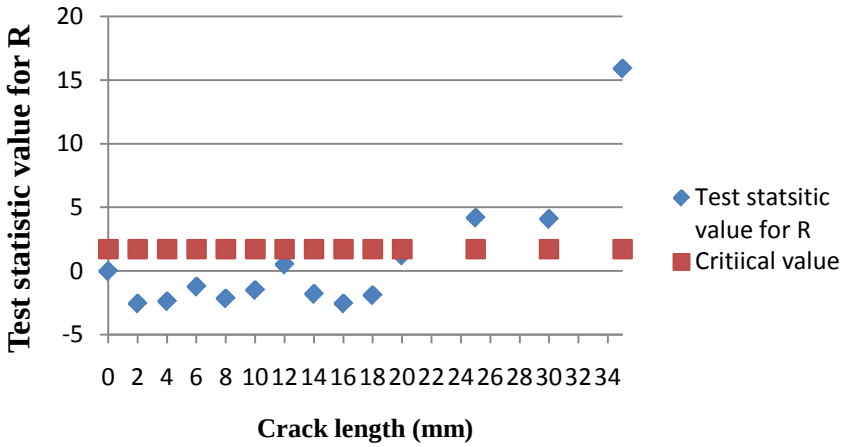


Figure 3.17: Test statistic value obtained by vibro-acoustic method with (a) 1$^{st}$, (b) 3$^{rd}$ and (c) 6$^{th}$ vibration mode.

Figure 3.18 gives examples of the zoomed power spectra revealing the decreasing

amplitude of the fundamental ultrasonic harmonics for increasing levels of 1st, 3rd and 6th vibration mode excitation. More detailed amplitude results are presented in Figure 3.19. The results show that the amplitude of the ultrasonic wave is dissipated with the increased levels of the LF excitation. When these results are compared with findings from Sections 3.1.4.2, which shows that the nonlinear hysteresis effect is negligible, it is clear that the energy dissipation mechanism observed for the 1st, 3rd and 6th vibration mode is not related to friction or hysteresis. This non-classical effect has been observed previously in glass [56-57] and explained as the acoustic equivalent of the L-G effect explained in Chapter 2. The L-G effect based on thermal-elastic coupling shows that the temperature effect could play an important role in vibro-acoustic nonlinear modulation.

(a)

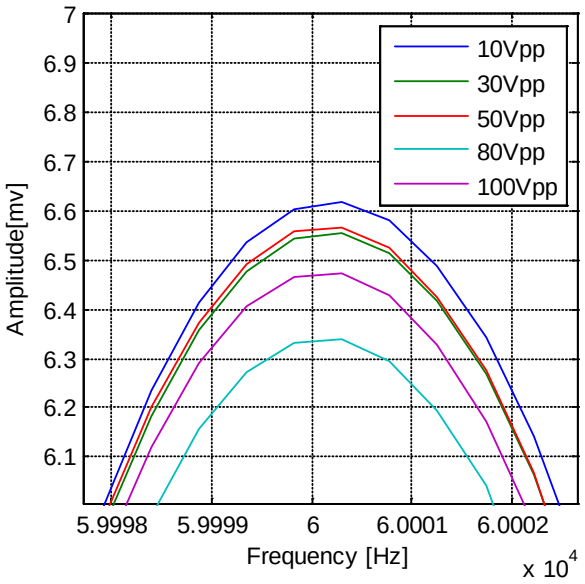

(b)

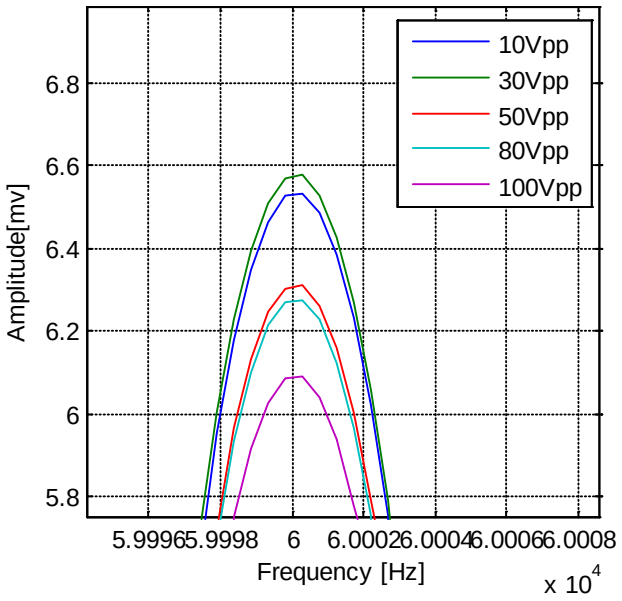


(c)

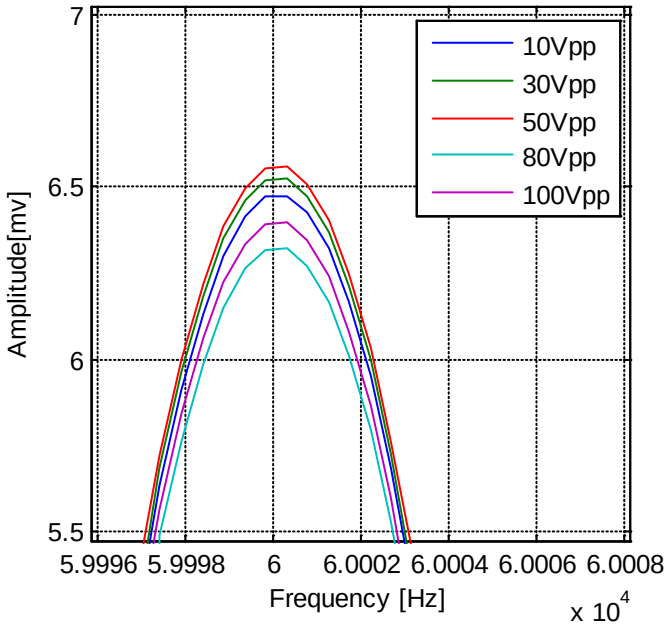


Figure 3.18: Zoomed power spectra for fundamental ultrasonic harmonics by increasing levels of (a) 1st, (b) 3rd and (c) 6th vibration mode excitation.

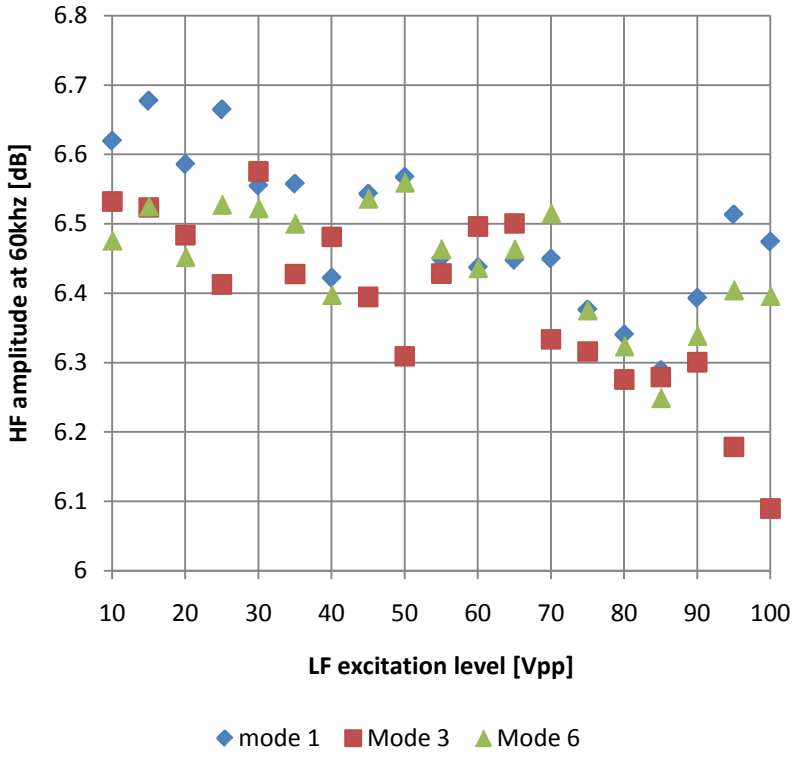


Figure 3.19: High-frequency amplitude against low-frequency excitation for cracked plate.

### 3.1.5 Lamb waves test

This section is mainly concerned with using Lamb waves for damage detection in a glass plate. The statistical approach of outlier analysis was applied to assess the damage severity.

#### 3.1.5.1 Experimental Procedure for Lamb waves test

The experiment setup is the same as mentioned previously in Section 3.1.3. The Lamb wave input signal was a five cycle sine wave with frequency of 125kHz and a peak to peak amplitude of 10V modulated by a Hanning window. The response signal was sampled with a frequency of 500MHz and recorded from 15 averages. The calculation of dispersion curves was achieved by commercial software *Vallen dispersion* [127] and illustrated in Figure 3.20.

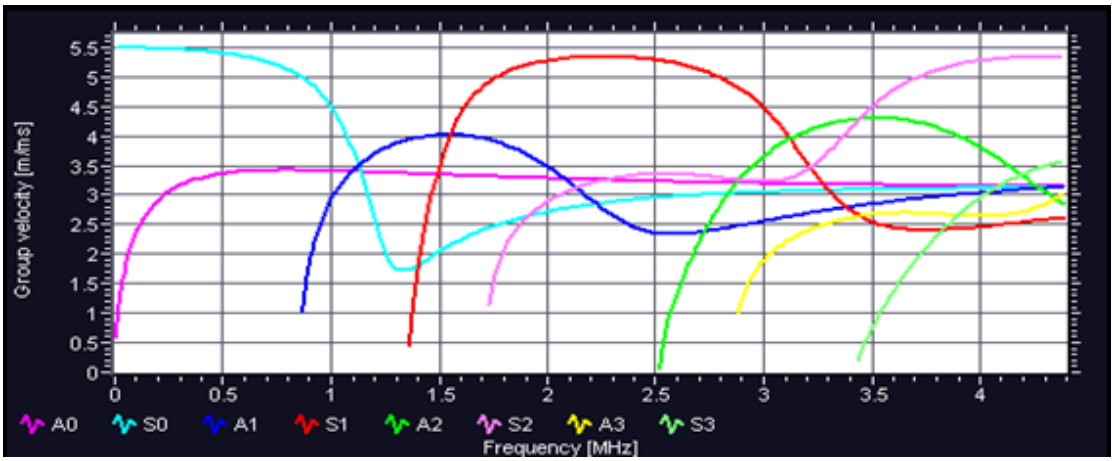


Figure 3.20: Lamb wave dispersion curves for soda-lime glass with thickness 2 mm.

According to the Lamb wave dispersion curve for glass in Figure 3.20, only the fundamental $S_0$ and $A_0$ Lamb wave modes were present in the structure with the 125kHz excitation frequency. Each waveform contained a 200μs duration of data. A time lag of 10ms between pulses was introduced to avoid disturbing signals from previously recorded waveforms. A sampling window was used to eliminate boundary reflection signals, as shown in Figure 3.21.

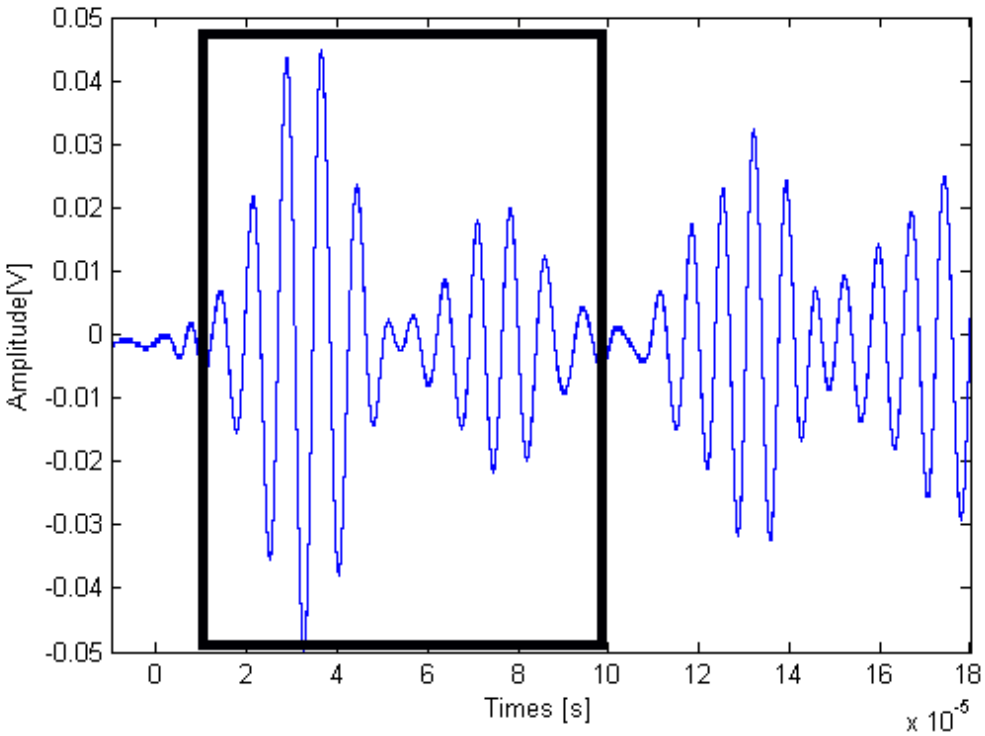


Figure 3.21: Outlier Analysis sampling window of Lamb wave response.

In order to get a benchmark of what the undamaged condition looked like, two sets of data were taken from the undamaged plate: 50 Lamb wave observations were taken as a ' healthy set ' and a further 50 observation were chosen as a ' test set '. The healthy set was used to calculate the mean and covariance needed for Equation (2.26) and the test set was applied for outlier analysis. This procedure gave confidence that outlier analysis could successfully classify undamaged samples as undamaged.

For each of the 13 damage levels, 50 observations were taken. The 1% exclusive threshold value for a 50 observation, 10-dimensional problem was found to be 46.9 after 1000 Monte Carlo trials of the algorithm discussed in Section 2.3.2. The selected 10-dimensional features were plotted as red circles in Figure 3.22. In addition, the graphs shown in Figure 3.23 demonstrate the delay of time of flight, as well as the energy dissipation, both of which are caused by damage.

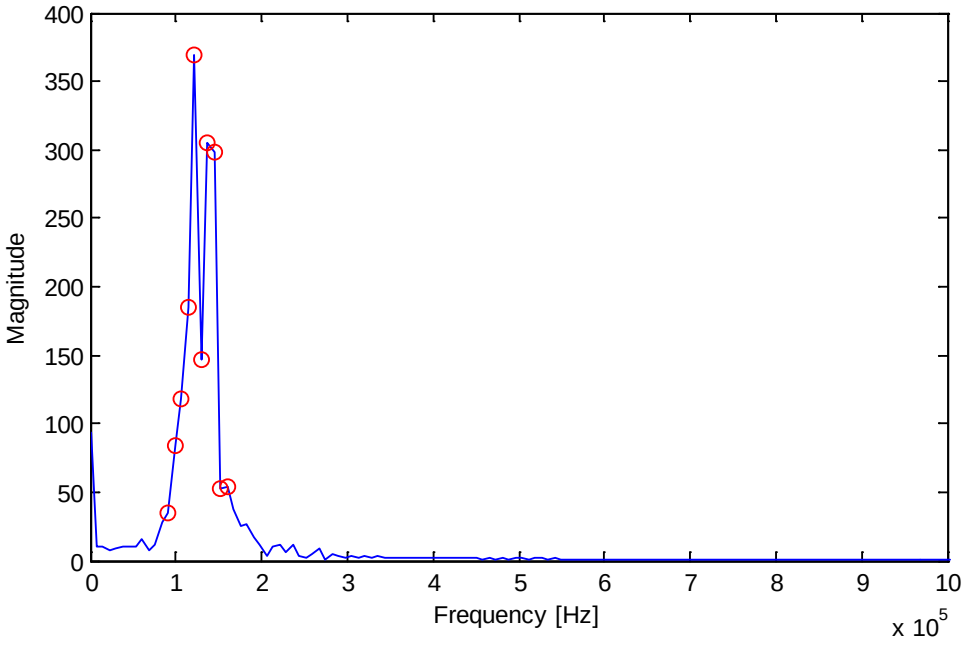


Figure 3.22: 10-dimension feature selected from frequency spectrum

(a)

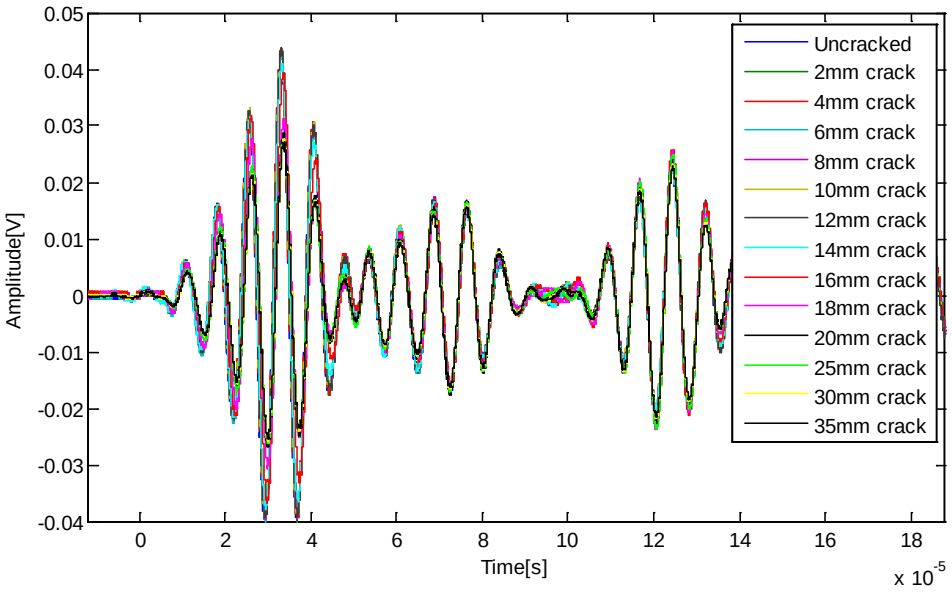


(b)

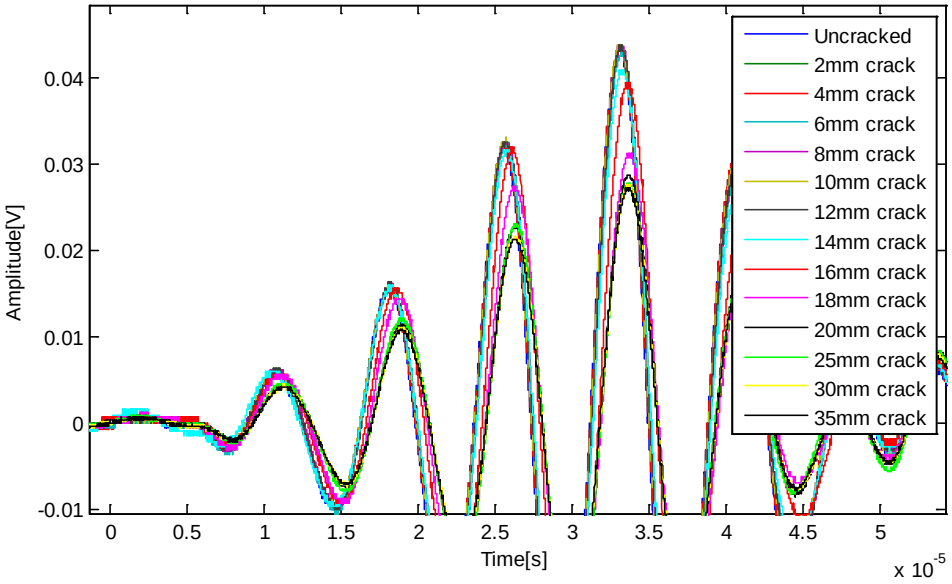


Figure 3.23: (a) Acoustic waveforms for various damage severities and (b) zoomed waveforms

### 3.1.5.2 Experimental results and discussion

The results obtained by outlier analysis are shown in Figure 3.24 with a logarithmic vertical scale. The results indicate successful classification for undamaged and damaged data. That means the undamaged data are all lying below the threshold level

(red line) and are classified as 'inliers' while all the damaged data are significantly above the damage detection threshold and are categorised as 'outliers'. In addition, The MSD values slightly fluctuated from the 2mm to the 4mm crack and then rose sharply for the 16mm crack and finally remained stable at the same level. Thus, outlier analysis is able in this case to give a rough indication of damage severity. In other words, more energy attenuation results in a higher MSD value. This is caused by the interaction between the elastic waves and the large sized crack. In general, the MSD will not necessarily grow monotonically with damage, so severity assessment is not always guaranteed.

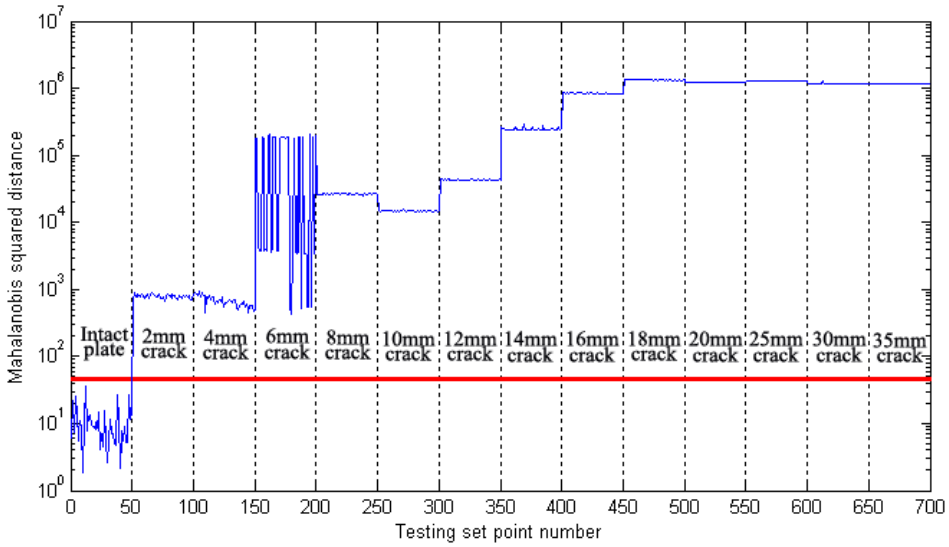


Figure 3.24: Outlier analysis classification results with logarithmic scales.

### 3.1.6 Summary

Section 3.1 describes the application of nonlinear acoustic and guided wave methods for damage detection in a glass plate. The work was mainly focused on single wave, vibro-acoustic wave and Lamb wave excitation. A Vickers indenter was used to introduce and grow a crack in the centre of the plate. Different crack lengths were investigated. Various nonlinear symptoms in the signal response were examined to find possible physical mechanisms.

A number of important conclusions can be summarised from the experimental work undertaken. Various nonlinear phenomena related to 1st, 3rd and 6th vibration modes have been investigated with respect to different crack modes. Three different nonlinear phenomena were observed: (a) non-classical L-G type dissipation, (b) the dissipation mechanism related to crack-wave interaction and (c) nonlinear elasticity. According to the experimental results, the intensity of modulation R for the 3rd (tearing crack mode) and 6th (sliding crack mode) vibration mode excitation is good for damage detection. Both the tearing and sliding crack motion can produce friction heat and high stress intensity in the crack interface which result in amplitude dissipation. In addition, the movement of crack surface for tearing and sliding modes are cross-directional to the propagation of the acoustic wave. As a result, the amplitude of acoustic wave may distort. For single wave excitation, the 1st and 3rd vibration modes are statistically significant for detecting a crack. For the 1st vibration mode (crack opening mode), the nonlinearity is caused by the asymmetry in the stress-strain characteristics for a breathing crack. For the 3rd vibration mode, the nonlinearity results from a stiffness change by interaction of the damage interface with a micro-slip displacement. Moreover, the frequency shift and damping estimation analysis do not reveal any useful information.

For the Lamb wave test, the outlier analysis method successfully classifies damage with a 100% rate. Meanwhile, the results exhibited a trend of increasing MSD values for growing crack length, hence outlier analysis was able to give an indication of damage severity in this case.

## 3.2 Aluminium plate test

### 3.2.1 Test specimen

A rectangular 150x400x2mm aluminium plate Al-2024 was next used as a test structure. The aluminium alloy Al-2024 has high strength, good fatigue resistance and

it is widely used in aircraft structures. In addition, the material properties of aluminium are totally different from glass. So it is essential to apply nonlinear acoustic and guided wave methods for addressing the fatigue damages. In this study, five holes located at both end of the plate were used to clamp the plate into a fatigue testing machine. A 3mm notch was made in the middle of the plate in order to introduce an inhomogeneous stress distribution and provide rapid crack initiation. The main material properties are shown in Table 3.5.

Table 3.5: Material properties of Al-2024 plate [128]

| | Al-2024 plate |
|---|---|
| Density $\rho$ [g/cm$^3$] | 2.78 |
| Modulus of elasticity $E$ [GPa] | 73.1 |
| Tensile strength $f_{t.k}$ [MPa] | 324 |
| Poisson's ratio $\upsilon$ | 0.33 |
| Shear modulus [GPa] | 28 |

## 3.2.2 Modal analysis

Modal analysis procedures in this section are similar to glass plate. More details are given in Section 3.1.2.

### 3.2.2.1. Modal analysis by FE method

The modal characteristics of the Alumnium plate were obtained from a modal analysis, using ANSYS workbench, for varying natural frequencies and mode shapes. The plate was analysed in the same way as glass plate

A graphic representation of modeling a crack can be seen in the Figure 3.25.

(a)

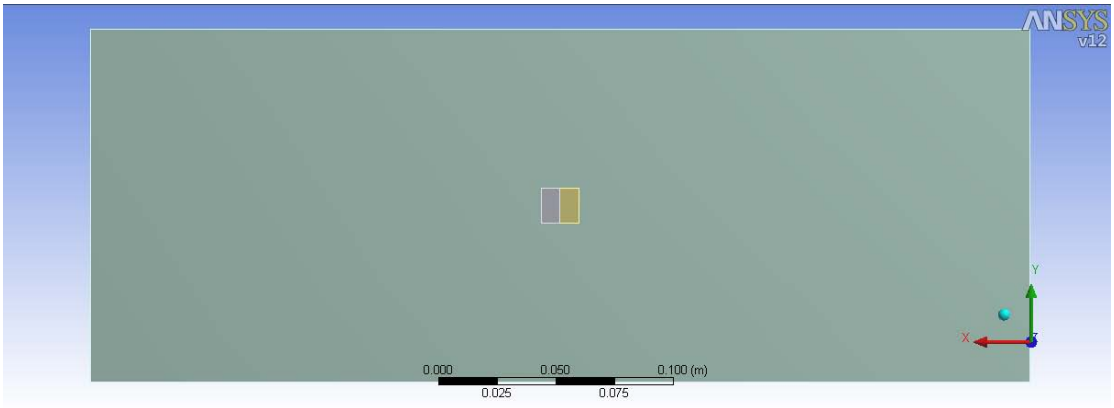


(b)

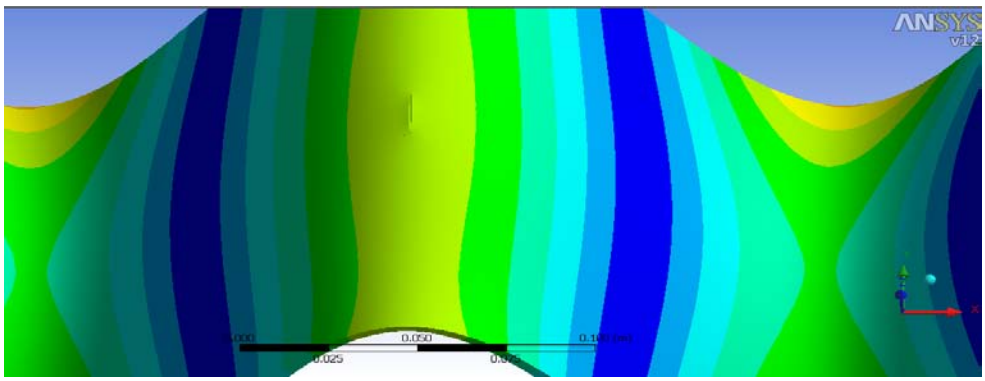


Figure 3.25: Modeling a crack in (a) two-dimensional (2-D) diagram (b) 3-D diagram.

The bar chart in Figure 3.26 shows the first six vibration modes corresponding to various crack mode behaviours for the aluminium plate. The same situation as Section 3.1.2.1, Due to the dominant value of the largest divergence in one direction, the values of other direction are hardly observed in the stacked bar chart. It is noticable that the CED for modes 1, 2, 3, 5 and 6 were far more prominent than mode 4. So modes 1, 3 and 6 were chosen for low frequency excitation which correspond to crack mode I (opening-closing action), crack mode III (tearing action) and crack mode II (sliding action), respecitively.

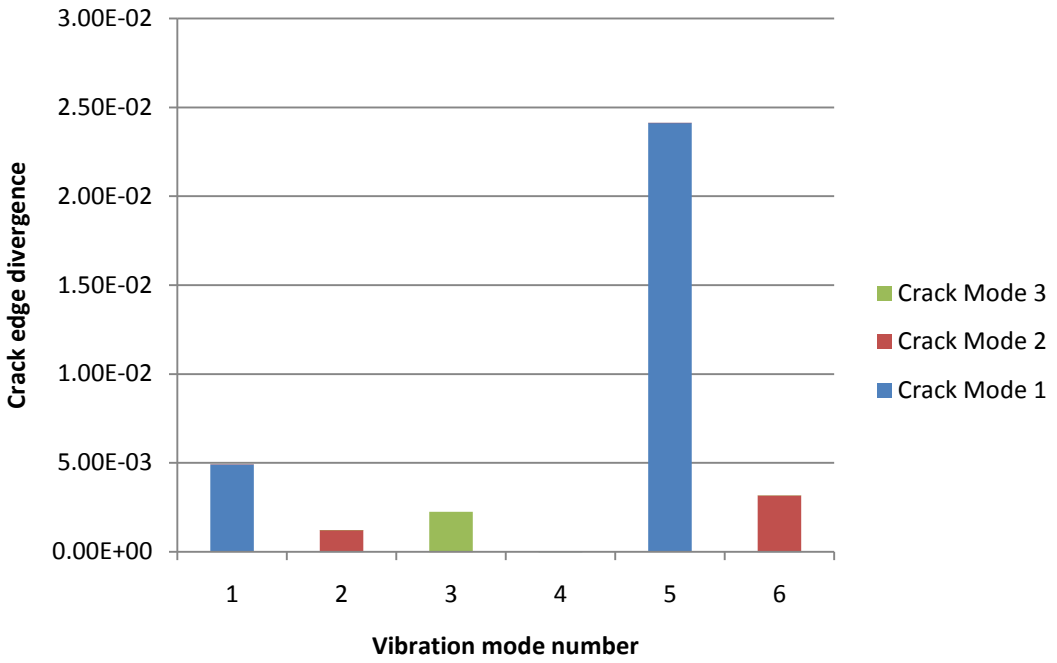


Figure 3.26: Crack edge divergence against various vibration modes with respect to crack modes.

The natural frequencies and mode shapes for modes 1, 3 and 6 of an undamaged aluminium plate are shown in Figure 3.27. These are the 66.9Hz first bending vibration mode (mode 1), 185.0 Hz second bending mode (mode 3) and 376.8Hz third torsional mode (mode 6).

Mode 1

66.9Hz

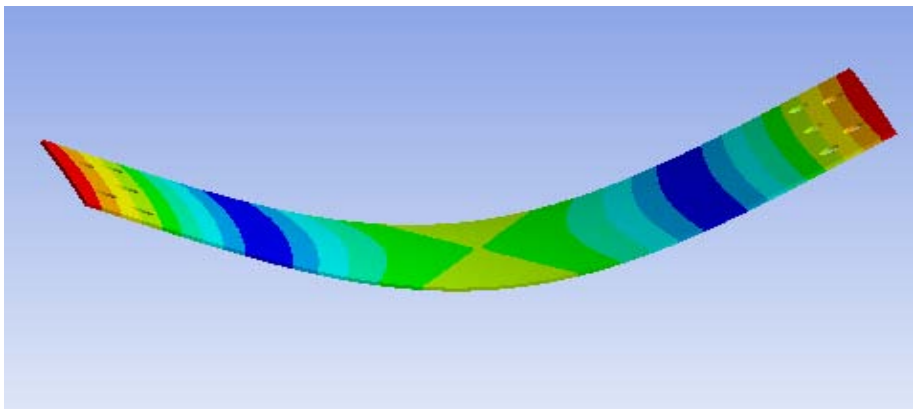

Mode 3

185.0Hz

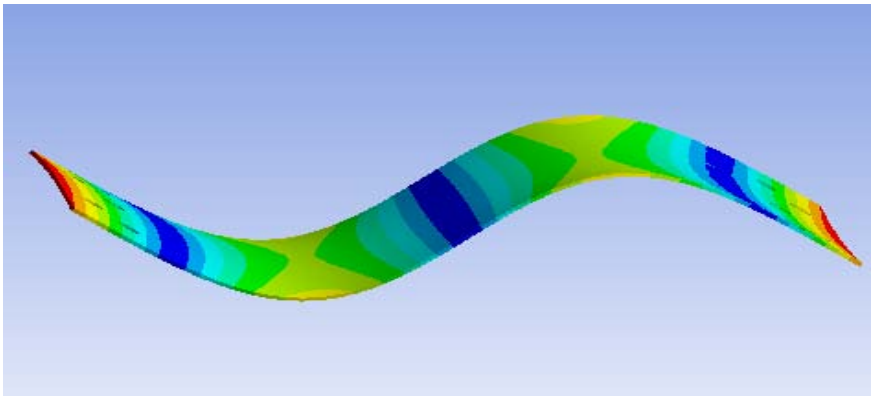

Mode 6

377.8Hz

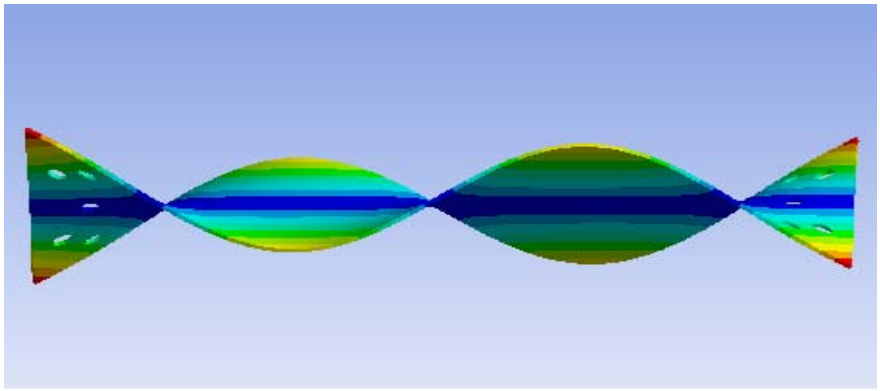

Figure 3.27: Natural frequencies and mode shapes for uncracked aluminium plate.

### 3.2.2.2. Modal analysis by analytical calculation

The calculation procedure is the same as mentioned in Section 3.1.2.2.

According to the Aluminium 2024 properties in Table 3.5, the analytical natural frequency values for 1st, 3rd and 6th modes are obtained as shown in Table 3.6

Table 3.6: The analytical natural frequency values for 1st, 3rd and 6th modes

| Mode sequence | 1 | 3 | 6 |
|---|---|---|---|
| Analytical mode value | 75.5Hz | 210.0Hz | 416.9Hz |

### 3.2.2.3. Experimental modal analysis

Experimental modal analysis was performed to establish the resonance frequencies of low-frequency modal excitation for the nonlinear acoustic tests. A 100Vpp swept sine signal, starting at 1Hz and increasing to 2000Hz in 2s was used to excite the (uncracked) plate. The response signal was sampled with a frequency of 5kHz.

Three low-profile, surface-bonded piezoceramic transducers were installed on the plate. A HBM-X60 2-component fast curing glue was used to attach the transducers. A PI Ceramics PL-055.31 stack actuator ($5\times5\times2$ mm) was used for low-frequency modal excitation. Two PI Ceramics PIC155 transducers (diameter 10mm; thickness 0.5mm) were used for ultrasonic wave excitation (this high frequency excitation was used in future vibro-acoustic tests rather than the modal analysis here) and for all response sensing. Figure 3.28 shows a schematic diagram of the plate with transducer locations.

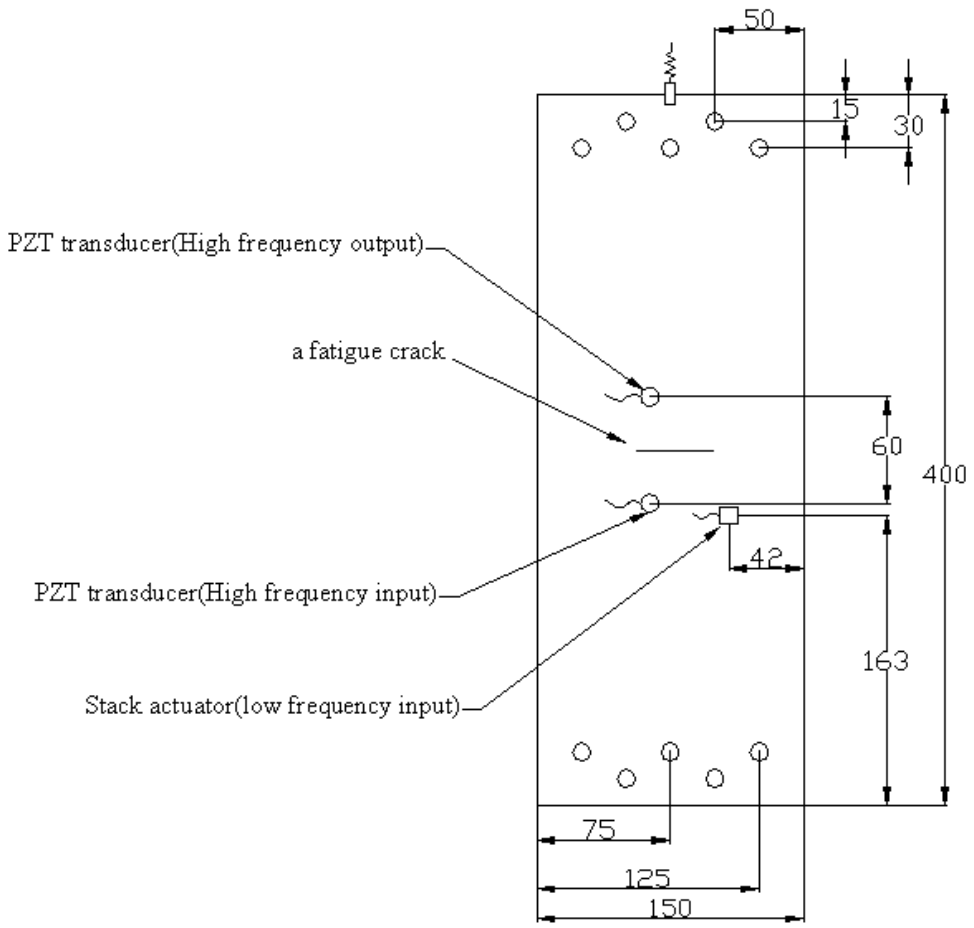


Figure 3.28: Schematic diagram of the alumnium plate.

The excitation and response data were used to calculate the FRF in order to reveal resonance frequencies. Figure 3.29 gives the magnitude of the experimental FRF. The first three excited modes were confirmed as the 1st, 3rd and 6th vibration modes for the analysed plate. These are the first three vibration modes leading to the largest crack divergence associated with the three crack modes shown in Figure 1.1. Based on numerical simulations of crack edge divergence (Section 3.1.2.1 ), excitation of the plate with the frequency corresponding to the 1st, 3rd, and 6th mode leads to crack mode I (opening), mode III (tearing) and mode II (sliding), respectively. As mentioned in Chapter 3.1.2.1, these crack modes lead to different nonlinear phenomena with respect to elastic and dissipative behavior. Therefore, frequencies 64.9, 179.8 and 351Hz - corresponding to the 1st, 3rd and 6th vibration modes, respectively - were selected for low-frequency excitation in the current nonlinear acoustic investigations.

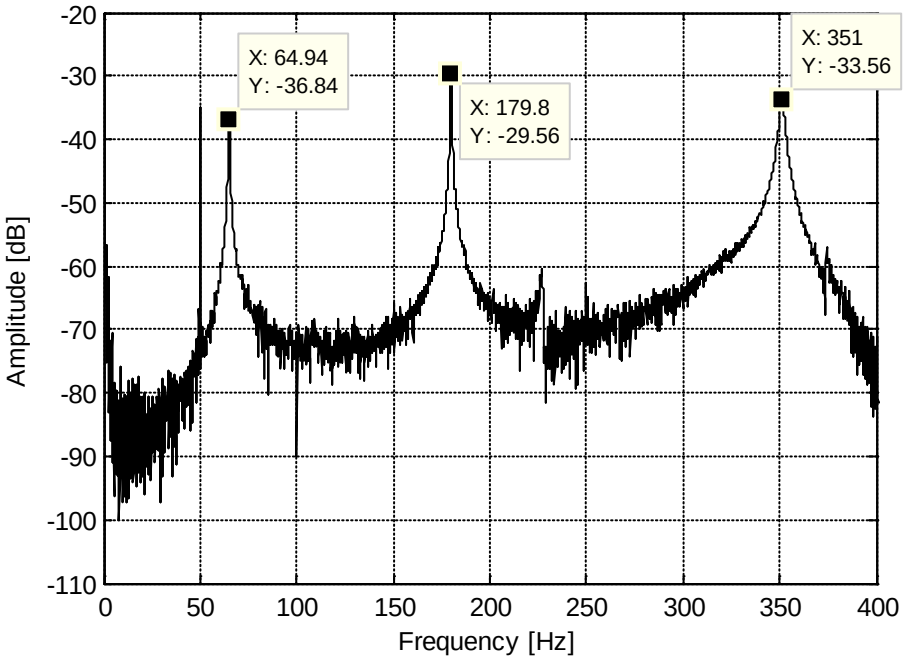


Figure 3.29: Modal analysis result obtained by vibration FRF.

The comparison of extracted natural frequencies by FE, analytical and experimental methods are summarised in Table 3.7. The deviation between analytical and experimental results ranges from 2.8% to 15.8%. The deviation from analytical method is larger than FE method. The main reason is that analytical method uses estimated value of a/b in calculation, which is 2.5 and the actual geometrical value is equal to 2.66.

Table 3.7: Comparison of extracted natural frequency methods base on FE, analytical and experimental methods

| | Mode 1 (Hz) | Mode 3 (Hz) | Mode 6 (Hz) |
|---|---|---|---|
| Natural frequency from experimental method | 64.9 | 179.8 | 351 |
| Natural frequency from Analytical method | 75.5 | 210.0 | 416.9 |
| Percentage deviation between experimental and analytical results % | 14 | 14.4 | 15.8 |
| Natural frequency from FE method | 66.9 | 185 | 377.8 |
| Percentage deviation between experimental and FE results % | 3.0 | 2.8 | 7 |

### 3.2.3 Experimental procedures for nonlinear acoustic tests

The experimental work was performed on a rectangular $150 \times 400 \times 2$ mm aluminium plate as mentioned in section 3.2.1. It included a classical modal test (Section 3.2.2.3), a single wave vibration test, a vibro-acoustic test and FRFs with varying excitation levels.

The low- and high-frequency excitation signals were generated using a two-channel TTi-TGA 1242, 40MHz arbitrary waveform generator. The low-frequency signal driving the stack actuator was additionally amplified to the required level with a PI E-505 LVPZT piezo-amplifier. Signal responses were acquired using a four-channel LeCroy Waverunner LT264, 350MHz, 1GS/s digital oscilloscope. The experimental setup is shown schematically in Figure 3.30.

The undamaged and damaged plate was tested by using various nonlinear acoustic approaches the same as described in the glass test.

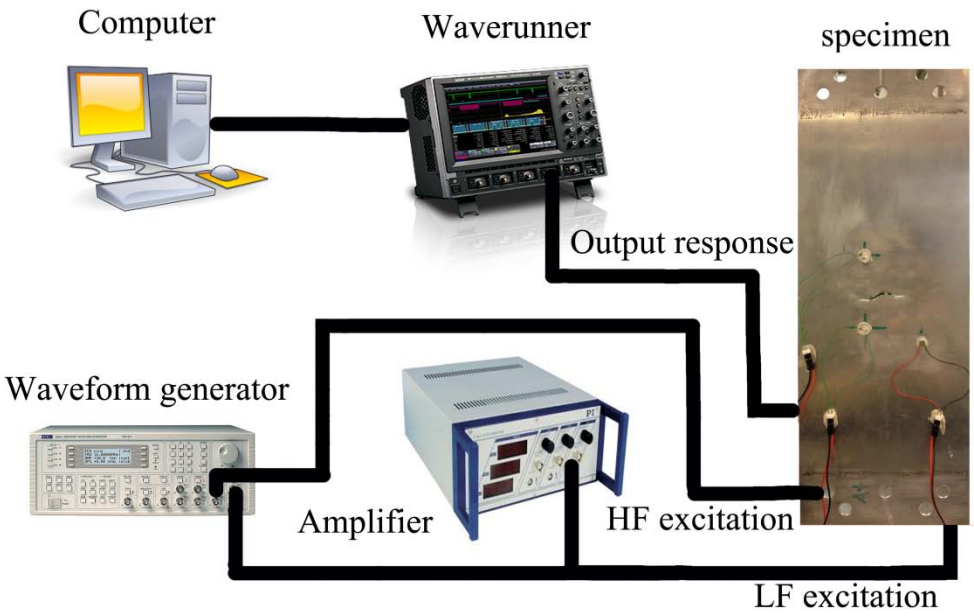


Figure 3.30: Experimental setup for the nonlinear acoustic test.

Metallic materials, such as aluminium, are particular vulnerable to fatigue damage (approximately 90% of metallic failure [129]) during their life-time under dynamic and fluctuating stress. It is noticeable that fatigue failure can occur at relative low stress levels compared to tensile or yield strength for static load and this failure may lead to a catastrophe without any warning. *Wöhler* [130] conducted the development of the 'S-N' curve, which indicates the relationship between stress amplitude and number of cycles to failure. A graphical representation of the S-N curve is shown in Figure 3.31. The S-N curves are based on the best-fitting curve of experimental data and they reveal an important finding that fatigue failure would not occur even at infinite high number of cycles when the applied stress is lower than the fatigue limit [131].

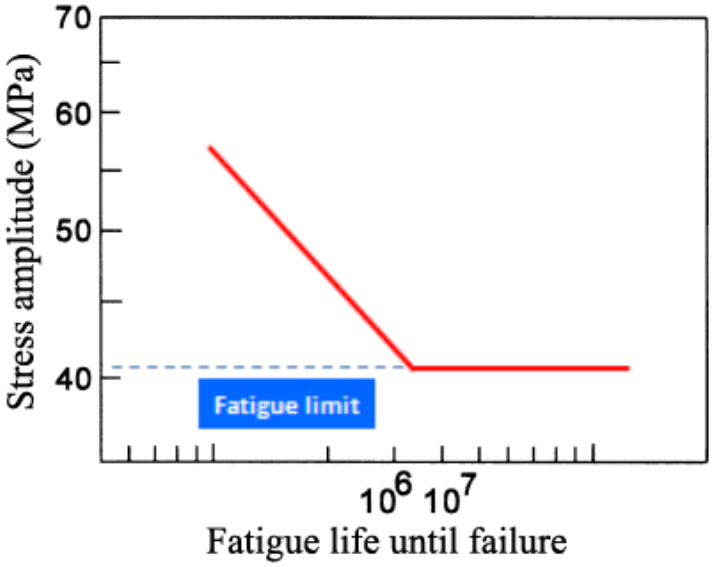


Figure 3.31: An example of S-N curve.

Fatigue life is usually divided into three different stages: crack initiation at high stress points, crack growth and final failure by fracture. In the crack initiation period, the crack nucleation is created by the formation of a slip step at microstructures (e.g. grain boundaries) within a material [132]. In the following stage, microcracks begin to accumulate and grow in a slow process from invisibility to visibility. Once cracks become visible, a more regular crack growth rate (the rate depends on the crack length, applied stresses and environmental effects) can be observed, and this is the starting point of the crack growth period [133]. If the crack has grown to the critical size, final fracture will take place with unstable crack propagation [131]. The process of fatigue damage development is shown in Figure 3.32. More details on fatigue testing are given in **Appendix C**

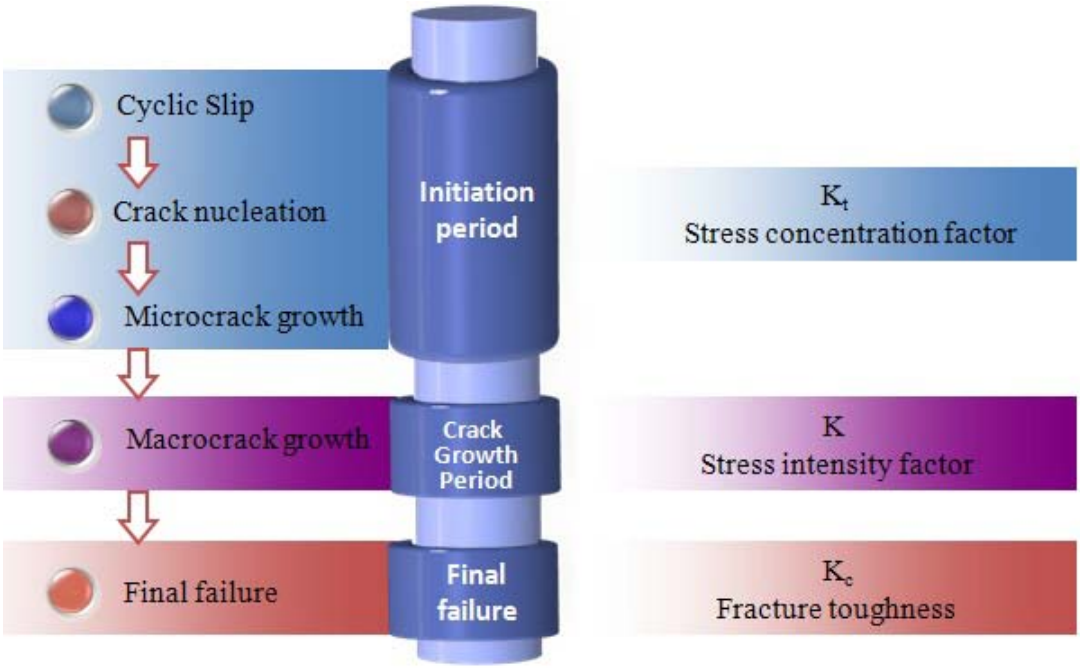


Figure 3.32: The process of fatigue damage development.

### 3.2.4.1 Experimental procedure for fatigue test

A crack propagation test was carried out on the aluminium plate by exposing it to cyclic loading. The fatigue experiment was performed in a *Schenck servo-hydraulic* test machine. Two fatigue cracks grew on both sides of the starter notch. A microscope was employed to precisely examine the extent of the cracks. The initial cracks were not observed until reaching a rather significant size (<2mm). After obtaining the first crack, the plate was removed from the fatigue test machine and a nonlinear acoustic test was performed. Then, the fatigue test was continued in order to obtain a larger crack. Figure 3.33 shows the aluminium plate with an 18mm crack.

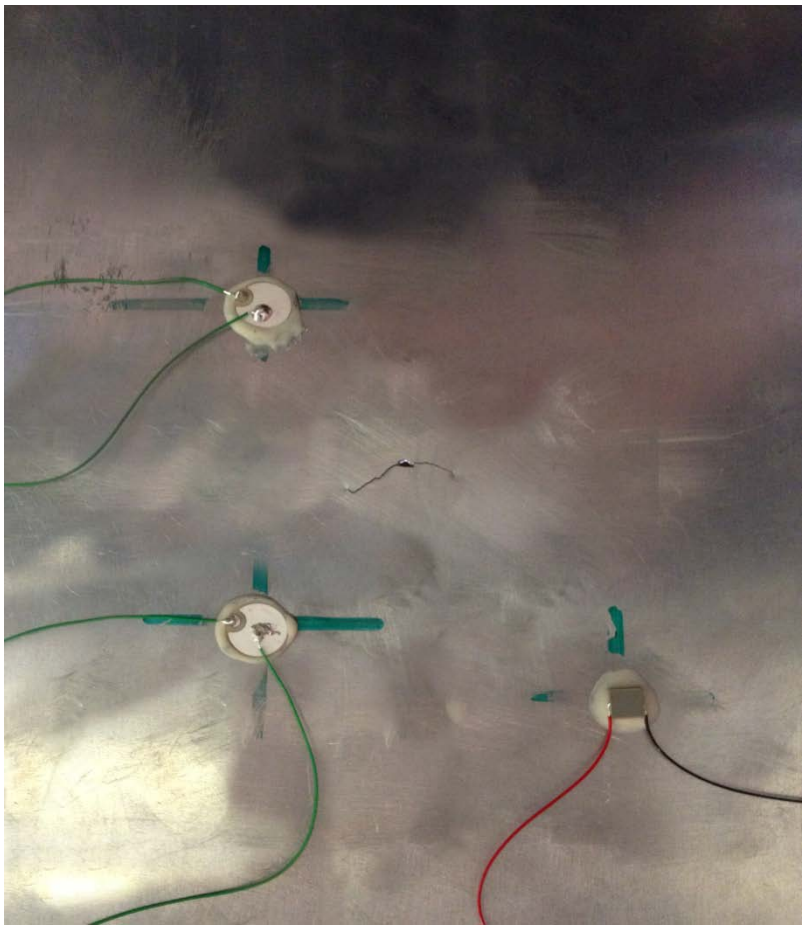

Figure 3.33: The aluminium plate with an 18mm crack.

These tests were repeated for the other crack lengths. The results are shown in Table 3.8. In addition, a 35mm crack was produced by a pre-load (applying tension on the bolts) from the fatigue testing machine rather than cyclic loading. Meanwhile, the crack is fully opened and it is different from previously obtained cracks. A 35mm crack was considered as large in this study.

Table 3.8: Number of cycles, loads and loading frequency to create a fatigue crack

| **Crack Length (mm)** | **No. Of cycle** | **Loads ( kN)** | | **Loading Frequency ( Hz)** |
|---|---|---|---|---|
| | | **Min** | **Max** | |
| **2** | 86456 | 3.8 | 25 | 1 |
| **5** | 23506 | 3 | 21 | 1 |
| **7** | 38002 | 2.8 | 18.8 | 1 |
| **9** | 22174 | 2.5 | 17.5 | 1 |
| **11** | 34482 | 2.4 | 15.6 | 1 |
| **13** | 20340 | 2.2 | 14.8 | 1 |
| **15** | 20367 | 2.1 | 14.2 | 1 |
| **18** | 22155 | 2 | 13.6 | 1 |

## 3.2.4 Experimental results

### 3.2.5.1 Single-wave vibration excitation

Figure 3.34 shows examples of power spectra from single-wave excitation tests using the 1$^{st}$, 3$^{rd}$ and 6$^{th}$ vibration modes. Two different plate conditions are analysed, i.e. the intact (or uncracked) plate and the plate with an 18mm crack (most severe). A clear pattern of higher harmonics can be observed in all analysed spectra, even for the uncracked plate. Observed from Figure 3.34(a), 3.34(b) and 3.34(c), the magnitude of second harmonics for the 18mm cracked plate with excitation of the 1$^{st}$, 3$^{rd}$ and 6$^{th}$ vibration modes increased by 7dB, 6dB and 10dB respectively.

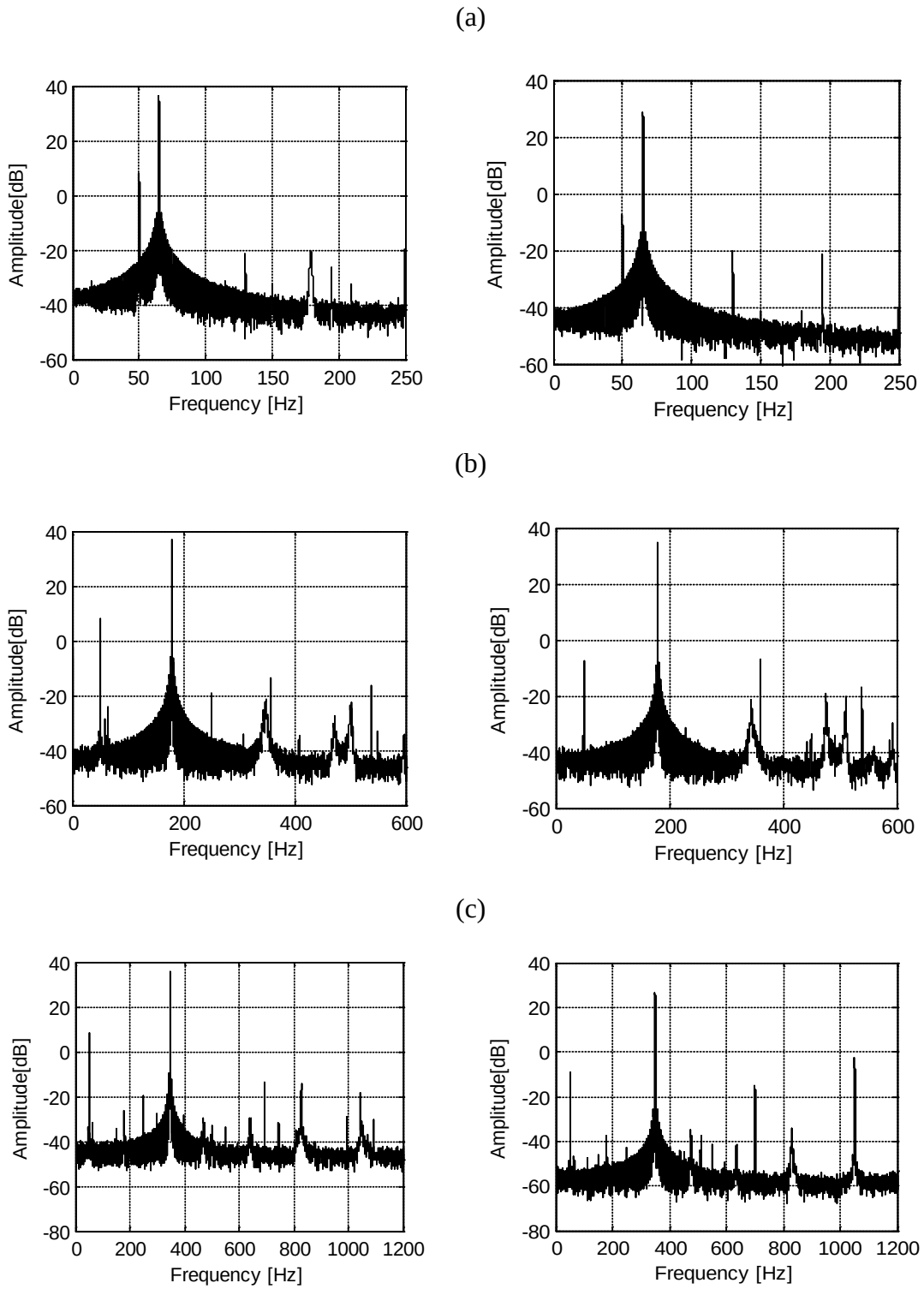


Figure 3.34: Power spectra density showing the fundamental peak and harmonics for the uncracked (left column) and 18mm cracked (right column) plate excited by (a) 1st, (b) 3rd, (c) 6th mode.

The amplitude of the second harmonic is shown further in Figure 3.35 for all crack lengths in order to reveal possible changes in the nonlinear perturbation coefficient. The figure gives the test statistic value for the perturbation coefficient β

against the crack length. Any test statistic value above the critical value line is considered as a nonlinearity resulting from damage. Observed from Figure 3.35(a), when the crack length reaches 7mm and beyond, the nonlinearity contributed by a fatigue crack can be detected for the first mode excitation. Similarly, statistically significant results are found for the 18mm crack and beyond with excitation of the third and sixth vibration mode (Figure 3.35(b) and 3.35(c)). It is easy to find that the $1^{st}$ mode is the most sensitive vibration mode to detect the crack by using the $\beta$ perturbation coefficient. Two reasons may explain this result. Firstly, the clapping mechanism, which is produced by the asymmetric stiffness for tension and compression of a breathing crack, is more effective than frictional loss caused by shear acoustic wave and damage. In addition, the $1^{st}$ vibration mode also introduced the largest stain level in the crack area: this may also affect the result.

(a)

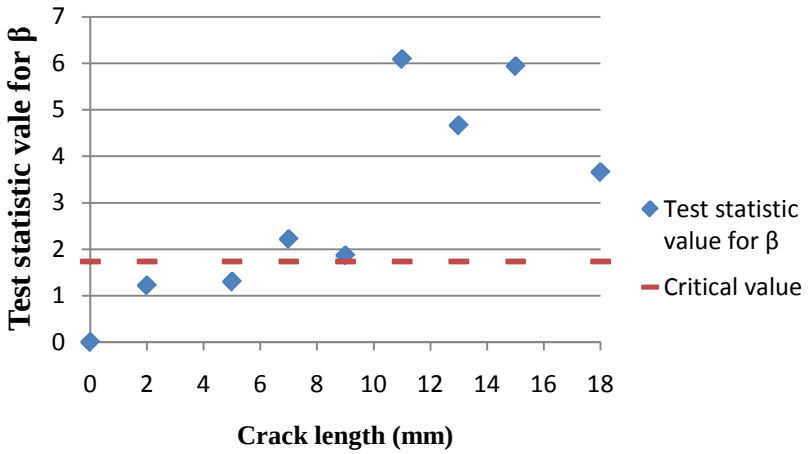


(b)

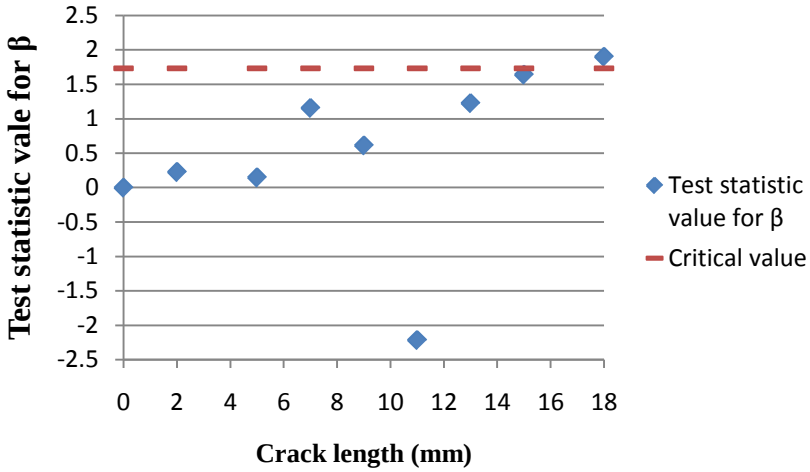


(c)

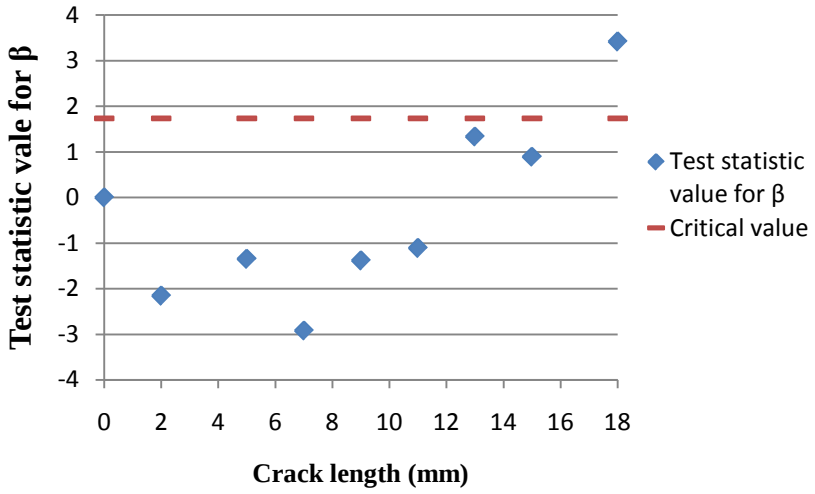


Figure 3.35: Test statistical value for $\beta$ against various crack severities of (a) 1st, (b) 3rd, (c) 6th mode and (d) ultrasonic nonlinearity on the damage.

### 3.2.5.2 FRFs with varying excitation levels test

Figure 3.36 reveals the comparisons of natural frequencies of various crack severities for the 1st, 3rd and 6th mode with increasing excitation amplitude. It seems that there is no significant reduction in natural frequencies with increasing the crack depth to 18mm. However, at a large crack situation (35mm), the natural frequencies for all three modes decease dramatically due to a great loss in the stiffness. Meanwhile, the large crack also contributes towards frequency shifting for the 1st and 3rd modes as excitation voltages increase.

(a)

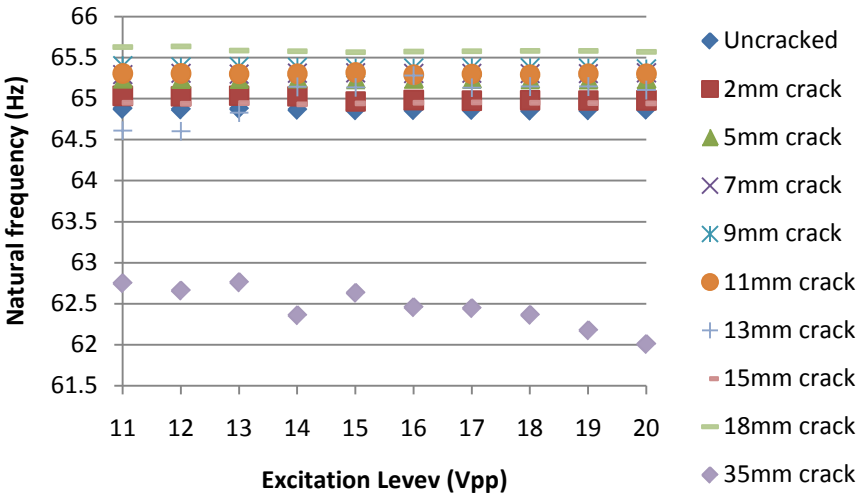


(b)

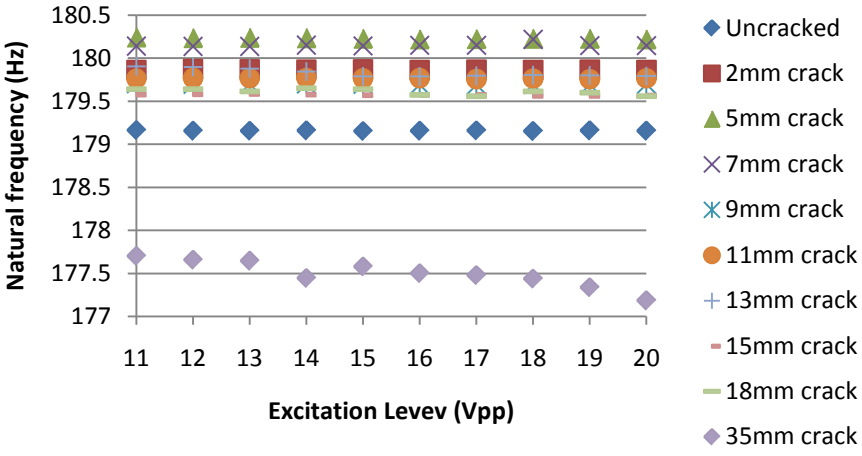

(c)

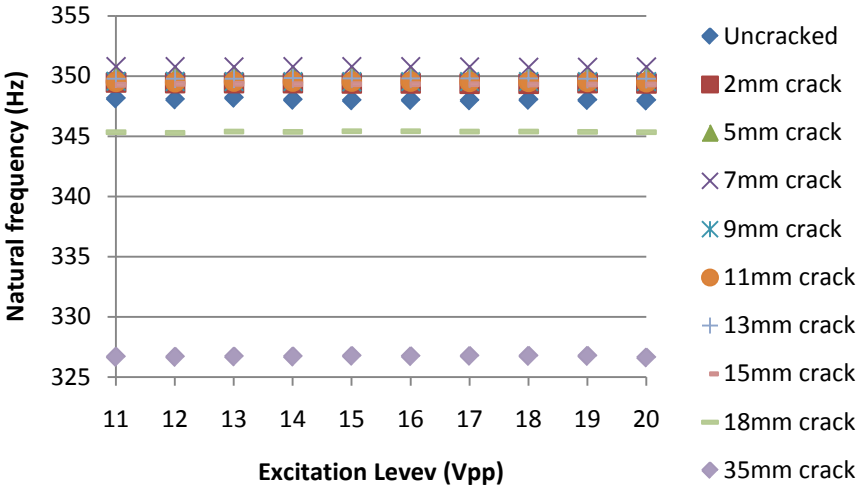


Figure 3.36: Comparisons of natural frequency with various crack severities for (a) 1st mode, (b) 3rd mode and (c) 6th mode with increasing amplitude levels of excitation.

Damping estimation analysis was performed in the next step for the FRFs used. The damping ratio for the 1st, 3rd and 6th vibration modes with different crack lengths are shown in Figure 3.37. Unfortunately the results do not show significant damping factor changes against crack length for all vibration modes.

(a)

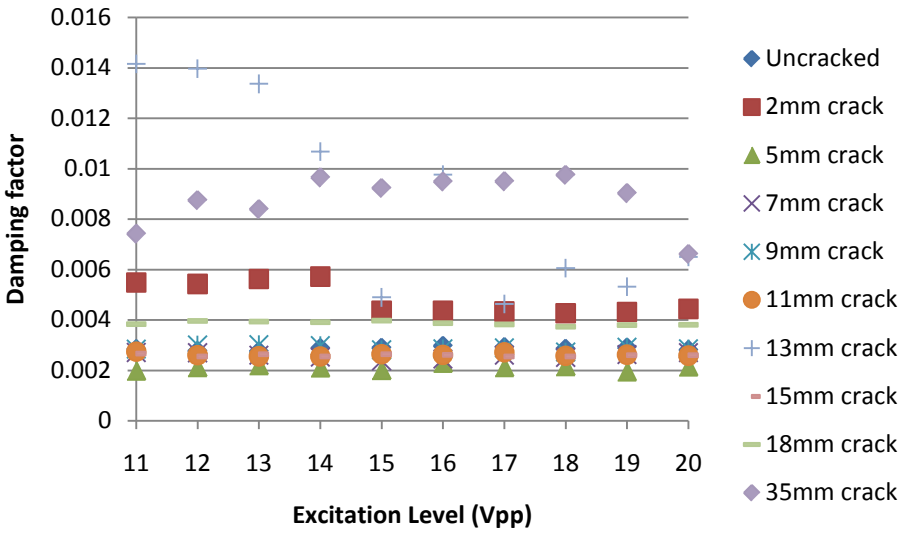

(b)

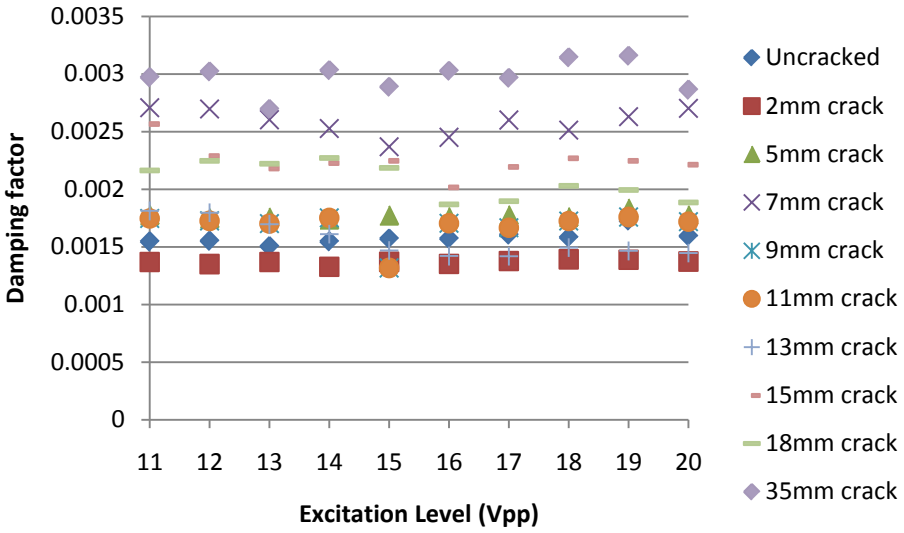


(c)

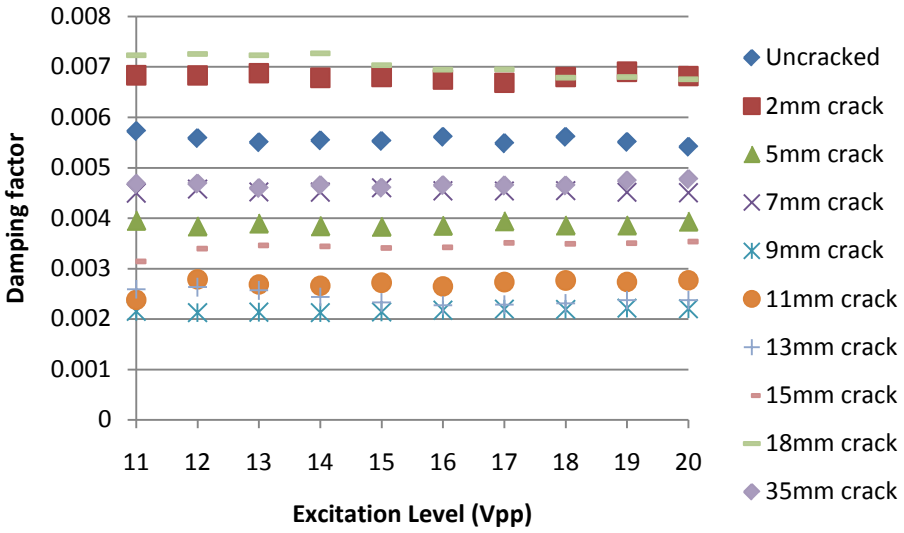


Figure 3.37: Comparisons of damping factor with various crack severities for (a) 1st mode, (b) 3rd mode and (c) 6th mode.

### 3.2.5.3 Combined vibro-acoustic excitation

The zoomed power spectra in Figure 3.38 reveal that the frequency spacing of sidebands corresponds to the low-frequency modal excitation, as expected. Although, some sidebands can be observed for the uncracked plate, their numbers and amplitudes increase significantly when the 18mm crack is present in the plate.

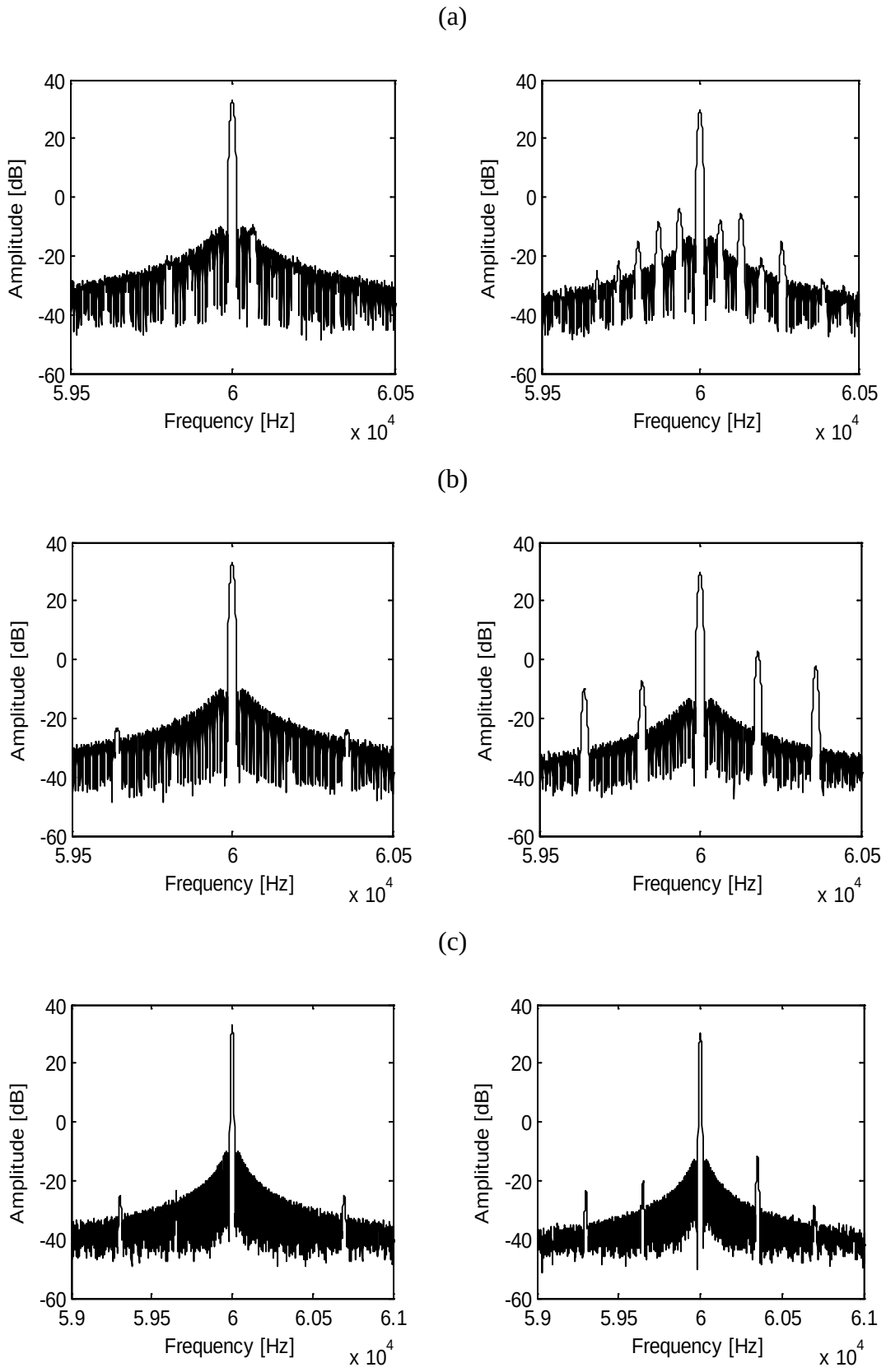


Figure 3.38: Zoomed power spectra from vibro-acoustic excitation tests using (a) 1st, (b) 3rd and (c) 6th vibration mode. Left column: uncracked plate; right column: 18mm cracked plate.

The amplitude of the carrier fundamental ultrasonic frequency and the first pairs of sidebands was used to calculate the intensity of the modulation parameter $R$ from Equation (2.6). The $R$ values for various amplitude levels of low-frequency vibration excitations are used as sample data for a hypothesis test. Figure 3.39(a) shows that the statistic test values for the 1st vibration mode excitation stay relatively unchanged (not statistically significant) until the crack length reaches 13mm. As observed from Figures 3.39(b) and 3.39(c), the smallest detectible crack lengths for the 3rd (tearing motion) and 6th (sliding motion) vibration mode excitations are 5mm and 2mm respectively. According to this result, the major mechanism behind the vibro-acoustic wave modulation is caused by frictional energy dissipation.

(a)

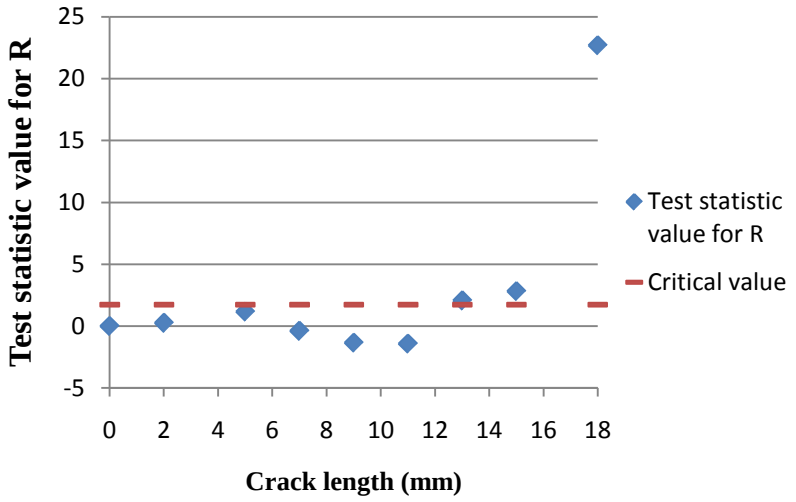


(b)

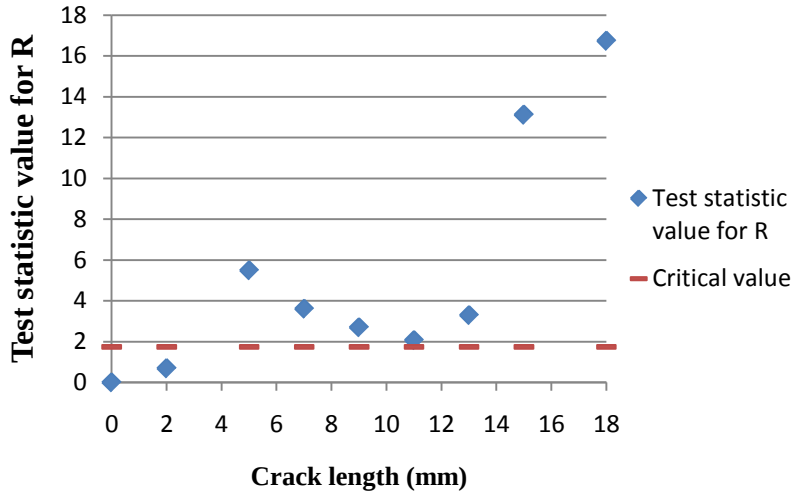

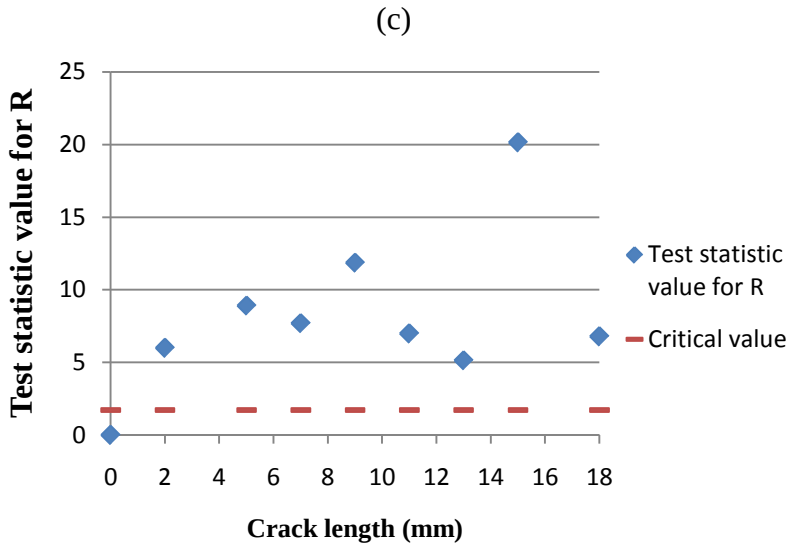


Figure 3.39: Test statistic value obtained by vibro-acoustic method with (a) 1st, (b) 3rd and (c) 6th vibration mode.

Figure 3.40 gives examples of the zoomed power spectra revealing the amplitude changing of the fundamental ultrasonic harmonics for increasing levels of 1st, 3rd and 6th vibration mode excitation. More detailed amplitude results are presented in Figure 3.41. The result clearly shows that amplitude of the ultrasonic wave sharply drops with the increased levels of the LF excitation for the first vibration mode. Similar experiment results were presented by Klepka *et al* [22]. When these results are compared with the findings from Sections 3.2.5.2, it is clear that the energy dissipation mechanism observed for the 1st vibration mode is not related to friction or hysteresis. If hysteresis is the reason for energy dissipation, it should be accompanied with an observable resonance frequency shifting. However, previous experimental results from Sections 3.2.5.2 show that there are no significant changes in resonance frequency. According to this, the hysteretic character is not the major nonlinearity mechanism attributed to energy dissipation in this case. Alternatively, thermal dissipation may result in HF wave energy loss. This non-classical effect has been observed previously in glass [56-57] and explained in Section 2.1.4. L-G effect based on thermal-elastic coupling shows that temperature effect could play an important role in vibro-acoustic nonlinear modulation.

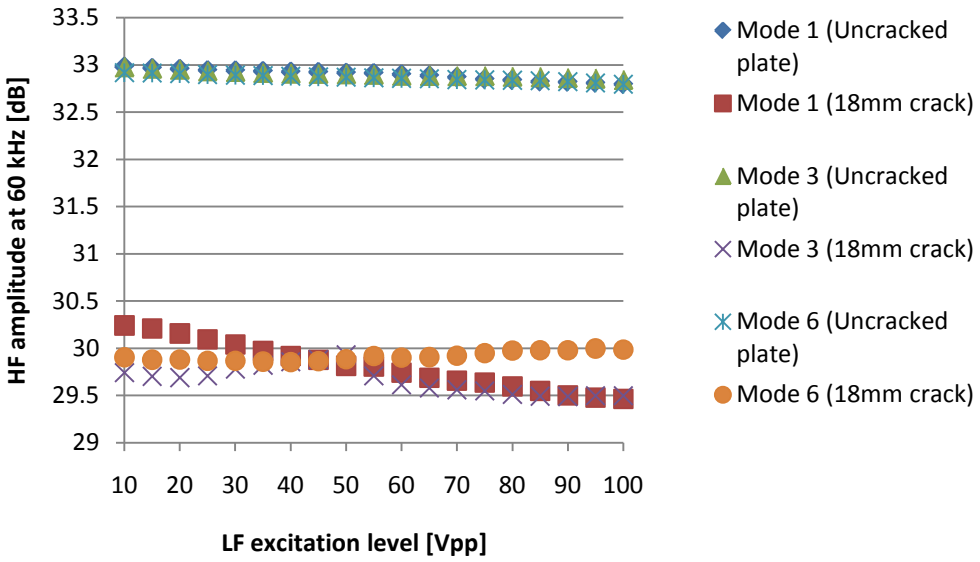


Figure 3.38: High-frequency amplitude against low-frequency excitation for uncracked and 18mm cracked plate.

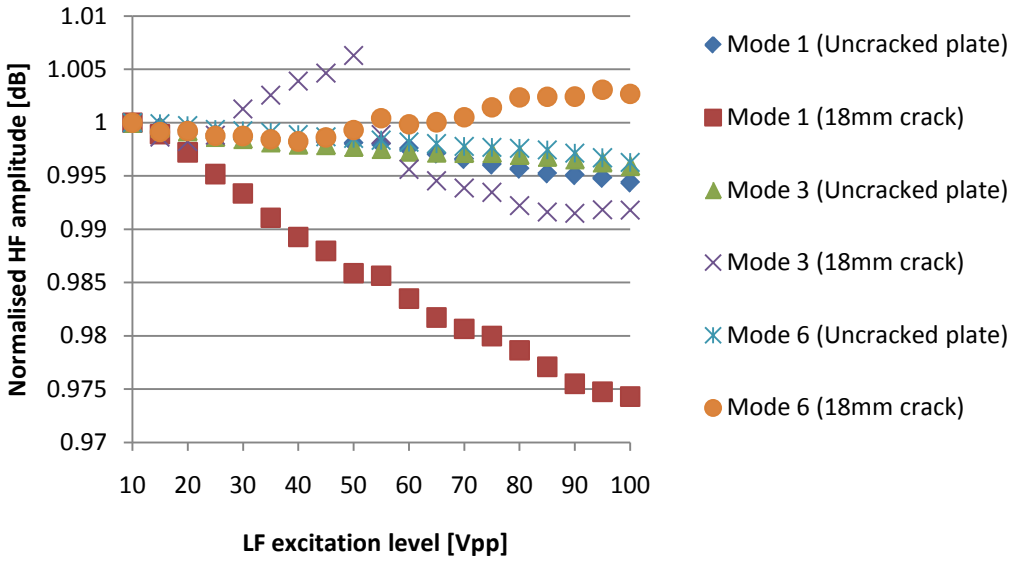


Figure 3.39: Normalise high-frequency amplitude against low-frequency excitation for uncracked and 18mm cracked plate.

### 3.2.6. Lamb wave test

The experiment is concerned with using Lamb waves for damage detection in an aluminium plate. The statistical approach of outlier analysis was applied to access the damage severity.

### 3.2.6.1 Experimental Procedure for Lamb waves test

The experiment set up is the same as mentioned in the previous Section 3.2.3. The Lamb wave input signal was a five cycle sine wave with frequency 225kHz and a peak to peak amplitude of 10V modulated by a Hanning window. The response signal was sampled with a frequency of 1GHz and recorded from 15 averages. The calculation of dispersion curves was achieved by commercial software *Vallen dispersion* [127] and is illustrated in Figure 3.42.

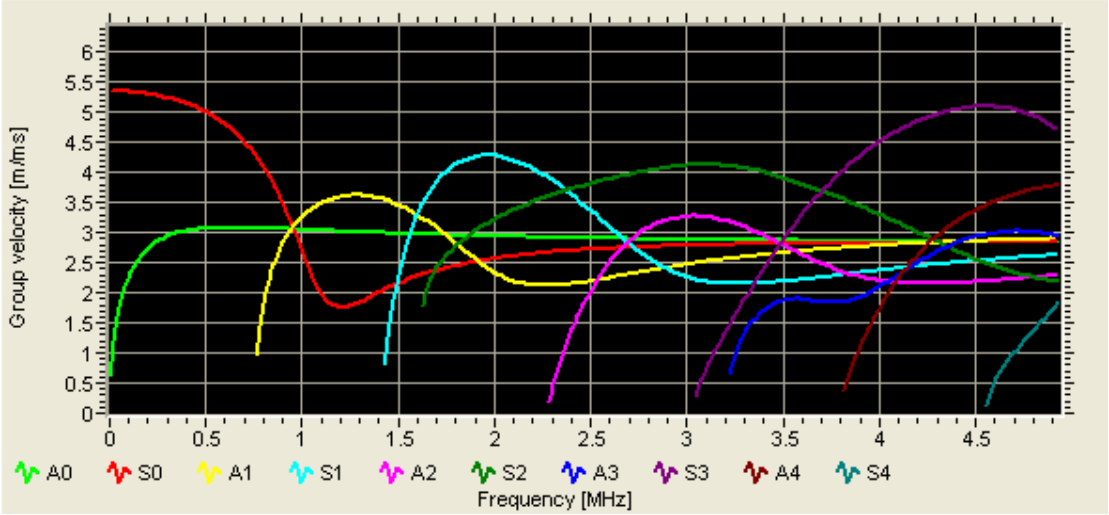


Figure 3.40: Lamb wave dispersion curves for aluminium 2024 with 2 mm thickness.

According to the Lamb wave dispersion curve for aluminium 2024 in Figure 3.42, only the fundamental $S_0$ and $A_0$ Lamb wave modes were present in the structure at the 225kHz excitation frequency. Each waveform contained a 100μs duration of data. A time lag of 10ms between pulses was introduced to avoid disturbing signals from previously recorded waveforms. A sampling window was used to eliminate boundary reflection signals, as shown in Figure 3.43.

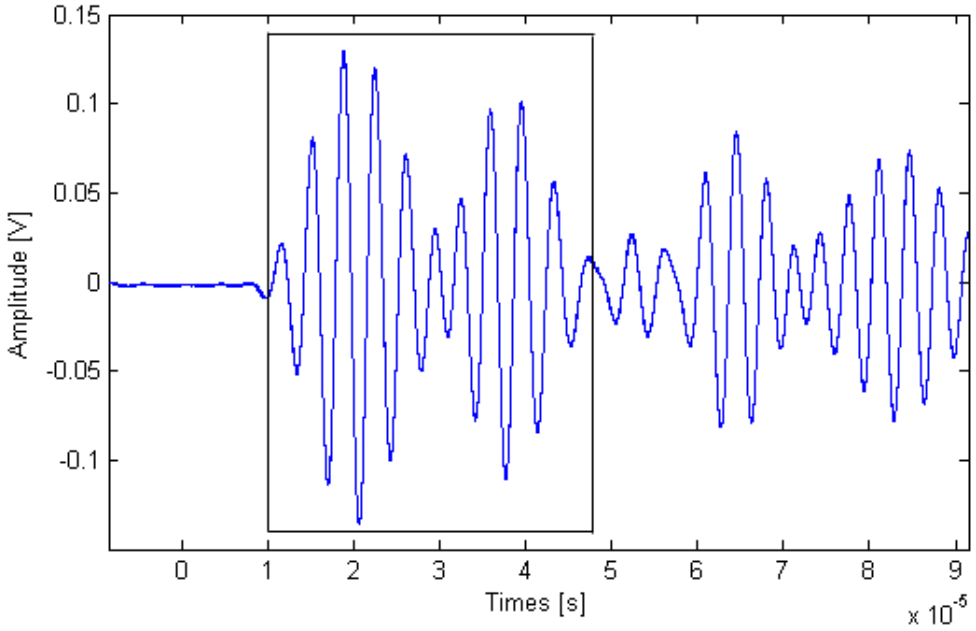

Figure 3.41: Outlier Analysis sampling window of Lamb wave response.

In order to get a benchmark of what the undamaged condition looked like, two sets of data were taken from the undamaged plate: 50 Lamb wave observations were taken as a ' training set ' and a further 50 observation were chosen as a ' test set '. The training set was used to calculate the mean and covariance needed for Equation (2.29) and the test set was applied for Outlier Analysis. This procedure gave confidence that outlier analysis could successfully classify undamaged samples as undamaged.

For each of the 9 damage levels, 50 observations were taken later. The 1% exclusive threshold value for a 50 observation, 10-dimensional problem was found to be 50.5 after 1000 Monte Carlo trials of the algorithm discussed in Section 2.3.2. In addition, the graphs shown in Figure 3.44 demonstrate the energy dissipation which is caused by damage.

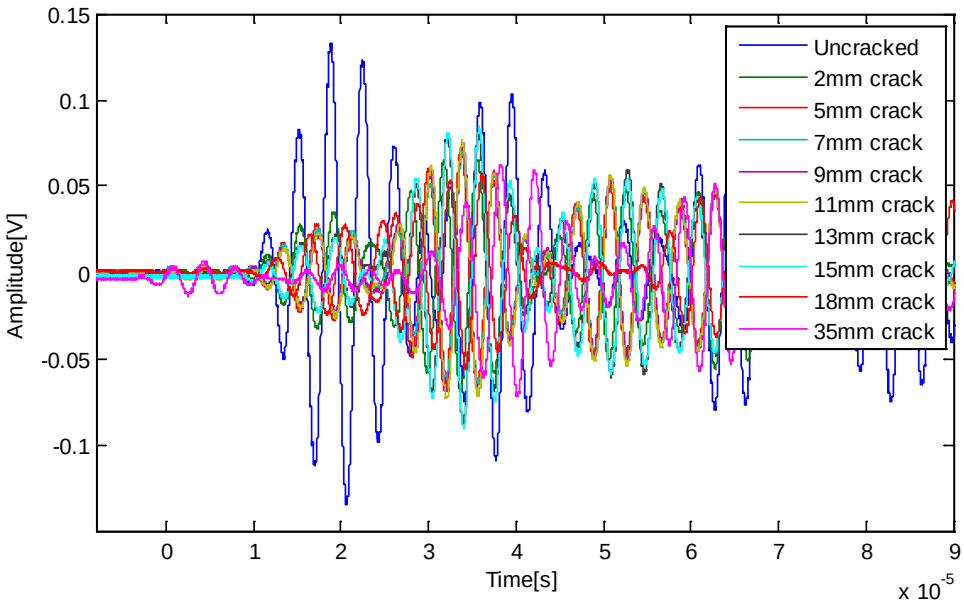


Figure 3.42: Acoustic waveforms for various severities

### 3.2.6.2 **Experimental results and discussion**

The results obtained by outlier analysis are shown in Figure 3.45 with a logarithmic vertical scale. The results indicate successful classification for undamaged and damaged data. That means the undamaged data are all lying below the threshold level (red line) and are classified as 'inliers' while all the damaged data are significantly above the damage detection threshold and are categorised as 'outliers'. In addition, the MSD values are slowly and steadily decrease from the 2mm to the 15mm crack and then rose dramatically over the following two damage severities. Thus, outlier analysis does not give a monotonic increase in the MSD value with increasing fatigue cracks in this study. This may be caused by the phase change when the Lamb waves interact with damage. However, when the crack is large enough, energy dissipation may overwhelm other effects and hence heavily influence the MSD value.

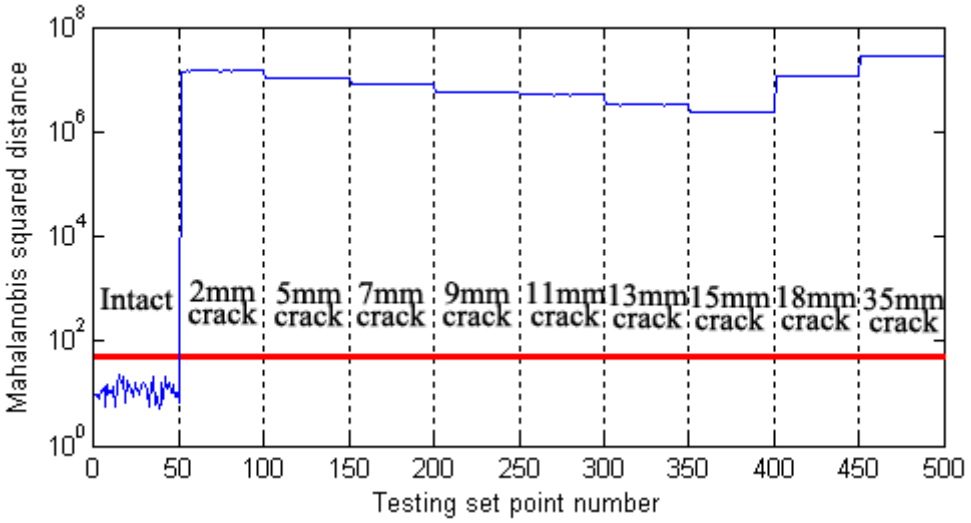

Figure 3.43: Outlier analysis classification results with logarithmic scales.

## 3.3 Summary

This chapter has demonstrated nonlinear acoustics and Lamb wave methods for analysing a fatigue crack in a glass and an aluminium plate. For nonlinear acoustic tests, the work was mainly focused on single wave excitation, FRFs with varying excitation levels test and vibro-acoustic excitation. The 1st, 3rd and 6th plate modes were selected for low-frequency modal excitation. Different crack lengths were investigated. Various nonlinear symptoms in signal response were examined to find possible physical mechanisms. Prior to the nonlinear acoustics method, modal parameters analysis on uncracked plate was presented. In addition, when a crack is present in the structure, there are three typical crack modes resulting from crack motion and different crack modes may contribute to various nonlinear mechanisms.

A number of important conclusions can be summarised from the experimental work undertaken. Three different nonlinear phenomena were observed: (a) non-classical L-G type dissipation, (b) the dissipation mechanism related to crack-wave interaction and (c) nonlinear elasticity. Meanwhile, the frequency shift and the damping estimation analysis did not reveal much useful information.

Comparing the results between the glass and aluminium plates, there are some

findings that need to be considered. For the single wave excitation, both glass and aluminium plates found that the 1st mode was the most sensitive vibration mode to detect the crack by using the β perturbation coefficient. This is related to the contact-type nonlinearity caused by the asymmetric stiffness for tension and compression of a breathing crack. In addition, the 3rd mode for the glass plate also showed a good sensibility to detect the crack. This is probably because of the friction forces between the damage interfaces. For the combined vibro-acoustic wave excitation, the 3rd and 6th modes showed a high sensitivity for detecting cracks in the glass and aluminium plate. Meanwhile, the 1st mode only detected the larger size cracks. According to these results, the major mechanism behind the vibro-acoustic wave modulation is caused by frictional energy dissipation. Furthermore, both glass and aluminium tests observed the L-G effect.

The application of outlier analysis on Lamb wave tests on the glass and aluminium plates successfully classified damage with 100% rate. Outlier analysis was able to give an indication of damage severity in the glass plate test. However, outlier analysis did not exhibit a trend of monotonically increasing MSD values in the aluminium test, hence it was not able to give an indication of damage severity in this case. Pearson *et al* [134] applied a cross correlation technique to compare signals in a undamaged structure with those at various damage levels. The experiment results showed a decreasing correlation of signals with increasing damage severity; hence the cross correlation technique was able to assess the damage severity in this case and can be a potential tool for estimating damage severity.

# Chapter 4

# 4 Damage detection and monitoring in composite laminates

## 4.1 Detecting impact damage on composite structures

Carbon Fibre Reinforced Polymer (CFRP) is the composite material that is most used in the aerospace and automotive industries. In consideration of the significant reduction in stiffness and strength of the composite structure caused by impact event, it is necessary to examine the material properties upon on an impact event. This section mainly focuses on low velocity impact events and the application of nonlinear acoustic and guided wave methods.

### 4.1.1 Test specimen

The laminate used as a test structure for this present research was a woven pre-impregnated (prepreg) CFRP manufactured by the *Advanced Composite Group* (ACG). The material used was MTM 56 resin system (42% RW with CF8160 Fabric 600g/m$^2$, 24k and $2\times2$ twill carbon fabric). The term MTM56 means the woven prepregs are based on an epoxy matrix that cures rapidly at 120 °*C* [135]. The term CF8160 indicates the fabric specification of the material, while 600g/m$^2$, 24k and $2\times2$ twill specify the fabric area density, number of filaments and the weave style, respectively. The prepreg was supplied in the form of fabric with a width of 1.25m. The prepreg roll was reserved in a refrigerator at approximately -18 °*C* .

### 4.1.2 Manufacturing the CFRP plates

The manufacturing procedure can be described as: material preparation, lay-up processing, autoclave processing, removing air in the vacuum bag, curing in the

autoclave and sawing the laminates [136].

The hand laminating technique has been chosen to manufacture the CFRP plates. This technique is effective and still widely used in industry [137]. The drawback of this technique is that the mould has only one smooth side and the final product highly relies on the skill of the operator.

In order to examine the feature of an impact event, the prepregs were fabricated to the same size of specimens ($150 \times 250 \times 4$ mm) with 4 layers. For the material preparation, the first step is taking out the prepregs from the refrigerator and keeping it at room temperature overnight. This step is helpful to reduce the viscosity of the resin [137]. The second step is to measure and draw the cut lines for the layers having fibres oriented at $0°$ and $90°$. Although the prepreg used in this study is woven fabric with twill weave style (interlacing of warp 0° fibres and weft 90° fibres) as shown in Figure 4.1, the mechanical properties are still not the same when oriented at $0°$ and $90°$ due to the manufacturing procedure for the prepreg. The third step is to clean the base for lay-up of the pregregs. The surface is required to be as smooth as possible and without any dirt on it. The preparation procedures are shown in Figure 4.2.

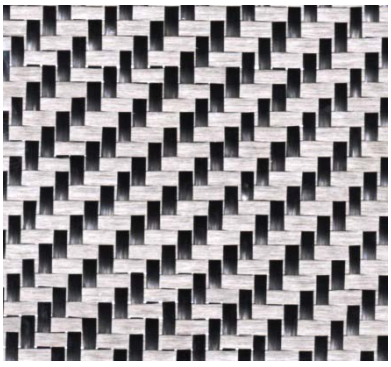

Figure 4.1: Woven prepreg with twill weave style [138].

(a)

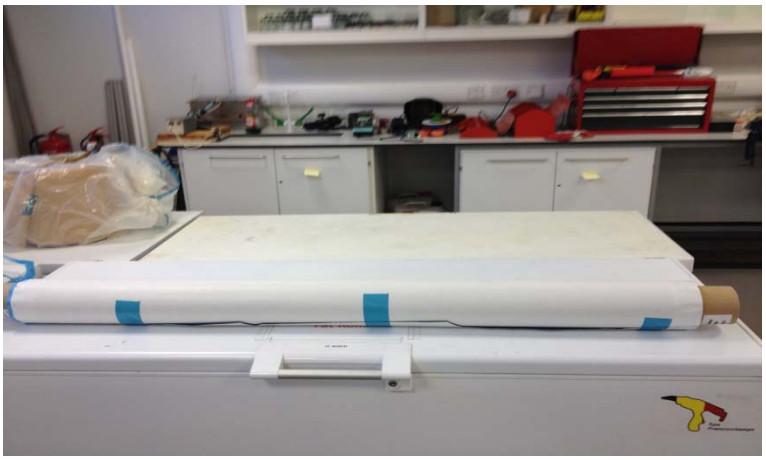

(b) (c)

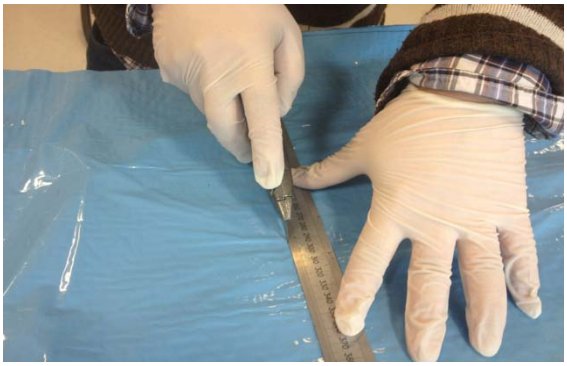

Figure 4.2: Material preparation (a) take out the roll of prepreg at room temperature, (b) measure and cut the width of fabric in the longitudinal direction for the 0° layer, (c) measure and cut the width of fabric in the transverse direction for the 90° layer.

After the preparation stage, the next step was to perform the lay-up of the prepregs on the surface of the base. The main contribution for the lay-up is to give the optimum strength and stiffness in the fibre orientations [139]. A schematic illustration of the composite plates with 4 plies [0, 90, 90, 0] is shown in Figure 4.3.

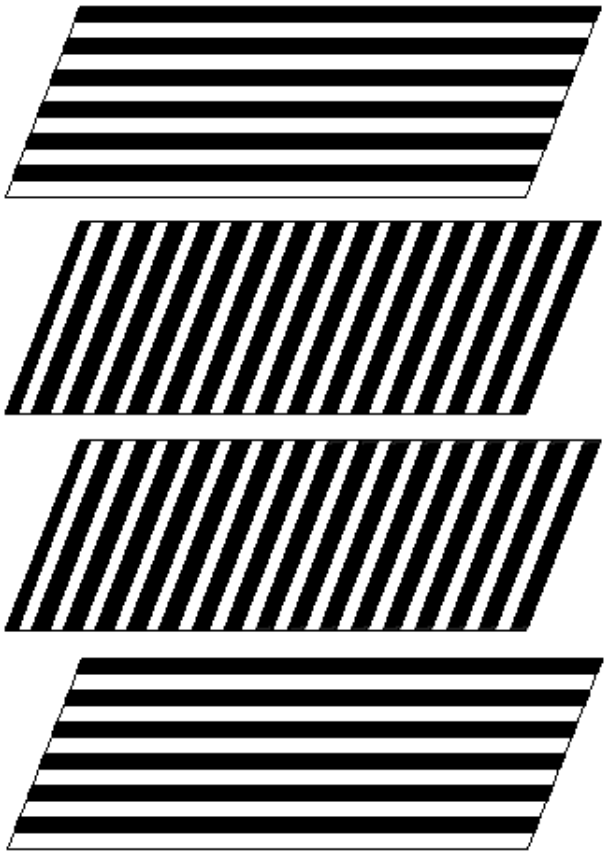

Figure 4.3: A schematic illustration of the composite plates with 4 plies [0, 90, 90, 0].

Once the base was prepared, layers were stacked on each other following by a designated sequence. A brush was then used to smooth the layer surface by removing entrapped air and to catalyse resin into the fibre reinforcement [137]. This step was repeated for each layer until finishing the lay-up. Furthermore, a sealed bag was applied on the fabric to remove air and to form a vacuum bagging film. Figure 4.4 illustrates these steps in detail.

(a) (b)

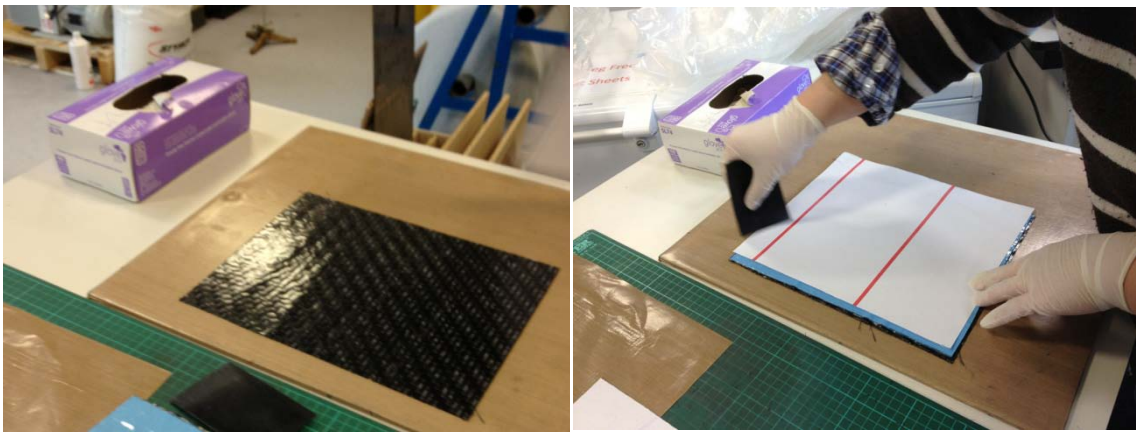

(c) (d)

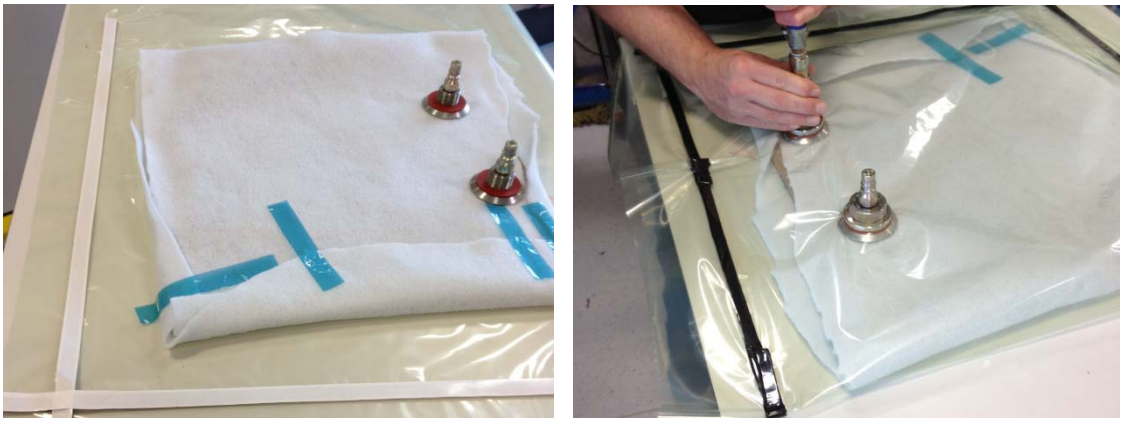

Figure 4.4: Main steps before the autoclave process (a) lay-up the fabrics, (b) using the brush to smooth the surface, (c) placing the vacuum bagging film, (d) vacuuming.

The autoclave procedure is an essential method for manufacturing most of the high-quality laminates in the aircraft, automotive and marine industries [140]. The mechanism of the autoclave procedure is to apply high pressure and temperature on the composite laminate and to make it become a single coherent structure by removing the redundant resin and air holes [141]. Figure 4.5 shows the curing process in the autoclave. Operating the autoclave can be divided into three stages. At the first stage, operating pressure of autoclave was increased to 0.62MPa and the temperature was raised up from room temperature to $120\,°C$ at a rate of $3\,°C/\min$. In the second stage, temperature and pressure were kept constant and held for 10 minutes to cure the laminates. In the third stage, the temperature was dropped to $80\,°C$ at a rate of $3\,°C/\min$. As a consequence, the excess heat can be scattered. Meanwhile, the

pressure was held at the same level to prevent voids growing. Until completing the cooling process, the pressure was released and the autoclave was turned off. Only the ventilation system kept working until the temperature of specimen decreased to room temperature. An illustration of the three stages of the autoclave processing is shown in Figure 4.6.

Figure 4.5: Curing process in autoclave.

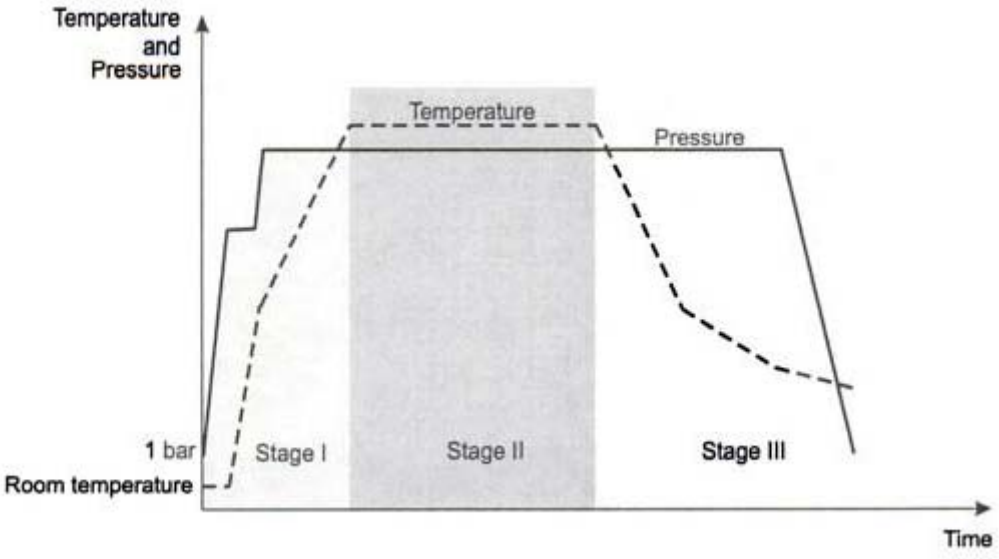


Figure 4.6: Temperature and pressure for three stages in the autoclave processing [141].

The final procedure is cutting the edge of the CFRP materials as shown in Figure 4.7.

Figure 4.7: Cutting the edge of CFRP.

### 4.1.3 Impact tests on composite structures

Detecting impact damage is a crucial concern in maintaining the structural integrity of composite structures. It guarantees the composite structures to perform safely and durably during service. Matrix cracks, interlaminate delamination, fibre fracture and debonding resulting from impacts are major failure modes in composite structures [142]. It is clear that various damage levels correspond to different impact energies and change the mechanical response of the material.

CFRP laminates were employed in the current study. CFRP based on carbon fibres in a polymer matrix are heterogeneous and anisotropic materials [143]. CFRP exhibit high strength-to-weight and stiffness-to-weight ratios in the fibre direction. However, a constant concern is the effect of impact loading on CFRP because significant damage can occur either during routine maintenance works or during the in-service condition and the damage is very difficult to detect by visual inspection [144]. The laminate used as a test structure for this present research was a woven prepreg CFRP. This woven fabric overcomes the short comings of unidirectional layers by enhancing the transverse tensile strength.

Pavier [145] experimentally demonstrated that low velocity impact can cause dramatic strength reduction and may lead to larger size damages under cyclic loading. Generally, a low velocity impact is defined as at an impact velocity less than 10m/s [146]. However, some researchers consider that less than 100m/s [144] or 20m/s [147] represent low velocity impact occurrences.

For impact testing, kinetic energy ($E_k = \frac{1}{2}mv^2$) and potential energy ($E_p = mgh_g$) play an important role in determining the damage on the test structures. It is clear that a heavy mass object with a lower dropping height and a light mass object with higher height have the equal potential energy but may produce different damage severity on the test structures. According to this reason, the height and the mass of the dropping impactor needs to be carefully chosen to simulate various types of impact.

Extensive studies [136, 144] reveal that the damage caused by a low velocity impact starts with matrix cracking before creating delaminations at the interface. This failure mode is a hidden risk that may tend to create invisible subsurface delaminations. As mentioned before, composites usually have strong impact resistance along the fibre orientations. However, the other directions are characterised as relatively weak

and have low impact resistance. So fibres are vulnerable to fracture when the unanticipated stresses are applied in the weak directions [136]. This failure mode is considered as the critical stage in composite structures. It is widely accepted that the presence of delaminations can significant reduce the stiffness and strength of CFRPs [148-150] and it is the most severe type of failure mode found in composite structures.

Abrate [144] illustrated that two types of matrix cracks are observed in composites subjected to low velocity impact: tensile cracks and shear cracks. Mobasher [151] explained that the tensile cracks are caused by in-plane normal stresses when these exceed the limits of the matrix transverse tensile strength. In addition, the transverse shear stresses result in shear cracks from the centre of the composite structures. An illustration of two types of matrix crack can be seen in Figure 4.8.

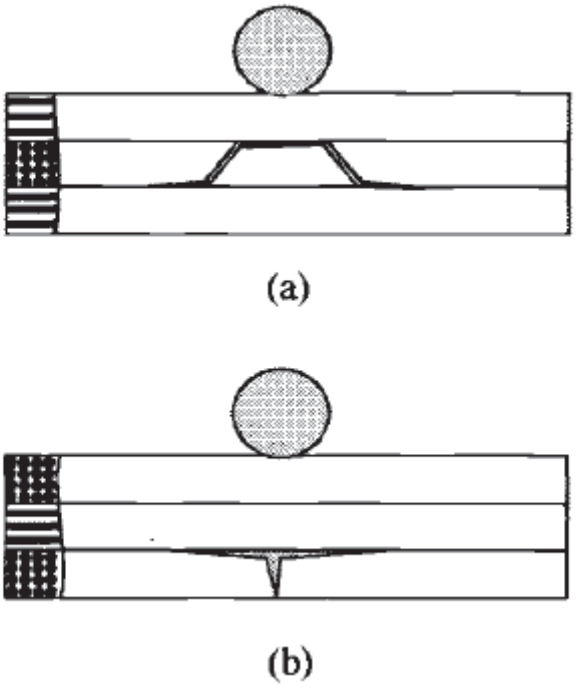


Figure 4.8: (a) Tensile crack and (b) shear crack introduced by impact [144].

The thickness of the composite plate is an important factor that affects the formation of matrix cracks. As mentioned by Abrate [144], the matrix cracks initiate at the first

contacted layer of the impacted thick plate due to the localised contact stress and the damage pattern is similar to a pine tree (Figure 4.9a). On the other hand, the matrix cracks orientated at the lower layer of the impacted thin plate are caused by bending stresses distributed on the back surface of plate and the damage pattern is similar to a reverse pine tree (Figure 4.9b).

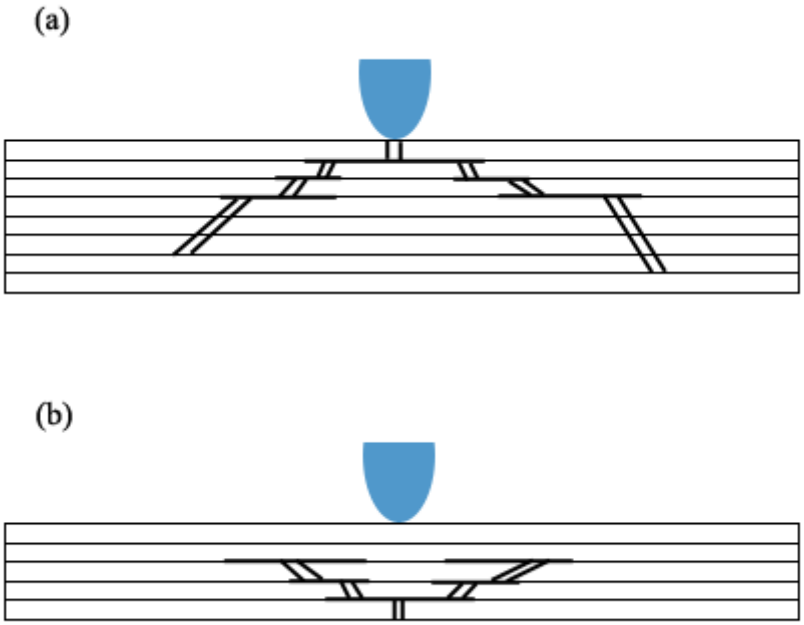


Figure 4.9: Impact damages on (a) a thick and (b) a thin plate.

Generally speaking, the low velocity impact test can be described as an energy transformation by following the law of energy conservation. In other words, the gravitational potential energy before the impact event is totally converted to the kinetic energy after the impact event [152]. The law of energy conservation can be expressed by:

$$mgh_g = \frac{1}{2}mv^2, \tag{4-1}$$

where $m$ is the mass of drop impactor, $h_g$ is the drop height, $g$ is gravitational acceleration, $v$ is the velocity of impact. Equation (4-1) can be rewritten as:

$$v = \sqrt{2gh_g}\ . \tag{4-2}$$

To simulate low velocity impact damage in the laminates by a foreign object, such as tools accidentally dropped on the structure, a drop weight test has been used. Varying

weights can be attached to an impactor. In the current test, an impactor having a total mass of 2.25kg was considered. The test specimen was mounted horizontally at the edges along the short axis using the clamping mechanism. The testing apparatus was equipped with an electromagnet to raise the impactor to the desired height as shown in Figure 4.10. The drop height ranges were 0.45-1.81m for a 10-40J impact energy test. In addition, a force transducer was mounted on the impactor to record the contact force history during the test. The impactor slid down guide rails and struck the clamped test specimen. A simple mechanical catching system was used to avoid double impacts. Figure 4.11 shows the fibre failure for the composite plate after a 40J impact test. The total progamme of tests on the 4-layer composite laminate is summarised in Table 4.1.

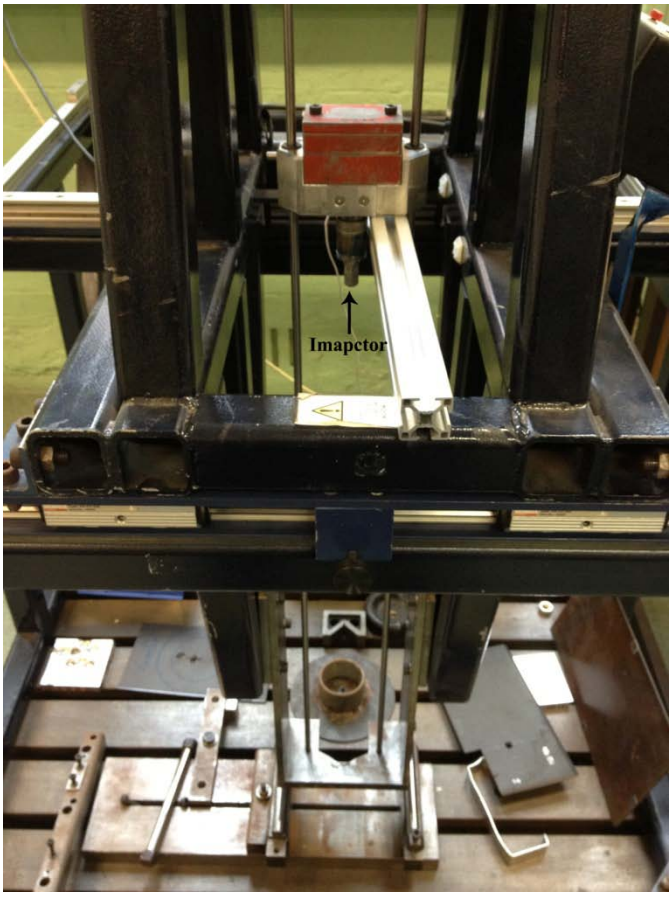


Figure 4.10: The impact test apparatus.

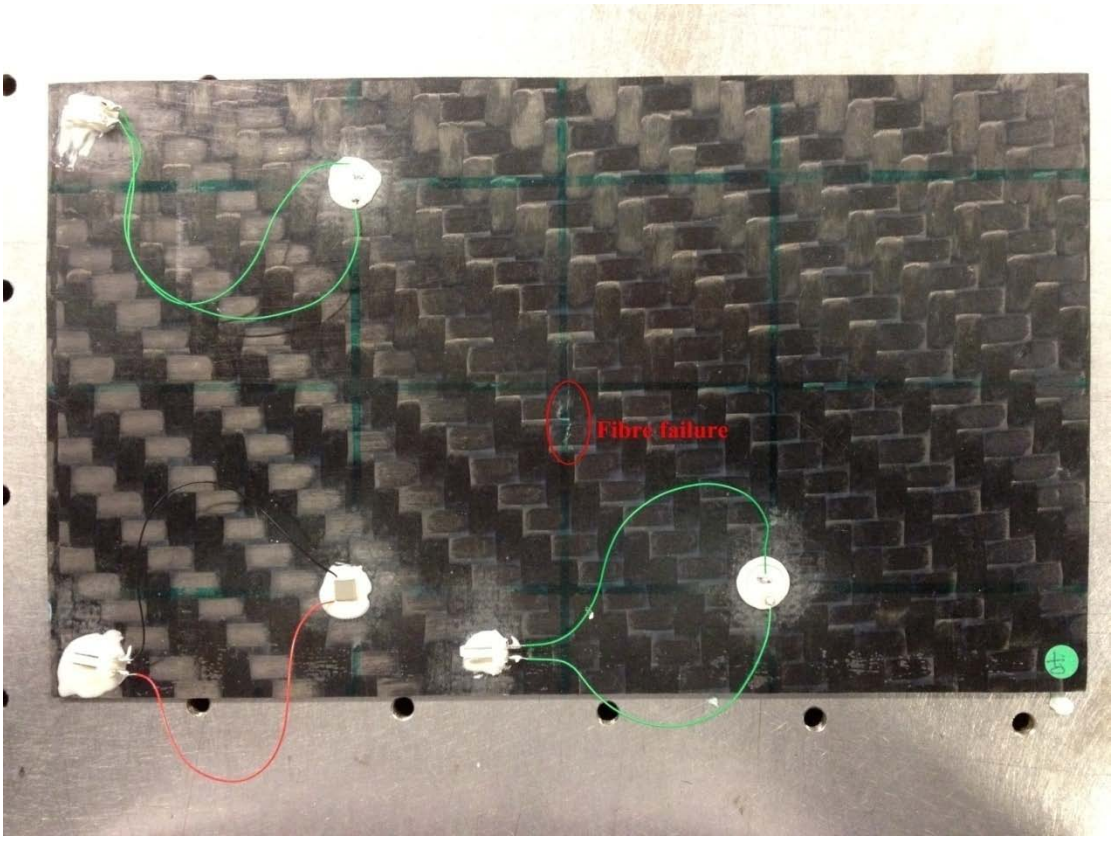


Figure 4.11: Fibre failure after 40J impact test.

Table 4.1: Impact results for 4-layer CFRP plates.

| Plate Number | Impact Energy (J) | Impact Mass (kg) | Drop Height (m) | Velocity (m/s) | Contact Force (N) |
|---|---|---|---|---|---|
| 1 | 10 | 2.25 | 0.45 | 2.97 | 1644 |
| 2 | 15 | 2.25 | 0.68 | 3.65 | 1973 |
| 3 | 20 | 2.25 | 0.91 | 4.22 | 2311 |
| 4 | 25 | 2.25 | 1.13 | 4.71 | 2699 |
| 5 | 30 | 2.25 | 1.36 | 5.16 | 3012 |
| 6 | 35 | 2.25 | 1.59 | 5.58 | 3355 |
| 7 | 40 | 2.25 | 1.81 | 5.96 | 3693 |

### 4.1.4 Modal analysis

Due to regrouping of the manufacturing company ACG, the main material properties for the laminates were not available. The FE modal analysis used similar woven laminates to simulate the CFRP laminate. There is no constraint applied on the model. The CFRP laminate combined 4 layers with [0, 90, 90, 0] orientations and the FE analysis for the bending and torsion vibration modes are shown in Figure 4.12.

(a)

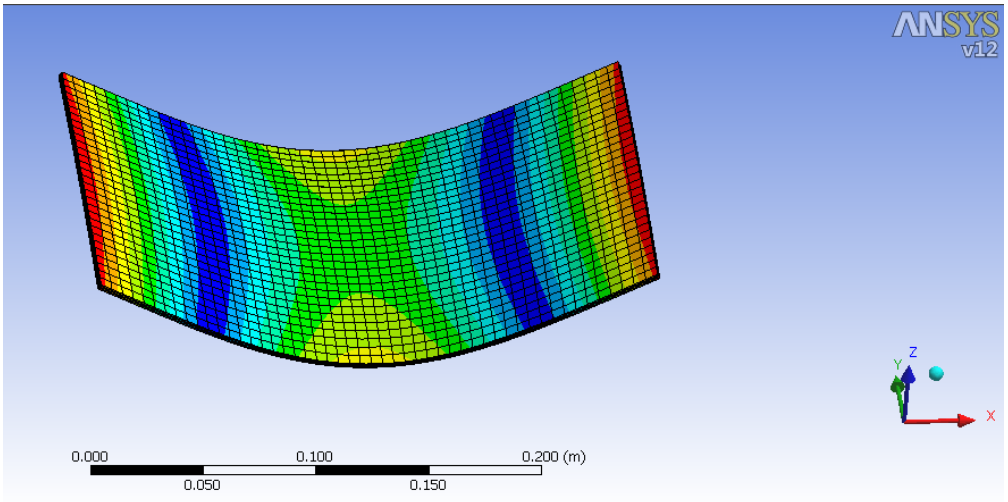


(b)

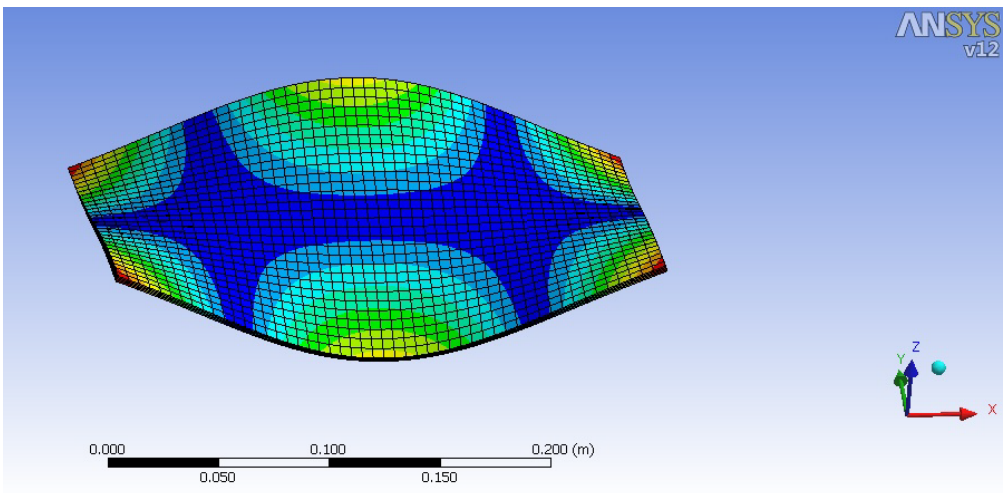


Figure 4.12: Mode shapes for (a) 2nd vibration mode and (b) 3rd vibration mode.

A hammer modal test was performed to validate the natural frequencies and mode shapes. After that, three low-profile, surface-bonded piezoceramic transducers were

installed on the plate. A HBM-X60 2-component fast curing glue was used to attach the transducers. A PI Ceramics PL-055.31 stack actuator ($5\times5\times2$ mm) was used for low-frequency modal excitation. Two PI Ceramics PIC155 transducers (diameter 10 mm; thickness 0.5 mm) were used for ultrasonic wave excitation (this high frequency excitation was used in future vibro-acoustic tests rather than modal testing here) and for all response sensing. The plate was freely suspended in all experimental tests. Figure 4.13 shows a schematic diagram of the plate with transducer locations.

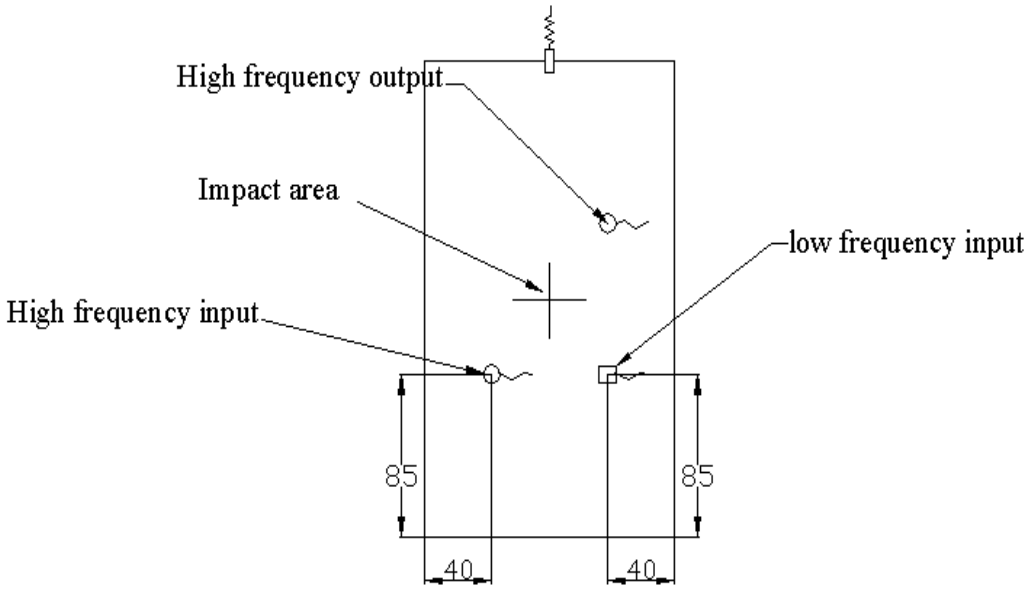


Figure 4.13: Schematic diagram of the composite plate.

Experimental modal analysis was performed to establish frequencies of LF modal excitation for the nonlinear acoustic tests. A swept sine signal, starting at 1Hz and increasing to 500Hz in 2s was used to excite the intact plate. The peak-to-peak amplitude of excitation was equal to 20V. The response signal was sampled with a frequency of 2kHz.

The excitation and response data were used to calculate the FRF in order to reveal resonance frequencies. Figure 4.14 reveals the amplitude of the experimental FRF. The second and third excited modes were confirmed as the first bending and second torsional vibration modes for the analysed plate by experimental tests with a free-free

boundary condition and were selected for low-frequency excitation in the current nonlinear acoustic investigations.

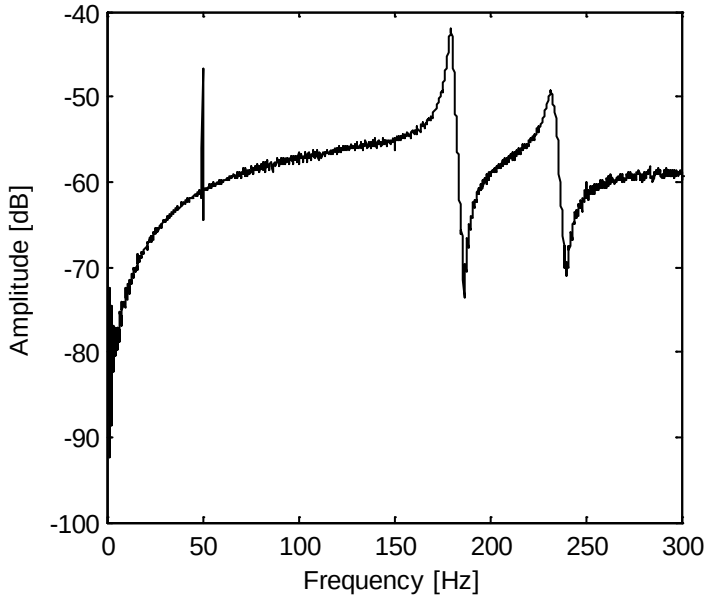


Figure 4.14: Vibration FRF from modal testing for CFRP laminate.

The experiment work was performed on seven rectangular $150 \times 250 \times 2$ mm CFRP laminates. It included a classical modal test (Section 4.1.4), a single wave vibration test, a vibro-acoustic test and FRFs with varying excitation level test.

Vibration excitation always involved one of the selected vibration modes. Various amplitude excitation levels were used. The maximum peak-to-peak amplitudes of the LF and HF excitation used were equal to 100 and 20V, respectively. The sampling rate used to acquire responses from the single-wave vibration excitation was equal to 20kHz. The sampling rate for vibro-acoustic signals and FRFs were equal to 500kHz and 2kHz.

## 4.1.5 Experimental results

### 4.1.5.1 Single wave vibration

Figure 4.15 shows examples of power spectra from single-wave excitation tests using

the 2nd and 3rd vibration modes. Two different plate conditions are analysed, the intact plate and the plate with impact damage. A clear pattern of higher harmonics can be observed in all analysed spectra, even for the undamaged plate. Observed from Figure 4.15(a) and 4.15 (b), the magnitude of the second harmonics for the 40J impact plate with excitation of the 2nd and 3rd vibration modes increasing 8dB and 15dB respectively.

(a)

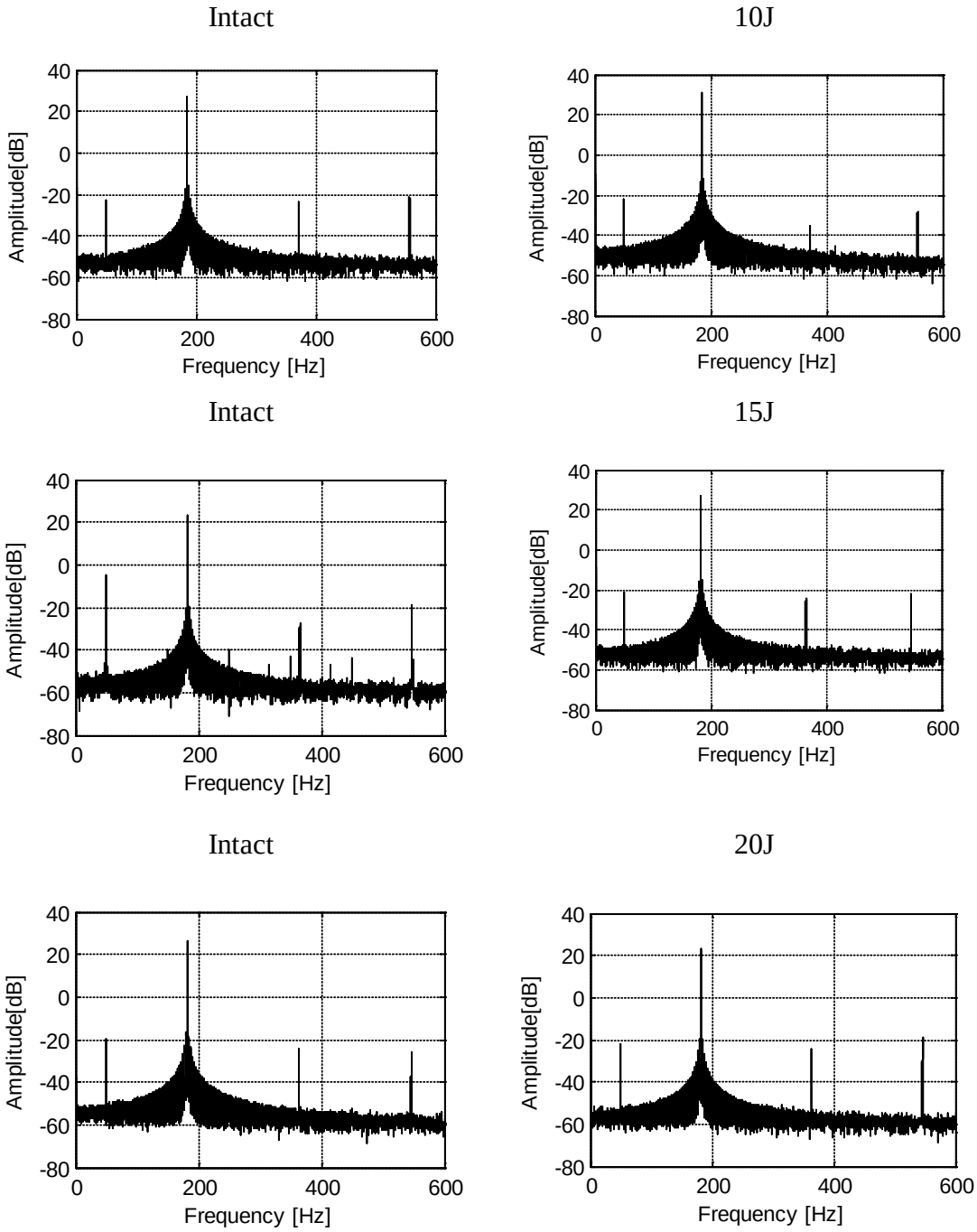

Intact

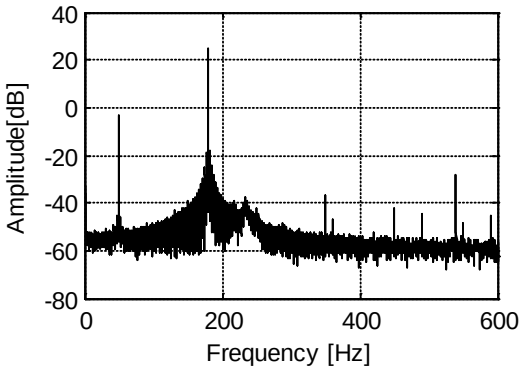


25J

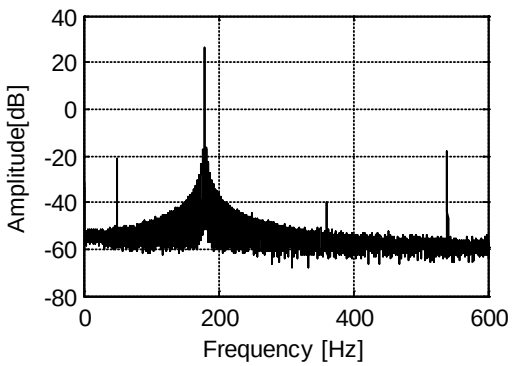


Intact

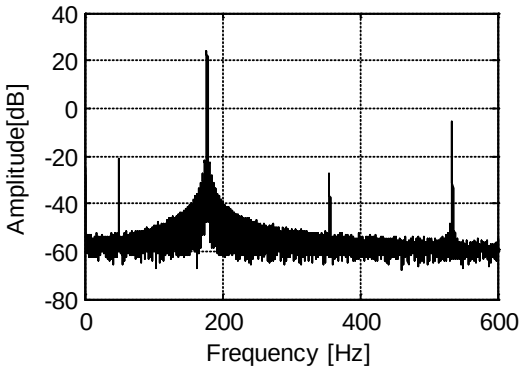


30J

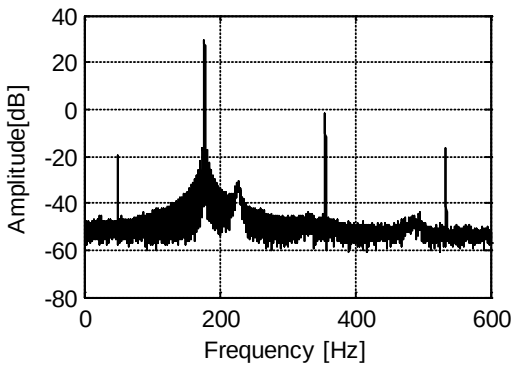


Intact

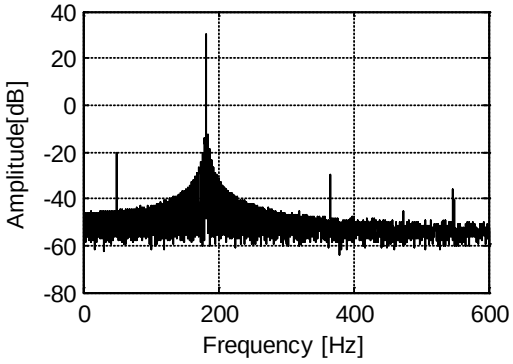


35J

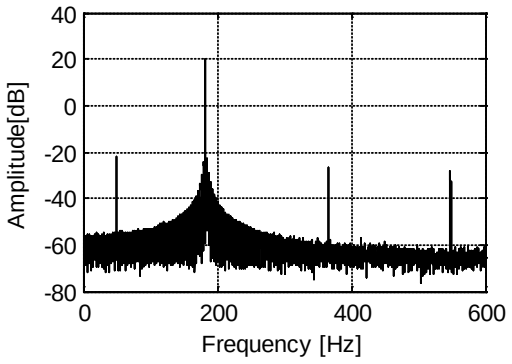

Intact

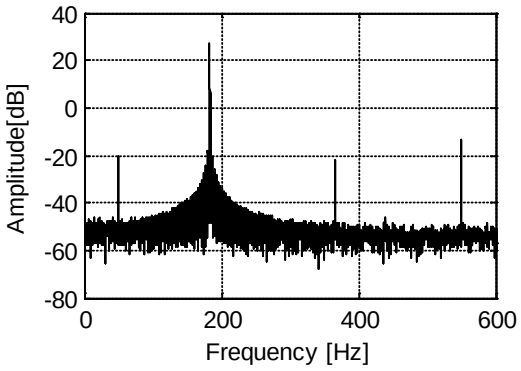


40J

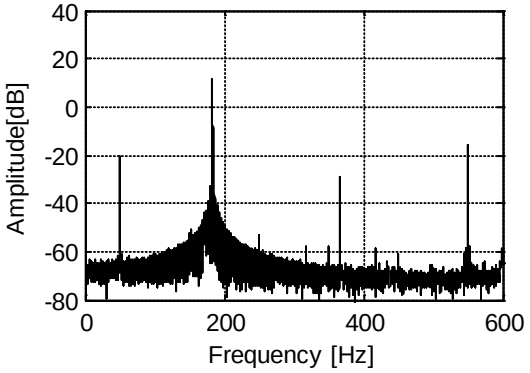


(b)

Intact

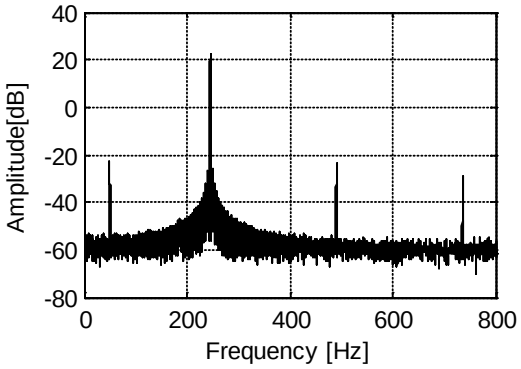


10J

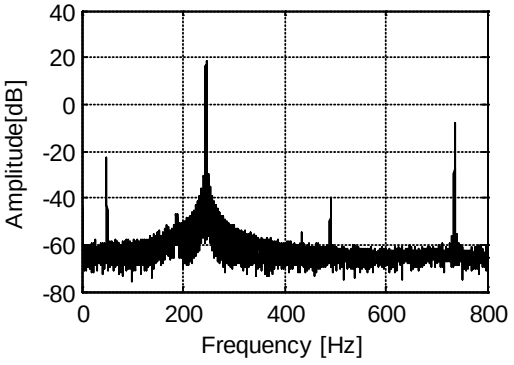


Intact

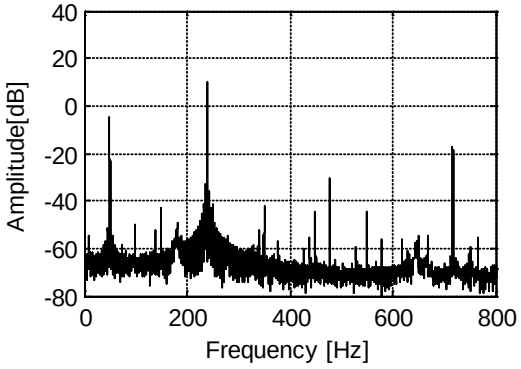


15J

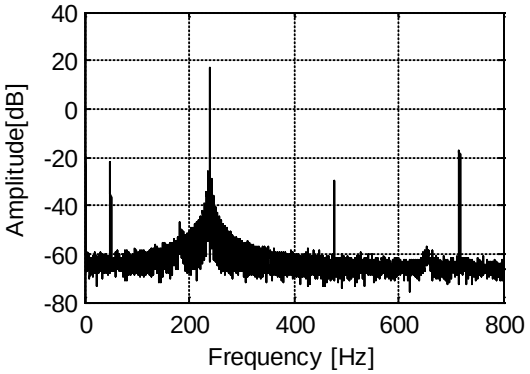

Intact

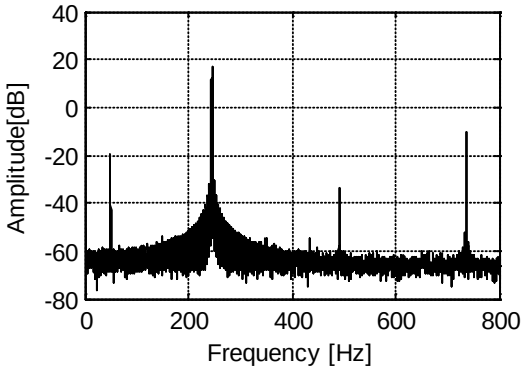


20J

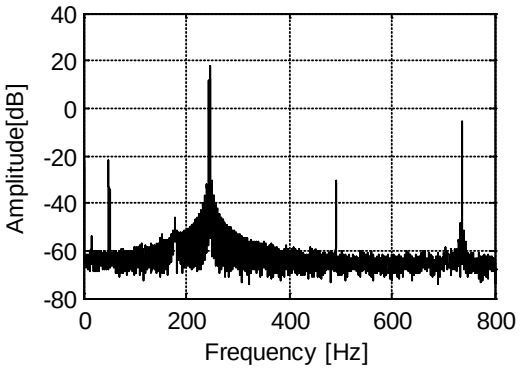


Intact

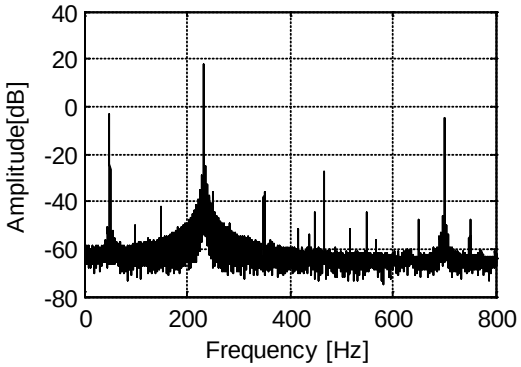


25J

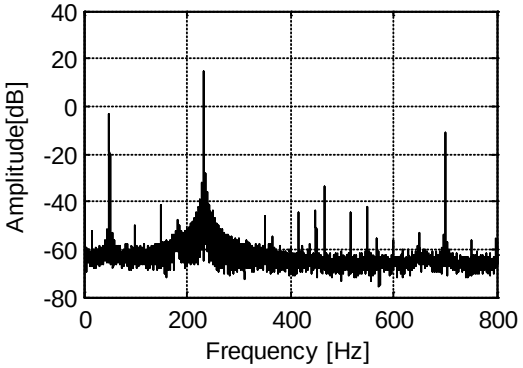


Intact

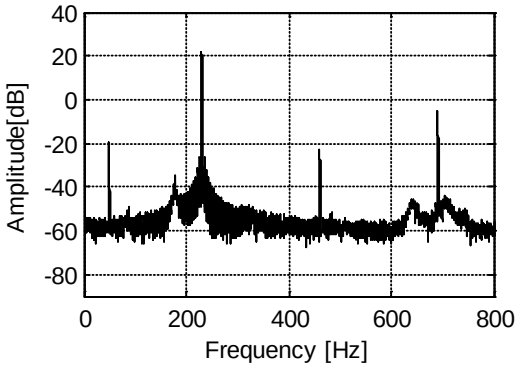


30J

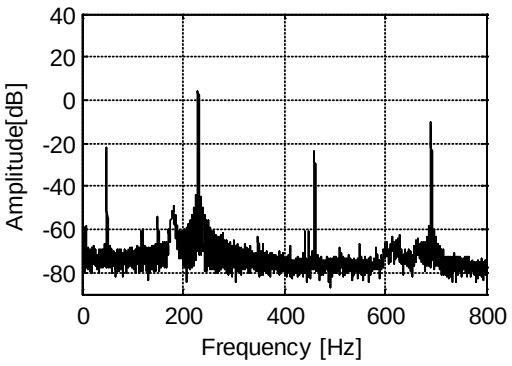

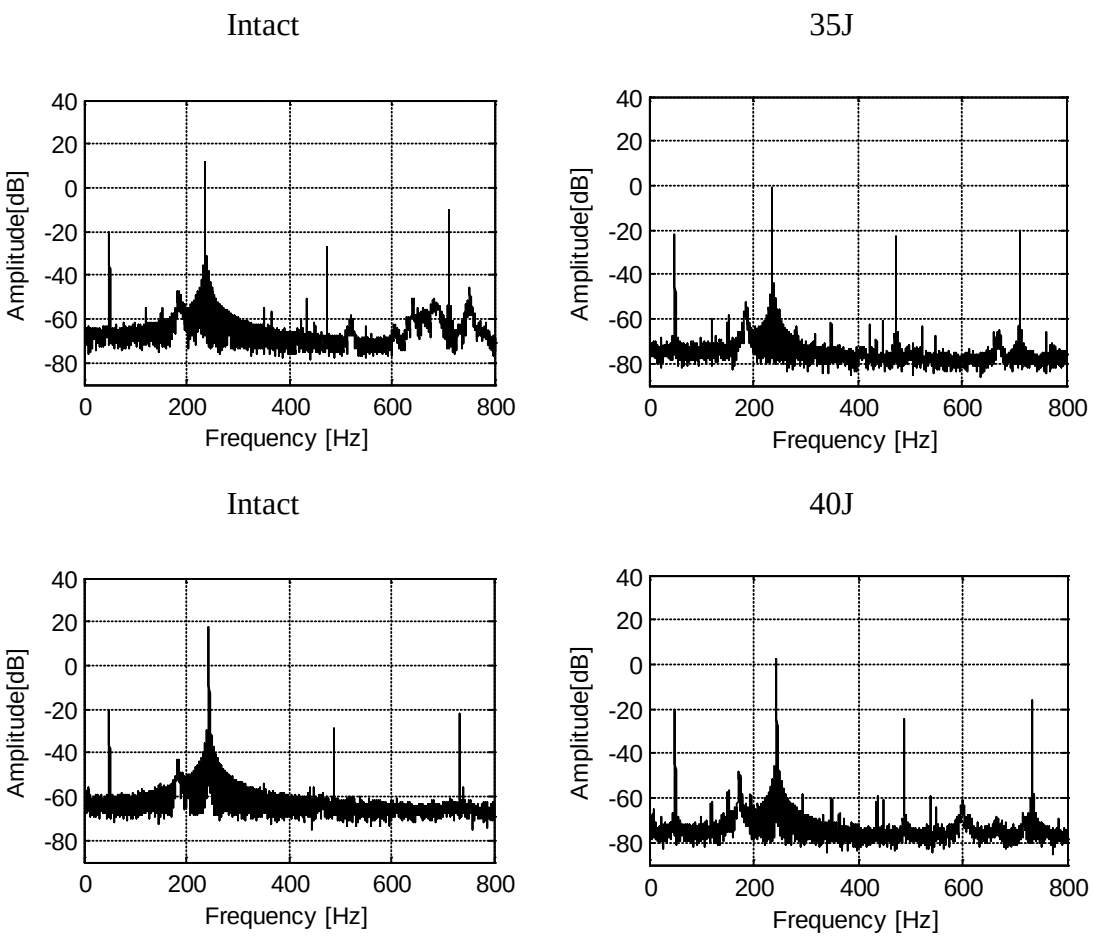


Figure 4.15: Power spectra density showing the fundamental peak and harmonics for the intact (left column) and impact (right column) plate excited by (a) 2nd and (b) 3rd mode.

The amplitude of the second harmonics is analysed further for all impact damage levels in order to reveal possible changes in nonlinear perturbation coefficient β. A test statistic is used to find out whether a result is statistically significant or if it occurs by coincidence. Figure 4.16 gives the test statistic value for the perturbation coefficient β against the impact energy. Any test statistic value above the critical value line is considered as nonlinearity resulting from damage. Observed from Figure 4.16(a), when the impact energy reaches 20J and beyond, the nonlinearity contributed by a suspected delamination can be detected for the second mode excitation. Similarly, statistical significant results are found for 30J and beyond with excitation of the 3rd vibration mode (Figure 4.16(b)). The results show that the 2nd mode (opening motion) is more sensitive that the 3rd mode. The 2nd vibration mode is related to the

opening-closing crack mode and the 3rd vibration mode is corresponded to the sliding crack mode. Thus, a clapping nonlinearity, which is caused by asymmetric stiffness for tension and compression of damage, is the major physical mechanism that attributes to harmonic generation. More details about the clapping nonlinearity are given in Section 2.1.2. In addition, the 2nd vibration mode also introduced a higher stain level in the impact area than the 3rd vibration mode. This may also affect the result.

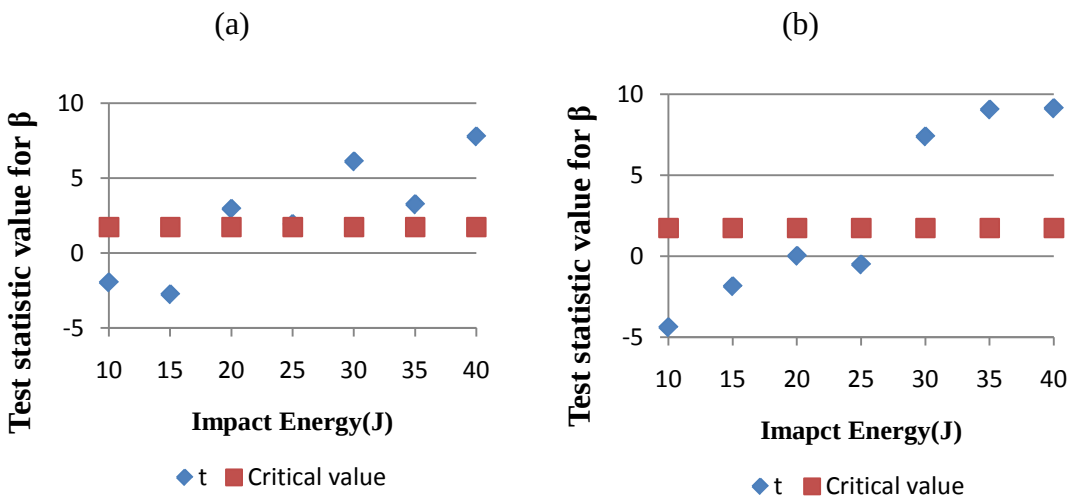


Figure 4.16: Test statistic value for the (a) 2nd and (b) 3rd vibration mode.

### 4.1.5.2 FRFs with varying excitation levels test

Figure 4.17 shows comparisons of natural frequency around the 2nd and 3rd mode for the undamaged and damaged plates. The data were obtained from FRFs with various amplitude levels of excitation. It seems that there is no significant change in natural frequencies with 10J impact energy. However, at large impact energy (40J), the natural frequencies for both modes deceases dramatically due to a great loss in the stiffness. In addition, frequency shifting for the 2nd and 3rd modes is not distinct in different impact levels.

(a)

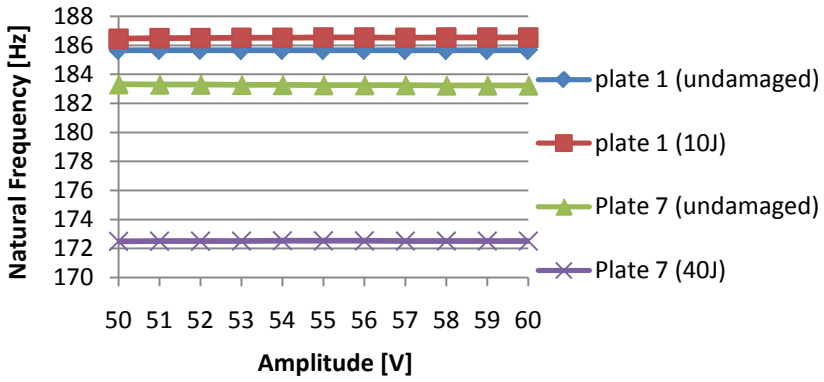


(b)

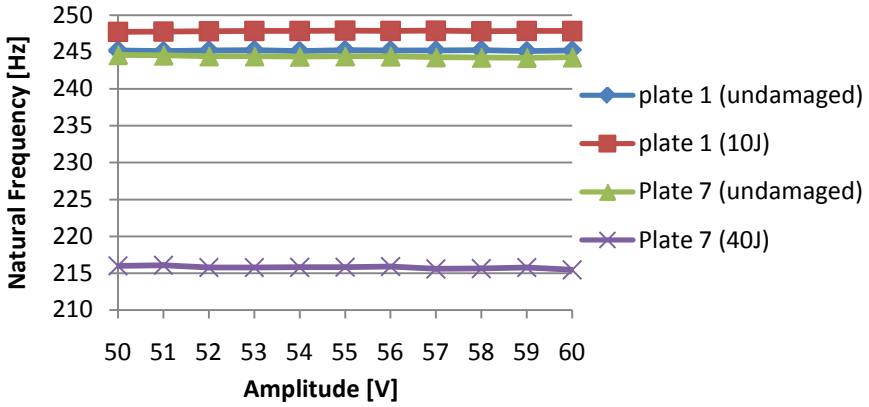


Figure 4.17: Comparison of experimental natural frequencies of the composite specimen after different impact energy for (a) 2nd and (b) 3rd vibration mode.

Damping estimation analysis was performed in the next step for the two vibration modes. The results of damping change against various impact energy levels are shown in Figure 4.18. The results do not show an increasing trend for the 2nd vibration mode. On the other hand, dramatically increasing damping changes were observed for mode 3 after the 20J impact test. Severe damage under the torsion mode may enhance mechanical damping by frictional sliding.

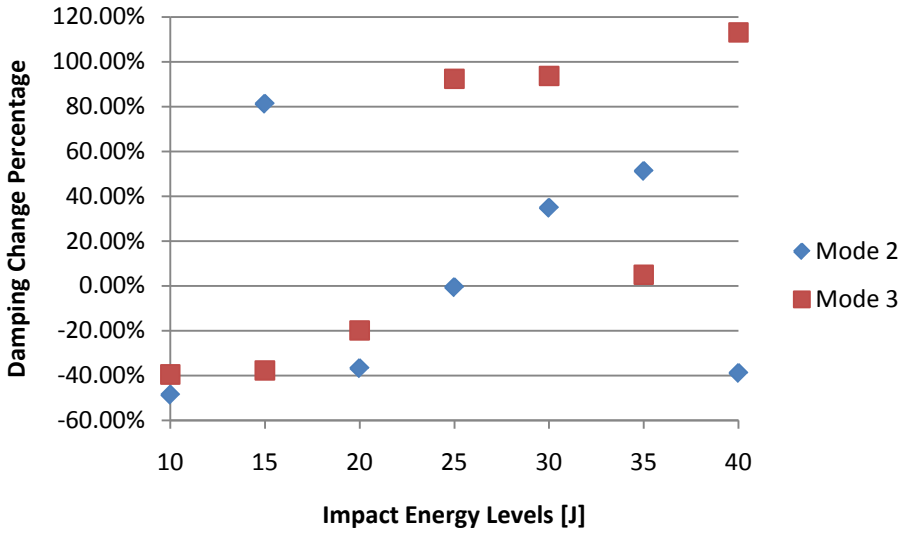


Figure 4.18: Comparisons of damping changes with various impact energies for (a) 2nd and (b) 3rd vibration mode.

### 4.1.5.3 Combined vibro-acoustic excitation

The zoomed power spectra in Figure 4.19 reveal that the frequency spacing of sidebands corresponds to the low-frequency modal excitation, as expected. Although, some sidebands can be observed for the undamaged plate, their numbers and amplitudes increase clearly after the 25J impact test.

(a)

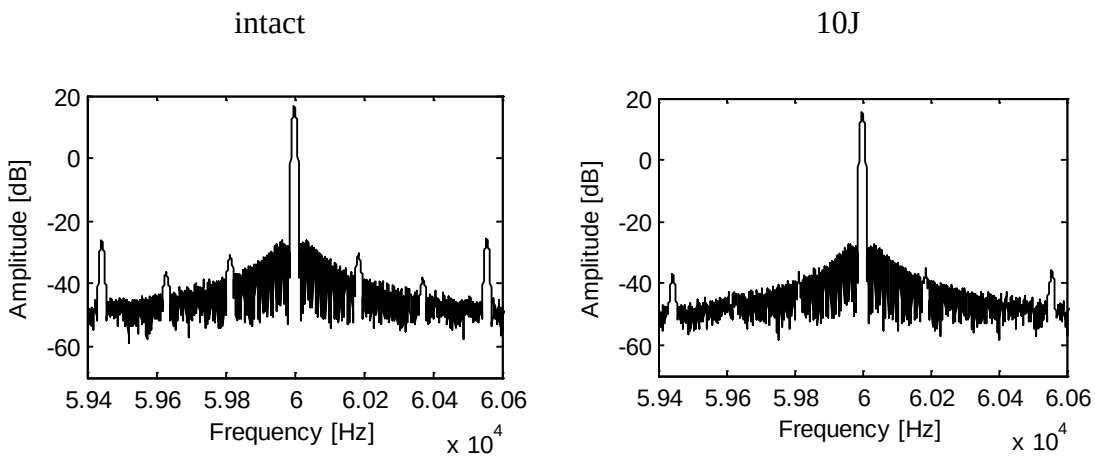

intact

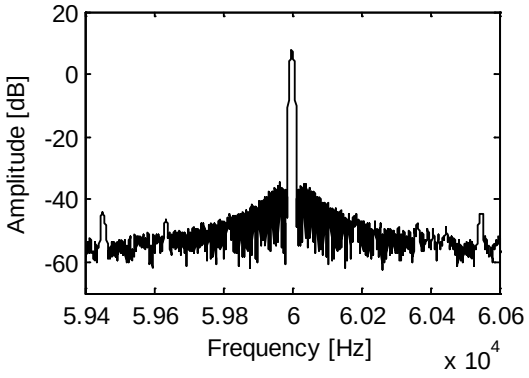


15J

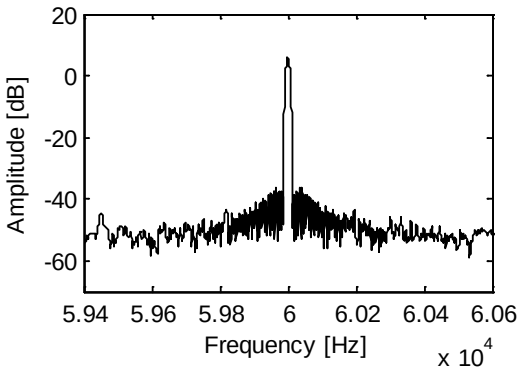


intact

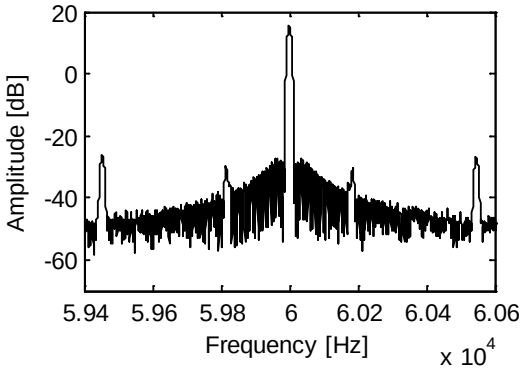


20J

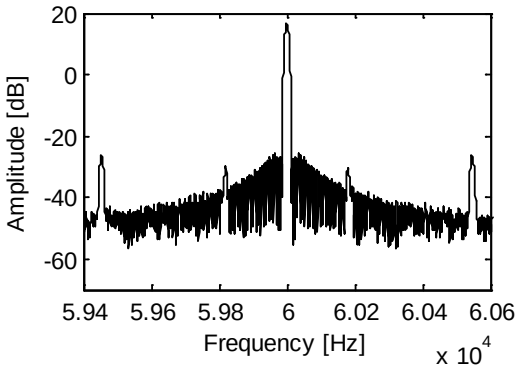


intact

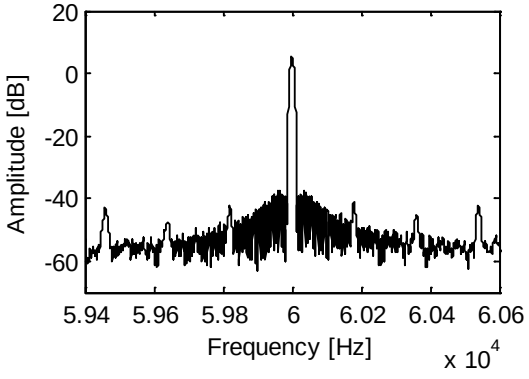


25J

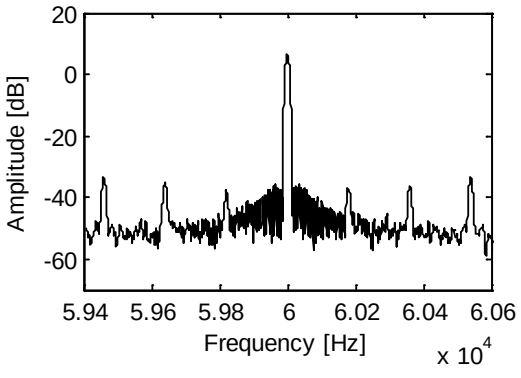

intact

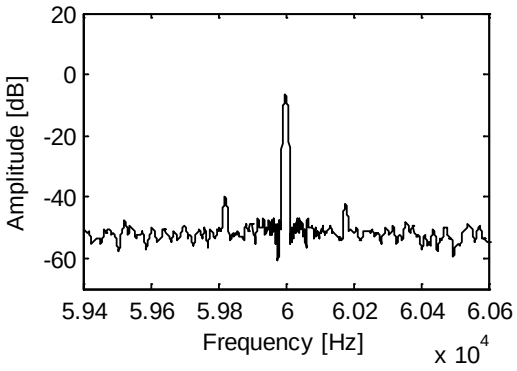


30J

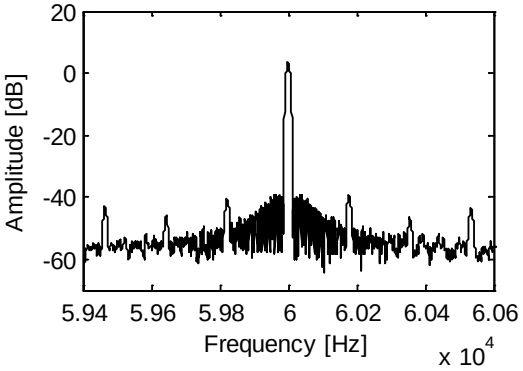


intact

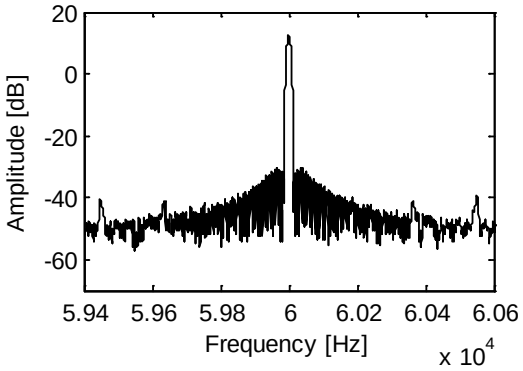


35J

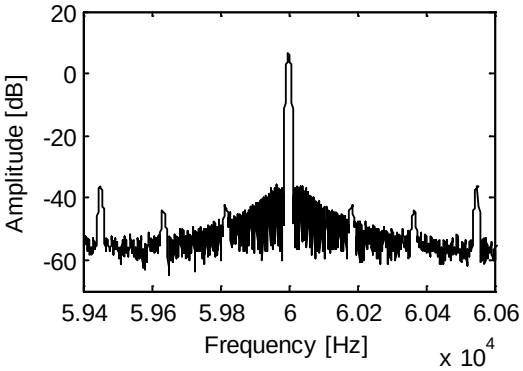


intact

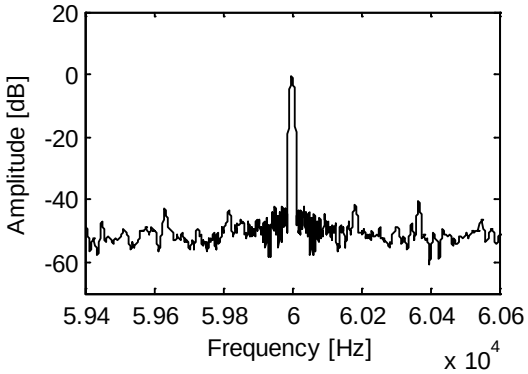


40J

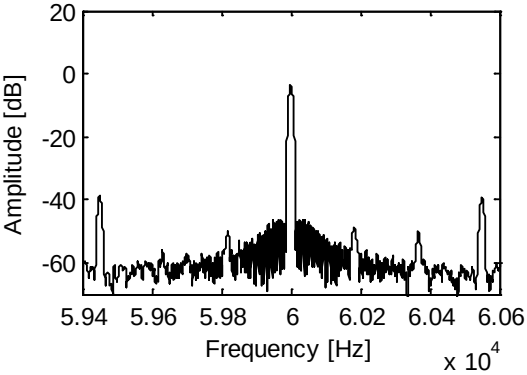

(b)

intact

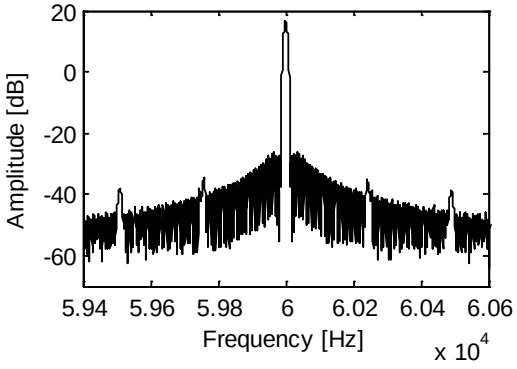


10J

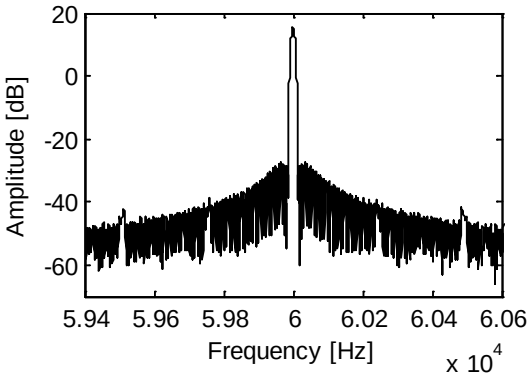


intact

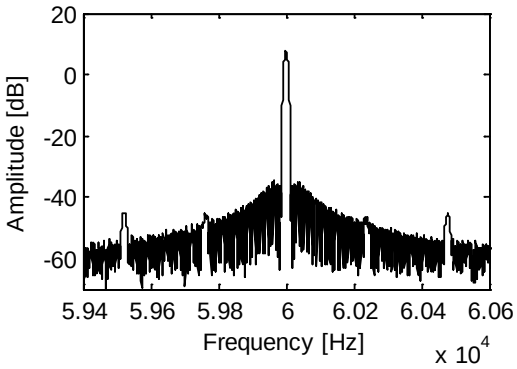


15J

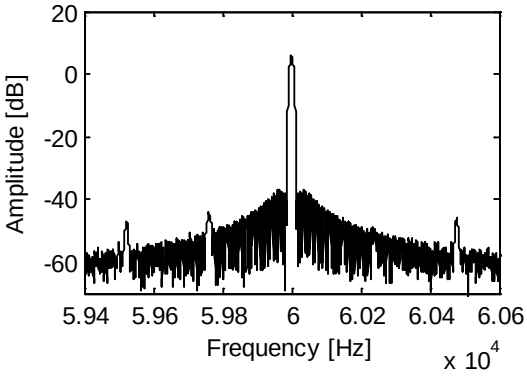


intact

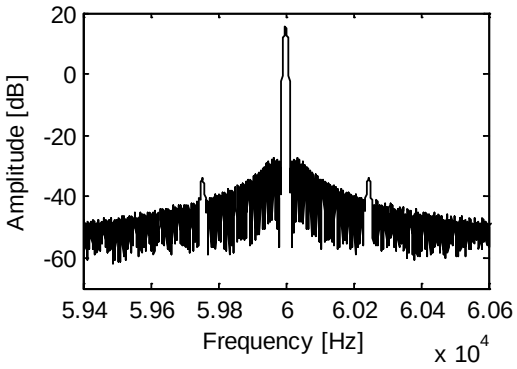


20J

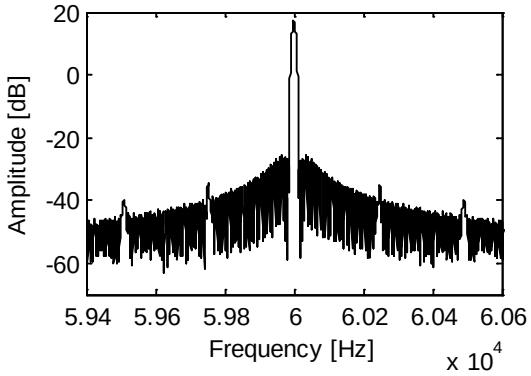

intact

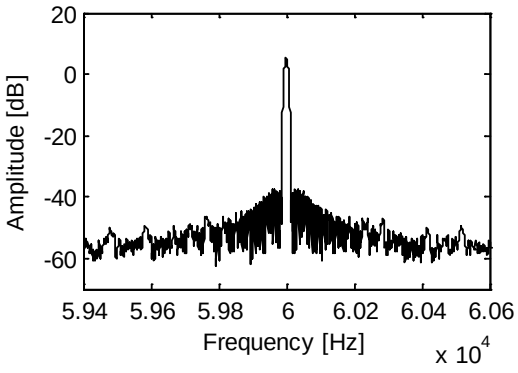


25J

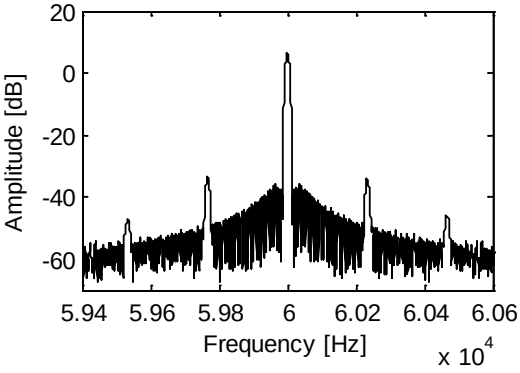


intact

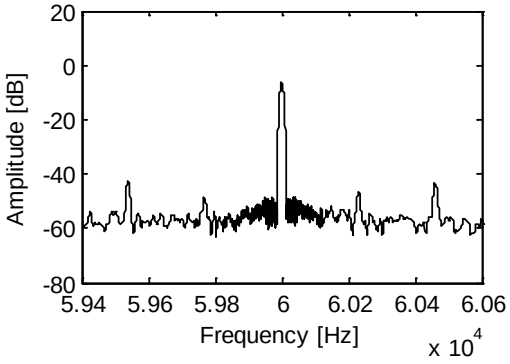


30J

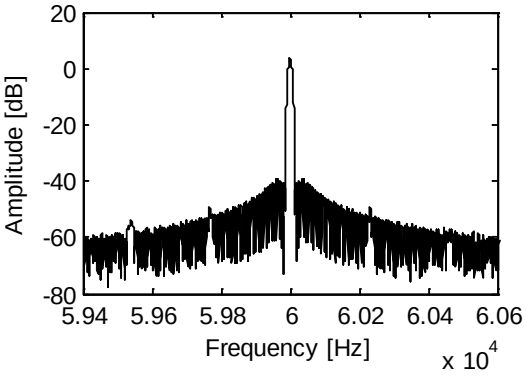


intact

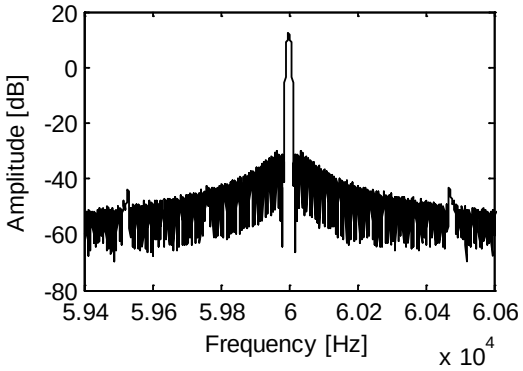


35J

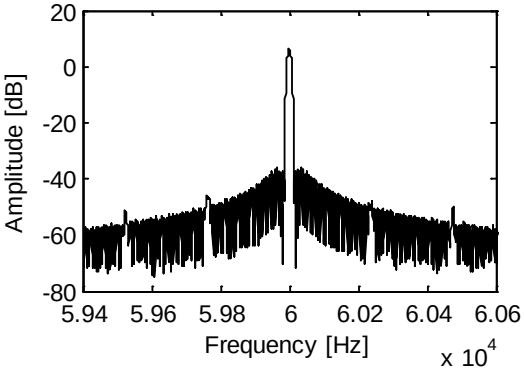

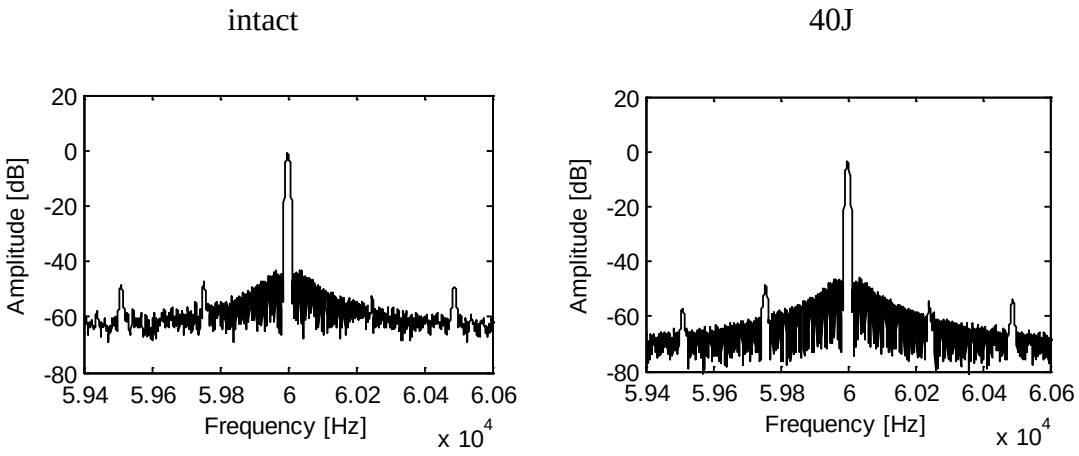


Figure 4.19: Zoomed power spectra from vibro-acoustic excitation tests using (a) 2nd and (b) 3rd vibration mode. Left column: intact plate; right column: impact test plate.

The amplitude of the carrier fundamental ultrasonic frequency and the first pairs of sidebands was used to calculate the intensity of modulation parameter *R* from Equation (2-7). The *R* values for various amplitude levels of low-frequency vibration excitations are used as sample data for a hypothesis test. Figure 4.20(a) shows that the statistic test values for the 2nd vibration mode excitation are below threshold (not statistically significant) until the 20J impact test. Observed from Figure 4.20(b), the smallest detectible expected delamination for the 3rd vibration mode excitation is caused by the 25J impact test.

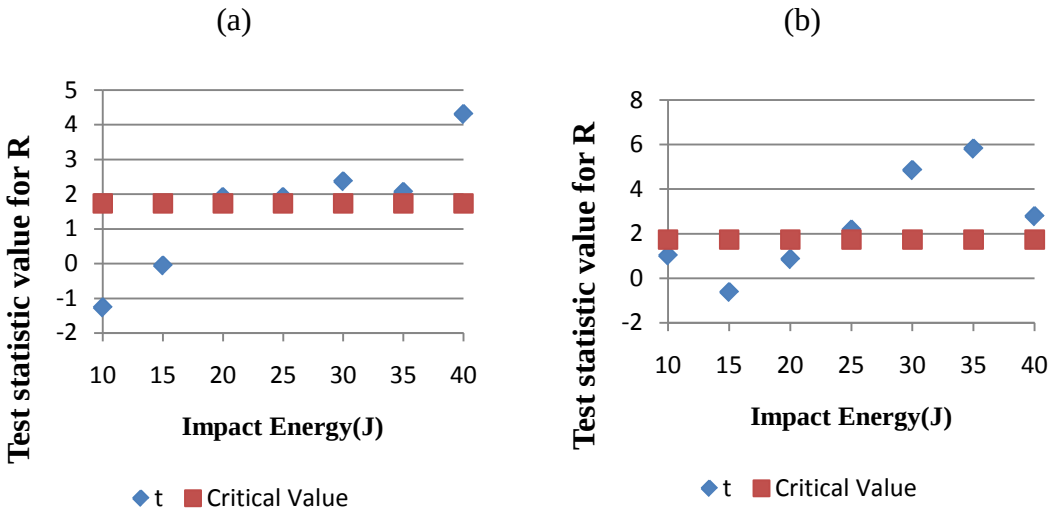


Figure 4.20: Test statistic value obtained by the vibro-acoustic method with (a) 2nd and (b) 3rd vibration mode.

### 4.1.6 Lamb wave test

In this work, two circular piezoelectic transducers were bonded to each plate to actuate and sense signals. Impact damage was introduced at the centre of the plates.

The aim of this work is to investigate the application of outlier analysis to Lamb wave data for detecting impact damage in CFRP structures and monitoring its extent.

#### 4.1.7.1 Experimental procedure for Lamb wave test

The Lamb wave input signal was a five-cycle sine wave tone burst with frequency 225kHz and a peak-to-peak amplitude of 20V modulated by a Hanning window. The response signal was sampled with a frequency of 500MHz and recorded from 15 averages. According to the Lamb wave dispersion curve for CFRP in Figure 4.21, only the fundamental $S_0$ and $A_0$ Lamb wave modes were present in the structure with the 225kHz excitation frequency. Each waveform contained a 200μs duration of data. A time lag of 10ms between pulses was introduced to avoid disturbing signals from previously recorded waveforms. A sampling window was used for eliminating boundary reflection signals, as shown in Figure 4.22. 10-dimensional features were selected from the FFT spectrum as shown in Figure 4.23.

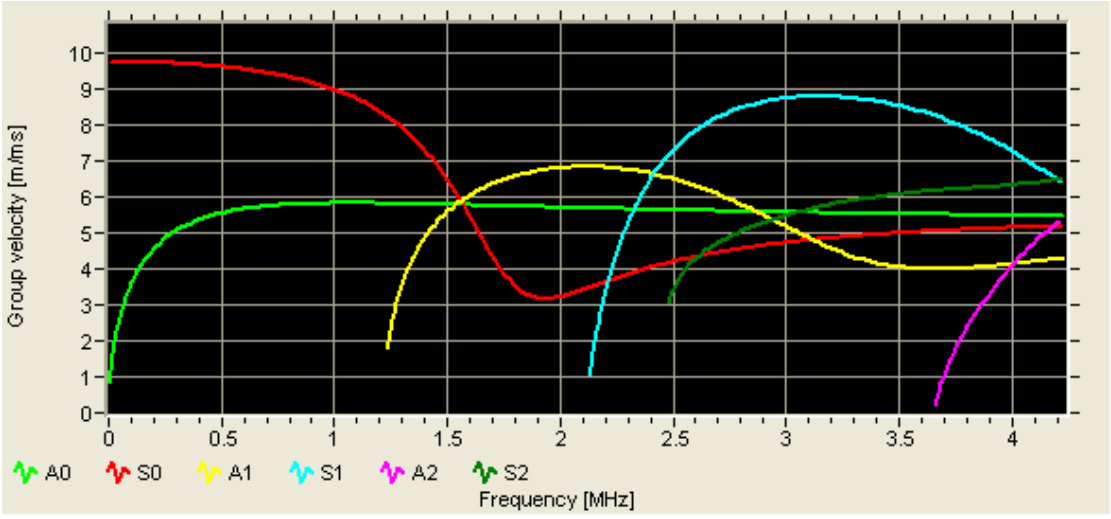


Figure 4.21: Lamb wave dispersion curves for CFRP with thickness 2mm.

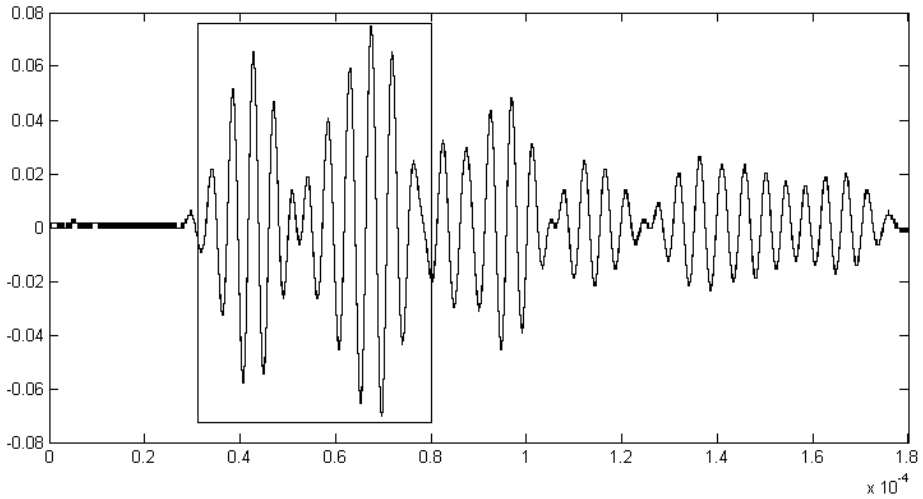


Figure 4.22: Outlier analysis sampling window of Lamb wave response.

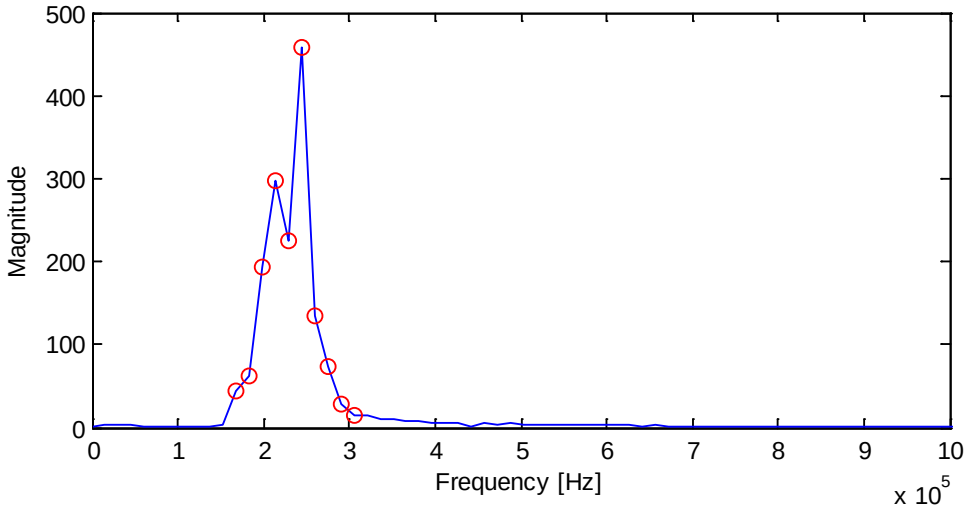


Figure 4.23: 10-dimension feature selected from frequency spectrum.

In order to get a benchmark of what the undamaged condition looked like, two sets of data were taken from the undamaged plate: 50 Lamb wave observations were taken as a 'healthy set' and a further 50 observation were chosen as a 'test set'. The healthy set was used to calculate the mean and covariance data needed for Equation (2.23) and the test set was applied for outlier analysis. This procedure gave confidence that outlier analysis could successfully classify undamaged samples as undamaged.

For each of the 7 damage levels, 50 observations were taken later. The 1% exclusive outlier threshold value for a 50 observation, 10-dimensional problem was found to be 50.1 after 1000 Monte Carlo trials of the algorithm.

### 4.1.7.2 Experimental results and discussion

The results obtained by outlier analysis are shown in Figure 4.24 with a logarithmic vertical scale. The results indicate successful classification for undamaged and damaged data. That means the undamaged data are all lying below the threshold level (red line) and are classified as 'inliers' while all the damaged data are significantly above the damage detection threshold and are categorised as 'outliers'. In addition, the MSD values slightly fluctuated from the 10J to 15J impact energy and then rose gradually to the 30J impact energy and finally dropped and remained stable for the 35J and 40J impact energy levels. Thus, outlier analysis does not give a monotonic increase in MSD value with increasing energy level. This may be caused by testing on different composite plates. Each plate has its unique intrinsic properties due to manufacturing processes. This means severity assessment is not available in this case.

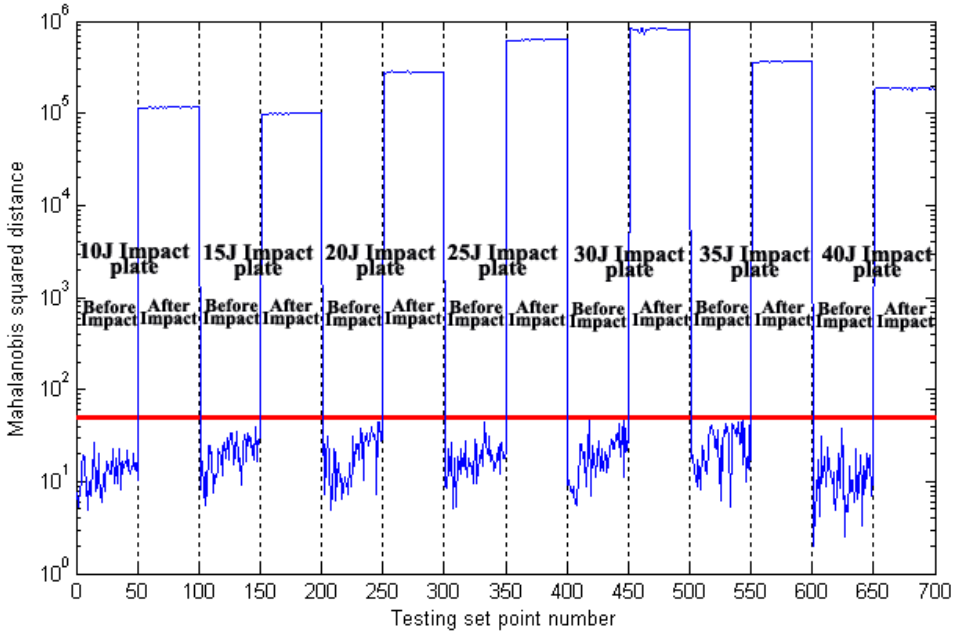


Figure 4.24: Outlier analysis classification results with logarithmic scales.

## 4.2 Damage detection on a composite laminate during a compression test

In this work, a CFRP with a stringer was investigated. The testing structures were

provided by Spirit AeroSystems (Europe) Ltd. Compression tests were performed at the *Advanced Manufacturing Research Centre* (AMRC). The CFRP was clamped at both ends. Two circular piezoelectic transducers were bonded to this plate to actuate and sense signals. Lamb waves were applied for detecting damage during the compression test. The test specimen underwent a compression test with the load starting at 5kN and increasing until the plate failed. The first test specimen ASTC-247-C failed at the base of the panel. However, the main concern of the failure mode is the delamination of the stringer during the test activity. For this reason, extra metal components were clamped to the base of test specimen ASTC-247-D to enhance the strength of the base. The aim of this work is to investigate the application of outlier analysis for detecting damage in the composite structures during the compression activity and monitoring its progress.

### 4.2.1 Experimental arrangements and procedure for Lamb waves test

A rectangular $750 \times 460 \times 6.5$ mm composite was used as a test structure. The plate was instrumented with two low-profile, surface-bonded piezoelectric transducers (PI Ceramics PIC155, diameter 10mm, thickness 0.5mm). A HBM-X60 2-component fast curing glue was used to attach the transducers. These transducers were used for ultrasonic wave excitation and for all response sensing. Figure 4.25 shows the transducer locations.

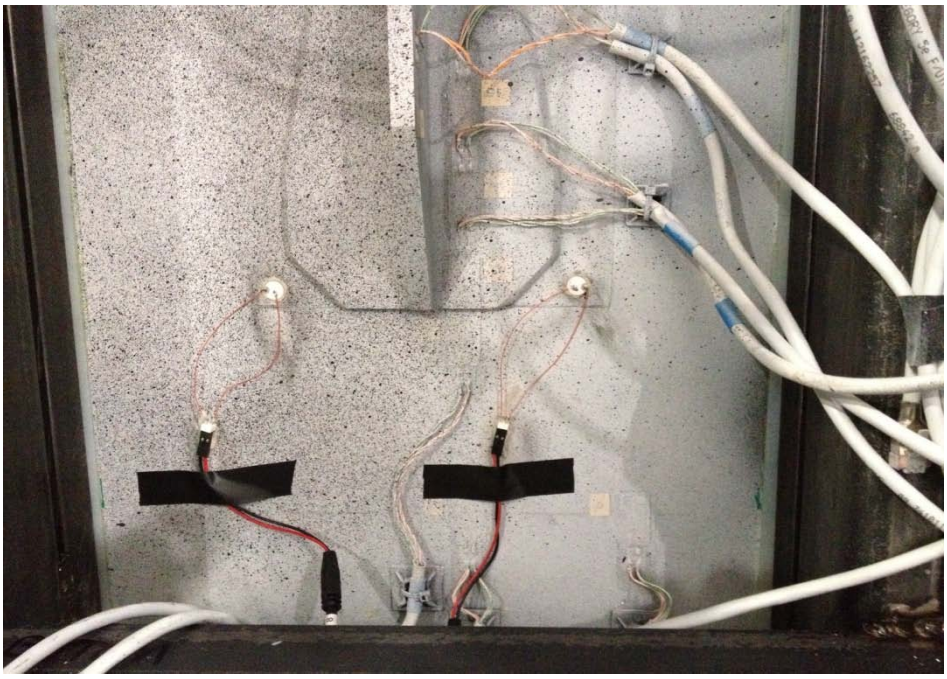

Figure 4.25: The arrangement of transducers.

An INSTRON 1000kN universal testing machine was used to compress the composite panel. The compression force started at 5kN and stopped when the panel failed. Figure 4.26 shows gross delamination of the stringer from the composite panel for the test case ASTC-247-D.

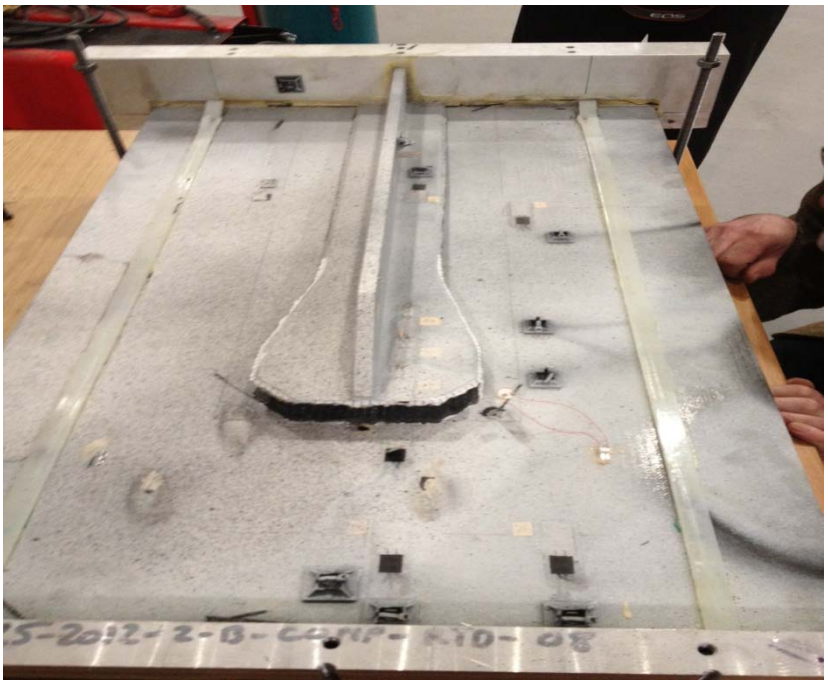

Figure 4.26: Delamination of composite plate (ASTC-247-D).

Lamb wave signals were generated using a two-channel TTi-TGA 1242, 40MHz arbitrary waveform generator. Signal responses were acquired using a four-channel LeCroy Waverunner LT264, 1Gs/s digital oscilloscope.

The Lamb wave input signal was five cycles of a sine wave with frequency 225kHz and peak to peak amplitude of 20V modulated by a Hanning window. The response signal was sampled with a frequency of 500MHz. According to the Lamb wave dispersion curve in Figure 4.27, only the fundamental $S_0$ and $A_0$ Lamb wave modes were present in the structure with the 225kHz excitation frequency. Each waveform contained a 200μs duration of data. A time lag of 15ms between pulses was introduced to avoid disturbing signals from previously recorded waveforms. A sampling window was used for eliminating boundary reflection signals, as shown in Figure 4.28.

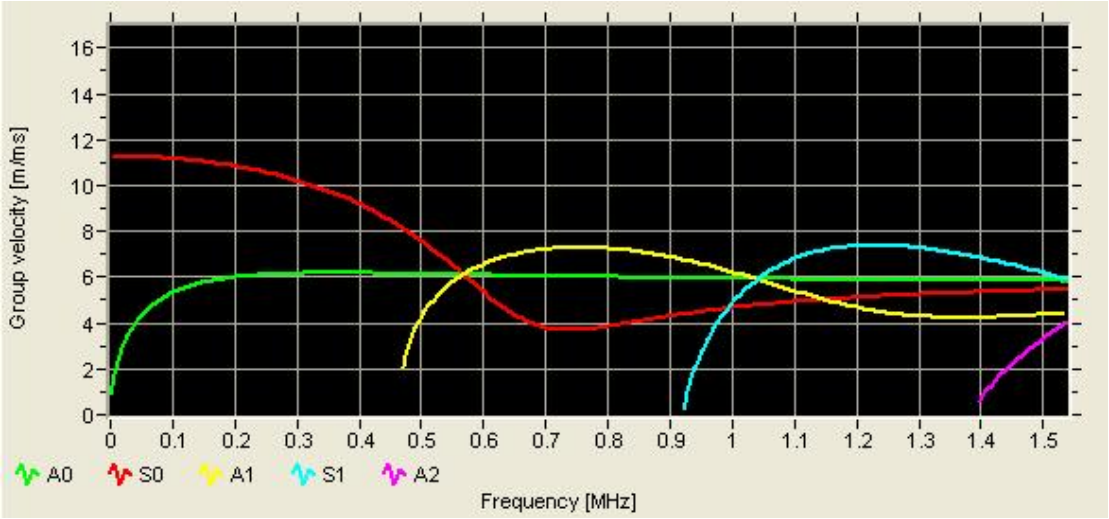


Figure 4.27: Lamb wave dispersion curves for composite with thickness 6.5 mm.

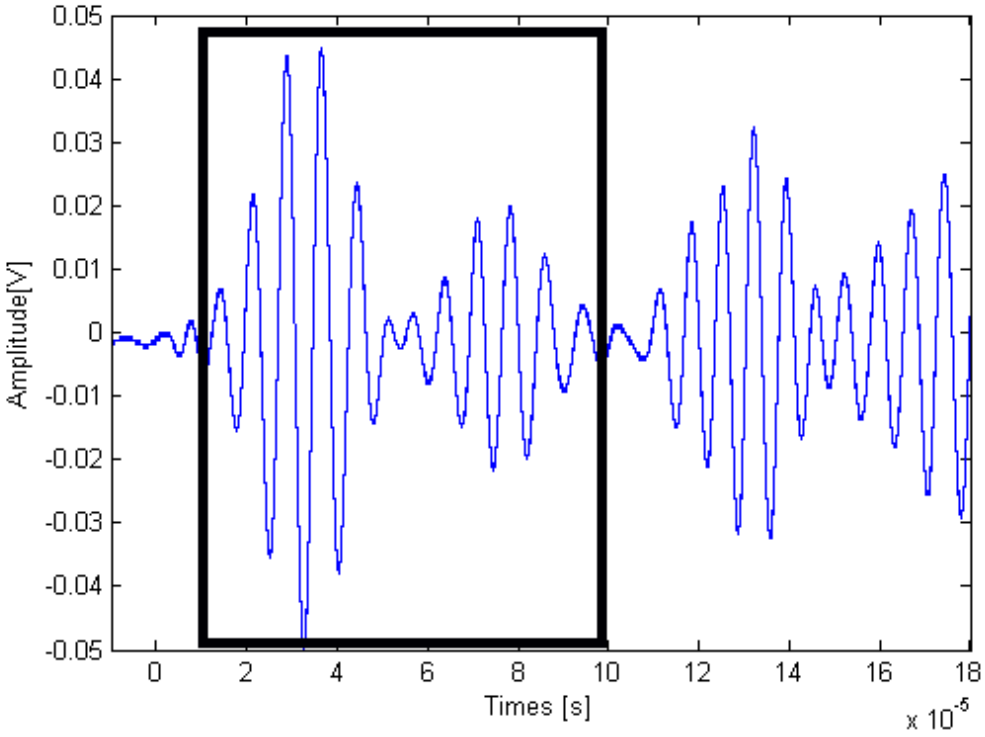


Figure 4.28: Outlier analysis sampling window of Lamb wave response.

In order to get a benchmark of what the undamaged condition looked like, two sets of data were taken from the undamaged plate: 50 Lamb wave observations were taken as a ' training set ' and a further 50 observation were chosen as a ' test set '. The training set was used to calculate the mean and covariance data needed for Equation (2.23) and the test set was applied for outlier analysis. This procedure gave confidence that outlier analysis could successfully classify undamaged samples as undamaged.

For the ASTC-247-D compression test, 62 observations were taken. The 1% exclusive threshold value for a 50 observation, 10-dimensional problem was found to be 62.5 after 1000 Monte Carlo trials of the algorithm.

### 4.2.2 Experimental results and discussion

The results for ASTC-247-D obtained by outlier analysis are shown in Figure 4.29 with a logarithmic vertical scale. The results indicate successful classification for undamaged and damaged data. That means the undamaged data are all lying below

the threshold level (red line) and are classified as 'inliers' while all the damaged data are significantly above the damage detection threshold and are categorised as 'outliers'. In addition, The MSD values for the loading test are steady increasing above the threshold between testing set point 51 and 77 (5kN-320kN). This may be caused by steadily increasing matrix cracking. Moreover, a sudden jump at testing set point 78 (331kN) could be initial delamintation of the stringer from the panel and the delamination growth until testing set point 99 (532kN). Furthermore, an abrupt jump occurs at testing set point 100 (540kN) which may manifest gross delamination. Finally, the data recording work stopped at point 112 (around 645kN) before noticing the first failure sound.

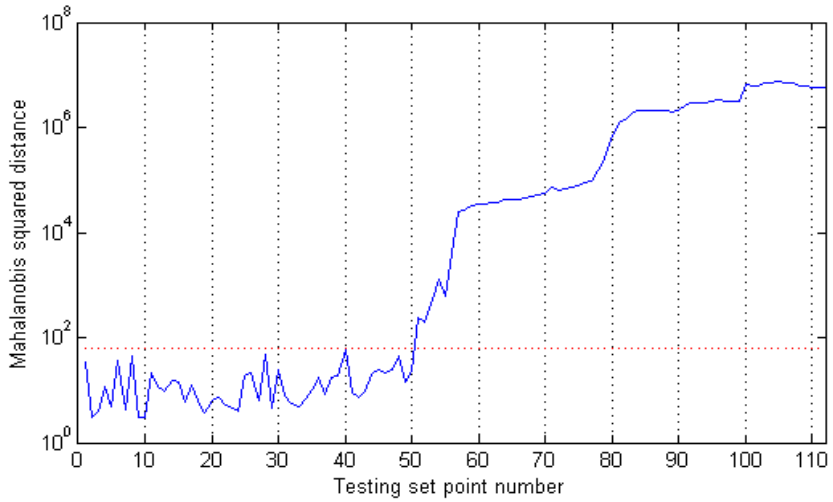


Figure 4.29: Outlier analysis classification results with logarithmic scales for case ASTC-247-D.

The results for the ASTC-247-C test obtained by outlier analysis are shown in Figure 4.30 with a logarithmic vertical scale. This experiment did not create gross delamination during the compression test and the first failure was at the base of the panel. Observed from the results, the undamaged data are all lying below the threshold level (red line) and 97% of damaged data are significantly above the damage detection threshold. A slight increase of MSD occurs at testing set point 77 (308kN) and is followed by fluctuation. This could be an initial delamintation of the stringer from the panel. However, significant changes of the MSD after testing set point 77 do not happen in this case due to prior failure of the base.


Figure 4.30: Outlier analysis classification results with logarithmic scales for case ASTC-247-C.

## 4.3 Conclusion

This chapter comprises analysis of impact tests and compression tests on CFRP structures.

The use of nonlinear acoustics for impact damage detection and assessment in CFRP was investigated. The work was mainly focused on single wave excitation and vibro-acoustic excitation and various FRFs. The 2$^{nd}$ and 3$^{rd}$ vibration modes were selected for low-frequency modal excitation. An impact test was performed to introduce damage in the centre of the plate. Various nonlinear symptoms in the signal response were examined to find possible physical mechanisms.

A number of important conclusions can be summarised from the experimental work undertaken. Two different nonlinear phenomena were observed: (a) the dissipation mechanism related to damage-wave interaction and (b) nonlinear elasticity. According to experimental results, the intensity of modulation, $R$, for the 2$^{nd}$ and 3$^{rd}$ vibration modes of excitation were good for damage detection. Meanwhile, the frequency shift did not reveal any useful information. In addition, the damping estimation analysis

was effective to detect damage for the torsion mode. For single wave excitation, the 2nd and 3rd vibration modes showed good results. Further work should investigate the sidebands and harmonics in undamaged specimens. It is required to explain intrinsic nonlinearities due to material, boundary effects or instrumentation.

The applications of outlier analysis for impact and compression damage detection in composite plates were investigated. Piezoelectric transducers have been used for introducing and receiving Lamb wave signals.

For the impact damage detection, damage in the centre of the plate was imposed by a drop test rig. The outlier analysis method successfully classifies damage with a 100% rate. However, the results did not exhibit a trend of monotonically increasing MSD values, hence outlier analysis was not able to give an indication of damage severity in this case.

For the compression damage detection, delamination of the stringer from the panel was generated by a compression using a INSTRON 1000kN universal testing machine. The outlier analysis method successfully classifies damage. Meanwhile, the results exhibited a trend of increasing MSD values for monitoring the initiation and growth of delamination; hence outlier analysis was able to give an indication of damage severity in this case. Further investigations are required to confirm the findings. The effect of transducer position should also be considered. It is also important to increase the number of measurements if possible due to employment of the statistical method.

# Chapter 5

# 5 Damage detection in a laboratory wind turbine blade

## 5.1 Introduction

Wind is a clean source of renewable energy that has been used for energy resource for more than a thousand years. Typical example is the windmill that converts wind energy to rotational energy. Since the growing fossil fuel crisis started in the 1970s, the energy prices have been dramatically increased [153]. In addition, global environmental issues have drawn a lot of attention. Concerning about the environmental threats and the rising energy prices, commercial wind turbines were introduced in 1980 [154]. In general, a wind turbine converts the kinetic energy of wind into electrical energy [155-156]. As mentioned by Jha [156], a wind turbine is designed for producing vast amounts of energy with eco-friendly effect compared to other energy resources. However, the operation and maintenance cost of a wind turbine cannot be ignored. According to Verbruggen's research [157], the operation and maintenance cost takes up 30%-35% of total cost of a wind turbine. One effective way is to reduce the life cycle costs and to extend the life of wind turbine structure by the application of structural health monitoring.

It is widely accepted that CFRP based wind turbine blades are susceptible to low velocity impact damage. The low velocity impact often causes internal damage and is hardly detected by eye. This damage although small, may lead to more severe damages and eventually failure without warning. This work presents damage detection on an impacted wind turbine blade by using modal analysis, nonlinear acoustics and Lamb waves. The LMS test lab system was used to extract the modal

parameters from experimental test of the blade with a fixed-free boundary condition.

## 5.2 Experimental modal analysis

The experimental modal analysis was performed orignally for a different project. The modal parameters, such as frequency and mode shape, were obtained by LMS Test.Lab and then the results would be used for nonlinear acoustic tests.

The wind turbine blade was placed on a test platform in a fixed-free configuration. As shown in Figure 5.1, the root of blade was clamped by a metal construction by using four bolts. A LDS V406 shaker was used to excite the blade, and thus the input for the FRFs was perpendicular to the direction of the blade surface.

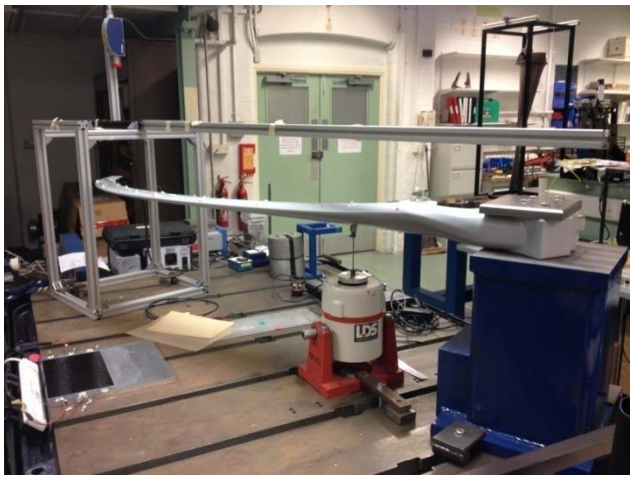


Figure 5.1: The geometric boundary condition of the wind turbine blade.

26 ICP (integrated circuit-piezo electric) unidirectional accelerometers of the PCB type were attached on the blade surface in order to measure the dynamic response of the structure. The arrangements of accelerometers are schematically shown in Figure 5.2.

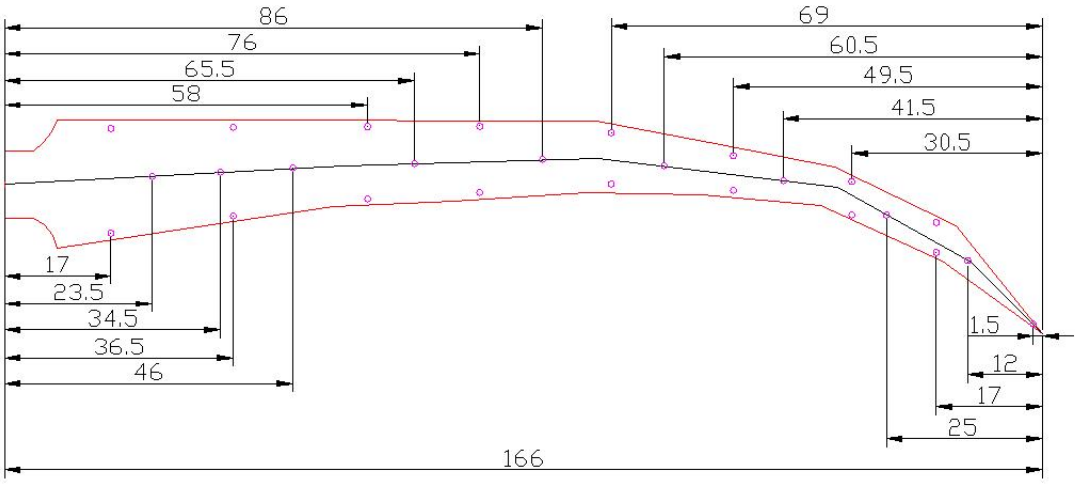


Figure 5.2: The distribution of 42 measurement points on the testing blade. The circles mark the accelerometer location.

The LMS SCADAS III system was used to acquire the testing data. The sampling frequency was set at 1024Hz with a resolution of 0.125Hz. The Polymax modal parameter estimation algorithm was used for the extraction of the frequencies and mode shapes of the blade. An example of an extracted FRF is shown in Figure 5.3

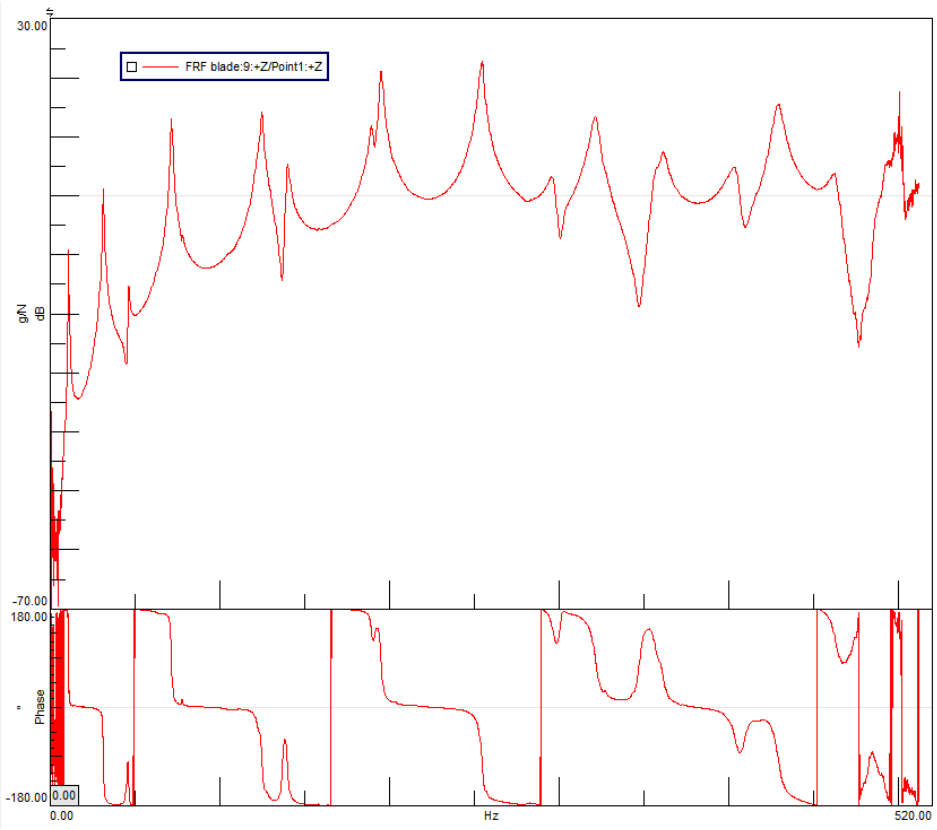


Figure 5.3: Figure 5.3: Plot of Extracted FRF from modal analysis.

The first 10 vibration modes are presented in Table 5.1.

Table 5.1: The first 10 modes of the blade, as measured by the LMS system.

| | Mode | | | | | | | | | |
|---|---|---|---|---|---|---|---|---|---|---|
| | 1 | 2 | 3 | 4 | 5 | 6 | 7 | 8 | 9 | 10 |
| Frequency (Hz) | 10.5 | 31 | 45.6 | 71.5 | 124.5 | 140.4 | 195.3 | 254.2 | 279.5 | 320 |

In the current study, the 3$^{rd}$ bending mode (4$^{th}$ vibration mode) was chosen for the low frequency excitation. The mode shape for the 4$^{th}$ vibration mode is shown in Figure 5.4; the eigen-frequency for the mode is 71.47Hz.

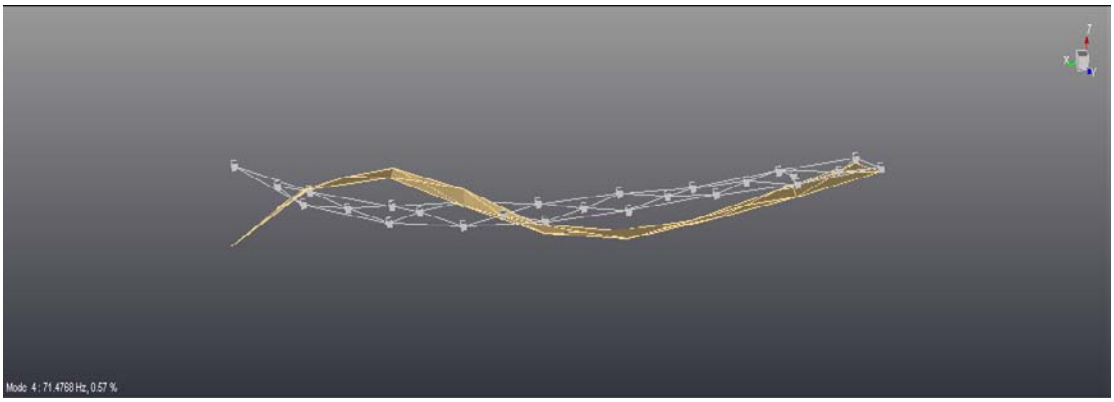


Figure 5.4: 4$^{th}$ vibration mode obtained by LMS system. The gray frame lines represent the undeformed states.

Based on the mode shape of the blade, the low frequency excitation points were allocated on the blade. In order to eliminate the effect of wave energy dissipation over long distance, the blade was divided into four parts and each part has a stack actuator (PI ceramic PL-055.31) used for low frequency excitation. Meanwhile, four PZTs (PI ceramic PIC155 transducers) around the centre stack actuator were employed for sensing and exciting high frequency signals. The placement of sensors is schematically shown in Figure 5.5.

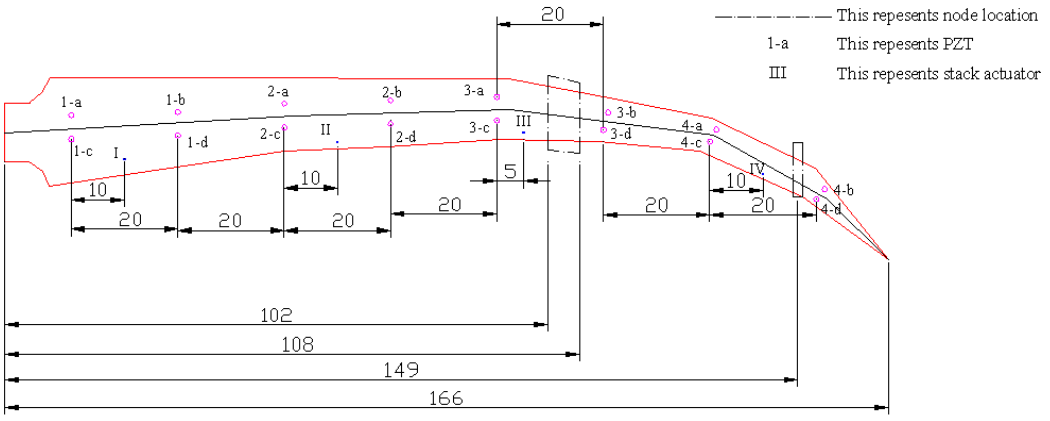


Figure 5.5: Schematic of the location of the sensors. The red circles represent the PZTs. The Roman numbers represent the stack actuators. The dash dot line areas manifest the nodal locations.

A swept sine signal, starting at 1Hz and increasing up to 500Hz in 2s was used to excite the intact blade. However, it found that the dynamic response for the 4th vibration mode was extremely weak when the swept sine signals were excited at positions I , III and IV . The reason is that these excitation locations are close to nodal points and constraints (it can also be considered as nodal point area). Although 71.5 *Hz* may not be the ideal excitation frequency at position I , III and IV some particular modes are dominant at these position, e.g., the $8^{th}$ vibration mode (257.5Hz) for position I , $6^{th}$ vibration mode (141.2Hz) for position III and $10^{th}$ vibration mode (308.6Hz) for position IV . The mode shapes for these three modes are shown in Figure 5.6.

(a)

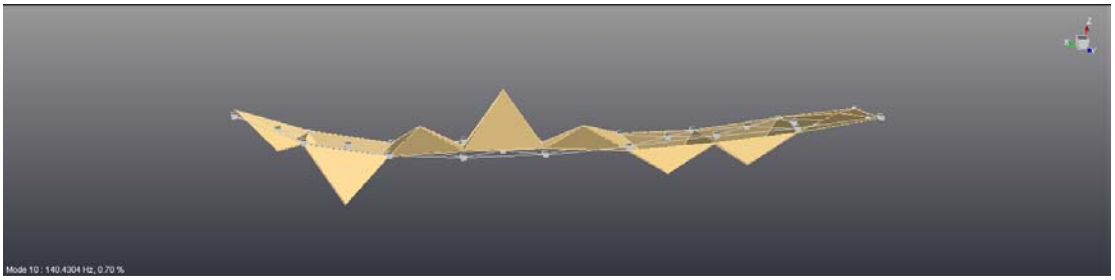

(b)

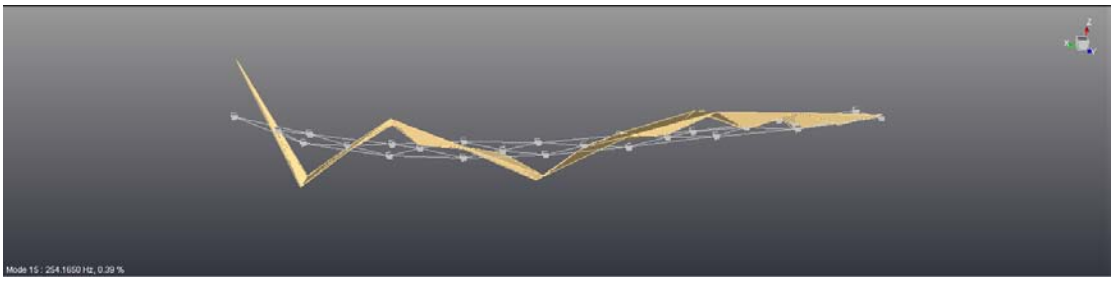

(c)

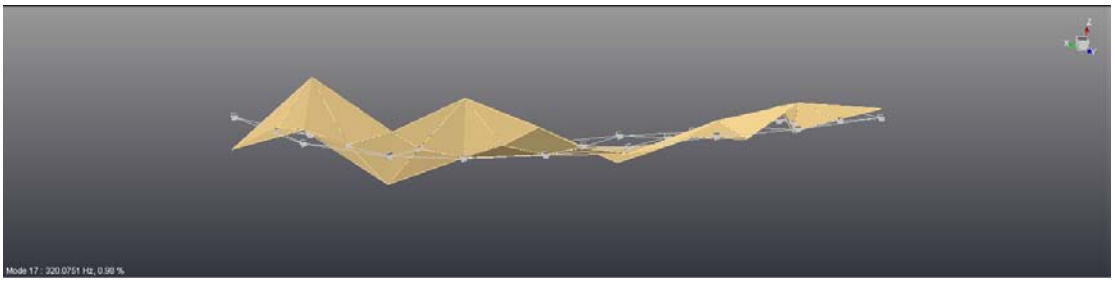

Figure 5.6: Mode shapes for (a) 6$^{th}$ mode, (b) 8$^{th}$ mode and (c) 10$^{th}$ mode. The gray frame lines represent the undeformed states.

## 5.3 Experimental procedure for nonlinear acoustic tests

The experimental procedure is similar to Section 3.1.3. The performance of the test has been divided in four sections with various low frequency excitations as mentioned in Section 5.1.1. The arrangement of high frequency, low frequency excitation transducers and signal receiving sensors are shown in Figure 5.7.

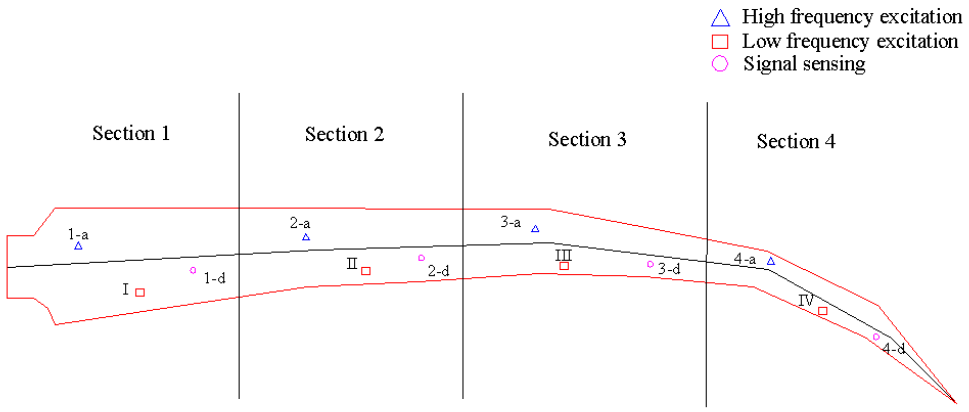


Figure 5.7: The arrangement of sensors. Blue triangle represents a high frequency excitation transducer. Red rectangle represents a stack actuator. Pink circle represents a receiving sensor.

A single impact hammer (Model: 086D20) integrated with PCB piezotronics was used to produce the impact damage and record the contact force. The target strike area is shown in Figure 5.8. The test blade was only constrained at the root and there was no support underneath the strike area. The contact force was recorded as 2247.3N.

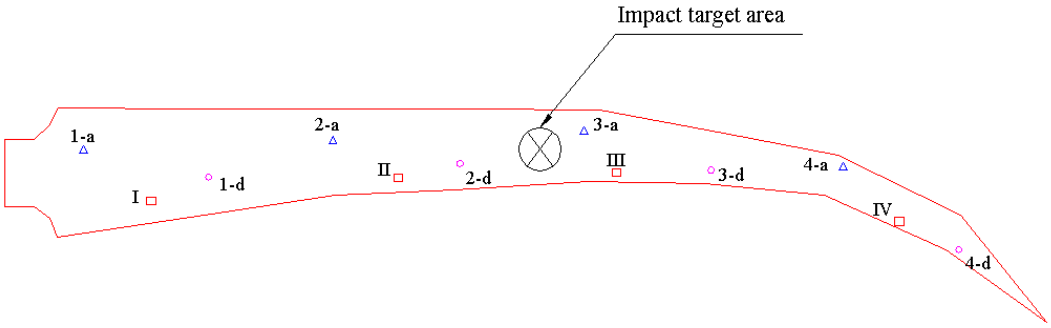


Figure 5.8: The target impact area.

## 5.4 Experimental results and discussion

Figure 5.9 shows examples of power spectra from single-wave excitation tests using the $8^{th}$, $4^{th}$, $6^{th}$ and $10^{th}$ vibration modes for test sections 1, 2, 3 and 4, respectively. Two different plate conditions are analysed, i.e. the intact blade and the damaged

blade with damage introduced by the hammer. A clear pattern of higher harmonics can be observed in all analysed spectra, even for the undamaged blade. It is clear that the magnitude of the second harmonics for Section 1, 2, 3 and 4 increasing 4dB, 17dB, 8dB and 7dB, respectively.

(a)

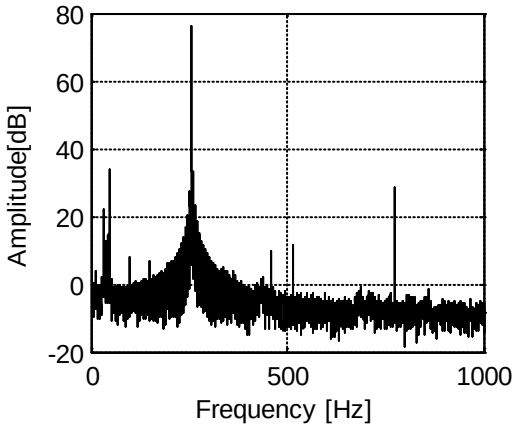


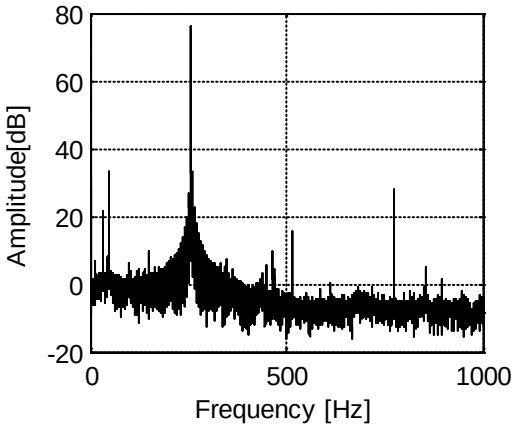


(b)

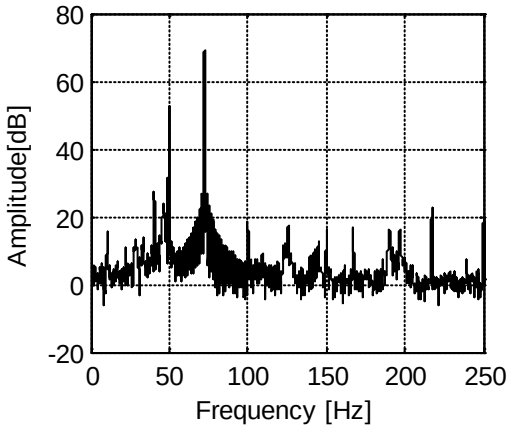


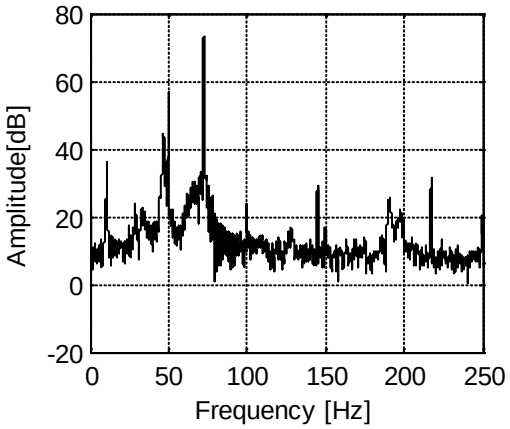


(c)

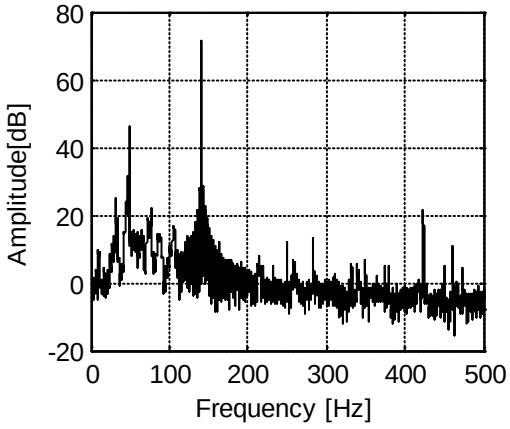


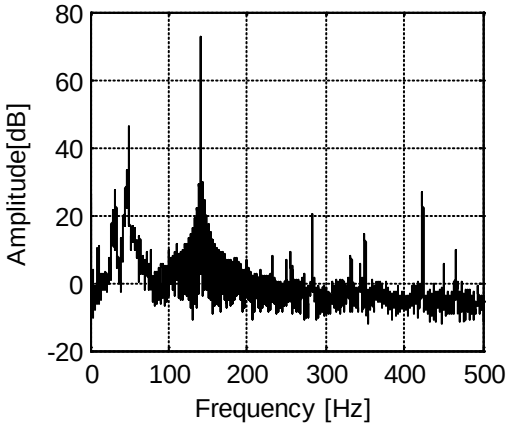

(d)

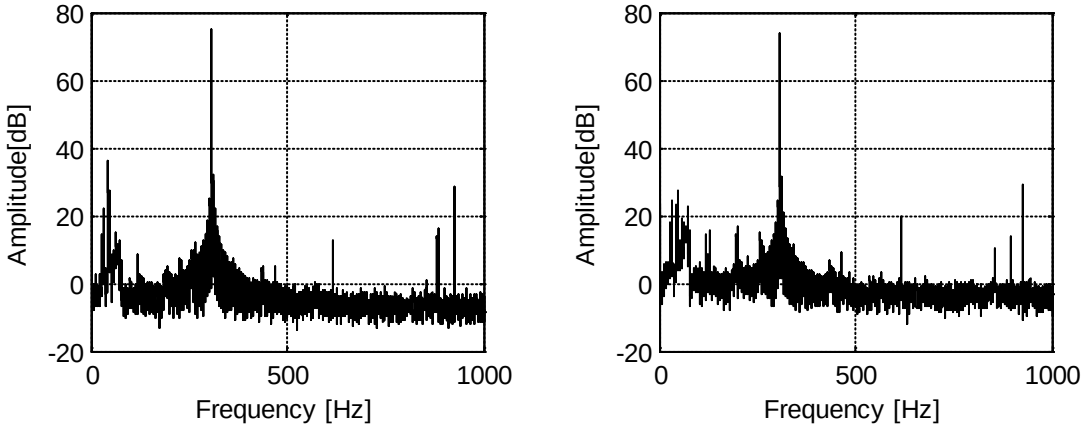


Figure 5.9: Power spectra density showing the fundamental peak and harmonics for the intact (left column) and impact (right column) blade excited by (a) 8$^{th}$ vibration mode for Section 1, (b) 4$^{th}$ vibration mode for Section 2, (c) 6$^{th}$ vibration mode for Section 3 and (d) 10$^{th}$ vibration mode for Section 4.

The Figure 5.10 gives the test statistic value for the perturbation coefficient β against the impact energy. Any test statistic value above the critical value line is considered as the nonlinearity result from damage. A statistically significant result is only found for the 4$^{th}$ vibration mode for Section 2 (Figure 5.10 b).

(a) (b)

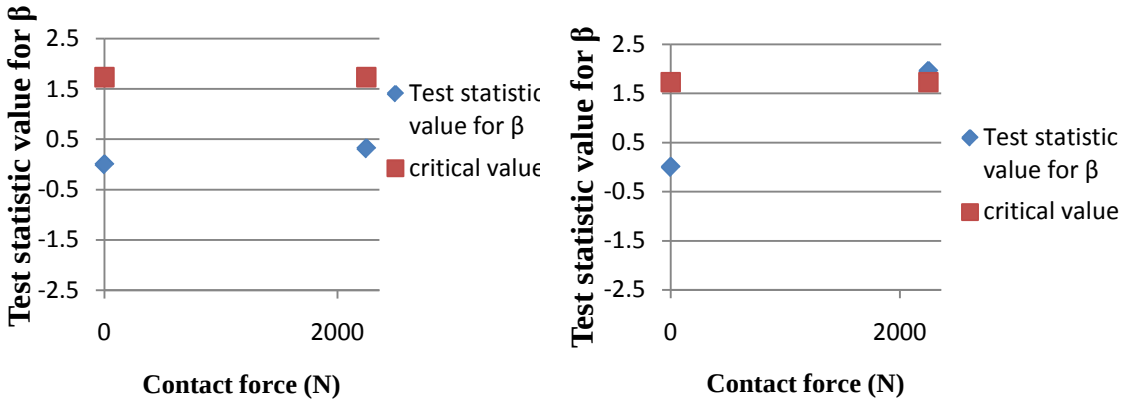

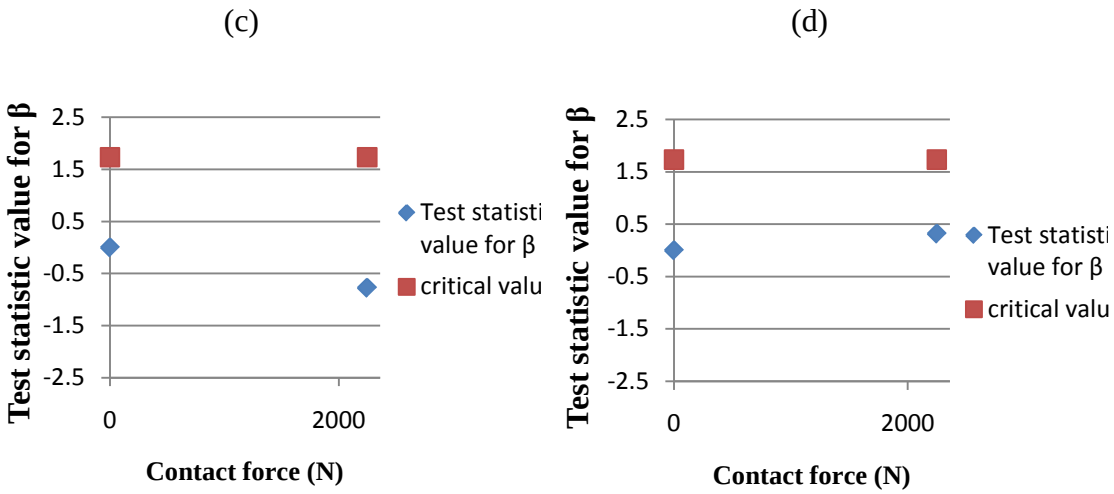


Figure 5.10: Test statistic value obtained by (a) 8th vibration mode for Section 1, (b) 4th vibration mode for Section 2, (c) 6th vibration mode for Section 3 and (d) 10th vibration mode for Section 4.

The zoomed power spectra in Figure 5.11 reveal that the frequency spacing of sidebands corresponds to the low-frequency modal excitation, as expected. Although, some sidebands can be observed for the undamaged blade and damaged blade, there is no significant change after the impact.

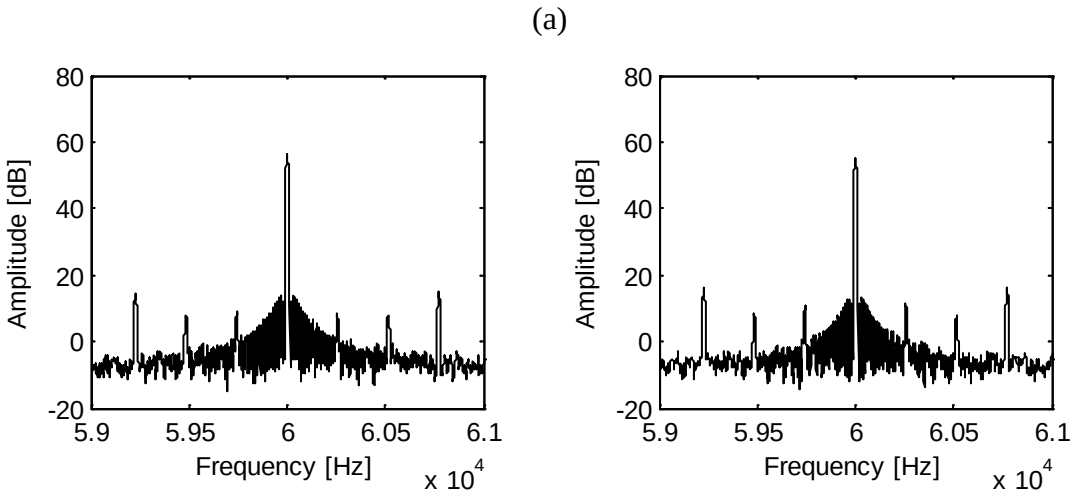

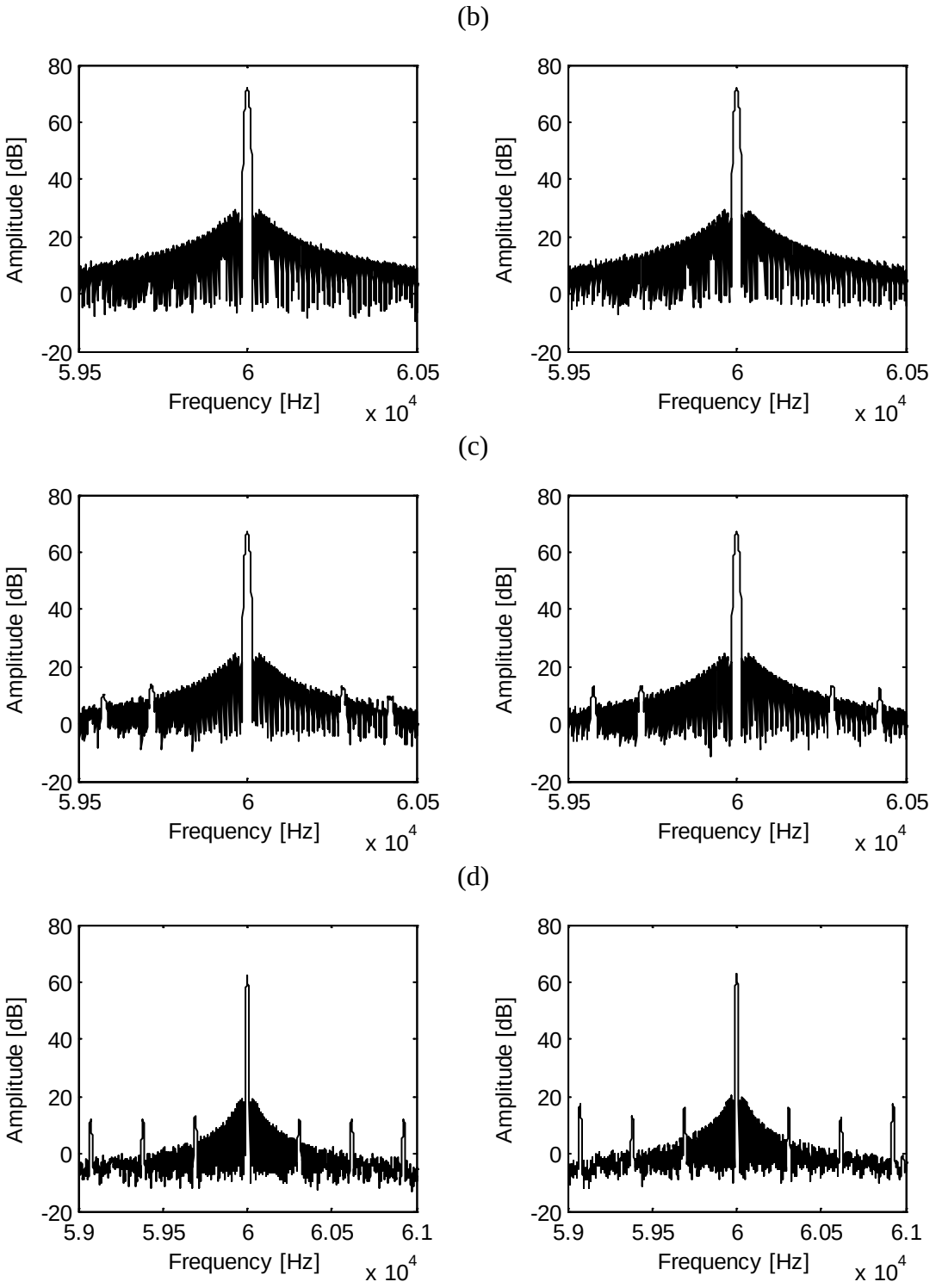


Figure 5.11: Zoomed power spectra from vibro-acoustic excitation tests using (a) 8$^{th}$ vibration mode for Section 1, (b) 4$^{th}$ vibration mode for Section 2, (c) 6$^{th}$ vibration mode for Section 3 and (d) 10$^{th}$ vibration mode for Section 4. Left column: intact blade; right column: impact test blade.

The amplitude of the carrier fundamental ultrasonic frequency and the first two pairs of sidebands was used to calculate the intensity of modulation parameter $R$ from

Equation (2-6). The *R* values for various amplitude levels of LF vibration excitations are used for sample data for a hypothesis test. Figure 5.12(a) shows that the statistic test values for all sections are below threshold. That means the results are not statistically significant in the current study. The reason for this result is that the modulation introduced energy dissipation is weak comparing to material nonlinearity in this case.

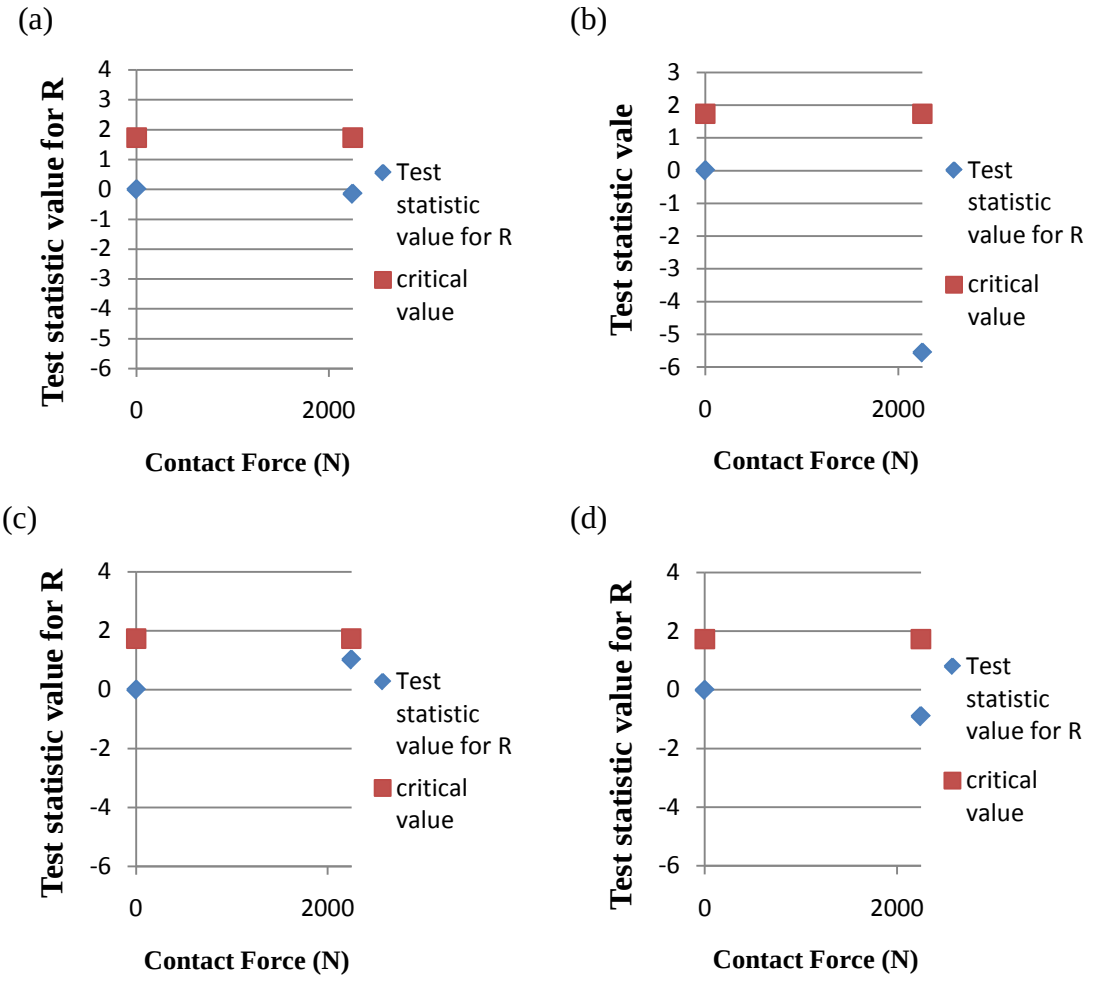


Figure 5.12: Test statistic value obtained by vibro-acoustic method with (a) 8$^{th}$ vibration mode for Section 1, (b) 4$^{th}$ vibration mode for Section 2, (c) 6$^{th}$ vibration mode for Section 3 and (d) 10$^{th}$ vibration mode for Section 4.

## 5.5 Guided wave test

In this work, seven pairs of piezoelectic transducers were bonded to the blade to actuate and sense signals. The placement of sensors is schematically shown in Figure 5.13. The arrows show the excitation-receiving relationship for sensors. The aim of

this work is to investigate the application of outlier analysis for detecting impact damage on wind turbine blades. In addition, damage localisation is another task for this study.

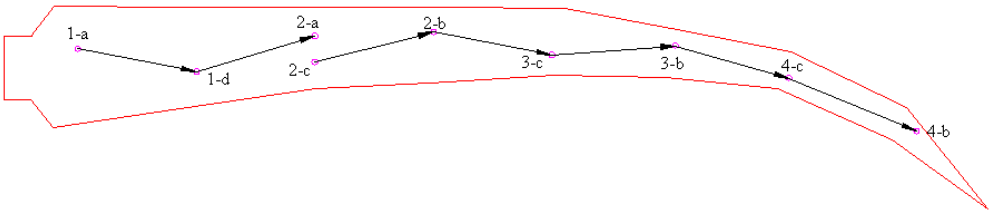


Figure 5.13: The arrangement of sensors and Lamb wave propagation direction.

### 5.5.1 Experimental procedure for the guided wave test

The first impact damage introduced by an impact PCB hammer is shown in Figure 5.8 (between 2-b and 3-c). As mentioned in Section 5.12, there was no support underneath the strike area.

The experiment set up is the same as mentioned in the previous Section 3.2.3. The guided wave input signal was a five cycle sine wave with frequency 165kHz and a peak to peak amplitude of 20V modulated by a Hanning window. The response signal was sampled with a frequency of 500MHz and recorded from 15 averages. The thickness of the test blade is variable. However, the blade has been divided into seven parts to perform the Lamb wave tests. Thus this study assumed that the thickness of each part is invariant due to short propagation distance. The calculation of dispersion curves was obtained by Raisutis [158] and illustrated in Figure 5.14.

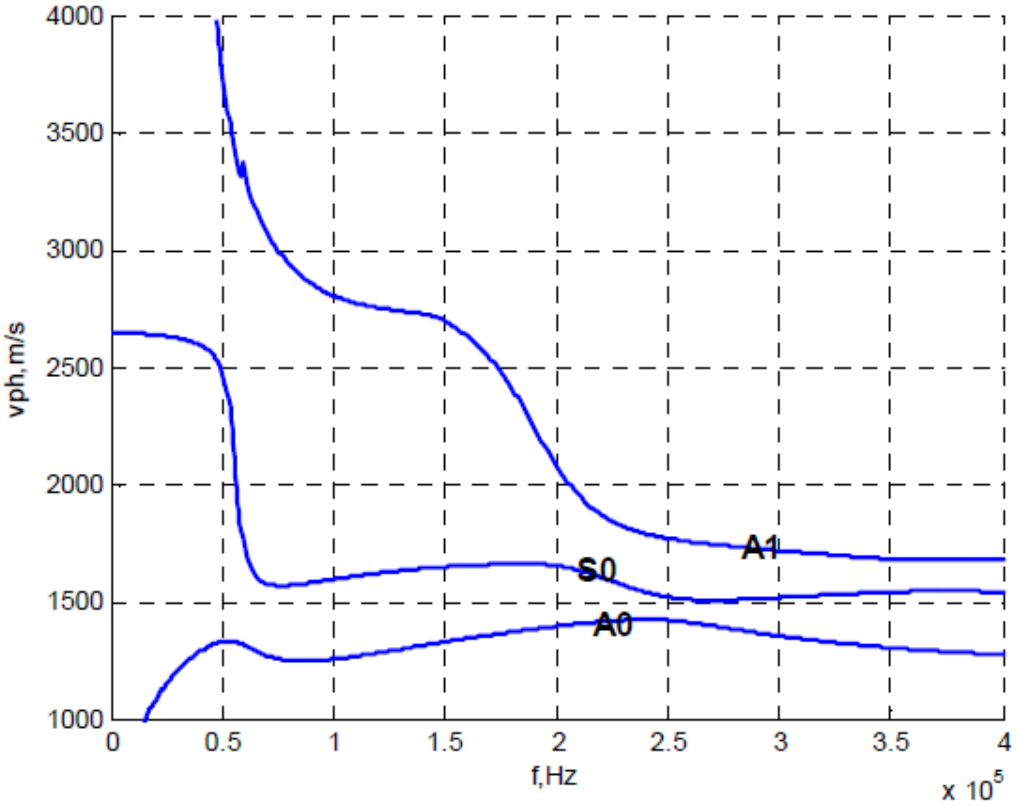


Figure 5.14: Dispersion curves for Glass Fibre Reinforced Plastic (GFRP) with 20 mm thickness [158].

The excitation frequency was 165kHz in this case. Each waveform contained a 200μs duration of data. An interval between pulses was set as 10ms. A sampling window was used to eliminate boundary reflection signals, as shown in Figure 5.15.

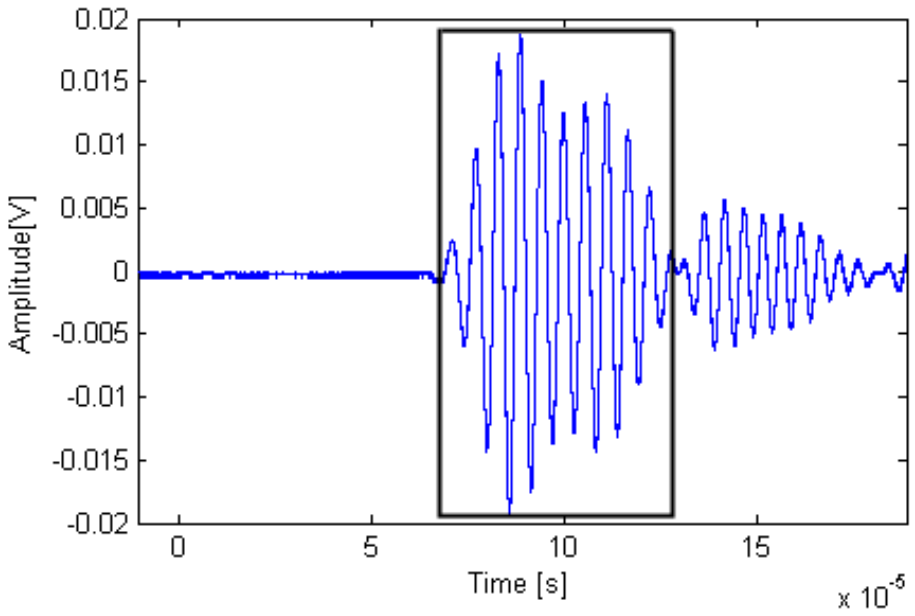


Figure 5.15: Outlier Analysis sampling window of guided wave response.

As mentioned before, two sets of data were taken from the undamaged blade: 50 guided wave observations were taken as a ' training set ' and a further 50 observation were chosen as a ' test set '. After the first impact, 50 additional observations were taken. The 1% exclusive threshold value for a 50 observation, 10-dimensional problem was found to be 55.5 after 1000 Monte Carlo trials of the algorithm discussed in Section 2.3.2.

Note that, the first impact damage failed to be localised due to a short time lag between impulses from the signal generator which meant that the diffuse field was excited rather than individual packets. Also the fact that there was no support underneath the blade when it was damaged may have caused damage at the root. This test - despite the problem - showed the interesting fact that the damage could be detected in the diffuse field and thus that attenuation was unlikely to cause unnecessarily high sensor densities in practice.

In the second test, the second impact damage introduced by an instrumented PCB hammer hit the same place as Figure 5.8. This time, a steel rod was placed underneath the lower shell of the blade in order to localise the impact damage. Moreover, four

pairs of sensors around the damage area were used in performing the guided wave test in order to confirm the findings. The placements of sensors are schematically shown in Figure 5.16.

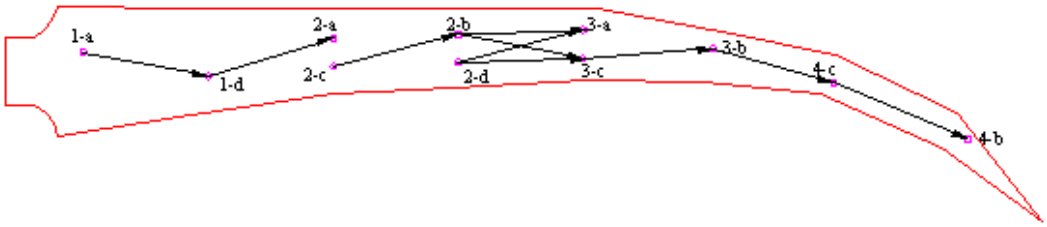


Figure 5.16: The arrangement of sensors and Lamb wave propagation direction.

The experiment of set up is similar to the first impact test. The guided wave input frequency was increased from 165kHz to 170kHz which give the better signal to noise ratio. A time lag between pulses was increased from 10ms to 500ms to reduce the reflected signals. Observed from Figure 5.17, there is a steadily increasing trend for MSD value; this means a 10ms lag may not avoid the reflected signal. Thus, increasing the time lag is necessary to allow the field to decay before the next ping. The second impact force was recorded as 2081.8N.

A benchmark was rebuilt again for the second impact test. Though the blade had an impacted damage after first hit, this study assumed that before the second hammer strike, the blade was in a new baseline condition. Based on this assumption, two sets of data were taken from the testing blade: 50 guided wave observations were taken as a ' training set ' and a further 50 observation were chosen as a ' test set '. After the second impact test, later 50 observations were taken. The 1% exclusive threshold value for a 50 observation, 10-dimensional problem was found to be 60.9 after 1000 Monte Carlo trials of the algorithm discussed in Section 2.3.2.

### 5.5.2 Experimental results and discussion

The results of the first impact test obtained by outlier analysis are shown in Figure

5.17 with a logarithmic vertical scale. The results indicate successful classification for undamaged and damaged data. That means the undamaged data are all lying below the threshold level (red line) and are classified as 'inliers' while all the damaged data are significantly above the damage detection threshold and are categorised as 'outliers'. In addition, The MSD values show that the damage between the root of the blade and the impacted area (1a1d, 1d2c and 2c2b) are more severe than any other place. Two factors may result in the failure of first the impact test. Firstly, there is no support underneath the lower shell of the blade. Therefore, the first impact produces more global damage rather than localised damage. Secondly, an increasing trend of MSD value for the undamaged stage manifests that reflected signals may affect the results.

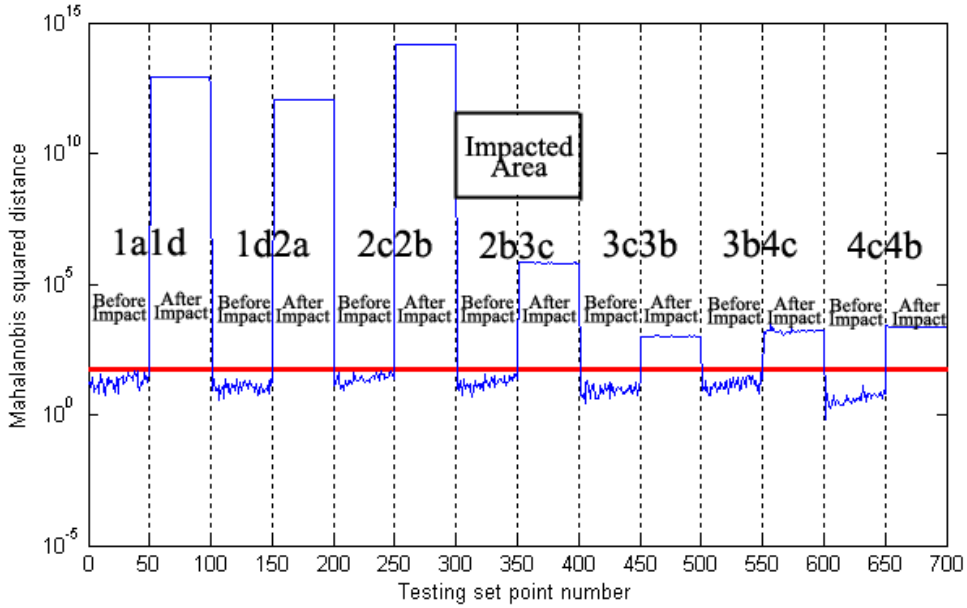


Figure 5.17: Outlier analysis classification results for the first impact test (1a1d, 1d2a, 2c2b, 3c3b, 3b4c and 4c4b indicate sensor groups).

For the second impact test, a steel rod was placed underneath the lower shell of the blade to localise the impact damage. In addition, the increased time lag helped to reduce the diffuse signals. The results of the second impact test obtained by outlier analysis are shown in Figure 5.18 with a logarithmic vertical scale. The results also show successful classification for undamaged and damaged data. This provides qualitative information that impact damage may be produced in the blade. In addition, The MSD shows that the values obtained around damage area are significantly above

the damage detection threshold. This means that outlier analysis may offer information about the localised damage.

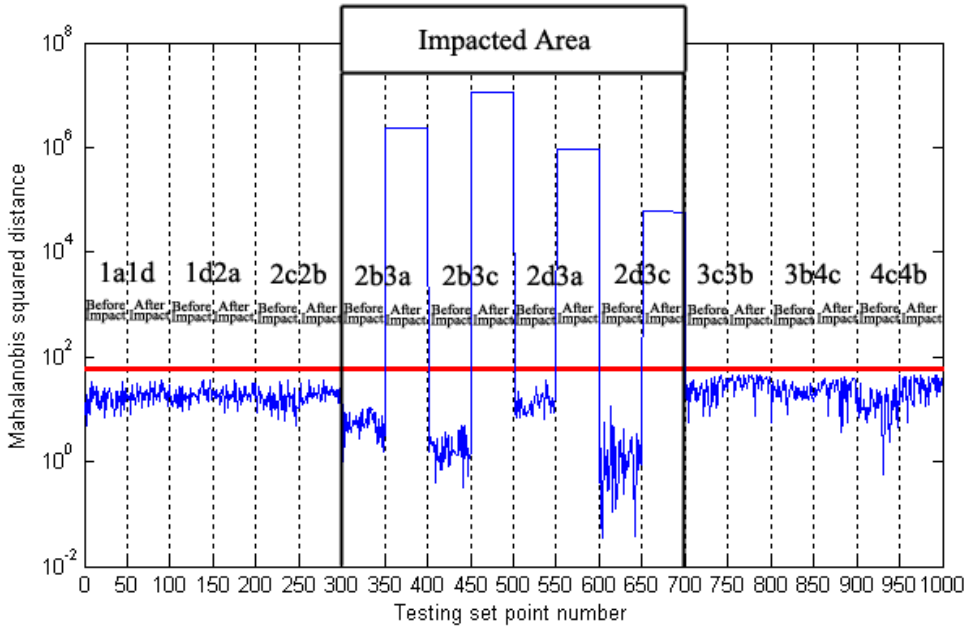


Figure 5.18: analysis classification results for the second impact test (1a1d, 1d2a, 2c2b, 2b3c, 2d3a, 2d3c, 3c3b, 3b4c, 4c4b indicate sensor groups).

## 5.6 Summary

This chapter mainly developed nonlinear acoustic and guided wave methods for analysing impact damage on a wind turbine blade. For nonlinear acoustic tests, a nonlinear elastic mechanism was observed. The vibro-acoustic method did not give any information to indicate damage present in the structure. The application of outlier analysis on guided wave tests successfully classified damage with 100% rate. Furthermore, outlier analysis was able to give an indication of probable position of the damage after the second impact test.

# Chapter 6

# 6 Conclusions and future work

## 6.1 Summary of research work presented

The motivation for this research work is to detect damage in structures made from various materials with different severities through the use of nonlinear acoustic techniques and Lamb wave methods. The aim of this work is to find out how effective these methods are to detect damage in different materials or structures. The experimental results showed that both methods are sensitive to fatigue crack detection on glass and aluminum plate, but Lamb wave methods are more effective in detect damage on composite structures.

This research work can be divided into three major areas/parts. The first part investigated fatigue crack detection in glass and aluminium plates. FE modeling was used to calculate the crack edge divergence for three different crack modes with opening-closing (crack mode I ), sliding (crack mode II ) and tearing (crack mode III ) actions. The 1$^{st}$, 3$^{rd}$ and 6$^{th}$ vibration modes were chosen for low frequency modal excitation which represent crack mode I , III and II , respectively. After that, FE modeling extracted the natural frequencies and mode shapes for the 1$^{st}$, 3$^{rd}$ and 6$^{th}$ modes. Experimental work was performed to analyse the effect of nonlinear acoustics by signal wave excitation, FRFs with varying excitation levels and vibro-acoustic excitation. Various physical mechanisms to account for these effects have been found. The application of outlier analysis on Lamb waves test was used to identify whether damage is present in the structure. Furthermore, outlier analysis was able to give a rough indication of damage severity for the glass plate. The second part focused on low-velocity impact damage and compression damage in CFRP. For the low-velocity impact test, seven CFRP plates were subjected to different levels of impact energy.

Nonlinear acoustic techniques and outlier analysis were applied to analyse impact damage as mentioned before. For the compression test, a CFRP panel with a stringer underwent a compression load starting at 5kHz and increasing until the panel failed. Outlier analysis applied to Lamb wave data was used to monitor the damage process of the compression test. The third part evaluated a real engineering structure by detecting damage from a hammer impact on a wind turbine blade. The impact tests were performed twice. The first test was failure to localise the impact damage. For the second impact test, a steel rod was placed underneath the lower shell of the blade in order to localise the damage. In addition, the time lag was increased from 10ms to 500ms to reduce the reflected signals and thus the diffuse field. Nonlinear acoustics were used to detect the damage and reveal the physical mechanism caused by this impact damage. Outlier analysis applied on Lamb waves was used to identify and localise the damage.

## 6.2 **Conclusions**

The work on nonlinear acoustic techniques and guided wave methods undertaken in this thesis has led to an extensive assessment of the potential of both methods for detecting various damage severities.

In order to aid decision-making in the presence of damage, statistical hypothesis testing was introduced for the first time into the vibro-acoustic SHM. Based on the hypothesis test, researchers can find out whether a result is statistically significant or occurs by coincidence.

Nonlinear acoustic techniques and guided wave methods have been applied on different materials (e.g. glass, aluminum and CFRP) and structures (e.g. plate, wind turbine, panel with a stringer) in order to find out the suitability for damage detection. Both techniques appeared to offer high sensitivity to detect fatigue crack on homogenous material. The guided wave methods were promising for detecting

damage on composite structures. The higher material nonlinearity for composite structure may be the main reason for lower sensitivities of nonlinear acoustic methods.

Different type tests contributing to material damage were investigated in this study: fatigue tests, impact tests with a hammer or a drop impactor, as well as compression tests. To the best of the author's knowledge, applying guided wave to monitor delamination in composite panel through compression test has not been implemented before.

Damage detection sensitivity, severity assessment and location have been explored in this study. By applying the vibro-acoustic method, the smallest detectable fatigue cracks in glass plate and aluminum plate were 6mm and 2mm, respectively. Meanwhile, the guided waves with outlier analysis successfully classified the undamaged and damaged data for glass and aluminum plate. For the composite plate test, nonlinear acoustic methods could detect a minimum of 20J impact damage, while the guided waves with outlier analysis could detect minimum 10J impact damage. For wind turbine blade test, the nonlinear acoustic approach did not show promising results, while guided waves identified the damage and gave an indication of probable position of the damage. Though guided wave with outlier analysis shows successful classification of undamaged and damaged data, severity assessment is not always guaranteed.

## 6.3 Recommendations for future work

After completing the current study, some recommendations will be made for further development.

In this study, most experimental works were based in the laboratory environment.

When the test structures are exposed to the outside world, the effects of the environmental variations (e.g. temperature, humidity, wind) must be carefully considered. Worden *et al* [159] demonstrated that environmental/operational conditions must be characterised and distinguished before using a reliable feature for revealing any structural condition; otherwise, these factors may cause false alarm. Data mining methods, such as The Least Median of Squares (LMS) or Least Trimmed Squares (LTS), could uncover hidden patterns of collected data and lead to identify the environmental variations or damage outliers [160]. In addition, 'mask effect' is another factor that cannot be ignored. Rousseeuw [100] and Dervilis [160] illustrated that the classical identification methods (outlier analysis) does not always identify outliers. If outliers have already contaminated the training data, the sample mean and covariance matrix will be affected. Therefore, the real outliers are masked. It is better to use robust estimators to against outliers in training data. Rousseeuw [161] suggested the Minimum Volume Ellipsoid Estimation (MVE) algorithm and Minimum Covariance Determinant Estimation (MCD) algorithm to solve this kind of problem. Further research work could be planned to utilise these robust regression techniques for outlier analysis.

For nonlinear acoustic testing, more post-processing methods (e.g. Signal processing method based on wavelet transform, bispectrum analysis [162]) can be used to analyse data and establish whether this may improve sensitivity to small damages.

In general, MSD will not necessarily grow monotonically with damage, so severity assessment is not always guaranteed. A signal processing based cross-correlation technique can be used to examine how similar two particular waveforms are to one another, and this technique has exhibited successful damage severity assessment. This technique may be carried out for guided wave damage detection [134].

For the sidebands and harmonics in undamaged specimens, further work is required to investigate intrinsic nonlinearities whether caused by material, boundary effects or

instrumentation.

In this study, nonlinear acoustic methods focus on plate and blade structures. They can be applied to other types of geometry also, such as water pipes, and give a huge potential in extensive industrial practice.

Unusual elastic materials, such as rocks, require one to understand their special elastic behaviour (discrete memory and slow elastic dynamics). Nonlinear acoustic methods may be valuable tools for exploring these elastic behaviours and utilising for detecting damage.

Investigation of environmental temperature effects on the Lamb wave propagation and piezoelectric sensors. In the fatigue tests, the thermo-elastic nonlinearity (L-G effect) caused by wave modulation was studied. Further investigations are required to confirm the findings by using infrared thermo-graphic techniques on the temperature field. This may include the effects of different crack modes, crack lengths and excitation amplitudes.

The effect of transducer position should also be considered. It is also important to increase the number of measurements if possible to increase the relevance of the statistical techniques.

For the wind turbine blade test, a different impact area needs to be considered. Further study can confirm the damage localisation techniques on the new impacted area.

# References


1. **C.R. Farrar and K. Worden**, *Structural Health Monitoring: A Machine Learning Perspective*. John Wiley & Sons, Inc. Hoboken, New Jersey, 2012.

2. **J. Lemaitre and R. Desmorat**, *Engineering Damage Mechanics:Ductile, Creep, Fatigue and Brittle Failures*. Springer Berlin Heidelberg. New York, 2005.

3. **W.J. Staszewski, C. Boller, and G.R. Tomlinson**, eds. *Health Monitoring of Aerospace Structures: Smart Sensor Technologies and Signal Processing*. John Wiley & Sons, Ltd, 2004.

4. **R.B. Jenal**, *Fatigue crack detection using nonlinear acoustic-analysis of vibro-acousitc modulations*, Ph.D. Thesis, The University of Sheffield, in Department of Mechanical Engineering, 2010.

5. **V.E. Nazarov, L.A. Ostrovsky, I.A. Soustova, and A.M. Sutin**, *Nonlinear acoustics of micro-inhomogeneous media. Physics of The Earth and Planetary Interiors*, **50**(1), 1988. 65-73.

6. **P.A. Johnson, A. Sutin, and K.E.A.v.d. Abeele**, *Application of nonlinear wave modulation spectroscopy to discern material damage*, in *Conference: 2. international conference on emerging technologies in NDT, Athens (Greece), 24-26 May 1999; Other Information: PBD: [1999]*. 1999. p. Medium: ED; Size: 9 p.

7. **R.A. Guyer and P.A. Johnson**, *Nonlinear Mesoscopic Elasticity: Evidence for a New Class of Materials. Physics Today*, **52**(4), 1999. 30-36.

8. **I.Y. Solodov and B.A. Korshak**, *Instability, Chaos, and "Memory" in Acoustic-Wave–Crack Interaction. Physical Review Letters*, **88**(1), 2001. 014303.

9. **P. Duffour, P. Cawley, and M. Morbidini**, *Vibro-acoustic modulation NDE technique. Part 1: Theoretical study. In: Thompson, DO and Chimenti, DE, (eds.) Review of Progress in Quantitative Nondestructive Evaluation. AMER INST PHYSICS*, **24A and 24B**, 2005. 608 - 615.

10. **B. Bhushan, J.N. Israelachvili, and U. Landman**, *Nanotribology: friction, wear and lubrication at the atomic scale. Nature*, **374**(6523), 1995. 607-616.

11. **P. Laugier and G. Haïat**, eds. *Bone Quantitative Ultrasound*. Springer, New York, 2011.

12. Airnation. *Bird Strike Hits US Airways 757 at Orlando, Damages Radome*. Available from: http://airnation.net/2012/05/14/bird-strike-us-airways-orlando/ accessed on 29/07/2013.

13. **Z. Parsons and W.J. Staszewski**, *Nonlinear acoustics with low-profile piezoceramic excitation for crack detection in metallic structures. Smart Materials and Structures*, **15**(4), 2006. 1110.

14. **F. Aymerich and W.J. Staszewski**, *Impact damage detection in composite laminates using nonlinear acoustics. Composites Part A: Applied Science and Manufacturing*, **In Press, Corrected Proof**, 2009.

15. **P. Duffour, M. Morbidini, and P. Cawley**, *A study of the vibro-acoustic modulation technique for the detection of cracks in metals. The Journal of the Acoustical Society of America*, **119** (3), 2006. 1463-1475.

16. **A. Hikata, B.B. Chick, and C. Elbaum**, *Dislocation Contribution to the Second Harmonic Generation of Ultrasonic Waves. Journal of Applied Physics*, **36**(1), 1965. 229-236.

17. **A. Klepka, W.J. Staszewski, D.d. Maio, and F. Scarpa**, *Impact damage detection in composite chiral sandwich panels using nonlinear vibro-acoustic modulations. Smart Materials and Structures*, **22**(8), 2013. 084011.

18. **K.-Y. Jhang**, *Nonlinear ultrasonic techniques for nondestructive assessment of micro damage in material: A review. International Journal of Precision Engineering and Manufacturing*, **10**(1), 2009. 123-135.

19. **D. Donskoy, A. Sutin, and A. Ekimov**, *Nonlinear acoustic interaction on contact interfaces and its use for nondestructive testing. NDT & E International*, **34**(4), 2001. 231-238.

20. **R.A. Guyer and P.A. Johnson**, *Nonlinear Mesoscopic Elasticity: The Complex Behavior of Granular Media including Rock and Soil*. WILEY-VCH. Weinheim, 2009.

21. **K. Worden and G.R. Tomlinson**, *Nonlinearity in structural dynamics: detection, identification and modelling*. IoP Publishing. London, 2001.

22. **A. Klepka, W.J. Staszewski, R.B. Jenal, M. Szwedo, T. Uhl, and J. Iwaniec**, *Nonlinear acoustics for fatigue crack detection – experimental investigations of vibro-acoustic wave modulations. Structural Health Monitoring*, 2011.

23. **K.E. A. Van Den Abeele, P.A. Johnson, and A. Sutin**, *Nonlinear Elastic Wave Spectroscopy (NEWS) Techniques to Discern Material Damage, Part I: Nonlinear Wave Modulation Spectroscopy (NWMS). Research in Nondestructive Evaluation*, **12**(1), 2000. 17-30.

24. **W.L. Morris, O. Buck, and R.V. Inman**, *Acoustic harmonic generation due to fatigue damage in high-strength aluminum. Journal of Applied Physics*, **50**(11), 1979. 6737-6741.

25. **F. Aymerich and W.J. Staszewski**, *Impact damage detection in composite laminates using*

*nonlinear acoustics. Composites Part A: Applied Science and Manufacturing*, **41**(9), 2010. 1084-1092.

26. **V. Zaitsev, V. Nazarov, V. Gusev, and B. Castagnede**, *Novel nonlinear-modulation acoustic technique for crack detection. NDT& E Int.*, **39**(3), 2006. 184.

27. **F. Aymerich and W.J. Staszewski**, *Experimental Study of Impact-Damage Detection in Composite Laminates using a Cross-Modulation Vibro-Acoustic Technique. Structural Health Monitoring*, 2010.

28. **M. Ryles, F.H. Ngau, I. McDonald, and W.J. Staszewski**, *Comparative study of nonlinear acoustic and Lamb wave techniques for fatigue crack detection in metallic structures. Fatigue & Fracture of Engineering Materials & Structures*, **31**(8), 2008. 674-683.

29. **W.A. Grandia and C.M. Fortunko**. *NDE applications of air-coupled ultrasonic transducers*. in *Ultrasonics Symposium, 1995. Proceedings., 1995 IEEE* (1995).

30. **M. Sun, W.J. Staszewski, R.N. Swamy, and Z. Li**, *Application of low-profile piezoceramic transducers for health monitoring of concrete structures. NDT & E International*, **41**(8), 2008. 589-595.

31. **W.H. Leong, W.J. Staszewski, B.C. Lee, and F. Scarpa**, *Structural health monitoring using scanning laser vibrometry: III. Lamb waves for fatigue crack detection. Smart Materials and Structures*, **14**(6), 2005. 1387.

32. **W.J. DeCoursey**, *Statistics and Probability for Engineering Applications*. Elsevier Inc. Oxford, 2003.

33. **R.L. Scheaffer, M. Mulekar, and J.T. McClave**, *Probability and Statistics for Engineers*. Duxbury Press. Pacific Grove, 2010.

34. **J.L. Devore and K.N. Berk**, *Modern Mathematical Statistics with Applications*. springer. London, 2012.

35. **K. Worden, G. Manson, and N.R.J. Fieller**, *Damage detection using outlier analysis. Journal of Sound and Vibration*, **229**(3), 2000. 647-667.

36. **K. Worden, S.G. Pierce, G. Manson, W.R. Philp, W.J. Staszewski, and B. Culshaw**, *Detection of defects in composite plates using Lamb waves and novelty detection. International Journal of Systems Science*, **31**(11), 2000. 1397-1409.

37. **K. Worden, G. Manson, and D. Allman**, *Experimental validation of a structural health monitoring methodology: Part I. Novelty detection on a laboratory structure. Journal of Sound and Vibration*, **259**(2), 2003. 323-343.

38. **D. Chetwynd, J.A. Rongong, S.G. Pierce, and K. Worden**, *Damage detection in an aluminium plate using outlier analysis. Fatigue & Fracture of Engineering Materials & Structures*, **31**(8), 2008. 629-643.

39. **A. Hikata, B.B. Chick, and C. Elbaum**, *Effect of dislocations on finite amplitude ultrasonic waves in aluminum. Appl. Phys. Lett.*, **11**, 1963. 195-196.

40. **M.A. Breazeale and J. Ford**, *Ultrasonic Studies of the Nonlinear Behavior of Solids. J. Appl. Phys.*, **36**(11), 1965. 3486 –3490.

41. **T. Bateman, W.P. Mason, and H.J. McSkimin**, *Third‐Order Elastic Moduli of Germanium. J. Appl. Phys.*, **32**(5), 1961 928 - 936

42. **O. Buck and W.L. Morris**, *Acoustic harmonic generation at unbonded interfaces and fatigue cracks. The Journal of the Acoustical Society of America*, **64**(S1), 1978. S33.

43. **I. Shkolnik**, *NONDESTRUCTIVE TESTING OF CONCRETES: NEW ASPECTS. Nondestructive Testing and Evaluation*, **10**(6), 1993. 351-358.

44. **A. S. Korotkov, M. M. Slavinskii, and A.M. Sutin**, *Variations of acoustic nonlinear parameters with the concentration of defects in steel. Acoustical Physics*, **40**, 1994. 71-74.

45. **P.B. Nagy**, *Fatigue damage assessment by nonlinear ultrasonic materials characterization. Ultrasonics*, **36**(1-5), 1998. 375-381.

46. **K.E.-A.V.D. Abeele, J. Carmeliet, J.A.T. Cate, and P.A. Johnson**, *Nonlinear Elastic Wave Spectroscopy (NEWS) Techniques to Discern Material Damage, Part II: Single-Mode Nonlinear Resonance Acoustic Spectroscopy. Research in Nondestructive Evaluation*, **12**(1), 2000. 31 - 42.

47. **V. Zaitsev, V. Nazarov, V. Gusev, and B. Castagnede**, *Novel nonlinear-modulation acoustic technique for crack detection. NDT & E International*, **39**(3), 2006. 184-194.

48. **D. Donskoy, K. Ferroni, A. Sutin, and K. Sheppard**, *A Nonlinear Acoustic Technique for Crack and Corrosion Detection in Reinforced Concrete*, in *Nondestructive Characterization of Materials VIII*, R. Green, Jr., Editor. 1998, Springer US. p. 555-560.

49. **D.M. Donskoy and A.M. Sutin**, *Vibro-Acoustic Modulation Nondestructive Evaluation Technique. Journal of Intelligent Material Systems and Structures*, **9**(9), 1998. 765-771.

50. **I.Y. Solodov**, *Ultrasonics of non-linear contacts: propagation, reflection and NDE-applications. Ultrasonics*, **36**(1-5), 1998. 383-390.

51. **J.-Y. Kim, V.A. Yakovlev, and S.I. Rokhlin**, *Parametric modulation mechanism of surface acoustic wave on a partially closed crack. Appl. Phys. Lett.*, **82**(19), 2003. 3203-3205.

52. **D. Broda, V. Hiwarkar, V.V. Silberschmidt, and W.J. Staszewski**, *Effect of crack induced nonlinearity on dynamics of structures: application to structural health monitoring. Journal of Physics: Conference Series*, **451**(1), 2013. 012015.

53. **M.I. Friswell and J.E.T. Penny**, *Crack Modeling for Structural Health Monitoring. Structural Health Monitoring*, **1**(2), 2002. 139-148

54. **M. Muller, A. Sutin, R. Guyer, M. Talmant, P. Laugier, and P.A. Johnson**, *Nonlinear resonant ultrasound spectroscopy (NRUS) applied to damage assessment in bone. The Journal of the Acoustical Society of America*, **118**(6), 2005. 3946-3952.

55. **V.E. Nazarov, A.V. Radostin, and I.A. Soustova**, *Effect of an intense sound wave on the acoustic properties of a sandstone bar resonator. Experiment. Acoustical Physics* **48**(1), 2002. 76-80.

56. **V. Zaitsev, V. Gusev, and B. Castagnede**, *Luxemburg-Gorky Effect Retooled for Elastic Waves: A Mechanism and Experimental Evidence. Physical Review Letters*, **89**(10), 2002. 105502.

57. **V.Y. Zaitsev, V. Gusev, and B. Castagnède**, *Observation of the "Luxemburg-Gorky effect" for elastic waves. Ultrasonics*, **40**(1-8), 2002. 627-631.

58. **L.A. Ostrovsky and P.A. Johnson**, *Dynamic nonlinear elasticity in geomaterials. Rivista del Nuovo Cimento*, **024**(07), 2001. 1-46.

59. **C. Pecorari**, *Adhesion and nonlinear scattering by rough surfaces in contact: Beyond the phenomenology of the Preisach–Mayergoyz framework. J. Acoust. Soc. Am.*, **116**(4), 2004. 1938-1947.

60. **R.A. Guyer, K.R. McCall, and K. Van Den Abeele**, *Slow elastic dynamics in a resonant bar of rock. Geophys. Res. Lett.*, **25**(10), 1998. 1585-1588.

61. **N. Krohn, R. Stoessel, and G. Busse**, *Acoustic non-linearity for defect selective imaging. Ultrasonics*, **40**(1-8), 2002. 633-637.

62. **K.E.A. Van Den Abeele**, *Elastic pulsed wave propagation in media with second- or higher-order nonlinearity. Part I. Theoretical framework. The Journal of the Acoustical Society of America*, **99**(6), 1996. 3334-3345.

63. **A. Klepka, T. Stepinski, T. Uhl, and W. Staszewski**, *Nonlinear Acoustics*, in *Advanced Structural Damage Detection: From Theory to Engineering Applications*. 2013, John Wiley &

Sons, Ltd: New York. p. 73-107.

64. **C. Pecorari and I. Solodov**, *Nonclassical Nonlinear Dynamics of Solid Surfaces in Partial Contact for NDE Applications,* in *Universality of Nonclassical Nonlinearity*, P. Delsanto, Editor. 2006, Springer New York. p. 309-326.

65. **C. Payan, V. Garnier, J. Moysan, and P.A. Johnson**, *Applying nonlinear resonant ultrasound spectroscopy to improving thermal damage assessment in concrete. The Journal of the Acoustical Society of America*, **121**(4), 2007. EL125-EL130.

66. **M. Meo, U. Polimeno, and G. Zumpano**, *Detecting Damage in Composite Material Using Nonlinear Elastic Wave Spectroscopy Methods. Applied Composite Materials*, **15**(3), 2008. 115-126.

67. **Y.-M. Cheong, M.K. Alam, and C. Kim**. *Nonlinear Parameters for a Diagnosis of Micro-Scale Cracks Using a Nonlinear Resonant Ultrasound Spectroscopy (NRUS),* AIP Conference Proceedings (2010).

68. **M. Muller, J.A. Tencate, T.W. Darling, A. Sutin, R.A. Guyer, M. Talmant, P. Laugier, and P.A. Johnson**, *Bone micro-damage assessment using non-linear resonant ultrasound spectroscopy (NRUS) techniques: A feasibility study. Ultrasonics,* **44**(Supplement 1), 2006. e245-e249.

69. **J.G. Sessler and V. Weiss.** *Crack Detection Apparatus and Method*. (1975) US, patent 3867836.

70. **V.Y. Zaitsev, A.M. Sutin, I.Y. Belyaeva, and V.E. Nazarov**, *Nonlinear Interaction of Acoustical Waves Due to Cracks and Its Possible Usage for Cracks Detection. Journal of Vibration and Control*, **1**(3), 1995. 335-344.

71. **P. Duffour, M. Morbidini, and P. Cawley**, *Comparison between a type of vibro-acoustic modulation and damping measurement as NDT techniques. NDT & E International*, **39**(2), 2006. 123-131.

72. **P.a.M. Duffour, M. and Cawley, P.** , *A study of the vibro-acoustic modulation technique for the detection of cracks in metals. The Journal of the Acoustical Society of America*, **119** (3), 2006. 1463-1475.

73. **M. Morbidini, P. Duffour, and P. Cawley**, *Vibro-Acoustic Modulation NDE Technique. Part 2: Experimental Study. AIP Conference Proceedings*, **760**(1), 2005. 616-623.

74. **L. Pieczonka, W.J. Staszewski, and F. Aymerich.** *Analysis of Nonlinear Vibro-Acoustic Wave Modulations Used for impact damage detection in composite structures*. in *Structural health monitoring 2012: proceedings of the sixth European workshop* Cagliari, Italy (2012).

75. **N.C. Yoder and D.E. Adams**, *Vibro-Acoustic Modulation Utilizing a Swept Probing Signal for Robust Crack Detection. Structural Health Monitoring*, **9**(3), 2010. 257-267.

76. **V. Zaitsev and P. Sas**, *Nonlinear Response of a Weakly Damaged Metal Sample: A Dissipative Modulation Mechanism of Vibro-Acoustic Interaction. Journal of Vibration and Control*, **6**(6), 2000. 803-822.

77. **H.F. Hu, W.J. Staszewski, and e. al.**, *Crack detection using nonlinear acoustics and piezoceramic transducers—instantaneous amplitude and frequency analysis. Smart Materials and Structures*, **19**(6), 2010.

78. **B.D. J. Jiao , S. Neild**, *Contact defect detection in plates using guided wave and vibro-acoustic modulation. 17th World Conference on Nondestructive Testing, Shanghai, China*, 2008. 25-28.

79. **R.A. Guyer, K.R. McCall, and G.N. Boitnott**, *Hysteresis, Discrete Memory, and Nonlinear Wave Propagation in Rock: A New Paradigm. Physical Review Letters*, **74**(17), 1995. 3491.

80. **L.D. Landau, E.M. Lifshits, A.M. Kosevich, and L .P. Pitaevskĭ** , *Theory of elasticity*. Pergamon Press. New York, 1986.

81. **L.D. Landau and E.M. Lifshitz**, *Theory of Elasticity*. Pergamon. New York, 1986.

82. **A.M. Sutin and P.A. Johnson**. *Nonlinear Elastic Wave NDE II. Nonlinear Wave Modulation Spectroscopy and Nonlinear Time Reversed Acoustics*. Golden, Colorado (USA), AIP (2005).

83. **I.A. Viktorov**, *Rayleigh and Lamb Waves: Physical Theory and Application*. Plenum Press. New York, 1967.

84. **Z. Su and L. Ye**, *Identification of Damage Using Lamb Waves*. 2009, Springer: New York.

85. **K. Worden**, *Rayleigh and Lamb Waves - Basic Principles. Strain*, **37**(4), 2001. 167-172.

86. **Z. Su and L. Ye**, *Identification of damage using lamb waves. From Fundamentals to Applications*. **Vol. 48**. Springer. New York, 2009.

87. **W. Ostachowicz, P. Kudela, M. Krawczuk, and A. Zak**, *Guided Waves in Structures for SHM The Time-Domain Spectral Element Method*. JohnWiley & Sons Ltd. Southern Gate, 2012.

88. **W.-X. Yao, J. Renard, N. Himmel, and W.-X. Yao**, eds. *Fatigue Behaviour of Fiber Reinforced Polymers: Experiments and Simulations*. DEStech Publications, Inc, Lancaster, 2012.

89. **E.A. Birt**, *Damage detection in carbon-fiber composite using ultrasonic Lamb waves. Insight - Non-Destructive Testing and Condition Monitoring*, **40**(5), 1998. 335-339.

90. **J.L. Rose**, *Ultrasonic waves in solid media*. Cambridge University Press. New York, 1999.

91. **K.F. Graff**, *Wave motion in elastic solids*. Dover Publications. New York, 1971.

92. **W. J. Staszewski, C. Boller, and G.R. Tomlinson**, eds. *Health monitoring of aerospace structures: smart sensor technologies and signal processing*. John Wiley & Sons, Chichester, 2004.

93. *Piezoelectric ceramic products*. Available from: http://www.piceramic.com/pdf/KATALOG_english.pdf accessed on 09/11/2013.

94. **S.S. Kessler, S .M. Spearing, and C. Soutis**, *Damage detection in composite materials using Lamb wave methods. Smart Materials and Structures*, **11**(2), 2002. 269.

95. **S.S. Kessler, S.M. Spearing, and C. Soutis**, *Damage detection in composite materials using Lamb wave methods. Smart Materials and Structures*, **11**(2), 2002. 269.

96. **M. Born and E. Wolf**, *Principles of Optics*. Pergamon Press. Oxford, 1970.

97. **P.P. Delsanto**, ed. *Universality of Nonclassical Nonlinearity:Applications to Non-Destructive Evaluations and Ultrasonics*. Spinger, New York, 2006.

98. **Charles R Farrar and Keith Worden**, *An introduction to structural health monitoring. Phil. Trans. R. Soc. A*, **365**(1851), 2007. 303-315.

99. **M. Gul and F. Necati Catbas**, *Statistical pattern recognition for Structural Health Monitoring using time series modeling: Theory and experimental verifications. Mechanical Systems and Signal Processing*, **23**(7), 2009. 2192-2204.

100. **P.J. Rousseeuw and A.M. Leroy**, *Robust Regression & Outlier Detection*. Wiley-Blackwell. Hoboken, New Jersey, 2003.

101. **R.S. Guh, F. Zorriassatine, J.D.T. Tannock, and C. O'Brien**, *On-line control chart pattern detection and discrimination—a neural network approach. Artificial Intelligence in Engineering*, **13**(4), 1999. 413-425.

102. **L. Tarassenko, A. Nairac, N. Townsend, and P. Cowley**. *Novelty detection in jet engines.* in *IEE Colloquium on Condition Monitoring, Imagery, External Structures and Health*. Birmingham (1999).

103. **D. Dasgupta and S. Forrest**. *Novelty-detection in time series data using ideas from immunology*. in *Proceedings of the International Conference on Intelligent SystemsReno*. Nevada (1996).

104. **G.A. Carpenter, M.A. Rubin, and W.W. Streilein**. *ARTMAP-FD: familiarity discrimination applied to radar target recognition*. in *Proceedings of the International Conference on Neural Networks*. Houston, TX (1997).

105. **G. Manson, K. Worden, and D. Allman**, *Experimental validation of a structural health monitoring methodology, Part II: Novelty detection on a Gnat aircraft. Journal of Sound and Vibration. Journal of Sound and Vibration*, **259**(2), 2003. 345-363.

106. **R. Ruotolo and C. Surace**. *A statistical approach to damage detection through vibration monitoring*. in *Proceeding of the 5th Pan American Congress of Applied Mechanics*. Peurto Rico (1997).

107. **D.A. Pomerleau**, *Efficient Training of Artificial Neural Networks for Autonomous Navigation. Neural Computation*, **3**(1), 1991.

108. **W.J. Staszewski and G.R. Tomlinson**, *Application of the wavelet transform to fault detection in a spur gear. Mechanical Systems and Signal Processing*, **8**(3), 1994. 289-307.

109. **S.E. Guttormsson, R.J.M. II, and M.A. El-Sharkawi**, *IEEE Trans. Energy Conversion. Elliptical novelty grouping for on-line short-turn detection of excited running rotors*, **14**(1), 1999.

110. **M.E. Hellman**, *The Nearest Neighbor Classification Rule with a Reject Option. Systems Science and Cybernetics, IEEE Transactions on*, **6**(3), 1970. 179-185.

111. **R.O. Duda, P.E. Hart, and D.G. Stork**, *Pattern Classification*. Wiley. New York, 2001.

112. **S. Forrest, A.S. Perelson, L. Allen, and R. Cherukuri**. *Self-non-self discrimination in a computer*. in *Proceedings of the IEEE Symposium on Research in Security and Privacy*. Oakland, CA (1994).

113. **N.J. Pizzi, R.A. Vivanco, and R.L. Somorjai**, *EvIdent™: a functional magnetic resonance image analysis system. Artificial Intelligence in Medicine*, **21**(1–3), 2001. 263-269.

114. **I. Antoniadou, K. Worden, and W.J. Staszewski**, *On damage detection in wind turbine gearboxes using outlier analysis. Industrial and Commercial Applications of Smart Structures Technologies*, **Vol. 8343**, 2012.

115. **S. Pavlopoulou, C. Soutis, and G. Manson**, *Non-destructive inspection of adhesively bonded patch repairs using Lamb waves. Plastics, Rubber and Composites*, **41**(2), 2012. 61-68.

116. **E. Akhmatskaya, N. Bou-Rabee, and S. Reich**, *A comparison of generalized hybrid Monte Carlo methods with and without momentum flip. Journal of Computational Physics*, **228**(6), 2009. 2256-2265.

117. **P. Mathé and E. Novak**, *Simple Monte Carlo and the Metropolis algorithm. Journal of Complexity*, **23**(4–6), 2007. 673-696.

118. **J.L. DeVore**, *Probability and Statistics for Engineering and the Sciences* 8th ed., Cengage Learning, Inc. Stamford, CT, 2010.

119. **J. Wurm**, *Glass Structures:Design and Construction of Self-Supporting Skins*. Springer. New York, 2007.

120. **J. He and Z.-F. Fu**, *Modal Analysis*. Elsevier Ltd. . Oxford, 2001.

121. **A.W. Leissa**, *The free vibration of rectangular plates. Journal of Sound and Vibration*, **31**(3), 1973. 257-293.

122. **C. Beards**, *Structural Vibration: Analysis and Damping*. Elsevier Science. Amsterdam, 1996.

123. **W. Thomson**, *Theory of Vibration with Applications*. CRC Press. Boca Raton, Florida, 1996.

124. **R. Blevins**, *Formulas for Natural Frequency and Mode Shape*. Krieger Publishing Company. Malabar, Florida, 2001.

125. **S.M. Ross**, *Introduction to Probability and Statistics for Engineers and Scientists*. Academic Press. London, 2009.

126. **G. Keller**, *Statistics for Management and Economics,9th ed*. Cengage Learning. Mason, 2011.

127. Y. Hayashi, H. Suzuki, and T. Kinjo.'*Vallen wavelet and dispersion progamme*', 2010, Available from: http://www.vallen.de/products/software/wavelet.

128. MATWEB. *Aluminum 2024-T4; 2024-T351*. ASM Aerospace Specification Matals Inc. Available from: http://asm.matweb.com/search/SpecificMaterial.asp?bassnum=MA2024T4.

129. **W.D. Callister**, *Materials Science and Engineering, 7th edn*. Wiley. New York, 2007.

130. **A. Wöhler**, *Über die Festigkeitsversuche mit Eisen und Stahl. Zeitschrift für Bauwesen*, **20**, 1870.

131. **C.R. Sohar**, *Lifetime Controlling Defects in Tool Steels*. *Springer Theses*. Springer. Berlin, 2011.

132. **W.H. Kim and C. Laird**, *Crack nucleation and stage I propagation in high strain fatigue—II. mechanism. Acta Metallurgica*, **26**(5), 1978. 789-799.

133. **J. Schijve**, *Fatigue of Structures and Materials*. Springer. Amsterdam, 2009.

134. **M.R. Pearson, M.J. Eaton, C.A. Featherston, K.M. Holford, and R. Pullin**, *Impact Damage Detection and Assessment in Composite Panels using Macro Fibre Composites Transducers. Journal of Physics: Conference Series*, **305**(1), 2011. 012049.

135. Cytec. *MTM 56 series datasheet*. Available from: http://www.cemselectorguide.com/pdf/MTM56.pdf accessed 10/01/2014.

136. **M.T.H. Sultan**, *Impact damage characterisation in composite laminates*, Ph.D. Thesis, The University of Sheffield, 2010.

137. **S.V. Hoa**, *Principles of the Manufacturing of Composite Materials*. DEStech Publications, Inc. Lancaster, 2009.

138. A. Hering. *Carbon fabric yc 3k 200 twill*. Available from: http://commons.wikimedia.org/wiki/File:Carbon_fabric_yc_3k_200_twill.jpg accessed on 31/07/2014/.

139. **V.V. Vasiliev and E.V. Morozov**, *Advanced Mechanics of Composite Materials* 2007, Elsevier Science Ltd: Oxford.

140. **A.A. Baker, S. Dutton, and D.W. Kelly**, *Composite Materials for Aircraft Structures*. American Institute of Aeronautics and Astronautics, 2004.

141. **S.G. Advani and E.M. Sozer**, *Process Modeling in Composites Manufacturing*. CRC Press. Boca Raton, 2010.

142. **N.K. Naik, Y. Chandra Sekher, and S. Meduri**, *Damage in woven-fabric composites subjected to low-velocity impact. Composites Science and Technology*, **60**(5), 2000. 731-744.

143. **S.R. Reid and G. Zhou**, eds. *Impact Behaviour of Fibre-reinforced Composite Materials and Structures*. CRC Press, Boca Raton, 2000.

144. **S. Abrate**, *Impact on Composite Structures*. Cambridge university press. Cambridge, 1998.

145. **M.J. Pavier and M.P. Clarke**, *Experimental techniques for the investigation of the effects of impact damage on carbon-fibre composites. Composites Science and Technology*, **55**(2), 1995. 157-169.

146. **W.J. Cantwell and J. Morton**, *The impact resistance of composite materials — a review. Composites*, **22**(5), 1991. 347-362.

147. **G.A.O. Davies and X. Zhang**, *Impact damage prediction in carbon composite structures. International Journal of Impact Engineering*, **16**(1), 1995. 149-170.

148. **B. Hayman**, *Damage Assessment and Damage Tolerance of FRP Sandwich Structures*, in *Sandwich Structures 7: Advancing with Sandwich Structures and Materials*, O.T. Thomsen, E. Bozhevolnaya, and A. Lyckegaard, Editors. 2005, Springer Netherlands. p. 27-43.

149. **K. Dransfield, C. Baillie, and Y.-W. Mai**, *Improving the delamination resistance of CFRP by stitching—a review. Composites Science and Technology*, **50**(3), 1994. 305-317.

150. **A.P. Christoforou**, *Impact dynamics and damage in composite structures. Composite Structures*, **52**(2), 2001. 181-188.

151. **B. Mobasher**, *Mechanics of Fiber and Textile Reinforced Cement Composites*. CRC Press. Boca Raton, 2011.

152. **D.E. Grady and N.A. Winfree**, *Impact fragmentation of high-velocity compact projectiles on thin plates: a physical and statistical characterization of fragment debris. International Journal of Impact Engineering*, **26**(1–10), 2001. 249-262.

153. ***National Research Council***. *Structural Integrity of Offshore Wind Turbines: Oversight of Design, Fabrication, and Installation - Special Report 305*. The National Academies Press. Washington, DC, 2011.

154. **P. Brøndsted and R.P.L. Nijssen**, *Advances in wind turbine blade design and materials*. Woodhead Publishing Limited. Cambridge, 2013.

155. **D. Wood**, *Small Wind Turbines: Analysis, Design, and Application*. Springer. London, 2011.

156. **A.R. Jha**, *Wind Turbine Technology*. CRC Press. Boca Raton, 2010.

157. **T.W. Verbruggen**, *Wind Turbine Operation & Maintenance based on Condition Monitoring. Energy research centre of the Netherlands. ECN-C-03-047*, 2003.

158. **R.Raišutis, E.Jasiūnienė, and E. Žukauskas**, *Ultrasonic NDT of wind turbine blades using guided waves. Ultrasound*, **63**(1), 2008.

159. **K. Worden, N. Dervilis, and E. Cross**, *Nonlinear Robust Regression Analysis as a Means of Exploring SHM Data*, in *ISMA2014*. 2014: Belgium.

160. **N. Dervilis, K. Worden, and E.J. Cross**, *On Robust Regression Analysis as a Means of*

*Exploring Environmental and Operational conditions for SHM Data. Journal of Sound and Vibration* 2014 (under review/submitted).

161. **P.J. Rousseeuw and K.V. Driessen**, *A Fast Algorithm for the Minimum Covariance Determinant Estimator. Technometrics*, **41**, 1998.

162. **U. Greb and M.G. Rusbridge**, *The interpretation of the bispectrum and bicoherence for non-linear interactions of continuous spectra. Plasma Physics and Controlled Fusion*, **30**(5), 1988. 537.

163. **P.C. Paris, M.P. Gomez, and W.E. Andeson**, *A Rational Analytical Theory of Fatigue. University of Washington*, **13**(1), 1961.

164. **C.E. Feddersen**, *Discussion to : Plane strain crack Toughness Testing of high strength metallic materials. ASTM, Special Technical Publication*, (410), 1966.

165. **R.J.H. Wanhill**, *Durability Analysis Using Short and Long Fatigue Crack Growth Data*, in *Aircraft Damage Assessment and Repair*. 1991: Barton, Australia.

# Appendix A

## Values of $t_{a_s,n}$

| n | $\alpha_s$ =.10 | $\alpha_s$ =.05 | $\alpha_s$ =.025 | $\alpha_s$ =.01 | $\alpha_s$ =.005 |
|---|---|---|---|---|---|
| **1** | 3.078 | 6.314 | 12.706 | 31.821 | 63.657 |
| **2** | 1.886 | 2.920 | 4.303 | 6.965 | 9.925 |
| **3** | 1.638 | 2.353 | 3.182 | 4.541 | 5.841 |
| **4** | 1.533 | 2.132 | 2.776 | 3.474 | 4.604 |
| **5** | 1.476 | 2.015 | 2.571 | 3.365 | 4.032 |
| **6** | 1.440 | 1.943 | 2.447 | 3.143 | 3.707 |
| **7** | 1.415 | 1.895 | 2.365 | 2.998 | 3.499 |
| **8** | 1.397 | 1.860 | 2.306 | 2.896 | 3.355 |
| **9** | 1.383 | 1.833 | 2.262 | 2.821 | 3.250 |
| **10** | 1.372 | 1.812 | 2.228 | 2.764 | 3.169 |
| **11** | 1.363 | 1.796 | 2.201 | 2.718 | 3.106 |
| **12** | 1.356 | 1.782 | 2.179 | 2.681 | 3.055 |
| **13** | 1.350 | 1.771 | 2.160 | 2.650 | 3.012 |
| **14** | 1.345 | 1.761 | 2.145 | 2.624 | 2.977 |
| **15** | 1.341 | 1.753 | 2.131 | 2.602 | 2.947 |
| **16** | 1.337 | 1.746 | 2.120 | 2.583 | 2.921 |
| **17** | 1.333 | 1.740 | 2.110 | 2.567 | 2.898 |
| **18** | 1.330 | 1.734 | 2.101 | 2.552 | 2.878 |
| **19** | 1.328 | 1.729 | 2.093 | 2.539 | 2.861 |
| **20** | 1.325 | 1.725 | 2.086 | 2.528 | 2.845 |
| **21** | 1.323 | 1.721 | 2.080 | 2.518 | 2.831 |
| **22** | 1.321 | 1.717 | 2.074 | 2.508 | 2.819 |
| **23** | 1.319 | 1.714 | 2.069 | 2.500 | 2.807 |
| **24** | 1.318 | 1.711 | 2.064 | 2.492 | 2.797 |
| **25** | 1.316 | 1.708 | 2.060 | 2.485 | 2.787 |
| **26** | 1.315 | 1.706 | 2.056 | 2.479 | 2.779 |
| **27** | 1.314 | 1.703 | 2.052 | 2.473 | 2.771 |
| **28** | 1.313 | 1.701 | 2.048 | 2.467 | 2.763 |
| **29** | 1.311 | 1.699 | 2.045 | 2.462 | 2.756 |
| **∞** | 1.282 | 1.645 | 1.960 | 2.326 | 2.576 |

# Appendix B

## Normal Probability plot for each damage level

(a) Undamaged Plate

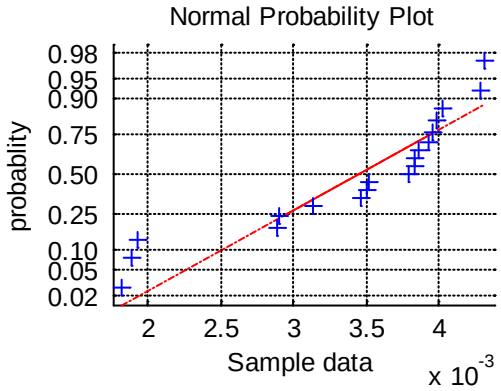


(b) 2mm crack

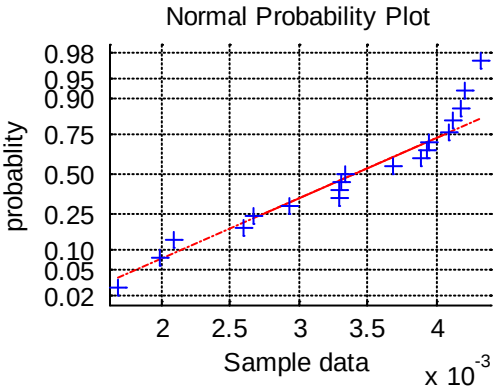


(c) 4mm crack

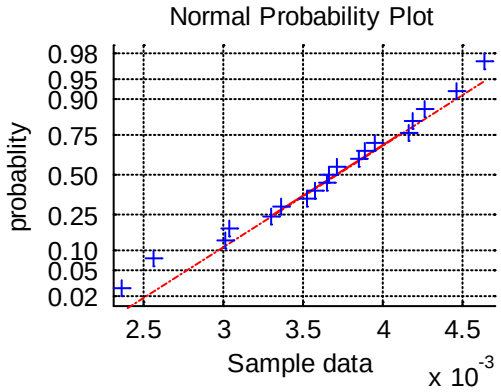


(d) 6mm crack

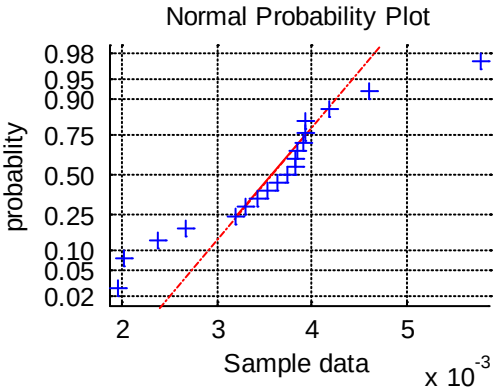


(e) 8mm crack

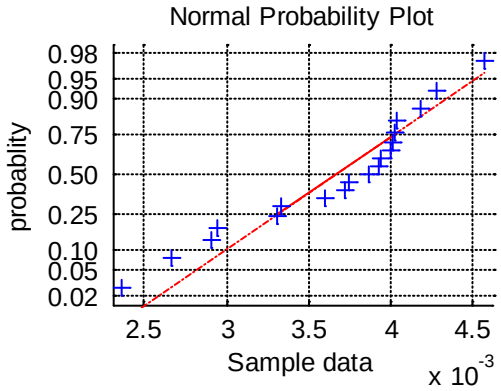


(f) 10mm crack

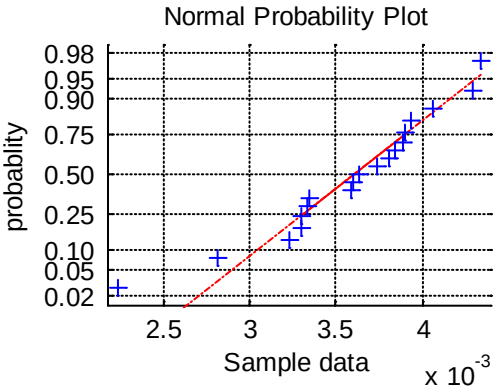

(g) 12mm crack

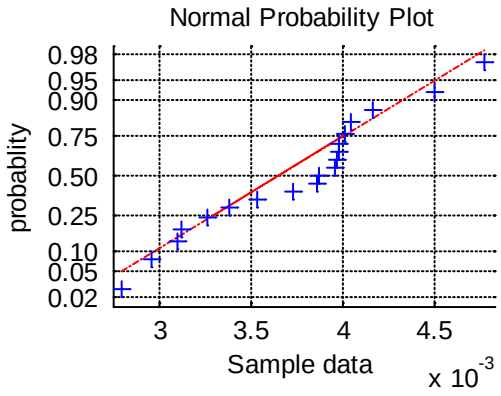


(h) 14mm crack

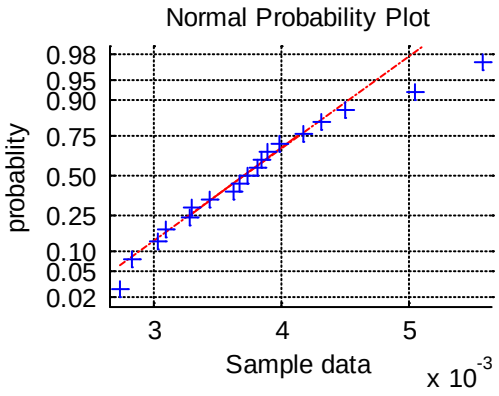


(i)16mm crack

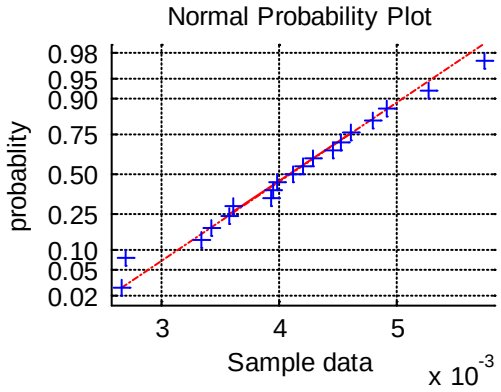


(j) 18mm crack

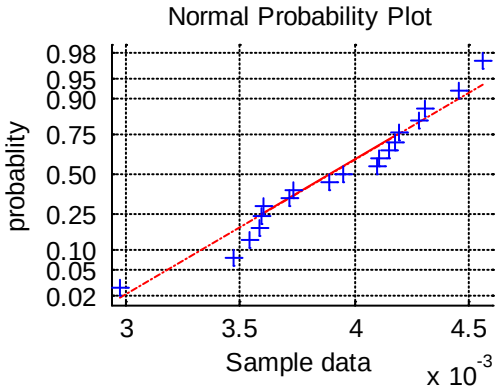


(k) 20mm crack

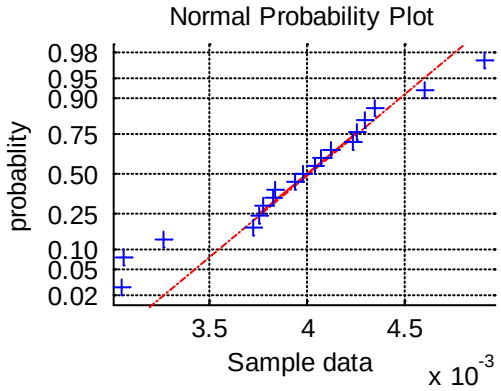


(l) 25mm crack

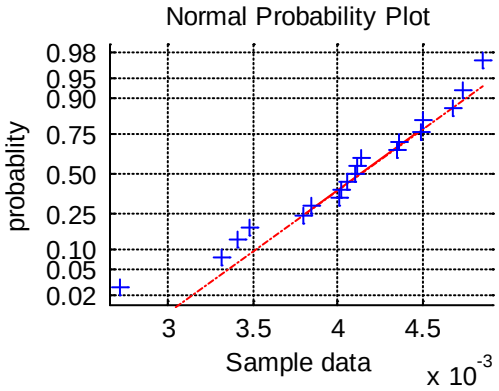

(m) 30mm crack

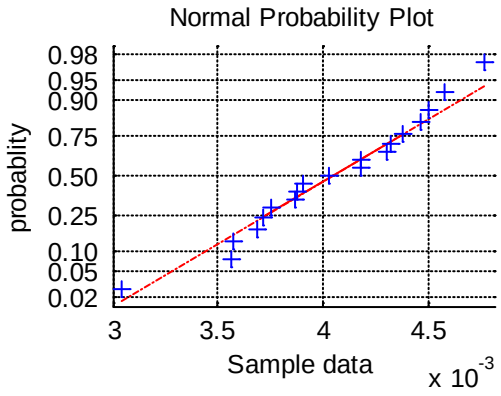


(n) 35mm crack

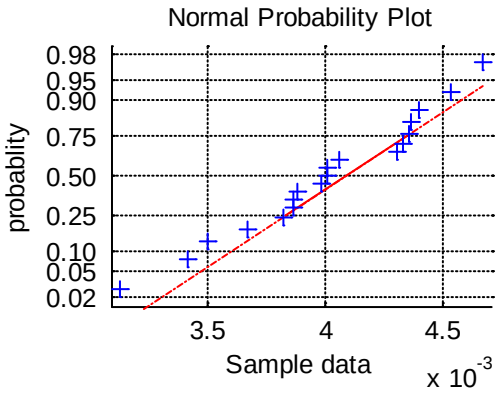

# Appendix C

## Fatigue test

Paris [163] presented that the crack growth period is governed by the crack propagation rate $da_c / dN$ and the range of stress intensity factor $\Delta K$ by the expression:

$$\frac{da_c}{dN} = z\Delta K^m \qquad \text{(C-1)}$$

where $a_c$ is the crack size, $N$ is the number of cycles, and $z$ and $m$ are material constants.

Taking logarithms of both sides of Equation (C-1) gives:

$$\log(\frac{da_c}{dN}) = m\log K + \log z \qquad \text{(C-2)}$$

The material constants $z$ and $m$ are determined by the loading frequency, environment and stress ratio, and can be derived from the slope and the intercept of the straight line calculated by logarithm (Figure C.1) [131]. Observed from Figure C.1, the lower asymptote at $\Delta K = \Delta K_{th}$ shows that there is no crack growth when the $\Delta K$ value is below this threshold level. Meanwhile, the upper asymptote occurs for a $\Delta K$ cycle when $K_{\max}$ approaches the fracture toughness $K_c$. That means that a $\Delta K$ cycle which exceeds the $K_c$ value will lead to a complete failure of the structure.

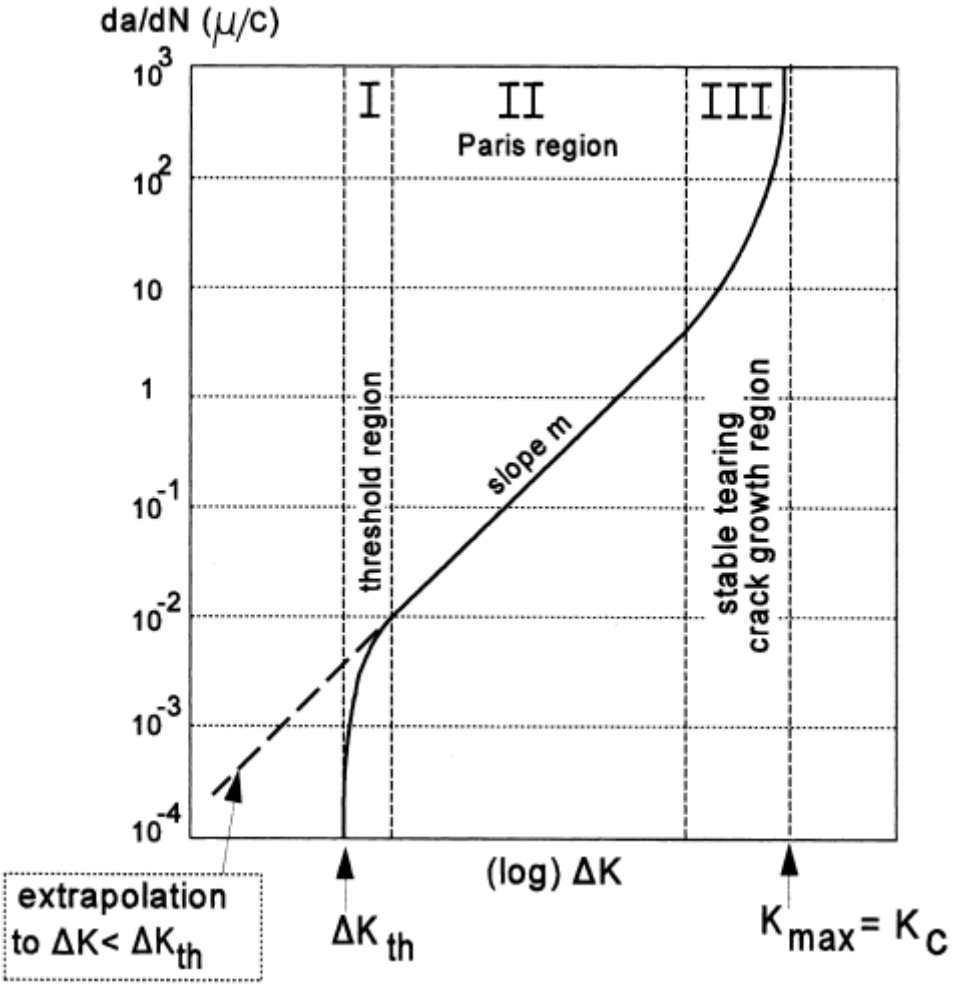


Figure C.1: The relationship between fatigue crack growth rate and stress intensity factor [133].

In the current study, a 3mm notch was made in the middle of the plate as a crack initiation source. When the external load is applied on the plate, the stress around the root of the notch is concentrated and results in a maximum stress $\sigma_{c,\max}$. In addition, a nominal stress $\sigma_0$ is defined as the stress when the stress concentration is removed. The ratio of $\sigma_{c,\max} / \sigma_0$ is named as the stress concentration factor $K_t$, which describes the severity of the stress distribution around a flaw of defined geometry and determines the crack initiation life [133].

After the crack initiation period, the followed crack growth period is the main concern of current study. The fatigue test produced various crack lengths in this period in order

to do the further acoustic tests. Gradually decreasing the applying stress in this case was helpful to control the crack growth rate. In the crack growth period, the stress intensity factor $K_c$ plays an important role in describing the stress concentration around the crack tip. It can be expressed as [133]:

$$K_c = \beta_c \sigma \sqrt{\pi a_c} \tag{C-3}$$

where $\beta_c$ is a dimensionless factor depending on the geometric aspects of the specimen, $\sigma$ represents the applied stress and $a_c$ is the crack length. In this study, the $\beta_c$ value for a specimen with a central crack can be obtained by [164]:

$$\beta_c = \sqrt{\sec(\pi a_c / b)} \tag{C-4}$$

where $b$ is the measured width of the specimen.

Wanhill [165] experimentally obtained the crack growth results for an aluminium 2024 plate with 2.3mm thickness which was also used in the current study. The results are shown in Figure 3.34. In order to avoid rapid fracture of the test specimen, as well as to predict the occurrence of expected crack length, a $K_c$ value of 10 was chosen to produce a small crack.

Rewriting Equation (3-5), the maximum applied stress $\sigma_{\max}$ can be expressed as:

$$\sigma_{\max} = \frac{K_c}{\beta_c \sqrt{\pi a_c}} = \frac{K_c}{\sqrt{\pi a_c \sec\left(\pi a_c / b\right)}} \tag{C-5}$$

Based on the elastic theory, the maximum applied load $P_{\max}$ can be obtained by:

$$P_{\max} = \sigma_{\max}(bh) \tag{C-6}$$

where $h$ is the thickness of the plate.

The stress ratio $R_s$ is used to define the ratio of minimum and maximum stress and can be written as:

$$R_s = \frac{\sigma_{\min}}{\sigma_{\max}} \tag{C-7}$$

where $\sigma_{\min}$ is the minimum stress. In the current study, $R_s$ is chosen as 0.25 to keep the test specimen always in tension.

According to Equation (C-7), the minimum applied load can be obtained by:

$$P_{\min} = \frac{\sigma_{\max}(bh)}{R_s} \tag{C-8}$$

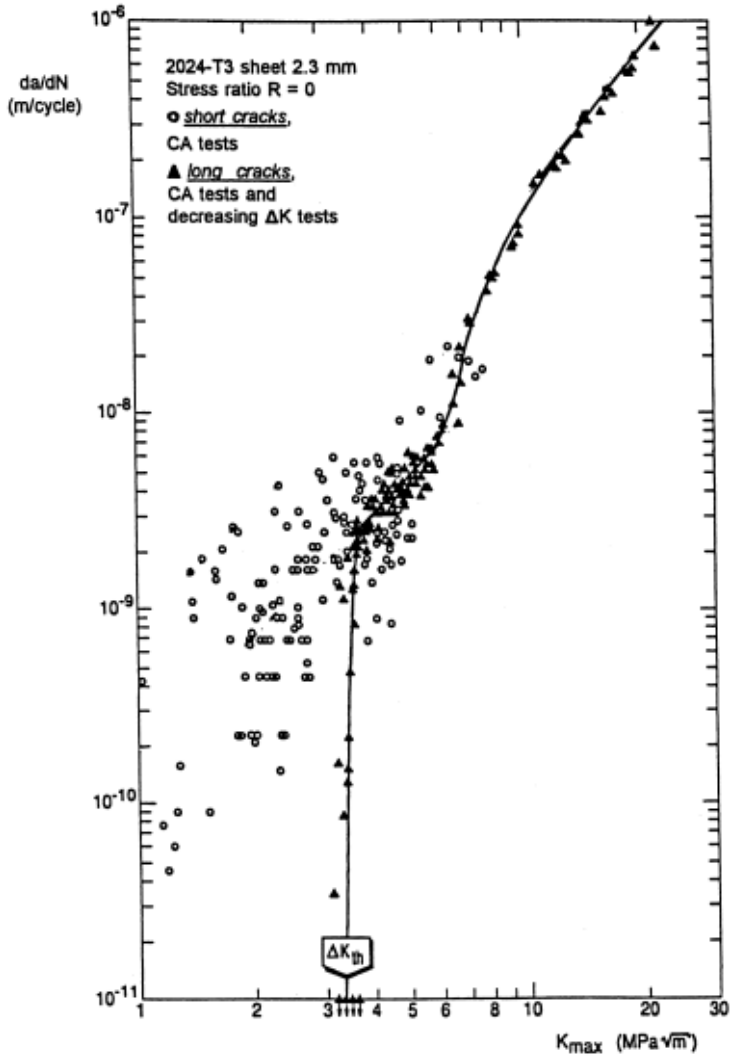


Figure C-2: Crack growth results for alumnium 2024 sheet with 2.3mm thickness [133].